Development of the shear wave magnetometer

Kilby, Charles F.

Award date:
1992

Awarding institution:
University of Bath

Development of the Shear Wave Magnetometer.

Submitted by Charles F. Kilby

for the degree of PhD

of the University of Bath

1992

ProQuest LLC
789 East Eisenhower Parkway
P.O. Box 1346
Ann Arbor, MI 48106-1346

PREFACE

Parts of this work were accepted for conference presentation and subsequent publication in the following paper:

Kilby C.F., P.T. Squire and S.N.M. Willcock : "Analysis and performance of a shear-wave magnetometer", Eurosensors VI, San Sebastian, October 1992. To appear in Sensors and Actuators

I would like to express my thanks to Patrick Squire for the project proposal and subsequent help and guidance throughout my studies. I am also very grateful to Dr. S.N.M. Willcock of Thorn EMI Central Research Centre for useful discussions and assistance along with Roger Twelvetrees and Ron Sanders for technical assistance. The project could not have been undertaken without the continued technical support of Mr B Ring, Mr. M. Tatar and Mr M Harriman of The University of Bath.

My thanks also extends to past and present members of the magnetism group for their support, namely Dr Mike Gibbs, Dr Andy Thomas, Dr Ian Collier, Mark Maylin, Del Atkinson, James Freestone, Selçuk Atalay and last but shortest Tamzin Lafford.

Many Thanks to Ann for waiting long hours at home and for feeding me during the final months of the project.

The project was funded by an SERC research grant and was sponsored through a CASE award by Thorn EMI Central Research Centre.

ABSTRACT

The project is concerned with a detailed investigation of the shear wave magnetometer initially proposed by Squire & Gibbs[1]. The magnetic field is measured via the magnetoelastic effect in amorphous magnetic ribbon material, using the phase of an ultrasonic shear wave. The amorphous ribbon shear wave assembly is known as the magnetic transducer. The magnetometer is a closed loop system which holds the amorphous alloy magnetic field transducer at zero field via a magnetic feedback loop. The closed loop system has the advantage of producing a linear system with a large dynamic range that is less sensitive to internal variations within the system electronics. The work was undertaken in order to investigate the operation of the magnetometer system and suggest improvements to optimise its performance.

A review of magnetic field measurement technology is made in order to place the system in perspective with other measurement techniques. Reviews of the magnetomechanical properties of amorphous ribbon and the propagation of magnetoelastic waves are also made as they represent essential background to the technique.

A study of the effect of an applied magnetic field on shear waves travelling along amorphous ribbon is made. The shear waves were found to display both a change in amplitude and a change in the total phase along the ribbon for a change in magnetic field. This is fully characterised.

Two models are developed to investigate the operation of the closed loop system. The linear response model examines the combined effects of both the amplitude and phase responses. These are approximated to by simple linear functions. The model demonstrated that the response of the magnetometer to magnetic field is highly dependent on the absolute phase change along the magnetic transducer.

The second model investigates the potential effects of changes in the absolute temperature on the magnetometer system. The results suggested a simple phase feedback temperature correction loop which is implemented and characterised.

The electronic components making up the system are characterised and optimised and generic points between different models of the same instrument discussed. The operation of the feedback loop is investigated.

The current ultimate performance of the system was measured as **100pT/Hz$^{1/2}$** at **1Hz** with a temperature coefficient of **9.5nT/°C**.

[1]Squire P.T. & Gibbs M.R.J. : "Shear-wave magnetometry using metallic glass ribbon.", *Electron. Lett.*, **23**, pp147-148, 1987.

Table of Contents

NOMENCLATURE

General Magnetic Parameters.

Symbol.	Description.	Units.
H	Magnetic field.	Am^{-1}
M	Magnetisation.	Am^{-1}
B	Magnetic Induction.	Tesla
μ_0	Permeability of free space.	Hm^{-1}
χ	Susceptibility.	-
D	Demagnetising factor (p56).	-
E_k	Anisotropy energy.	Jm^{-3}
K_n	Anisotropy constants.	Jm^{-3}
σ	Stress.	Nm^{-2}
λ_s	Saturation magnetostriction.	-
C_q	Magnetostriction quadratic coefficient.	$A^{-2}m^2$
Q^{-1}	Internal friction.	-
k	Magnetoelastic coupling constant.	-
B	Magnetoelastic coupling coefficient.	Jm^{-3}
θ	Magnetic moment orientation angles.	Radians
ϕ	(defined specifically where used in text.)	/
β		Degrees

Elastic-Wave Parameters.

μ	Shear modulus.	Nm^{-2}
E	Young's modulus.	Nm^{-2}
κ	Fractional change in shear modulus with applied field.	$A^{-1}m$
C , V_s	Shear-wave velocity.	ms^{-1}
t	Time	s
ω	Shear-wave oscillation frequency.	Rads/s
λ	Shear-wave wave length.	m
ϕ_0	Phase change along ribbon.	Radians
L	Length of ribbon.	m
ρ	Density.	Kgm^{-3}

d	Thickness of ribbon/film	m
A	Cross sectional area of ribbon/film	m^{-2}

System Model Parameters.

H_0	External field to be measured.	Am^{-1}
h	Modulation field.	Am^{-1}
i_m	RMS current producing modulation field.	A
ω_0	Shear wave propagation frequency.	Rads/s
ω_m	Modulation field frequency.	Rads/s
A_1	Shear-wave propagation amplitude.	V
A_2	Shear-wave received amplitude.	V
β	Mixer (phase detector) gain $\beta=kA_1$.	-
V_{mix}	Mixer (phase detector) output.	V
x	Normalised field to be measured $x=H_0/h$.	-
a_1	Amplitude of the shear-waves for no applied field.	V
b_1	Normalised linear amplitude response coefficient.	$A^{-1}m$
c_1	Field shift related to coercivity.	Am^{-1}
d_1	Normalised quadratic amplitude response coefficient.	$A^{-2}m^2$
e_1	Quadratic component of field shift.	Am^{-1}
a_2	Instrumentation phase offset	Radians
b_2	Linear Phase response coefficient	$Rads/Am^{-1}$
c_2	Field shift related to coercivity.	Am^{-1}
d_2	Quadratic phase response coefficient.	$Rads/A^2m^{-2}$
e_2	Quadratic component of field shift.	Am^{-1}
K	Feedback loop gain of magnetometer system.	-
τ	Lock-in amplifier time constant.	s
τ_{eff}	Feedback loop effective time constant.	s
T	Temperature	°C (or Kelvin)
L_T	Transducer length at a fixed arbitrary temperature.	m
μ_T	Shear modulus at a fixed arbitrary temperature.	Nm^{-2}
V_T	Transducer Volume at a fixed arbitrary temperature.	m^3
α_1	Coefficient of linear expansion	$°C^{-1}$
α_2	Temperature coefficient for shear modulus	$°C^{-1}$

γ	Quadratic coefficient describing the field dependence of the shear modulus $A^{-2}m^2$
η	Grouped constants $\eta = (\alpha_2 - \alpha_1)/2$
ψ	Grouped constant $\psi = (2C_q + \gamma)H_0$
$\mathbf{X_n}$ - $\mathbf{Y_n}$	Fourier coefficients

1 INTRODUCTION.

1.1 Aim of Study.

Many techniques have been developed for measuring magnetic fields. The method employed depends on the field range to be measured. Low magnetic field measurements are presently dominated by rugged relatively simple fluxgate magnetometers which through continual development over the past 30 years have attained a large dynamic field range with a minimum detectable magnetic field or noise floor in the order of some tens of picoteslas. More specialised techniques have been developed which can measure very low magnetic fields. These devices were initially developed for the measurement of the magnetic properties of materials although in many cases their application has diversified. The most sensitive and possibly the best known of these instruments are the SQUID magnetometers with noise floors in the order of a few femtoteslas. All the specialised techniques, however, tend to be limited by either their complexity or small dynamic ranges.

This study has been concerned with a novel method for measuring magnetic fields. The shear-wave magnetometer was initially proposed by Squire & Gibbs [1987a] as a technique which could possibly out-perform fluxgate magnetometers but retain a basic simplicity in design and ruggedness in construction. The aim of this work was to optimise the proposed system for the measurement of magnetic fields and to pin-point limiting factors in its operation.

The principle of operation of any magnetometer can be separated into two distinct regions into which investigations can be undertaken:

1. The physical quantity on which the magnetic measurement is based.

2. The method employed for extracting a measurement of the magnetic field from the physical quantity.

The work carried out was broadly separated into these two areas. The physical quantity was the magnetic behaviour of iron-based amorphous transition metal-metalloid alloys and can be quantified in the behaviour of the shear-wave magnetometer's magnetic transducer element. The remaining area is encompassed by the instrumentation system used to extract a measurement from the transducer element.

The remainder of this chapter covers a brief introduction to metallic glasses and their properties which relate to sensor applications. This is followed by an outline of the underlying principle behind the Shear-wave magnetometer. The ensuing chapter goes on to review low field magnetic field measurement. This is followed by a more detailed examination of the magnetomechanical and mechanical properties of the amorphous alloy related to the operation of the Shear-wave magnetometer. The investigations undertaken on the Shear-wave magnetometer are then presented and discussed.

1.2 Properties of Amorphous Metal Alloys for Sensor Applications.

A sensor or transducer is a device which transforms one physical phenomenon into a different physical quantity. In general a transducer is employed to transform a quantity which is difficult to measure directly into one which can be more easily manipulated. In the case of magnetic field measurements the desired result would be to produce an electrical signal, such as a voltage, which is proportional to the applied magnetic field. Amorphous metal alloys or metallic glasses exhibit a range of magnetomechanical properties. This is a transformation from a magnetic effect to a mechanical effect and in many cases has an accompanying inverse effect. Metallic glasses would therefore appear to be ideal transducer materials for a variety of sensor applications.

Iron-based amorphous transition metal-metalloids are alloys which typically contain anything from 40 to 80 atomic percent of Iron with the remainder of the composition being made up of proportions of elements such as nickel, cobalt,

molybdenum, manganese, chromium, silicon, boron or carbon. The alloys can be formed by a variety of techniques which tend to rely on the rapid quenching of the molten alloy in the liquid phase. This produces a structure with an atomic arrangement which did not have time before solidification to form into a more favourable crystalline lattice. In general the materials considered here were produced commercially by a melt spinning technique in which the molten alloy is forced onto the surface of a cooled rapidly revolving wheel. This produces long ribbons of material with typical minimum thickness dimensions of 15μm to 30μm and widths of up to 200mm. Limitations in the minimum attainable thickness are mainly of a mechanical nature such as controlling the separation between the spinning wheel and the molten alloy injection nozzle. On a laboratory scale however, materials as thin as 3μm have been achieved, Yagi *et al* [1988] and Choh *et al* [1992]. The limitations on the maximum thickness and ribbon width come about mainly due to problems in achieving the required cooling rate of $10^6 Ks^{-1}$ for the mass of material in question. Consideration is also given in chapter 4 to amorphous materials produced by sputter deposition. Methods of producing amorphous alloys are covered more extensively by Liebermann [1983] and Moorjani and Coey [1984]. An introduction to the sputter deposition of thin films can be found in Stuart [1983].

The mechanism of formation of the amorphous alloy produces an amorphous phase which is metastable with respect to both crystallisation and structural relaxation. The rate of change tends to be negligible at ambient temperatures but increases for higher temperatures approaching the crystallisation temperature. The amorphous phase can be stabilised by the introduction of solute atoms into the atomic arrangement such as silicon and carbon. These have the effect of inhibiting the migration and rearrangement of the atoms in the amorphous phase to that of a crystalline structure.

The mechanical properties of amorphous alloys result directly from the absence of grain boundaries in the amorphous phase unlike polycrystalline alloys. They are very

hard and flexible having yield strengths of 1500 to 2000 MPa, Boll [1989]. They tend to resist corrosion as there are no preferentially oxidised grain boundaries. Both mechanical and magnetic properties can also be tailored through compositional changes as the alloys are stable over a wide compositional range. Heat treatment of the material can also be used to modify the properties of the material although this causes enbrittlement of the alloy which reduces the number of potential applications. Chen [1983] reviews the changes in physical properties of metallic glasses during heat treatments. The dimensions of the available material do not tend to restrict their applications to magnetic sensors and in the case of the Shear-wave magnetometer is of a positive advantage. This is discussed in terms of the demagnetising field in chapter 3. The following sections outline the magnetic properties of the amorphous alloys pertinent to magnetic sensor applications. A review of amorphous alloys and sensing applications was given by Hernando *et al* [1988].

1.2.1 Magnetisation Curves.

The magnetisation curve of a ferromagnetic material can be used to illustrate a number of magnetic parameters. These parameters are useful in quantifying the magnetic behaviour of a material. Figure 1.1 shows a general magnetisation curve or hysteresis loop of the magnetisation of a material against the field applied to it.

$\mathbf{M_s}$, this is the saturation magnetisation and corresponds to the rotation of all the magnetic moments into the direction of the applied field. The absence of grain boundaries which would produce magnetic domain pinning sites and a low crystalline anisotropy result in amorphous alloys being magnetically soft. The susceptibility χ of a soft magnetic material is high and is defined in equation 1.1. Where **H** is the applied field and **M** the magnetisation.

$$\chi = \frac{M}{H} \qquad 1.1$$

The differential susceptibility is the slope of the magnetisation curve at any field H and is zero when the material is in magnetic saturation. The initial susceptibility is given by the value of the differential susceptibility on the initial magnetisation curve, Figure 1.1b, when the magnetisation and applied field are both zero, Jiles [1991]. A material with a high susceptibility is desirable for the production of Fluxgate magnetometers. This property of amorphous alloys has been implemented in these types of sensors by a number of authors Engelter [1986], Mermelstein [1986a] & [1992] and Nielsen *et al* [1990].

The magnetic induction of a material **B** is given by equation 1.2. μ_0 is the permeability of free space.

$$B = \mu_0 (H + M) \qquad 1.2$$

In an amorphous alloy the saturation induction $\mathbf{B}_s$ approximates to $B_s = \mu_0 M$ as a direct consequence of the high susceptibility.

$\mathbf{H}_c$ in Figure 1.1 is the coercivity. This is the field needed to reduce the magnetisation to zero from saturation and is distinct from the coercive field which is the magnetic field needed to reduce the magnetisation to zero from an arbitrary level.

$\mathbf{M}_r$ is the remanent magnetisation, the magnetisation of the material when the applied field is reduced to zero after having first driven the material into saturation. The remanence ratio is given by the ratio of the remanent magnetisation to the saturation magnetisation.

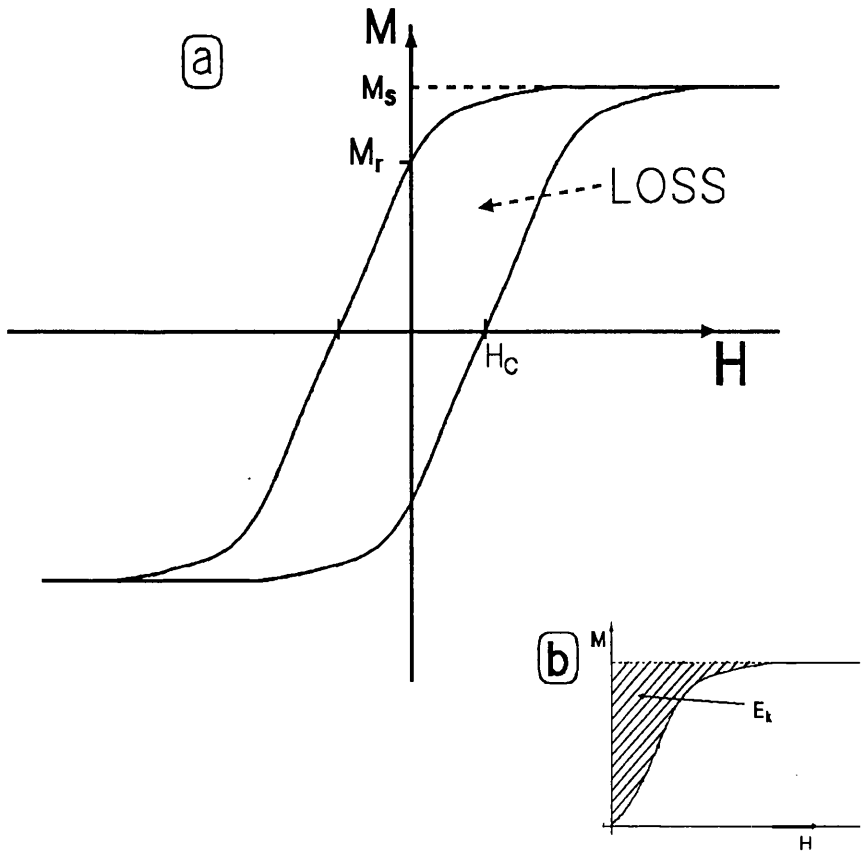

Figure 1.1a Shows an idealised major hysteresis loop.

1.1b Shows the initial magnetisation curve from zero applied field to magnetic saturation of the magnetisation. The parameters depicted in the figures are discussed in the text.

The energy loss per unit volume of the material in taking the material through a complete magnetisation cycle is also shown in Figure 1.1. This loss includes eddy current losses if the magnetisation cycle is not traversed quasi-statically, Cullity [1972]. Eddy current losses in amorphous alloys are not as pronounced as for polycrystalline iron as iron-based amorphous alloys have resistivities an order of magnitude greater than that

for Iron, Rao [1983].

$\mathbf{E_k}$ as defined in Figure 1.1 is the anisotropy energy and is the energy per unit volume required to rotate all the magnetic moments into the direction of the applied field. This has associated with it an anisotropy field $\mathbf{H_k}$ which is the magnitude of the applied field which rotates all the moments into its direction. The anisotropy energy can be divided into a number of separate contributing energies, Crystal, Shape, Stress, Induced and Exchange. Crystal anisotropy tends to be negligible in amorphous alloys because of the absence of any long range order. As the name suggests the anisotropy energies have associated directionalities. The total anisotropy energy will be the tensor sum of these and in general will define an axis of minimum energy known as the easy axis. Magnetic moments will tend to lie in the easy axis because of this favourable energy minimum. Rotation out of the easy axis into a different magnetisation direction requires energy input. In general for a well defined uniaxial anisotropy the anisotropy energy at an angle ϕ away from the easy axis is given by equation 1.3, where $\mathbf{K_n}$ are constants, Jakubovics [1987].

$$E_k = \sum_{n=0}^{\infty} K_n \sin^{2n}\phi \qquad 1.3$$

In general in as cast amorphous alloy ribbons the main contribution to the anisotropy is from cast in stresses, Hodson [1986]. The casting stresses can be removed in an annealing process leaving a sample with shape dominated anisotropy. An easy axis can then be defined by a field annealing process discussed more fully in chapter 3.

1.2.2 Magnetostriction.

When a ferromagnet is magnetised or cooled from the paramagnetic state to a temperature below its Curie point it invariably undergoes a change in its dimensions. The dimensional change can be divided up into three contributing effects.

1. In the case of cooling to a temperature below the Curie temperature the effect is known as spontaneous magnetostriction.

2. Forced volume magnetostriction is the change in volume of the material with applied field and may reach values as high as several percent. This however, is only significant at high fields or as the temperature approaches absolute zero, Moorjani and Coey [1984]. Volume magnetostriction, therefore has little relevance to practical device applications.

3. The more important effect for sensor applications is the change in strain experienced on the application of a magnetic field and was first observed by Joule [1842]. The expansion of a material in an applied field is generally referred to as positive magnetostriction. In some cases notably Nickel negative magnetostriction occurs and a contraction is observed. The converse of magnetostriction is the stress contribution to the anisotropy energy. For a positively magnetostrictive material such as a high Iron content amorphous alloy, applying a tensile stress produces an easy axis parallel to it. The contribution to the anisotropy energyE_σ in the direction θ from the applied stress σ is given by equation 1.4, Cullity [1972].

$$E_\sigma = \frac{3}{2}\lambda_s \sigma \sin^2\theta \qquad 1.4$$

λ_s is the saturation magnetostriction, the fractional change in length between a demagnetised material and the material at magnetic saturation measured along the direction of the applied field. For an isotropic medium such as an amorphous alloy with no well defined easy axis the magnetostriction at an angle θ from the field direction is given by equation 1.5, Jiles [1991].

$$\lambda_s(\theta) = \frac{3}{2}\lambda_s\left(\cos^2\theta - \frac{1}{3}\right) \qquad 1.5$$

Where λ_s is the saturation magnetostriction along the direction of magnetisation.

The magnetostriction of materials is very structure sensitive which makes it difficult to produce a general expression for the relation between magnetostriction and field. For a material with a uniaxial anisotropy and a field applied perpendicular to this an expression for the magnetostriction in terms of the magnetisation can be formulated, equation 1.6 Jiles [1991].

$$\lambda(M) = \frac{3}{2}\lambda_s\left(\frac{M}{M_s}\right)^2 \qquad 1.6$$

Figure 1.2 shows the magnetostriction measured along the direction of the applied field for a ribbon of commercially available amorphous alloy magnetised along the long axis. The sample had an induced uniaxial anisotropy in the plane of the ribbon, perpendicular to the long axis, obtained through field annealing, Thomas [1990]. The magnetostriction about zero field is quadratic in behaviour and can be described by a quadratic coefficient C_q, Thomas [1991]. A high quadratic coefficient is synonymous with very pronounced changes in the magnetostriction with magnetic field. This effect has been employed by a number of authors to produce magnetostrictive magnetometers, Dandridge *et al* [1980], Kersey *et al* [1984], Pratt *et al* [1984] and Pantinakis and Jackson [1986].

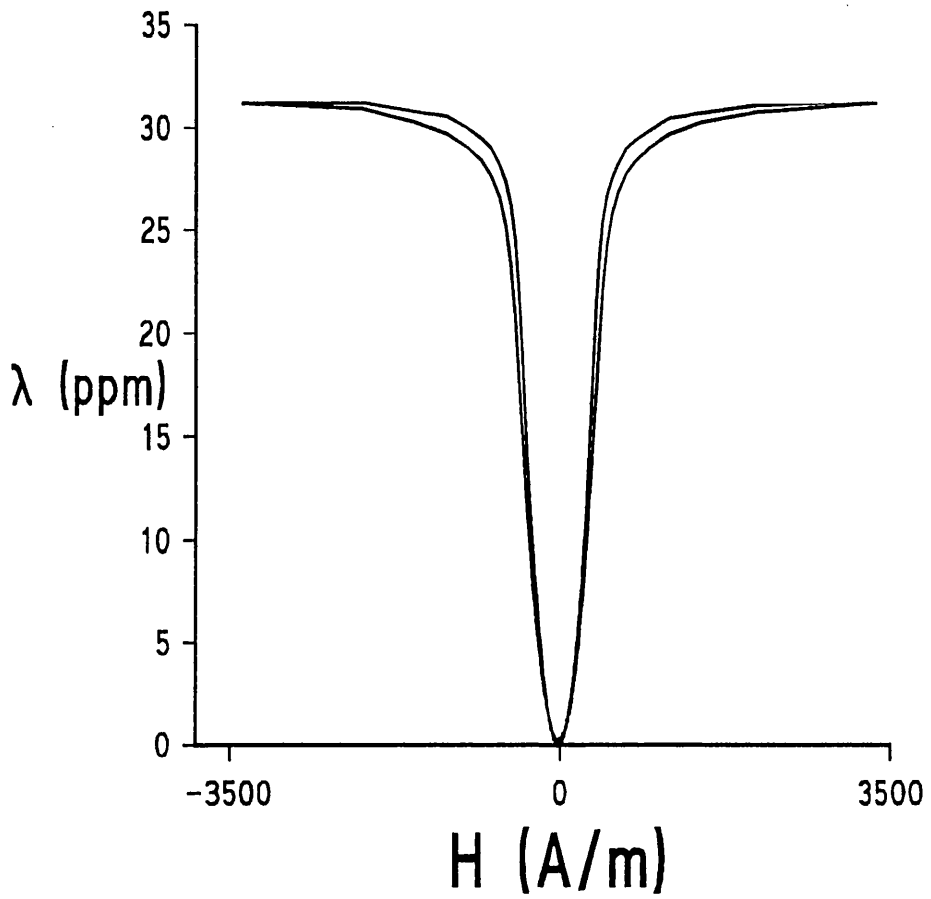

Figure 1.2 Change in length with applied field for a ribbon field annealed across its width. (VAC0040 $Fe_{40}Ni_{40}B_{20}$ Transverse Field Annealed 350°C for 40min).

1.2.3 Field Dependence of the Elastic Moduli.

The elastic moduli of ferromagnetic materials are field dependent as a direct result of their magnetostriction. The change in Young's modulus ΔE, when a demagnetised sample of a ferromagnetic material is magnetically saturated is of the order of six percent for Nickel and less than one percent for pure Iron, Cullity [1972]. The change in the Young's modulus for an amorphous alloy however, can be of the order of eighty percent

and depends on the composition and the heat treatment the alloy has undergone, Berry and Pritchet [1976a].

On the application of a stress to a demagnetised specimen both elastic and magnetoelastic strain are produced and the Young's modulus in the demagnetised state is given by equation 1.7.

$$E_d = \frac{\sigma}{\varepsilon_{el} + \varepsilon_{me}} \qquad 1.7$$

Where σ is the stress, ε_{el} the elastic strain and ε_{me} the magnetoelastic strain. For a magnetically saturated specimen the magnetoelastic strain is zero as no further domain rotation occurs and the Young's modulus in this case is given by equation 1.8.

$$E_s = \frac{\sigma}{\varepsilon_{el}} \qquad 1.8$$

The fractional change in the Young's modulus is thus given by equation 1.9, Cullity [1972].

$$\frac{\Delta E}{E_d} = \frac{E_s - E_d}{E_d} = \frac{\varepsilon_{me}}{\varepsilon_{el}} \qquad 1.9$$

For an isotropic material the ΔE effect or fractional change in Young's modulus can be related to other elastic moduli such as the shear modulus through Poisson's ratio ν. The shear modulus μ is given by equation 1.10, Thurston [1964].

$$\mu = 2(1+\nu)E \qquad 1.10$$

An example of the typical form of the field dependence of the Young's modulus in an amorphous alloy is shown in Figure 1.3, Thomas [1990]. The field dependent

modulus normalised to the modulus at magnetic saturation is an even function with applied fields. The alloy used was the same as that used to produce Figure 1.2 and has undergone a similar magnetic anneal.

The ΔE effect has been employed mainly in the construction of variable signal delay lines and examples of such devices can be seen in Webb *et al* [1979] and Imamuta *et al* [1985]. The principle of the variable delay line is the underlying basis for the operation of the Shear-wave magnetometer.

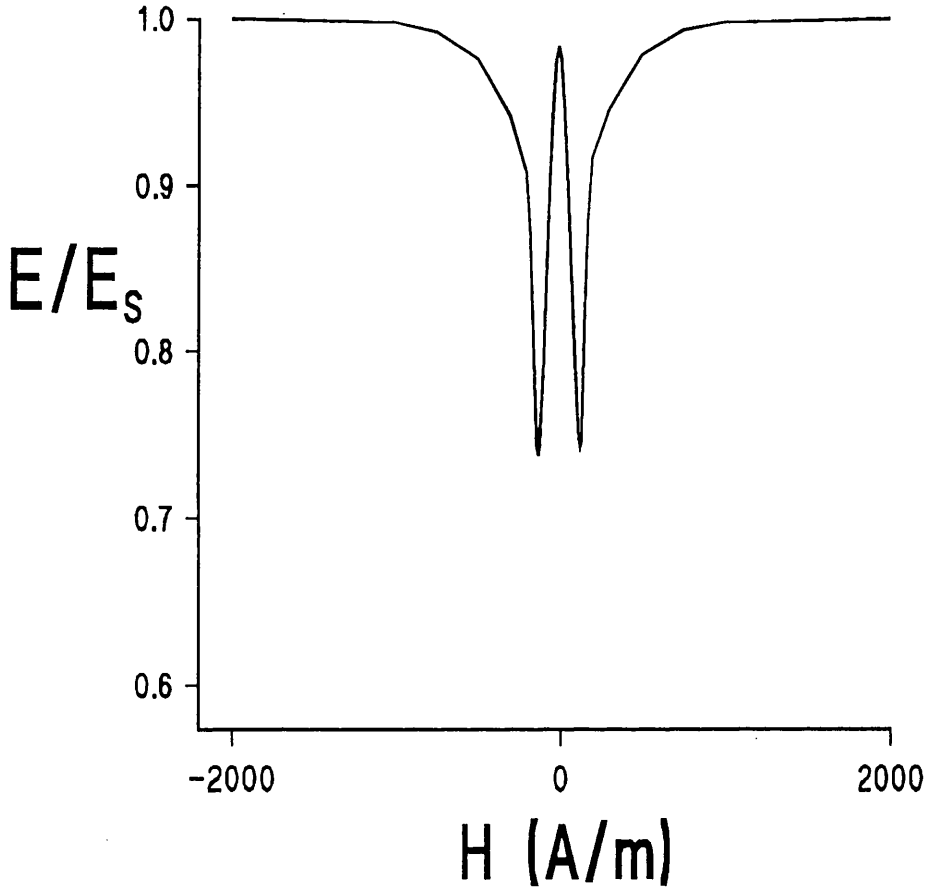

Figure 1.3 Change in Young's modulus with applied field for a ribbon annealed across its width. (VAC0040 $Fe_{40}Ni_{40}B_{20}$ T.F.A. 350°C 10 min)

1.2.4 The Shear-wave Magnetometer.

The Shear-wave magnetometer is based on the magnetoelastic effect and specifically the magnetic field dependence of the shear modulus. The technique depends on the change in the propagation velocity of an elastic wave in a medium if the elastic moduli of the medium change. Amorphous metal alloys would appear ideal for this type of transducer application as the large changes in elastic moduli with applied field suggests a large change in the propagation velocity of elastic waves along a length of amorphous ribbon.

1.2.4.1 Underlying Principles of Operation.

The elastic waves in solids are normally combinations of many modes and types of modes. The longitudinal and flexural groups of modes depend on two elastic moduli whereas the shear modes depend only on one elastic modulus. If shear-waves are launched along a ribbon and the ribbon is below a certain thickness, it is possible to restrict the modes present to the point where only the nondispersive zero order shear-wave is propagated, Meeker and Meitzler [1964]. The transverse shear-wave velocity in the medium is then given by equation 1.11, where μ is the shear modulus of the material and ρ its density.

$$C = \sqrt{\frac{\mu}{\rho}} \qquad 1.11$$

Shear-waves can be launched along a ribbon using a piezoelectric transducer bonded to the ribbon surface. This is a conventional method for launching shear-waves in thin ribbon shear mode strip delay lines, May [1964]. Figure 1.4 depicts a ribbon of material of length **L** with two piezoelectric transducers mounted at each end. The transducers are manufactured so that their polarisation direction is along their long axis.

The transducer T_1 is shown as the transmitter and when a sinusoidally varying electric field is applied across it, it propagates shear-waves along the ribbon. The transducer T_2 transforms the phase shifted shear wave back to a sinusoidal signal after transmission along the ribbon. The whole assembly of piezoelectric transducers and ribbon is referred to as the magnetic field transducer.

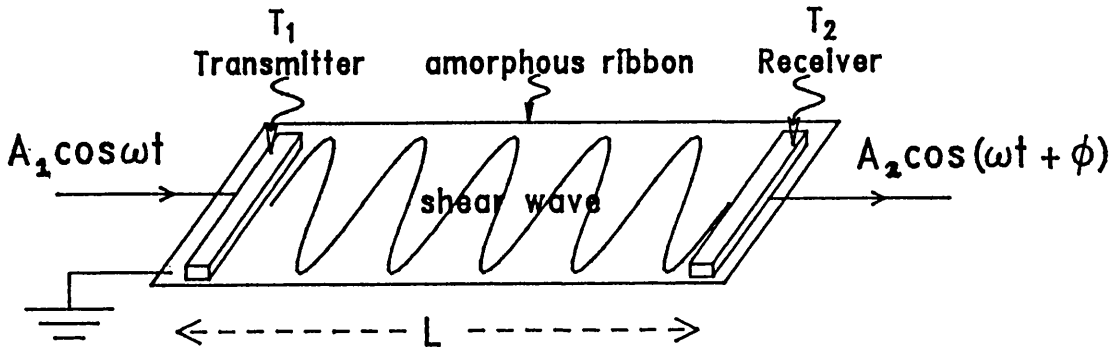

Figure 1.4 Schematic of the magnetic field transducer.

A measurement of the magnetic field can be achieved by measuring the change in the velocity of the shear-wave along the ribbon via a measurement of the change in the phase of the wave detected by the piezoelectric transducer T_2. The phase difference between the two transducers for a wave travelling along a length of ribbon is given by equation 1.12.

$$\phi = \frac{\omega L}{c} = \omega L \sqrt{\frac{\rho}{\mu}} \qquad 1.12$$

For an amorphous alloy both the elastic moduli and the length of the sample are dependent on the magnetic field applied. The change in phase observed at the piezoelectric transducer $\mathbf{T_2}$ on the application of a magnetic field is thus given by equation 1.13.

$$\Delta\phi = \frac{\pi L}{\lambda}\left[\frac{2}{L}\frac{\partial L}{\partial H} - \frac{1}{\mu}\frac{\partial \mu}{\partial H}\right]\Delta H \qquad 1.13$$

Where $(1/L)(\partial L/\partial H)$ is the fractional change in length per unit applied field and $(1/\mu)(\partial \mu/\partial H)$ is the fractional change in the shear modulus per unit applied field. Examination of the illustrative field dependences of magnetostriction and Young's modulus in figure 1.2 and figure 1.3 respectively would suggest that as the fractional change in length with applied field is much smaller than the field dependent modulus, the magnetostriction term could be ignored. The field dependent phase change would then be given by equation 1.14.

$$\Delta\phi = -\frac{\pi L}{\lambda}\left(\frac{1}{\mu}\frac{\partial \mu}{\partial H}\right)\Delta H \qquad 1.14$$

The magnetic field transducer thus performs a transformation from a magnetic field measurement to a phase measurement.

1.2.4.2 Practical Shear-wave Magnetometer.

Figure 1.5 shows a schematic diagram of the closed loop Shear-wave magnetometer system as described by Squire and Gibbs [1988a]. The magnetic field transducer consists of a length of amorphous ribbon with piezoelectric transducers T_1 and T_2 bonded to the amorphous ribbon using either silver-loaded epoxy or cyanoacrylate adhesive.

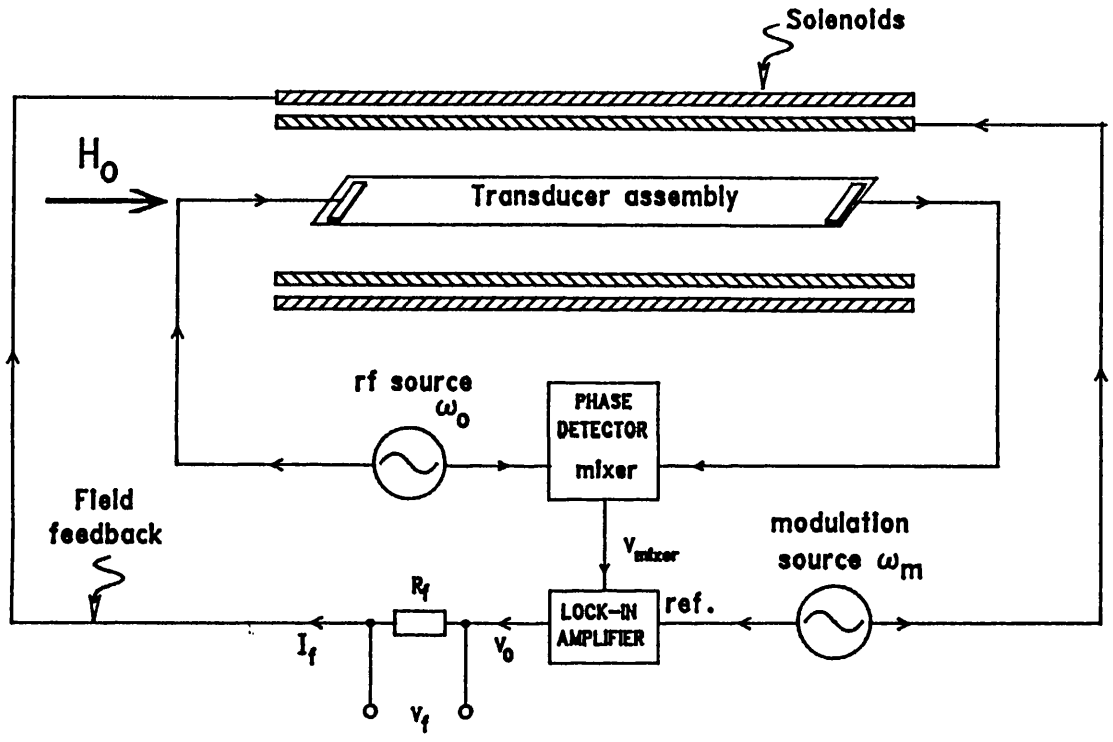

Figure 1.5 Closed loop shear wave magnetometer system.

The typical phase dependence with magnetic field, observed about zero applied field, for a shear wave travelling along the amorphous alloy ribbon is shown in Figure 1.6. The phase response is an even function with magnetic field as a direct consequence of the even nature of the elastic modulus dependence on magnetic field. ϕ_0 is the fixed phase shift for the length of ribbon **L** and $\Delta\phi$ is the additional magnetically induced phase shift for any applied field **H**. Thermal and mechanical noise produce unacceptably high phase noise if the system is operated at d.c. The phase is thus modulated by applying a low frequency oscillating magnetic field to the amorphous ribbon via a solenoid coil. The application of the modulation signal at a fixed field of $\mathbf{H_0}$ is also depicted on Figure 1.6 along with the resultant field modulated phase. $\mathbf{H_0}$ is the external magnetic field which is to be measured and **h** is the modulation amplitude or depth, at the modulation frequency ω_0. The even nature of the phase response about zero field gives a modulated phase output which put simply consists of a Fourier series of the modulation signal. The magnitude of the harmonic terms depends on the exact nature of the phase response and the magnitude of $\mathbf{H_0}$.

The important features of the modulated phase response can best be considered if for simplicity the phase response is assumed to be linear. When no external field is applied to the transducer arrangement the modulated phase consists purely of a term at twice the modulation frequency. If the externally applied field is greater than the modulation depth then the modulated phase is at the modulation frequency. If the externally applied field is less than the modulation depth but not zero then the modulated phase consists of a field dependent fourier series containing a term at the modulation frquency as well as higher harmonics.

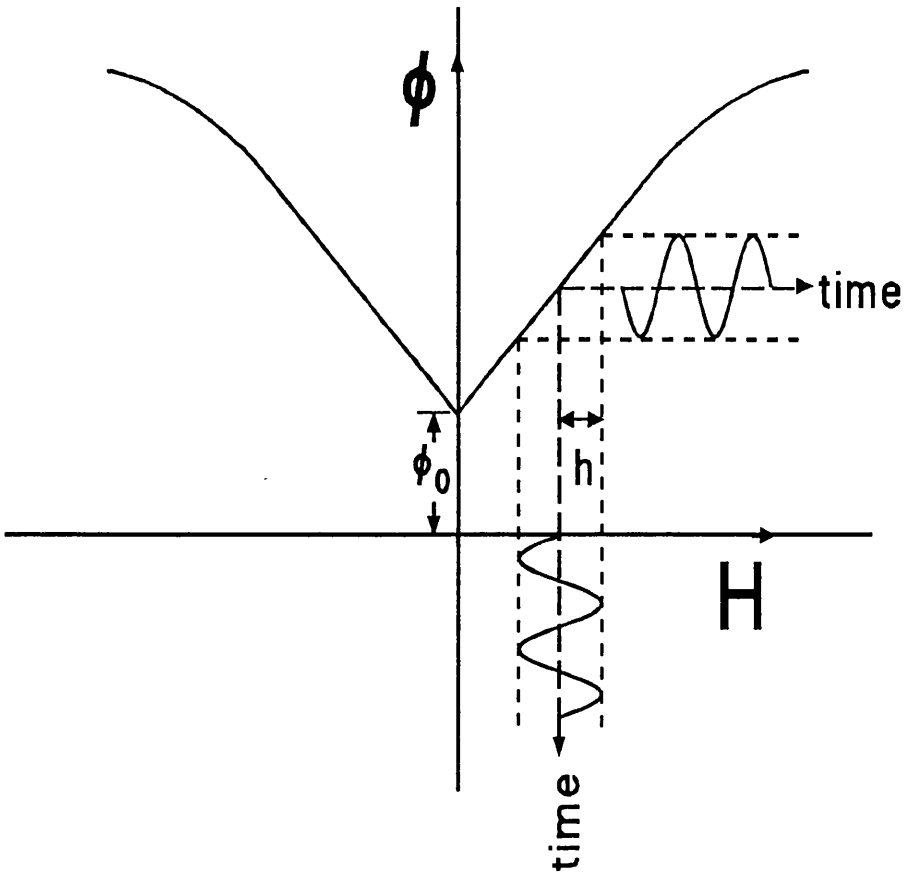

Figure 1.6 Magnetic field transducer phase characteristic.

The field modulated phase change is detected using a double balanced mixer. The operation of an ideal mixer is to multiply the two input waveforms. If the drive signal for transducer T_1 is taken as the reference or local oscillator signal equation 1.15 and the output from the transducer T_2, equation 1.16, is applied to the signal input of the mixer then the output of the mixer is given by equation 1.17.

$$V_1 = A_1 \cos \omega t \qquad 1.15$$

$$V_2 = A_2 \cos(\omega t + \phi_0 + \Delta\phi) \qquad 1.16$$

$$V_{mix} = \frac{kA_1A_2}{2}[\cos(2\omega t + \phi_0 + \Delta\phi) + \cos(\phi_0 + \Delta\phi)] \qquad 1.17$$

$$\Delta\phi = f(H_0 + h\sin\omega_m t)$$

k is a constant associated with the gain of the mixer and ω is the oscillation frequency of the shear-waves. Ignoring high frequency terms the output of the mixer is a function of the fixed phase and the field dependent phase which is modulated at a frequency ω_m. The output of the mixer is thus a function of the phase change and contains a term at ω_m which can be measured using a lock-in amplifier referenced to the modulation frequency. The form of the lock-in amplifier output is shown in Figure 1.7. The output of the lock-in amplifier is used to drive a solenoid in a field nulling feedback loop configuration. Any shift away from the null field condition on the phase response will be detected as a term at the modulation frequency by the lock-in amplifier. Provided the lock-in amplifier reference phase is correctly selected a corresponding nulling field is generated in the feedback solenoid; this nulls the applied field and maintains the operation of the system about the zero field position on the phase response. The current in the feedback loop is thus a direct linear measure of the applied field. The magnetometer is a vector device which can measure fields at frequencies down to d.c. The dynamic range of the magnetometer system is limited only by the ability of the lock-in amplifier to drive the feedback loop.

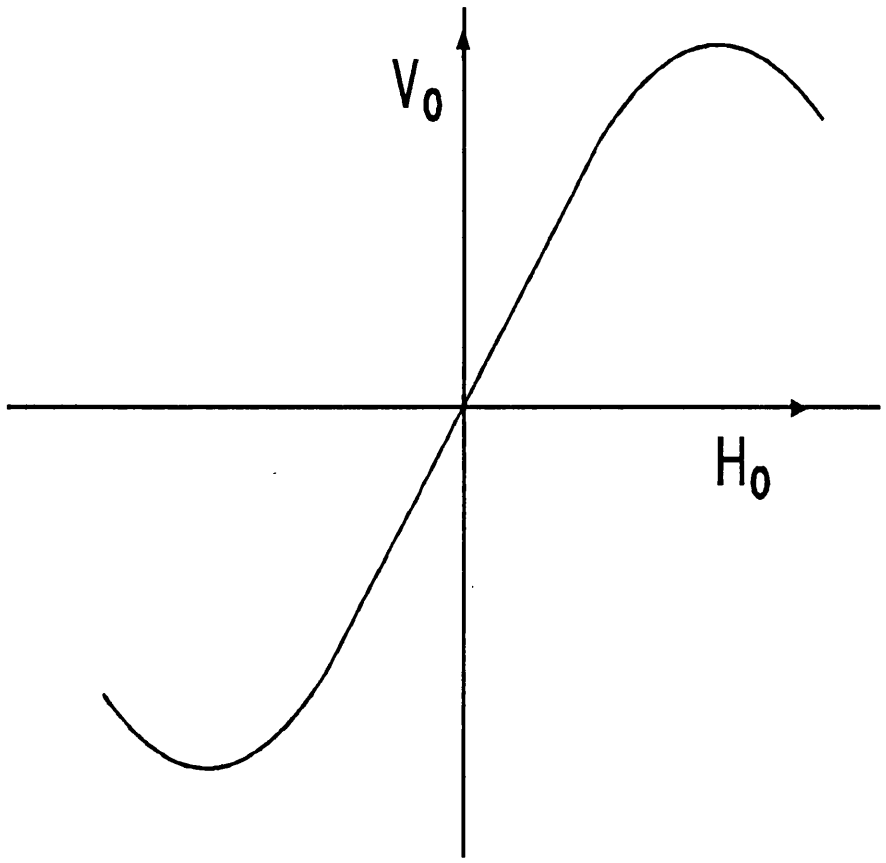

Figure 1.7 Lock-in amplifier output voltage against applied field

1.2.4.3 Performance of the Shear-wave magnetometer.

A minimum detectable field of the order of 2.5pT has been proposed for shear-waves at a frequency of 20MHz propagating along a 1m length of ribbon (Squire and Gibbs [1987a]). A conservative estimate of 0.025 per (A/m) for the fractional change of the shear modulus with applied field was made from figures available on binary alloys, Kikuchi *et al* [1978]. In practice Squire and Gibbs [1988a] have achieved results of the order of 2.5nT in a bandwidth of 1.6Hz, with a drift of similar order over the recording time of three minutes. This result was achieved using a 25cm length of 'as received'

$Fe_{40}Ni_{40}B_{20}$ (VAC0040) amorphous ribbon. In proposing the minimum detectable field an estimate was made of the fractional change in shear modulus per unit applied field. For as-received material this is quite small and thus will affect the sensitivity. Although the field annealed ribbons are more favourable for this application because of their increased response to magnetic field, the increased magnetoelastic coupling brings about a large attenuation of the shear-waves in the annealed ribbons and a loss of the field dependent phase response possibly due to stresses introduced in mounting the transducer arrangement, Kiss *et al* [1989]. For both 'as received' and annealed ribbons there is a steep fall off of the received amplitude at high frequencies which limits the operation frequency of the system, Tsuya *et al* [1977] and Squire and Gibbs [1988a]. The phase noise as measured by Squire and Gibbs [1988a] was, however, substantially lower than that used in the estimation of the magnetometers performance. The previous effects are discussed further in chapters 3 and 4.

2 REVIEW OF LOW FIELD MAGNETIC MEASUREMENTS.

2.1 Introduction.

The science of magnetic field measurement has been well developed for a number of years. There are numerous techniques, none of which are universally applicable to all types of measurements. The choice of technique is governed mainly by the field range to be measured; this can be anything from a few femtoteslas up to a few Tesla. Other considerations include temperature, large background field fluctuations, very stable field environments, fixed or swept fields, short or long time observations and cost.

Three review papers concerning magnetic measurements were presented at the 12th Annual Conference On Magnetism And Magnetic Materials, Dwight [1967], Foner [1967] and Humphrey [1967]. These papers serve as a good review of the development of magnetic field measurement up to that time. They were supplemented by a further review by Foner [1981] which emphasized that the basic principles had remained the same but had been refined and augmented by novel developments. This refinement has continued over the past decade and an increased interest has been shown in utilising the favourable magnetic properties of amorphous metal alloys. Mermelstein [1986a], Engelter [1986], Nielsen *et al* [1990] and Sobhendu *et al* [1992] have used amorphous alloys in an attempt to improve established measurement techniques. New methods have also been developed such as the magnetostrictive magnetometers, Pantinakis and Jackson [1986] and Mermelstein and Dandridge [1987a]. Another device which relies on the large magnetic field dependent strain is the Fibre Optic Magnetometer which was proposed from work carried out by Yariv and Winsor [1980]. The Shear-wave Magnetometer which is the focus of this study can also be grouped with these new devices and relies on the field dependence of the shear modulus μ.

The following chapter reviews well established techniques in the low field region,

such as the fluxgate magnetometer, the resonance magnetometer and thin film magnetometers which have minimum sensitivities in the picotesla and nanotesla ranges, and the SQUID magnetometer which has minimum sensitivities in the femtotesla range. These low field technologies are studied so as to demonstrate the present state of the art in this field region and to emphasise the importance of the studies being carried out on the Shear-wave magnetometer and the strain dependent magnetometers which are also covered in this review. These technologies are being developed with the intention of obtaining a measurement technique which can reliably and cheaply cover the field range between the SQUID magnetometer and the fluxgate magnetometer and other devices.

2.2 Fluxgate Magnetometer.

2.2.1 Basic Fluxgate Operation.

The Fluxgate magnetometer is based on the variation of the permeability of a core of magnetic material. The basic Fluxgate sensor consists of a core of magnetic material surrounded by a pick-up coil as shown in Figure 2.1.

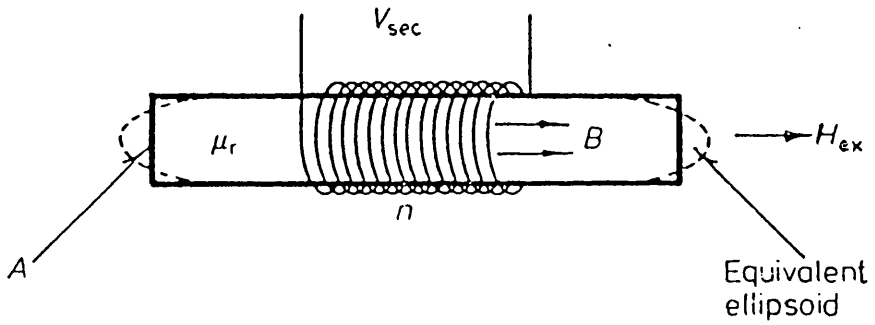

Figure 2.1 The basic Fluxgate arrangement, after Primdahl [1979].

The external field $\mathbf{H}_{ex}$ along the core axis produces a magnetic flux **BA** in the core of cross sectional area A. If the permeability μ_r of the core material is changed, the flux changes and a voltage $\mathbf{V}_{sec}$ is induced in the pick up coil given by equation 2.1

$$V_{sec} = nA\frac{dB}{dt} \qquad 2.1$$

B is proportional to $\mathbf{B}_{ex}$ for small $\mathbf{B}_{ex}$ and the factor of proportionality μ_a is the apparent permeability, equation 2.2. The apparent permeability depends on the core material and on the geometrical shape of the core. The effects of the material geometry are discussed in chapter 3.3. A theoretical and experimental treatment of this effect is given by Primdahl [1979] and Primdahl *et al* [1989].

$$B = \mu_a B_{ex} \qquad 2.2$$

Figure 2.2 shows a typical magnetisation curve for a ferrite material. The slope μ_a varies periodically when a periodically changing magnetising field H is applied. This can be achieved in the arrangement shown in Figure 2.1 using a drive coil also surrounding the core. The drive field also has the effect of inducing a large voltage in the pick-up coil. One method for overcoming this large induced signal is to use a sensor arrangement known as a Vacquier sensor which was developed in the early 1940s (Gordon and Brown [1972]); other sensor arrangements are also used and will be discussed later. The Vacquier sensor consists of two oppositely magnetised cores placed inside the same pick-up coil so that the opposed magnetisations cancel and the only flux change is that caused by the constant external field $\mathbf{H}_{ex}$, the field to be measured and the changing permeability μ_a.

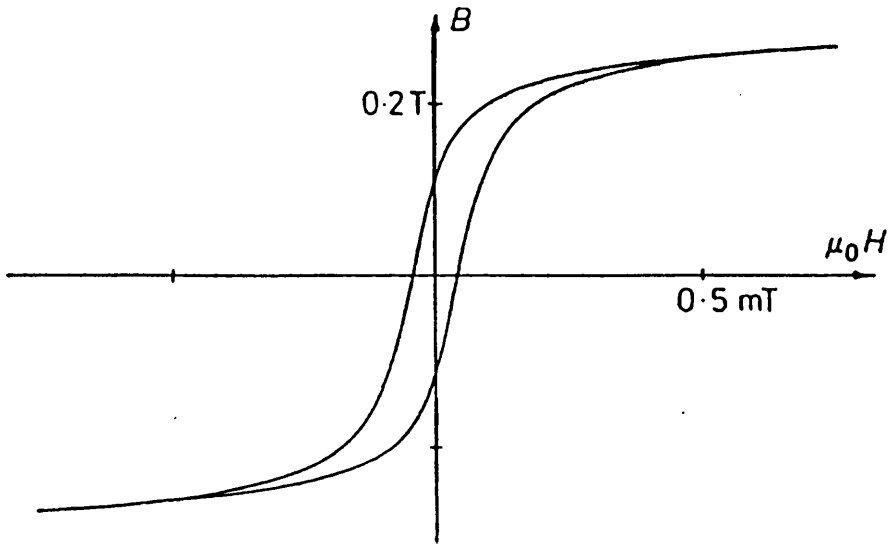

Figure 2.2 Typical magnetisation curve **B** against μ_o**H** for a ferrite core, after Primdahl [1979]

Combining equation 2.1 and equation 2.2 we obtain the output voltage across the pick-up coil as a function of the external magnetic field $\mathbf{B}_{ex}$ and the time varying permeability μ_a, equation 2.3.

$$V_{scc} = nAB_{ex}\frac{d\mu_a}{dt} \qquad 2.3$$

If the driving field **H** is assumed to change sinusoidally then it is possible to derive the form of the changing permeability from Figure 2.2. The permeability waveform is shown in Figure 2.3 along with that of the drive field.

The permeability is a periodic function, whose period is half that of the driving field, containing the second and higher even harmonics of the drive field. This is a consequence of the permeability passing through its maximum near the zero crossings of the drive field. Due to hysteresis the peaks of μ_a occur $\Delta\phi$ after the zero crossing of **H**, where $\Delta\phi$ is given by equation 2.4.

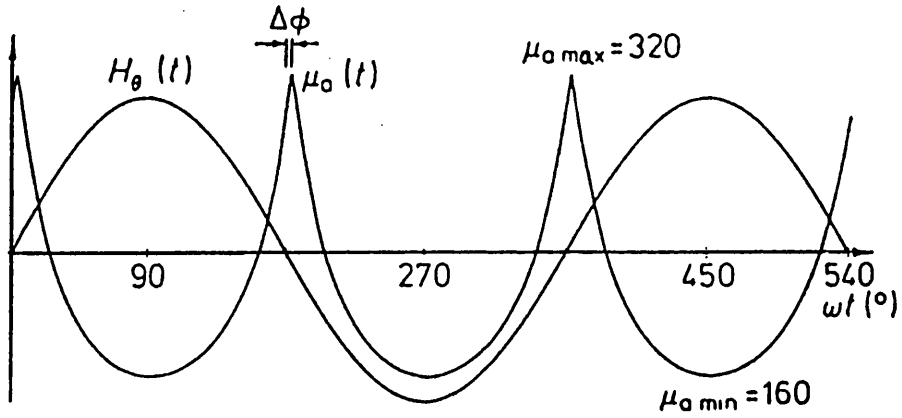

Figure 2.3 Apparent permeability μ_a and driving magnetic field **H** as functions of time, after Primdahl [1979].

$$\Delta\phi = \sin^{-1}\left(\frac{H_1}{H_o}\right) \qquad 2.4$$

H_1 is the driving field corresponding to the point of inflection of the magnetisation curve, and H_o is the driving amplitude of magnetising signal.

The μ_a function can be approximated by a cosine waveform of twice the drive frequency shown in equation 2.5 with a phase delay $\Delta\phi$ relative to the drive waveform.

$$\mu_a \sim \left(\frac{1}{2}\right)[\mu_{a_{max}} + \mu_{a_{min}} + (\mu_{a_{max}} - \mu_{a_{min}})\cos(2\omega t + \Delta\phi)] \qquad 2.5$$

Substitution of equatic$_{max} + \mu_{a_{min}} + (\mu_{a_{max}} - \mu_{a_{min}})\cos(2\omega t + \Delta\phi)]$

$$V_{sec} = -nA\,\omega B_{ex}(\mu_{a_{max}} - \mu_{a_{min}})\sin(2\omega t + \Delta\phi) \qquad 2.6$$

The second harmonic of the output voltage is thus directly proportional to the field to be detected. A d.c. signal can be recovered by mixing $\mathbf{V}_{sec}$ with a second harmonic signal obtained from the drive signal.

2.2.2 Practical Fluxgate Sensors.

Numerous sensor geometries have been developed to produce the required variation in core permeability. One of the first arrangements to be used was a ring core sensor, Aschenbrenner and Gonbau [1936]. The ring core arrangement is shown in Figure 2.4 along with the Vacquier and Förster sensors which were developed in the early 1940s. Single core sensors, despite the presence of a large unbalanced flux, have also been extensively used.

All the sensors mentioned above have the magnetising field H parallel to the external field $\mathbf{B}_{ex}$ and as a result are normally classified as parallel sensors. Sensors can also be constructed which have the magnetising field orthogonal to the external field, the pick-up coil is decoupled from the magnetising field and thus the magnetising field does not induce a large voltage in the pick-up coil and only a single core is needed. Figure 2.5 shows some examples of orthogonal sensors.

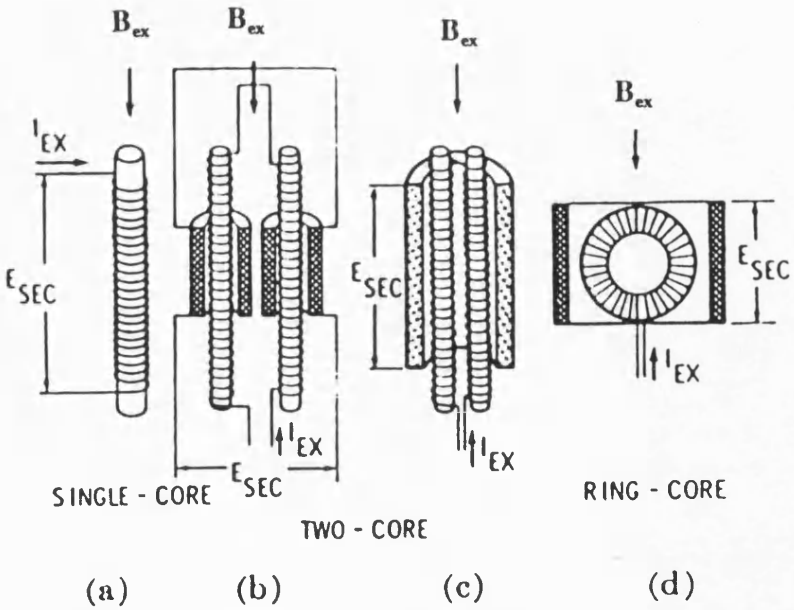

Figure 2.4 a) Single core, b) Vacquier, c) Förster, d) Aschenbrenner and Goubau [1936], after Primdahl [1979]

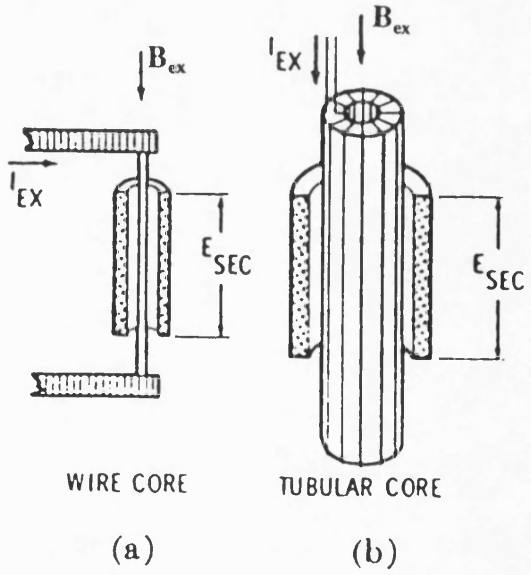

Figure 2.5 Orthogonal sensors a) Alldredge, b) Schonstedt.

The sensors discussed above can all utilise the second harmonic detection technique described earlier. In practical magnetometers the d.c. signal obtained from the mixing process is used in a feedback arrangement to drive a field nulling coil surrounding the core so that the core does not become saturated in high fields. Other techniques have also been developed for obtaining the magnitude of the detected field: for instance the difference between the positive and negative peak values of the output, Acuna and Pellerin [1969].

In all the cases considered the sensors detect the vector component of the magnetic field; they tend to be small, rugged and relatively simple as well as covering a large field range when used in a feedback configuration. More comprehensive reviews of the fluxgate magnetometers operation can be found in Gordon and Brown [1972] and Primdahl [1979].

2.2.3 Sensor Noise.

The noise observed from a fluxgate magnetometer can be divided into three contributions

1) Johnson noise for constant temperature and magnetisation current I.

2) Barkhausen noise for changing magnetisation current.

3) Thermal noise due to fluctuations in the ambient temperature.

The Johnson noise which is independent of frequency is dominated by the Barkhausen noise which is frequency dependent and is normally referred to as the 1/f noise although the exponent is not always found to be equal to -1 and can range from -0.6 to -1.5. As a result of the $1/f^{\alpha}$ dependence a noise measurement is not really useful unless the upper and lower frequency range in which the measurement was taken is stated, Snare and McPherron [1973].

Fluxgate magnetometers have been under development for a number of years and

as a result many noise measurements have been reported. Table 2.1 gives an outline including recent measurements taken on magnetometers implementing amorphous alloys in their construction as well as commercially available magnetometers. The frequency range stated is that in which the measured RMS noise amplitude was taken. Wherever possible a computed RMS noise amplitude for a normalised frequency range is provided so that a comparison between magnetometers can be made. The computed RMS noise was calculated by preforming an integration over the frequency range assuming a 1/f dependence for the noise spectrum, Snare and McPherron [1973]. The figure can only be taken as a guide as in some of the cases the spectrum does not have a 1/f dependence.

A direct comparison of the results shown in Table 2.1 is difficult because no standard method for recording the sensor noise has been adopted. The computed RMS noise provides a guide but should not be taken as an absolute measure of the sensor noise and unfortunately can only be calculated from RMS noise figures taken within a stated frequency range. Peak to peak measurements cannot be converted exactly into RMS figures due to the $1/f^{\alpha}$ nature of the noise spectrum. Table 2.1 does however demonstrate some important trends, amorphous alloy based sensors do not yet out perform the earlier fluxgate sensors but have attained similar order of magnitude minimum detectable fields. Most notable of these is the sensor developed by Nielsen *et al* [1991] which has overcome some of the earlier operating temperature limitations of Shirae [1984]. Also of interest is that the commercially available sensors only attain noise levels in the upper noise region of the much earlier research devices, Bagg [1988]. Although recent sensors do not appear to out-perform earlier sensors of Lanzerotti [1973] and Snare and McPherron [1973], the time that has passed since these measurements were taken and the ambiguity

between the noise measurement techniques must label the more recent measurement of Shirae [1984], Narod *et al* [1985], Ripka *et al* [1990] and Nielsen *et al* [1991] to be the present state of the art.

Table 2.1 Reported fluxgate sensor noise performances.

Reference	Date	Sensor type	frequency range f_1-f_2 (Hz)	Measured RMS noise amplitude / pT f_1-f_2	Computed RMS noise amplitude / pT 0.01-10 Hz
Scouten	1972	Ring-core	"d.c." to 1	35 p-p	-
Dyal & Gordon	1973	Ring-core	0.01 - 10	40 p-p	-
Lanzerotti	1973	Double-rod	0.002 - 0.126	-	14
Snare & McPherron	1973	Ring-core	$2x10^{-3}$ - 0.5	-	8
Candidi *et al*	1974	tubular core	0.02 - 5	260	290
Acuna	1974	Ring-core	0.025 - 12.5	13	14
Hedgecock	1975	Helical	0.01 - 2.5	70	78
McPherron *et al*	1975	Double-rod	10^{-3} - 1	85	85
Shirae	1984	Amorphous T_c=50°C	0.1 - 16	2.5	3.5
Takeuchi and Harada	1984	Amorphous	"d.c." to 0.05	130	-
Narod *et al*	1985	Amorphous	0.05 - 6	22	32
Mermelstein	1986a	Amorphous	"d.c." to 1	15000	-
Engelter	1986	Amorphous	Sensor BW 0 - 22	5000 p-p	-
Mermelstein *et al*	1987	Amorphous	BW=2.5	120	-
Primdahl *et al*	1989	Ring-core	0.02 - 1	100	180
Nielsen *et al*	1990	Amorphous hairpin	0.1 - 0.5	133	276
Ripka *et al*	1990	Annular circles	0.01 - 1	50 p-p	-
Gershenson	1991	High temp. super-conducting	0.2 - 1	150	650
Nielsen *et al*	1991	Amorphous	0.05 - 6	17	25
Sobhendu *et al*	1992	Amorphous	"d.c." -	10000	-
Dowty LNMS/1 Bagg [1988]	-	Ring-core a.c. Only	Sensor BW 0.005 - 10	250	-
Thorn EMI LNS1-3 Bagg [1988]	-	Ring-core a.c. only	Sensor BW 0.006 - 1.1	2400 p-p	-
Thorn EMI LNR2-3HB Bagg [1988]	-	Ring-core	0.2 - 10	320 p-p	-

The temperature dependence of the output of fluxgate magnetometers has been shown to be proportional to the field being measured, Trigg *et al* [1971]. Temperature coefficients for ring core sensors have been measured and are in the order of 5×10^{-5}/°C, Primdahl [1970] and Trigg *et al* [1971]. Although for small field the magnetometer drift is small, for a magnetometer subjected to larger fields such as the earth's field the drift would be considerable, some 1 - 10 nT/°C. Methods for achieving temperature stabilisation at high measurement fields have been suggested, Primdahl [1979]. A simple electronic temperature compensation technique suggested by Primdahl [1970] has been shown to reduce the temperature coefficient by at least an order of magnitude. This would reduce temperature fluctuations to less than 1nT/°C which is concurrent with recent commercial drift figures of ±0.3nT/°C, Willcock [1992].

2.3 Resonance Magnetometers.

2.3.1 Basic Resonance Magnetometers.

Resonance magnetometers make use of the resonant response of an atomic or molecular system subjected to a static magnetic field $\mathbf{H}_0$ generally in the presence of a secondary oscillating field $H_1 \cos \omega t$. The principle originally arose from the Zeeman effect which showed that characteristic atomic frequencies can be magnetic field dependent.

For simplicity we shall consider a spin one half system in which the internal state can be described by a magnetisation vector **M**, Hartmann [1972]. This magnetisation is perturbed by a number of factors such as the external magnetic field, the static component of which will be considered to define the Z axis of a reference frame. Equation 2.7 defines the total external magnetic field

$$H = H_0 + H_1 \cos \omega t \qquad 2.7$$

The system will posses two energy levels due to $\mathbf{H}_o$, $m = \pm 1/2$ separated by an energy difference shown in Figure 2.6 and given by equation 2.8

$$\hbar\omega_o = \hbar|\gamma| H_o \qquad 2.8$$

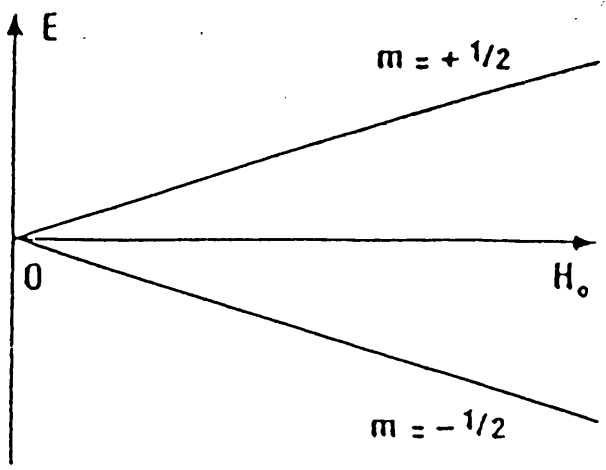

Figure 2.6 Energy levels for a spin one half system $\gamma < 0$, Hartmann [1972].

γ is known as the gyromagnetic ratio, and is positive or negative constant dependent on the atomic system. Relaxation processes also act on **M** driving it to an equilibrium value $\mathbf{M}_r$ with a relaxation time T_r. It is also possible to orientate the system via optical pumping which produces an equilibrium magnetisation $\mathbf{M}_p$ in a time T_p. $\mathbf{M}_p$ is different to $\mathbf{M}_r$ and if both are acting on the system then the magnetisation will attain an equilibrium value $\mathbf{M}_e$, shown in equation 2.9, in a time τ, equation 2.10.

$$\mathbf{M}_e = \left[\left(\frac{1}{T_r}\right)\mathbf{M}_r + \left(\frac{1}{T_p}\right)\mathbf{M}_p\right]\tau \qquad 2.9$$

$$\frac{1}{\tau} = \frac{1}{T_r} + \frac{1}{T_p} \qquad 2.10$$

It can be shown that the equation governing the magnetisation **M** is given by equation 2.11.

$$\frac{d\mathbf{M}}{dt} = \gamma(\mathbf{M} \times \mathbf{H}) - \frac{1}{\tau}(\mathbf{M} - \mathbf{M}_e) \qquad 2.11$$

The solution of equation 2.11 can take many forms depending on the relative orientations of the magnetisations.

If we consider $\mathbf{M}_e$ parallel to H_o, H_1 small and along the x axis as in Figure 2.7a and that $\omega_o \gg \frac{1}{\tau}$ then the solution to equation 11 has a resonance for $\omega = \omega_o$ and the resonance frequency ω_o is related to the amplitude of the static field by equation 2.12.

$$\omega_o = |\gamma| H_o \qquad 2.12$$

A magnetometer which depends on this type of response is known as a *Tuned resonance magnetometer.*

If we now consider $\mathbf{M}_e$ directed along the x axis and $\mathbf{H}_1$ parallel to $\mathbf{H}_o$ as in Figure 2.7b, the solution of equation 11 can give a response similar to that shown in Figure 2.8 centred around H_o=0 with $\Delta H_o = 2/|\gamma|\tau$. In the central region of the curve the amplitude of the response is directly proportional to the external field. A magnetometer which depends on this type of response is known as an *Incremental resonance magnetometer.* A more complete review of resonance magnetometers is given by Hartmann [1972] and also in Grivet and Malner [1967].

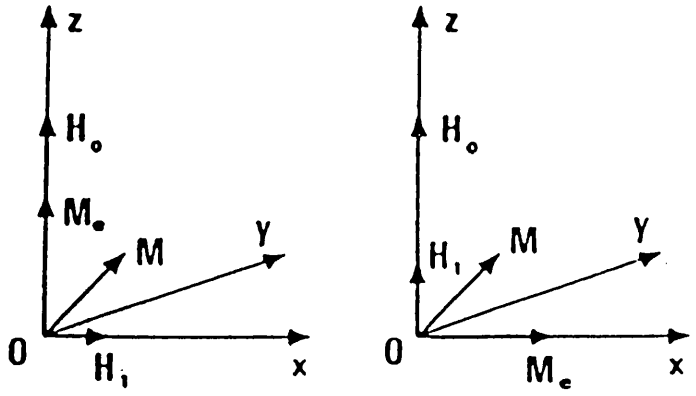

Figure 2.7 a) M_e parallel to H_0 b) M_e along x axis, Hartmann [1972].

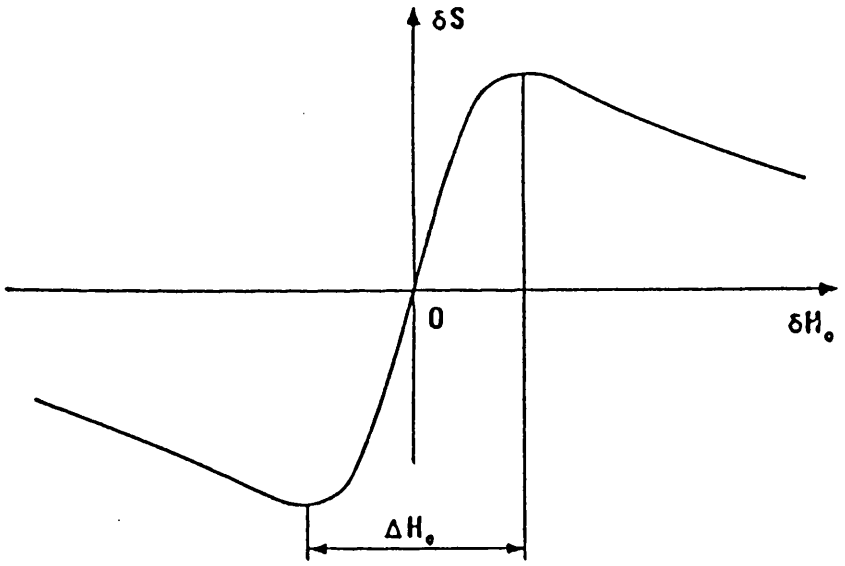

Figure 2.8 Response curve of the incremental resonance magnetometer, Hartmann [1972].

2.3.2 Performance of Resonance Magnetometers.

The field region of interest for resonance magnetometers lies in the region $10fT \leq H_o \leq 50mT$. This is an enormous field range and cannot be covered by a single magnetometer. The dynamic range of resonance magnetometers is limited in the case of the tuned resonance magnetometer by difficulties encountered with the electronics necessary to accommodate a large frequency range . The incremental magnetometer range is limited by the turning points in the response curve at the extremes of ΔH where the response is no longer single valued. Although the underlying theory is somewhat involved, resonance magnetometers are now fairly well understood. They are essentially scalar devices sensitive to the amplitude of the static magnetic field and not its direction. It is, however, possible to retrieve information about the field direction by applying test fields from mutually orthogonal Helmholtz coils surrounding the sensor.

The first practical resonance magnetometer appeared in 1953 and was a non optically pumped, tuned resonance device making use of the magnetic resonance of protons in water. The sensitivity of a tuned resonance device depends on the width of the resonance peak and in the case of the proton magnetometer the practical limit for the sensitivity is in the order of 0.1nT, Hartmann [1972]. The proton magnetometer does, however, possess one of the best accuracies of the resonance devices in that the value of the field obtained from the device agrees closely to that of a calibrating field calculated in an absolute manner. Improvements on the sensitivity can be achieved by optical pumping which has the effect of narrowing the response peak as well as increasing the signal to noise ratio. The proton magnetometer is not continuously driven as in the optically pumped magnetometer and there is thus a degradation in the signal to noise ratio. Sensitivities in the region of 3pT can be achieved for the optically pumped magnetometer although with less accuracy, Bloom [1962]. Work has continued on refining resonance magnetometers and the specification for two of the more recent

devices are shown in Table 2.2.

Incremental resonance magnetometers have the ability to work down to zero field levels, as an amplitude and not a resonance is being observed and for this reason tend to be used as a null field detectors of very high sensitivity. Sensitivities of down to 30fT have been reported, Dupont-Roc *et al* [1969].

Table 2.2 Recent resonance magnetometer specifications.

Reference	Date	Type of sensor	Operating field range μT	Measured RMS noise amplitude / $pT/\sqrt{Hz}$	White noise bandwidth / Hz	Drift
Kernevez and Glénat	1991	Scalar	20 - 70	10	0.0001 - 0.1	None
Duret *et al*	1991	Vector	±65	160	0 - 25	None

2.4 Magnetic Thin-film Magnetometers.

2.4.1 Magnetic Thin-films.

Magnetic thin films are of the order of 20-500nm thick and are normally made of non-magnetostrictive Ni-Fe alloys which have been vapour deposited onto a glass substrate in the presence of a parallel magnetic field to the substrate. These thin films possess several unique properties which include the absence of domain walls, a well defined uniaxial anisotropy with an easy axis of magnetisation parallel to the field present during film deposition, low eddy current losses and high sheet resistivity.

Along the easy axis a square hysteresis loop can be observed with coercivity $\mathbf{H}_c$ in the order of 160-400Am^{-1}. Measurements along the orthogonal hard axis yield a nearly closed hysteresis loop which exhibits magnetic saturation at positive and negative fields equal to the anisotropy field $\mathbf{H}_k$. The simplest description of the magnetisation process

in thin films is to assume that the film is a single domain in which all magnetic changes occur by the rotation of **M** under the influence of the uniaxial anisotropy energy and the applied field (Irons and Schwee [1972]). The form of the hysteresis loop is thus due to the rotation of the magnetisation vector **M** from the easy axis into the hard axis when a field equal to H_k is applied along the hard axis. When the field is removed the magnetisation rotates back to its stable position along the easy axis. The magnetisation remains in the plane of the film due to the large demagnetising factor normal to the plane of the film.

2.4.2 Thin-film Magnetometers.

There are numerous types of thin film magnetometers which rely on various principles for their operation. The more common systems will be covered briefly, highlighting the basic principles of operation.

TypeI The first reported thin film magnetometer consisted of a thin film element with a sinusoidal excitation field applied along its hard axis with an amplitude greater than $\mathbf{H_k}$, West *et al* [1963]. If no field is present along the easy axis, then in the region of the sinusoid when it decreases from H_k to 0 the magnetisation in half of the film will rotate to the positive easy axis direction and the other half to the negative easy axis direction. In this case there will be no net flux along the easy axis direction. If, however, there is a field to be measured along the positive easy axis direction then the majority of the flux will rotate in this direction and a signal will be observed in a pick-up coil along the easy axis with a frequency twice that of the sinusoid along the hard axis.

TypeII The theory of operation of this magnetometer was explained by Castro and Stucki [1966]. Basically it relies on an excitation field along the easy axis. The field to be

measured is applied along the hard axis and determines the direction of rotation of the magnetisation and hence the phase of the output signal.

TypeIII A bias field is applied along the hard axis with a mean value H_k causing the magnetisation to be very sensitive to a modulation field along the easy. The magnetisation thus oscillates about the hard axis typically with an amplitude that depends on the amplitude of the modulation and is typically in the order of 30°. In the absence of a field to be measured along the easy axis the rectified signal from a pick-up coil along the easy axis contains even harmonics of the modulation frequency but no component at the modulation frequency. If a field is then applied along the easy axis a fundamental component will appear in the rectified output with an amplitude proportional to the applied field and a phase which is determined by the direction of the applied field.

TypeIV Proposed by Bader and Fussel [1965] this magnetometer relies on a small modulation field along the hard axis $\mathbf{H_H}$ which causes the magnetisation to rotate from the easy axis. This produces a hard axis component given by equation 2.13 from Irons and Schwee [1972].

$$\mathbf{M_H} = \frac{\mathbf{M}H_H}{H_k + H_B + H} \qquad 2.13$$

Where $\mathbf{H_B}$ is a bias field along the easy axis and **H** the field to be measured also applied along the easy axis. The hard axis permeability is then a function of the unknown field, equation 2.14.

$$\mu = \frac{B_H}{H_H} = \frac{\mu_0 \mathbf{M}}{H_k + H_B + H} \qquad 2.14$$

TypeV A thin film is biased near ferromagnetic resonance and the impedance which is proportional to the unknown field is measured. The field to be measured and the bias field are directed at right angles to an exciting field all three lying in the plane of the film. The film is placed between the conductors of a shorted section of stripline to provide a circuit impedance of 50Ω when the film is at ferromagnetic resonance. The bias field is then adjusted so that the real part of the impedance is about half this. The real part of the impedance is then monitored and is a measure of the unknown field, Schwee and Irons [1968].

TypeVI Abadeer and Ellis [1971] proposed a magnetometer with two excitation fields at different frequencies superimposed along the easy axis and the field to be measured along the hard axis.

TypeVII Instead of an excitation field a current is passed down the thin film and a change in resistance observed is used as a measure of the applied field. The magnetoresistive effect comes about due to spin orbit coupling, the distortion of the electron orbits in an applied field brings about an increased scattering of the conduction electrons and thus a change in the resistance. Resistance changes for Ni-Fe films are typically of the order of 2-3% but can be increased by the addition of Cobalt to the film. This increases the resistance change to approximately 4%, Dibbern [1983]. Much greater changes in the resistance can be observed in multilayered media such as a Co/Cu layered structure. The Giant magnetoresistive effect however, tends to be comparitively magnetically hard reaching saturation for fields of the order of one Tesla, Greig *et al* [1992].

Magnetoresistive sensors can be mabe compact and respond rapidly to changes in field. This made them ideal for magnetic recording applications, Smith [1991], or rotary sensors, Campbell [1990]. For these applications the fields to be detected are relatively

high and a high spatial resolution is required. The maximum reported field resolution for a high sensitivity magnetic field measuring device is of the order of $0.6nT/\sqrt{Hz}$, Pant and Krahn [1991].

2.4.3 Thin-film Magnetometer Performance.

Table 2.3 gives a summary of the performances of the various configurations of magnetometers that have been discussed. The *TypeIV* magnetometer has a low noise, low power requirement and is fairly simple in construction, as a result it is the only thin-film magnetometer that has been produced in quantity. Magnetoresistive magnetometers are becoming more extensively used but mainly for magnetic recording applications although their compact size and relatively simple accompanying circuitry make them very competitive as magnetic field sensing devices. The noise in the magnetometers is mainly due to the noise in the electronics and to temperature effects which dominate the residual film noise. All the thin film magnetometers are vector devices.

Table 2.3 Thin-film magnetometer noise levels

Type	Reference	Date	Detection limit / nT	Bandwidth used Hz
I	West *et al*	1963	0.1	1
II	Castro and Stucki	1966	1.0	1
III	Frank	1966	1.0	1
IV	Bader and Fussel	1965	0.1	1
V	Schwee and Irons	1968	10	10^8
VI	Abadeer and Ellis	1971	50	-
VII	Paul *et al*	1970	1.0	10^3
	Hoffman *et al*	1984	1	at 1
	Pant and Krahn	1991	$0.6/\sqrt{Hz}$	-

2.5 SQUID Magnetometers.

Superconducting Quantum Interference Devices or SQUIDs are superconducting devices which, with their associated circuitry are vector magnetic flux sensors of very high sensitivity. Consideration will only be given to the performance of SQUID devices and some of the limiting factors in their operation, as the detailed theory of their operation is outside the scope of this review and is covered extensively in dedicated reviews by Gallop and Petley [1976], Koch [1989] and Swithenby [1980].

2.5.1 SQUID Magnetometer Performance and Limitations.

The SQUID magnetometer has an intrinsic maximum sensitivity due to quantum limitations of the order of $2fT/\sqrt{Hz}$, Swithenby [1980]. This intrinsic sensitivity has not as yet been achieved although sensitivities in the order of $10fT/\sqrt{Hz}$ were obtained by Cohen and Kaufman [1975]. To achieve such high sensitivities large background fields must be removed by extensively shielding the sensor and the field to be measured. Field measurements can be carried out in the presence of large background field but with reduced sensitivity.

A major limiting factor in the use of SQUID magnetometers is the necessity for a superconducting environment. The design and construction of containment vessels for the liquid helium coolant is thus a critical factor. An important consideration is the minimisation of the frequency of replenishing the helium reservoir and with modern Dewars can be as infrequent as 100 days, Davis *et al* [1977]. SQUID Dewars invariably use radiation shields to achieve a high temperature stability in order to avoid magnetic interference caused by the temperature dependent paramagnetic or nuclear magnetism of the Dewars. The radiation shields are cooled by the helium vapour boiled off from the main helium reservoir. Liquid nitrogen is avoided as a coolant because the bubbling of the nitrogen introduces additional noise from paramagnetic dissolved oxygen. High temperature SQUID magnetometers employing nitrogen as a coolant have been constructed but high degrees of mechanical stability are required to obtain a minimum field noise of $0.6pT/\sqrt{Hz}$ at 10Hz which has a $f^{-\frac{1}{2}}$ dependence up to 100Hz, Miklich *et al* [1990] and $0.9pT/\sqrt{Hz}$ white noise above 0.3Hz and a $\frac{1}{f}$ dependence below 0.3Hz, Yi Zhang *et al* [1992].

SQUID magnetometer systems as a result of these limitations tend to be very

complex with the further disadvantages that it is necessary for the Dewar to remain approximately upright and that the overall cost of the magnetometer system tends to be excessively high.

2.6 Amorphous Alloy Strain Dependent Magnetometers.

Three types of Amorphous alloy magnetometers will be considered here. Other strain dependent magnetometers have been developed which rely on the large magnetostrictions observed in rare earth-iron intermetallic compounds, Chung *et al* [1992] and have achieved sensitivities in the order of 200pT, Chung *et al* [1991], however, apart from this brief mention they will not be covered here. Two of the amorphous alloy magnetometers rely on direct measurements of the magnetostriction of amorphous alloys, Pantinakis and Jackson [1986] and Dandridge *et al* [1980]. The third technique proposed by Mermelstein and Dandridge [1987a] relies on the field dependent coupling between the magnetisation and the strain modes. All three magnetometers are vector devices measuring the longitudinal field component in the plane of ribbon, Mermelstein and Dandridge [1987b]. This is by no means a complete survey but is intended to give some insight into the present state of the technology of the amorphous alloy based strain dependent magnetometers.

2.6.1 Basic Optical Fibre Magnetometer.

The optical fibre magnetometer is based on the magnetostriction exhibited by an amorphous alloy. If an amorphous alloy ribbon has a well defined magnetic easy axis then the strain observed in the ribbon about H=0 takes the form shown in Figure 1.2 and follows the coherent rotation model of Livingston [1982] with a quadratic coefficient C_q for small field defined in equation 2.15. The coherent rotation model will be more fully discussed in chapter 3.

$$\lambda = C_q H^2 \qquad 2.15$$

where H is perpendicular to the easy axis, $C_q = (3/2)(\lambda_s/H_k^2)$ and,$\lambda = \delta l/l$,λ_s is the saturation magnetostriction, $\mathbf{H}_k$ is the anisotropy field, δl is the length change and l the length of the ribbon. For large fields the strain no longer conforms to the coherent rotation model but eventually reaches a saturation value.

If the ribbon is subjected to a magnetic field of the form of equation 2.16 then the strain in the sample at the oscillation frequency ω_m of $\mathbf{H}_{ac}$ along the direction of **H** about H=0 is given by substituting for the magnetic field in to the differential strain equation obtained from the differential of the coherent rotation approximation with respect to **H**. The field modulated strain is then given by equation 2.17.

$$H = H_{dc} + H_{ac} \sin \omega_m t \qquad 2.16$$

$$\lambda_{\omega_m} = 2C_q \omega_m H_{ac} H_{dc} \cos \omega_m t \qquad 2.17$$

The expression for the modulated strain is only valid in the region where the strain obeys the coherent rotation model. Over large field ranges the strain at ω_m follows the curve shown in Figure 2.9. The peaks in Figure 2.9 occur at the points of inflection of the curve shown in Figure 1.2 as the ribbon approaches magnetic saturation.

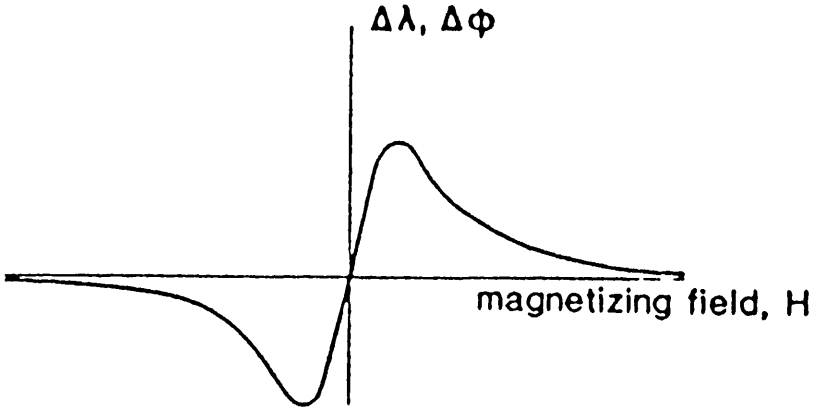

Figure 2.9 A. C. Strain observed in amorphous alloy ribbon, after Kersey *et al* [1985]

If $\mathbf{H}_{ac}$ is a modulation field of known amplitude then the external magnetic field $\mathbf{H}_{dc}$ is directly proportional to the strain observed in the ribbon between the points of inflection of Figure 1.2. By bonding an optical fibre to the ribbon the magnetostriction is coupled to the fibre. The change in length of the fibre can then be measured interferometrically.

2.6.2 Optical Fibre Magnetometer Performance.

The first experimental optical fibre magnetometer was reported by Dandridge *et al* [1980]. The sensing element consisted of an optical fibre with nickel or metallic glass magnetostrictive material directly deposited onto the fibre. Detection of the strain induced in the fibre was accomplished by phase tracking techniques. A sensitivity of 1nT per metre of sensor in a 0.5m sensor at 100Hz was achieved. The main disadvantage with this system was the limited dynamic range achievable due to the sensor element approaching magnetic saturation. The dynamic range can be improved as well as removing variations in the sensitivity due to hysteresis effects by incorporating the magnetometer in a closed loop feedback system as demonstrated by Kersey *et al* [1984]. The closed loop system maintains the operation of the system about the H=0 position of Figure 2.9 by feeding back a control current to a coil surrounding the sensor which nulls the applied field. Sensitivities of 1.25nT/m in a 0.5m sensor at frequencies below 2Hz with a dynamic range greater than 10^5, Kersey *et al* [1984], and 50pT/m in a 0.5m sensor at frequencies from d.c. to ≈20Hz were achieved, Kersey *et al* [1985]. A fundamental limit calculated from the interferometer noise floor of 3fT has been proposed for the minimum detectable field that can be measured using the D.C. optical fibre magnetometer, Bucholtz *et al* [1987a] from interferometer limitations discussed by Dandridge *et al* [1982]. Other limitations are also introduced from thermal strain and eddy currents, Mermelstein [1985]. The effect of external nonmagnetic perturbations

such as stress and acceleration which effect the magnitude of the quadratic coefficient have been investigated by Bucholtz *et al* [1988]. The maximum sensitivity has probably not yet been achieved because of reductions in the quadratic coefficient by locally induced stress due to the fibre alloy bond and by demagnetisation factors, Bucholtz *et al* [1985] and [1987b]. Over long periods of time, the long-term drift characteristics of the magnetometer set limits on the reproducibility and hence the accuracy of magnetic field measurements. The long term stability of these sensors is about an order of magnitude greater than their noise floors with 10nT for a 0.1m sensor over 13hrs being achieved by Koo *et al* [1986]. The temperature coefficient of expansion for amorphous alloys is of the same order of magnitude as the magnetostriction and so the obvious limitation to stability is the thermal drift associated with the linear expansion of the materials.

Table 2.4a summarises the development of the D.C. Optical Fibre magnetometer. Dynamic ranges are not stated as the only published data was that of Kersey *et al* [1984]. Of less significance here is the A.C. Optical Fibre magnetometer summarised in Table 2.4b. The results obtained by Bucholtz *et al* [1989a] are significant however because of the large measurement bandwidth over which the sensor has a white noise frequency spectrum.

Table 2.4a Summary of the development of the D.C. Optical Fibre magnetometer.

Reference	Date	Sensor Type (Amorphous)	Field Resolution / nT	Active length of material / m	Field Resolution nT/m of material	Bandwidth for noise measurement / Hz
Dandridge *et al*	1980	Ribbon	2	0.5	1	at 100
Pratt *et al*	1984	Ribbon	10	0.1	1	"d.c" to 1
Kersey *et al*	1984	Ribbon	2.5	0.25	0.625	-
Kersey *et al*	1985	Ribbon	0.1	0.5	0.05	"d.c." to 20
Mermelstein	1986a	Ribbon Cylinder	2.6	-	-	"d.c." to 1
Koo *et al*	1986	Ribbon	4	0.05	0.2	-
Bucholtz *et al*	1987a	Ribbon	$0.02_{rms}/\sqrt{Hz}$	-	-	at 10
			$0.2_{rms}/\sqrt{Hz}$	-	-	at 0.1
Koo *et al*	1989	Wire	$1_{rms}/\sqrt{Hz}$	0.05	$0.05_{rms}/\sqrt{Hz}$	at 1
Dagenais *et al*	1989	Ribbon Cylinder	$0.013/\sqrt{Hz}$	-	-	at 1
			$0.046/\sqrt{Hz}$	-	-	at 0.1
Vohra and Bucholtz	1991	Ribbon	$5/\sqrt{Hz}$	0.005	$0.025/\sqrt{Hz}$	0.025 - 10

Table 2.4b Summary of the development of the A.C. Optical Fibre magnetometer.

Reference	Date	Sensor Type (Amorphous) "a.c." operation only	Field Resolution / nT	Active length of material / m	Field Resolution nT/m of material	Bandwidth for noise measurement / Hz
Bucholtz *et al*	1989 a	Ribbon Cylinder	0.026 $_{rms}/\sqrt{Hz}$	-	-	0.1 - 10^6
Bucholtz *et al*	1989 b	Ribbon Cylinder	$7X10^{-6}/\sqrt{Hz}$	-		at $34X10^3$
Davis *et al*	1992	Ribbon	$0.018/\sqrt{Hz}$	-	-	10^3 - $5X10^4$

2.6.3 Piezoelectic Signal Recovery Magnetometer.

This magnetometer is identical in operation to the closed loop optical fibre magnetometer with the exception that the strain in the amorphous alloy sensor is detected by a piezoelectric transducer and not the complex optical arrangement of the Optical Fibre magnetometer , Pantinakis and Jackson [1986]. A sensitivity of $0.2nT/\sqrt{Hz}$ for a 0.17m sensor at low frequencies was achieved.

2.6.4 Magnetisation and Strain Mode Coupled Magnetometer.

The operation of this magnetometer is based on the field dependent coupling between the magnetisation and the strain modes of an amorphous metal alloy Mermelstein [1986c]. If an oscillating stress is applied to a magnetostrictive ribbon an oscillating magnetisation is generated in the ribbon. The amplitude of the oscillating magnetisation is proportional to the external field applied to the ribbon. The oscillating stress is applied to the ribbon by placing the ribbon on a piezoelectric substrate with a

highly viscous liquid interface between the ribbon and substrate. The magnetisation oscillations can be detected by a pick-up coil surrounding the ribbon and the amplitude of the signal measured, Mermelstein and Dandridge [1987a].

A fundamental limit to the resolution of this device has been calculated to be $\approx 5fT/\sqrt{Hz}$ from thermal fluctuations of the magnetisation. This limit is reduced however, to $0.1pT/\sqrt{Hz}$ by Johnson noise in the pick-up coil, Mermelstein and Dandridge [1987c]. In practice the minimum detectable field was found to be $8pT/\sqrt{Hz}$ at 1Hz with an approximate $\frac{1}{f}$ rise in the noise floor, Mermelstein [1992]. The minimum detectable field at 5mHz was approximately $104pT/\sqrt{Hz}$. The sensor element is inexpensive and easily constructed with relatively simple processing electronics due to the intrinsic linearity of the response of the magnetostrictive amorphous alloy. The magnetometer can also be easily configured to measure first and second order field gradients but with reduced sensitivity in each case, Mermelstein and Dandridge [1988] & [1990].

2.7 Comparison of Magnetometer Sensitivities.

A precise comparison of the different magnetometer performances is hindered by the different formats in which the sensitivities are presented. Figure 2.10 does however provide an approximate guide to the present state of the magnetic measurement techniques discussed in this chapter. The data was extracted from published noise power spectrums for the different magnetometers except the fluxgate of Nielsen *et al* [1991]*. In this case the noise spectrum was assumed to have a 1/f dependence and the spectrum was then approximately calculated from the published noise power density.

The solid lines in Figure 2.10 represent fitted curves to the data obtained from the published spectra. In all cases the function chosen was that shown in equation 2.18 with parameters optimised for each data set. The fitted curve was only plotted over the range of available data. Table 2.5 summarises the calculated coefficients for each fit.

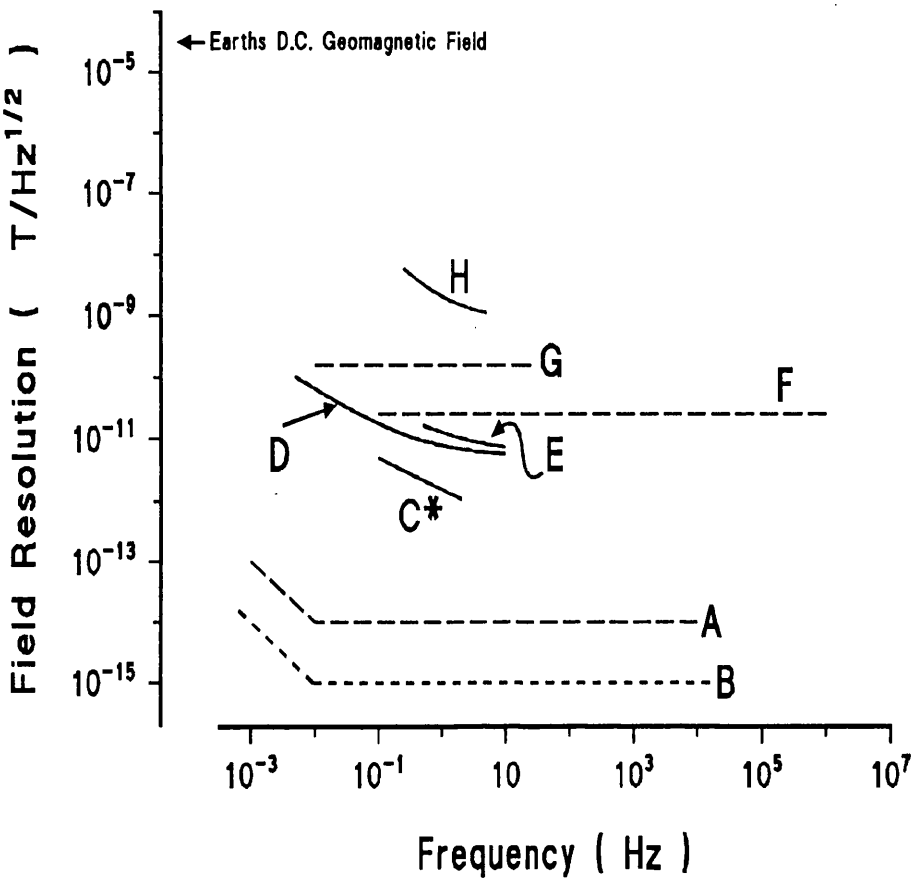

Figure 2.10 Published magnetometer noise spectrums.

A SQUID magnetometer - Cohen and Kaufman [1975].

B Ideal SQUID magnetometer - Swithenby [1980].

C Fluxgate magnetometer - Nielsen *et al* [1991].

D Magnetisation Strain mode - Mermelstein [1992].

E D.C. Fibre Optic magnetometer - Dagenais *et al* [1989].

F A.C. Fibre Optic magnetometer - Bucholtz *et al* [1989].

G Resonance Magnetometer - Duret *et al* [1991].

H Amorphous Wire based Fibre Optic Magnetometer - Koo *et al* [1989]

$$N_{(f)} = af^b + C \qquad 2.18$$

Table 2.5 Summary of the coefficients for the fitted curves.

Curve	Coefficient		
	$10^{-12}a$	b	$10^{-12}C$
C	1.53	-0.51	-
D	2.62	-0.68	5.31
E	7.25	-0.60	5.68
H	1100	-1.07	94.5

Figure 2.10 illustrates that in general appart from the SQUID magnetometer a sub PicoTesla resolution has not yet been achieved. In all the cases discussed there are limitations in the commercial viability of the magnetometers brought about by the measurement techniques employed. For example the SQUID magnetometer requires a superconducting environment, the Fibre Optic magnetometer is optically quite complex and there is some uncertainty of the stability of the viscous bond with time and temperature for the strain mode coupled magnetometer. The inherent simplicity of the Shear-wave magnetometer thus gives it the potential to compete with all of these magnetic field measurement techniques.

3 MECHANICAL AND MAGNETOMECHANICAL PROPERTIES OF AMORPHOUS ALLOY RIBBONS.

3.1 Introduction.

The following chapter briefly reviews the mechanical and magnetomechanical properties of the amorphous alloy ribbons. The effects pertinent to the operation of the Shear-wave magnetometer only are considered expanding on aspects already introduced in chapter 1 in order to place the various effects in perspective. The subject of creating an easy axis for magnetisation within the material through induced anisotropy is introduced. The effects of the ribbon dimensions and surface features on the anisotropy and the hysteresis loop parameters are then discussed. This is followed by a study of the effect the induced easy axis has on both the magnetostriction and the elastic moduli and finally the degree of magnetoelastic coupling and magnetoelastic damping are examined.

3.2 Induced Anisotropy Through Magnetic Annealing.

The idea that amorphous alloys are not isotropic in their behaviour but are in-fact anisotropic was introduced in chapter 1 in terms of an easy axis with an energy minimum into which the magnetic moments of the material will tend to lie. The glassy structure itself is macroscopically isotropic and therefore the amorphous alloy should have no intrinsic magnetic anisotropy. From examination of structural evidence in terms of a dense random packed structure (DRP) Egami [1981] has shown that the structure demonstrates considerable short range order which can produce localised easy axes within the material. In the production of amorphous alloy ribbon considerable stresses are frozen into the structure due to differential cooling rates . These stresses have the effect of producing a stress induced anisotropy with an easy axis along the length of the ribbon. This effect can also be overwhelmed by more localised stress centres which

produce complex localised macroscopic magnetic states. The stress anisotropy can be removed by annealing the ribbon which induces thermal relaxation of the stresses within the structure and is commonly referred to as a stress relief, Luborsky *et al* [1975]. On completion of the stress relief the dominant anisotropy is that induced by the physical dimensions of the sample. In this case the easy axis tends to lie along the long axis of the ribbon due to demagnetising effects. The shape induced anisotropy is discussed in terms of the demagnetising field and the shape factor in chapter 3.3.

The anisotropy of the material can be further tailored by the process of field annealing. Field annealing induces an easy axis in the direction of a magnetic field which is applied during the annealing process. The phenomenon of field annealing can be accounted for by the selective replacement of single atoms in the DRP structure such as to bias the initially random distribution of atomic anisotropies from the short range order, Becker [1978]. The temperature of the anneal must be below the Curie point of the alloy yet high enough and applied for a suitably long time to impart enough thermal energy so that substantial atomic diffusion can occur. The field applied in order to develop the maximum anisotropy must be large enough to magnetically saturate the sample. The exact magnitude of the annealing parameters to produce an optimum field anneal has been covered by a number of authors. Thomas [1991] presents a comprehensive survey of the effects of field annealing commercially available iron-based amorphous materials. The process of magnetic annealing has also been shown by Berry and Pritchet [1975a] to be reversible. If the sample is further annealed then it will return to the stressed relieved configuration if no field is applied. If a field is applied then the easy axis will be redefined into the direction of the present applied field. The reversibility of the field annealing process limits the potential operating temperature of devices employing prepared samples as over a period of time the imparted thermal energy will corrupt the annealed state. Gibbs [1990] has reviewed other methods for controlling anisotropy and has

indicated that stress annealing (Nielsen *et al* [1985]) and surface crystallisation (Ok and Morrish [1981a] & [1981b]) are promising as alternative methods. Surface crystallised amorphous materials have the disadvantage that surface crystallites tend to encourage crystal growth throughtout the bulk of the material. The considerably greater anisotropy energies induced via surface crystallisation compared to other methods has the advantage of producing a less strain dependent material which will be perturbed less easily by external strain. Brugel *et al* [1988] have suggesting that this treatment along with its non reversibility would be advantageous for device applications.

3.3 Physical Dimensions and Surface Features of Amorphous Ribbons.

The dimensions of the amorphous ribbon sample and the surface features observed on amorphous ribbons can play a considerable role in contributing to the overall anisotropy of the sample. The shape anisotropy has its origins in the demagnetising field. If a ferromagnetic body is placed in an applied field, because of the discontinuity at the surfaces of the normal component of magnetisation an effect at the end surfaces that resembles free magnetic poles in opposition to the applied field is observed. The internal field within the specimen $\mathbf{H}_i$ is then given by equation 3.1 where $\mathbf{H}_0$ is the applied field and $\mathbf{H}_D$ the demagnetising field.

$$H_i = H_0 - H_D \qquad 3.1$$

The magnitude of the demagnetising field depends on both the magnetisation of the sample and the sample dimensions. The demagnetising field is normally expressed in terms of the product of a shape dependent demagnetising factor **D** and the magnetisation of the material **M**, equation 3.2.

$$H_D = DM \qquad 3.2$$

The magnitude of **D** depends very much on the separation of the end surfaces of the sample. If these are closely spaced then the demagnetising factor tends to be large whereas if they are widely separated then **D** is small. In the case of a length of amorphous ribbon where the length is much greater than the width the demagnetisation factor for an applied field along the long axis would be much smaller than that for a field applied transversely across the width. Ribbon material thus has a shape anisotropy with an easy axis along the long axis of the ribbon. For an ideal stressed relieved amorphous ribbon this would be the predominant anisotropy. The calculation of the demagnetising factor is a geometric problem which becomes complicated for even the simple ribbon case. A useful approximation to the ribbon geometry used throughout this work is to assume an ellipsoid with semi axis ***a*** corresponding to the long axis of the ribbon, ***b*** corresponding to the width and a ribbon thickness ***c*** (***a>b»c***). The demagnetising factors for general ellipsoid figures were calculated by Osborn [1945].

The surfaces of as cast amorphous ribbon material are not optically smooth but exhibit surface features which effect its magnetic properties. The casting process produces two topologically different faces. The face that was in contact with the quenching wheel exhibits a distribution of irregular indentations of various dimensions elongated in the casting direction which come about due to air pockets being trapped between the wheel and the ribbon during formation. The free surface is much smoother but shows some elongated features reflecting the structure on the wheel surface. An excellent illustration of this can be seen in the optical micrographs taken by Lemcke [1989]. The differential cooling rates caused by the air pockets produce stress in the ribbon and the air pockets themselves produce a non uniform surface magnetisation which results in a uniaxial surface shape anisotropy which contributes to the overall anisotropy. Ding *et al* [1990] have investigated the effects of polishing the surfaces of amorphous $Fe_{78}Si_9B_{13}$ and have demonstrated over an order of magnitude decrease in

the anisotropy of as cast ribbon on improving the surface finish. Surface features also influence the dependence of the hysteresis loop parameters $\mathbf{H_c}$ and $\mathbf{B_r}$ on the thickness of the ribbon. If the thickness of an amorphous ribbon is reduced either in the formation process or post production by either chemical or mechanical processes then the coercivity. is seen to increase and the remanent field decrease, the material becomes magnetically harder due to an increase in the surface pinning of domains, Kulik *et al* [1991]. Becker [1981] observed that on initial etching of the prepared amorphous ribbons the coercivity for different alloy compositions rapidly increased or decreased before settling to a relationship $H_c \propto 1/d$, where **d** is the ribbon thickness. This was explained in terms of the sum of two different pinning contributions from the topologically different surfaces. If the total pinning from the surfaces of the cast material is greater than the pinning from the identical surfaces of the etched material then the coercivity initially falls. The converse of this also holds explaining an initial sharp rise in the coercivity. The effect of the thickness of the material on the propagation of elastic waves is discussed in chapter 4.

3.4 Magnetostriction and Elastic Moduli.

An introduction to the idea of magnetostriction and a change in the elastic moduli with applied field was presented in chapter 1. The magnetostriction and the elastic moduli are intrinsically linked through the field dependent strain of the material under consideration. These effects have been investigated for a varied range of alloy compositions by many authors, Berry and Pritchet [1975a], Mitchell *et al* [1979], Baczewski *et al* [1984] and Gibbs [1991] to name but a few. Gibbs [1992] has recently presented a review in which he considers the development of magnetostrictive materials and celebrates 150 years since the discovery of magnetostriction by Joule [1842]. The techniques used to observe the phenomena vary considerably. One method for measuring

changes in the elastic moduli, specifically the Young's modulus is the vibrating reed described by Berry and Pritchet [1975b]. The apparatus allows mechanical damping and resonant frequency measurements to be made on the ribbon in its flexural modes of vibration. From these measurements the changes in Young's modulus and the damping coefficient for the alloys can be calculated. The damping coefficient is discussed in chapter 3.5. Mechanical damping occurs due to the dissipation of mechanical energy from stress induced domain movement. The magnetostriction can be measured by a number of methods; an example of an indirect method is to measure the magnetisation of the sample under strain, Spano *et al* [1982]. Examples of direct measurement techniques are measurements using a strain gauge bonded to the sample, O'Handley [1977], or a Fibre-Optic Dilatometer as described by Squire and Gibbs [1987b]. Thomas and Gibbs [1992] account for the larger observed values of magnetostriction from the fibre-Optic method in terms of a free sample with no perturbations imposed on it due to bonding strains. In this respect the direct measurement of magnetostriction using this method would seem to be the more appropriate giving the response of the unloaded material.

Observations of the effect of field annealing on the magnitude of both the magnetostriction and the change in Young's modulus for an Fe-P-C amorphous alloy were made by Berry and Pritchet [1975a]. Starting with a sample that had undergone a stress relief anneal to obtain a reference state, transverse (across the width of the ribbon) and longitudinal (along the ribbon length) magnetic field anneals were performed. The magnetostriction and the change in the Young's modulus were measured in terms of their field dependence for a magnetic field applied longitudinally along the prepared ribbon. It was apparent from their work that the longitudinal anneal suppressed the overall change in the magnitude of both the Young's modulus and the magnetostriction. The transverse anneal, however, had the result of increasing the magnitude of both field

dependent effects. The differences between the two preparations were explained in terms of the induced easy axis of magnetisation lying parallel to the annealing field. For the transverse field annealed material the demagnetised state has domains with magnetisation vectors which tend to align parallel to the easy direction separated by 180° walls as seen in Figure 3.1.

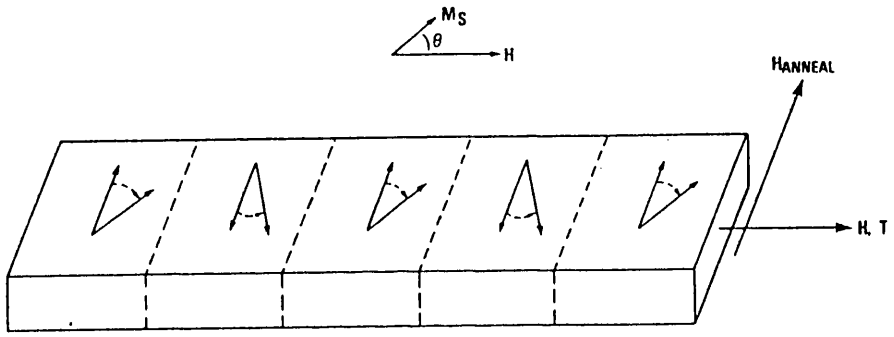

Figure 3.1 Domain configuration of an idealised transverse field annealed ribbon, After Wun-Fogle *et al* [1989].

When a magnetic field is applied along the easy axis direction the change in Young's modulus tend to be small as 180° domain walls are not stress active and the magnetic domains are not susceptible to rotation. When the magnetic field is applied perpendicular to the easy axis the rotation of the magnetic moments into the direction of the applied field as depicted in Figure 3.1 must be accompanied by domain rotation or growth. This enhances the stress sensitivity and causes an increase in the magnitude of the field dependent Young's modulus. Livingston [1982] proposed a simple model to explain the

magnetic phenomena in transversely annealed amorphous alloys. The model was based on the coherent rotation of the magnetic moments when a magnetic field is applied longitudinally along the ribbon axis perpendicular to the induced easy axis. Squire [1990] presented a more generic model for an induced easy axis at an arbitrary angle in the ribbon plane rather than perpendicular to the long axis. Figure 3.2 shows the general magnetic state for which the model returns expressions for the magnetisation, engineering magnetostriction and the field dependence of the Young's modulus. θ defines the orientation of the induced easy axis from the ribbons longitudinal axis. σ and **H** are the longitudinal stress and applied magnetic field respectively and **x** is the mean wall displacement. The angles ϕ_1 and ϕ_2 are the angles of the neighbouring magnetic moment from the easy axis. The engineering magnetostriction is defined in equation 3.3, Datta *et al* [1984]. θ_i is the initial angle of magnetisation from the ribbon axis and θ_f the angle of magnetisation on the application of a magnetic field.

$$\lambda_c = \frac{3}{2}\lambda_s(\cos^2\theta_f - \cos^2\theta_i) \qquad 3.3$$

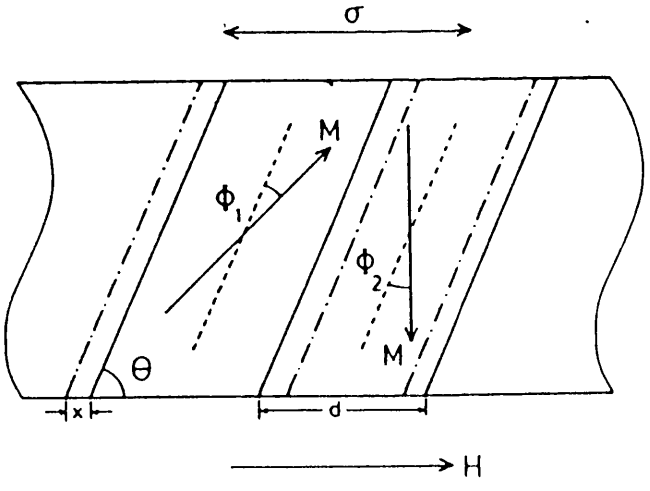

Figure 3.2 Magnetic domain structure assumed by Squire [1990].

The proposed model included contributions to the free energy density from the uniaxial anisotropy $\mathbf{U_a}$, magnetostatic energy $\mathbf{U_m}$, magnetoelastic energy $\mathbf{U_e}$ and the domain wall energy $\mathbf{U_w}$. The total free energy density is thus given by equation 3.4.

$$U = U_a + U_m + U_e + U_w \qquad 3.4$$

Expressions for the physical parameters are obtained by minimising the free energy with respects to the moment orientation angles ϕ_1 and ϕ_2 and the domain wall displacement **x** such that equation 3.5 is satisfied.

$$\frac{\partial U}{\partial \phi_1} = \frac{\partial U}{\partial \phi_2} = \frac{\partial U}{\partial x} = 0 \qquad 3.5$$

The three equations obtained from the above relations can be solved simultaneously to give ϕ_1, ϕ_2 and **x** in terms of the applied field and the material parameters. The field dependence of the Young's modulus was calculated by the same method as Livingston [1982] by defining the Young's modulus as shown in equation 3.6.

$$\frac{1}{E} = \frac{\partial \varepsilon}{\partial \sigma} \qquad 3.6$$

A similar solution to that of Livingston [1982] is returned but with an additional factor $\mathbf{F(h;\theta,\gamma)}$; this is a function of the reduced field **h** given by the applied field divided by the anisotropy field, the easy axis direction θ and the reduced strain energy given by equation 3.7 where **K** is the anisotropy energy.

$$\gamma = \frac{3\lambda_s \sigma}{4K} \qquad 3.7$$

The normalised variation in the Young's modulus is then given by equation 3.8. E_s is the modulus at magnetic saturation

$$\frac{E_s - E}{E} = \frac{\Delta E}{E} = \frac{9}{8}\frac{\lambda_s^2 E_s}{K} F(h;\theta,\gamma) \qquad 3.8$$

The function $F(h;\theta,\gamma)$ for a range of easy axis orientations and no applied stress ($\gamma = 0$) is shown in Figure 3.3. The discontinuity observed for $\theta = 80°$ was explained by Squire [1989] in terms of moments flipping from angles greater than 90° to the applied field to angles less than 90° as the applied field is increased in magnitude. The observation of the discontinuity, the disagreement with measured data for the magnitude of $\Delta E/E$ at zero applied field and the form of the curve at the anisotropy field prompted the introduction of a spread in both the magnetic moments and the easy axis direction to the model in terms of a Gaussian distribution, Squire [1989]. The model was then found to account for all the salient features observed in the experimental data. Figure 3.4 demonstrates the typical experimentally observed field dependences for one particular amorphous alloy composition. The data was obtained using a vibrating reed method and a number of separate samples were produced. Each sample was annealed in a magnetic field to produce the required easy axis orientation after undergoing an initial stress relief, Thomas [1991].

The most important magnetostriction parameter in terms of device applications that can be obtained from the model is the quadratic coefficient for small field about H=0. The zero stress condition is only considered as the expression becomes over complicated for non zero stress. The result obtained for the intrinsic quadratic coefficient C_Q is shown in equation 3.9. This is the quadratic coefficient defined in terms of the magnetisation rather than the applied field and allows comparisons between different

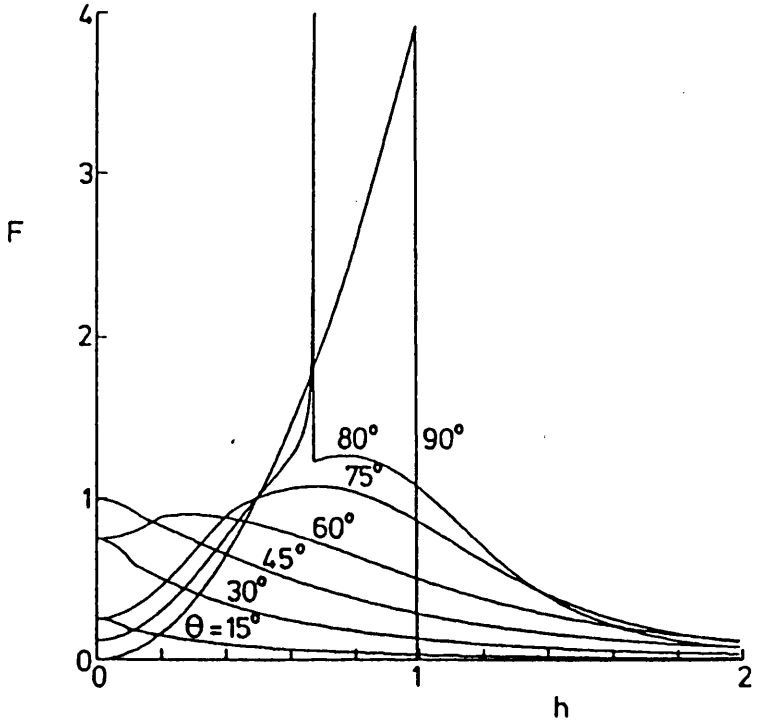

Figure 3.3 Function used in the calculation of the change in Young's modulus with applied field from Squire [1990].

materials to be undertaken without having to account for effects caused by sample geometries. c is the ratio of the susceptibility for a longitudinally annealed sample to that of a transversely annealed sample.

$$C_Q = \frac{3}{2}\left[\frac{(c-1)\sin^2 2\theta - 2\sin^2\theta\cos 2\theta}{2(\sin^2\theta + c\cos^2\theta)^2}\right]\left(\frac{\lambda_s}{M_s^2}\right) \qquad 3.9$$

Experimentally measured magnetostriction curves obtained from the same samples used to produce Figure 3.4 are shown in Figure 3.5. The measurements were carried out using the Fibre-Optic dilatometer and are reproduced from Thomas [1991]. For both the magnetostriction and the field dependent Young's modulus both the Squire and

Livingston models predict a maximum in the magnitudes of both effect for samples which have an in-plane induced easy axis perpendicular to the applied field direction. This would appear to be confirmed by the results of Figure 3.4 and Figure 3.5. This finding along with equation 3.6 and equation 3.7 would suggest that to obtain an optimum overall response to an applied field a low anisotropy energy coupled with a high saturation magnetostriction and a perpendicular in-plane easy axis would be desirable. This is borne out in the work carried out on magnetostriction by Thomas [1991] in which he states; "It was concluded that a high anisotropy constant is not essential for maximum λ_e, rather that the anisotropy be sufficiently developed to produce a uniaxial character."

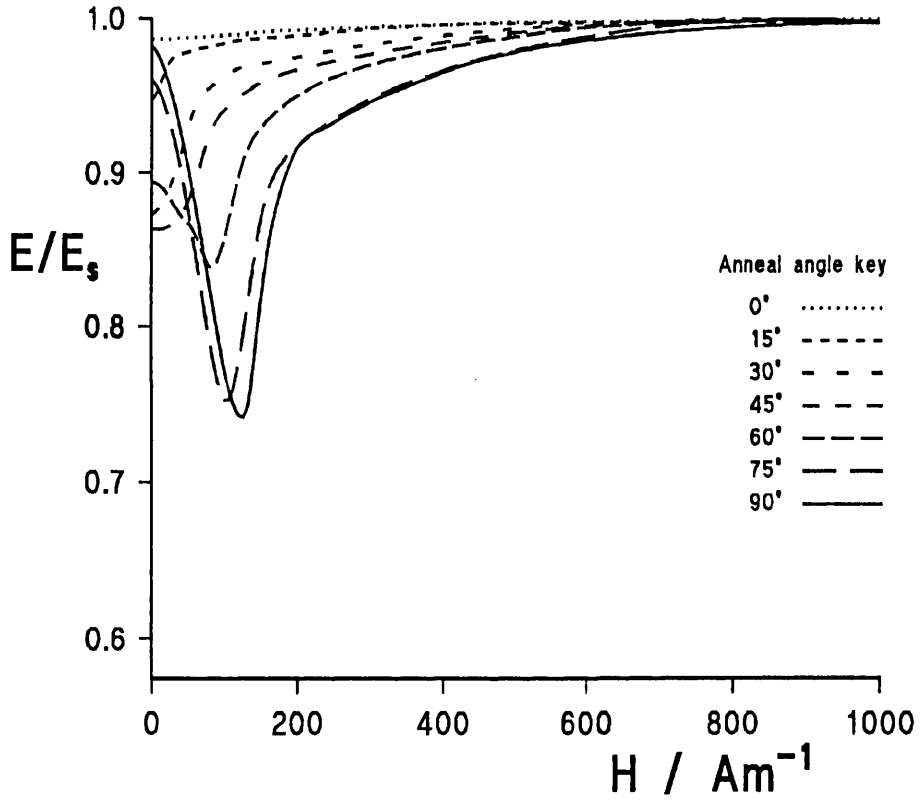

Figure 3.4 Normalised field dependence of the Young's modulus for a range of induced easy axis directions (VAC0040 $Fe_{40}Ni_{40}B_{20}$), Thomas [1991].

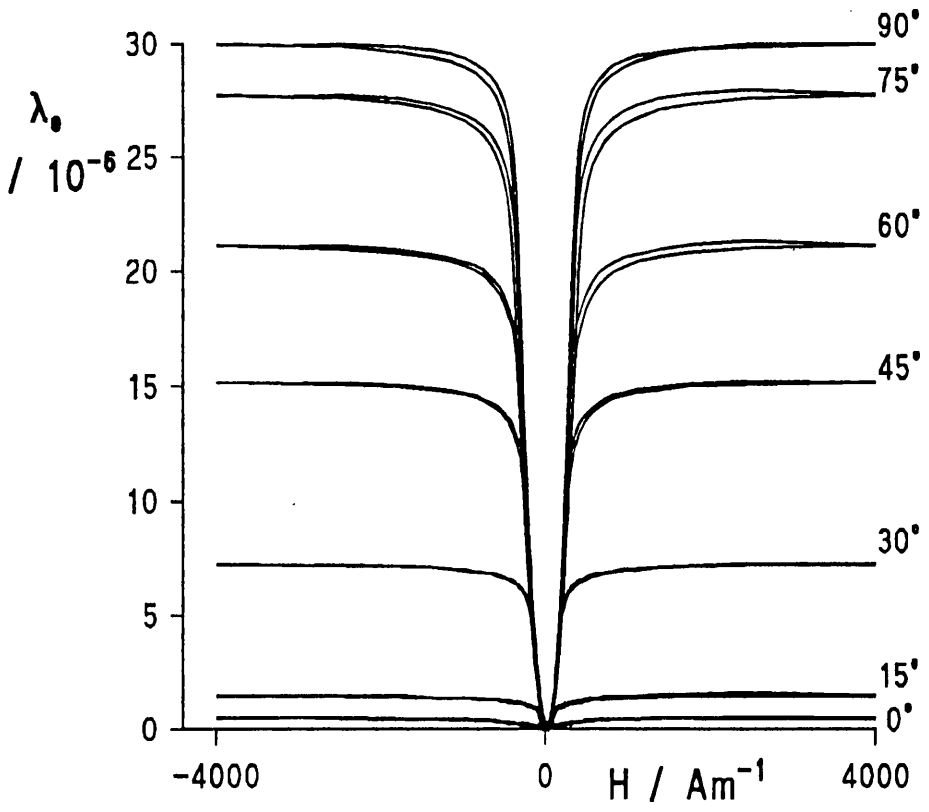

Figure 3.5 Field dependence of the engineering magnetostriction for a range of induced easy axis directions (VAC0040 $Fe_{40}Ni_{40}B_{20}$), Thomas [1991].

A detailed study of the compositional dependence of an amorphous alloy on both the magnitudes and forms of the Young's modulus and the magnetostriction is beyond the scope of this short review. The effects can be studied briefly in so far as presenting experimental data on a range of alloy compositions. Reported data on the observed variations in the Young's modulus for different alloys that have been transversely field annealed are shown in Table 3.1. Table 3.2 summarises the maximum observed engineering magnetostriction and the quadratic coefficients for range of alloy compositions which have also undergone a transverse field anneal. Two values for each alloy composition are shown in Table 3.1 for the Young's modulus and are normalised

against the saturation Young's modulus $\mathbf{E_s}$. These values along with the bias field value at which the minimum in modulus was observed were calculated where possible from the published data. The presented form of the data represents a concise approach to comparing responses from different materials. The minimum in the modulus ratio demonstrates the overall magnitude of the change in the Young's modulus. The absolute value of the modulus ratio at zero field along with the modulus minimum field value give an indication of whether a well defined transverse easy axis has been induced. For a well defined transverse easy axis with a minimised spread in moments Squire and Gibbs [1989] predict a near unity value for the zero field modulus ratio. The bias field for the minimum modulus ratio gives an indication of the anisotropy field and thus the size of the induced anisotropy which would have to be reasonably large in order to produce a well defined easy axis. Taking into account these issues it would appear that the annealing treatment carried out by Brouha and van der Borst [1979] has not produced a well defined easy axis whereas the treatments undertaken by Berry and Pritchet [1975a] and Gibbs [1991] were more successful. For sensor applications and especially for the Shear-wave magnetometer the overall magnitude of the change in the modulus is of less importance than how sensitive the modulus is to a small change in field. Consideration of all three material values quoted in Table 3.1 would suggest that for instance, although the overall change in the magnitude for the Young's modulus is greater for the material studied by Berry and Pritchet [1975a], the annealing process carried out on the material studied by Gibbs [1991] produced a sharper response. Similarly examination of the data of Mitchell *et al* [1979] shows a sharper response for the Fe-Si-B alloy than for the Fe-Co-B alloy investigated by these authors. Detailed investigation of the effects of increasing the cobalt content in Iron based amorphous alloys were carried out by Arai & Tsuya [1978]. Iron based alloys with low cobalt content exhibit large variations in the Young's modulus and the magnetostriction. Both of these effects are rapidly reduced

with increased cobalt content. Cobalt based alloys are not considered here as they have small negative magnetostriction and subsequently low values for the change in the Young's modulus with applied field, Baczewski *et al* [1984]. The largest overall change in the magnitude of the Young's modulus was observed by Wun-Fogle *et al* [1986] in a smooth surface variant of the commercially available alloy METGLAS 2605SC.

The change in the shear modulus of amorphous alloys with applied field can be measured using a torsional pendulum arrangement as described by Atalay and Squire [1992a]. The field dependent shear modulus of amorphous wires have been extensively investigated. The composition of the Amorphous wires $Fe_{77.5}Si_{7.5}B_{15}$ is similar to that of the commercially available amorphous ribbon METGLAS 2605S2. Comparative measurement between the field dependence of the Young's modulus and the shear modulus have shown that they both retain the same qualitative features, Atalay and Squire [1991a]. This is as would be expected from the link between the two moduli through Poisson's ratio. Optimally annealed samples of the amorphous wire have been shown to have a similar overall ΔE effect to METGLAS 2605S2 with $E_0/E_s = 0.92$, $E_{min}/E_s = 0.4$ at a field H= 250 A/m and a engineering magnetostriction of λ_e= 55 ppm, a radial domain structure perpendicular to the long axis of the wire has been proposed to account for this, Atalay and Squire [1992b]. The minimum observed in the shear modulus was 0.2 for optimally prepared material. The field dependent shear modulus of amorphous ribbons have been less extensively investigated. The non symmetric axial geometry of the ribbons introduces complications into the torsional pendulum measurements in the form of longitudinally induced stresses, Madurga *et al* [1984]. Kiss *et al* [1989] however, have carried out measurements on transversely annealed ribbons of composition $Fe_{78}Si_{10}B_{12}$. The normalised shear modulus was found to exhibit considerable hysteresis with applied field with a minimum of 0.44 at 500 A/m and 0.6 for no applied field. The hysteresis and the overall magnitude of the shear modulus change were seen to decrease

rapidly with the application of a tensile stress with the minimum in the modulus shifting towards larger magnetic fields. This is demonstrated in Figure 3.6 which shows the stress dependence for a field annealed alloy. High frequency measurement of both the Young's modulus and the shear modulus were undertaken by Kobelev and Soifer [1986] using a pulse echo technique on untreated METGLAS 2605SC. For a shear wave transmitted along the ribbon a minimum was observed in the velocity from which the normalised shear modulus was calculated to be 0.9 at a longitudinally applied field of 550 A/m. The zero field modulus was 0.95 of the saturation modulus.

Table 3.1 Reported Young's modulus variations with field for transverse field annealed alloys.

Alloy	$\frac{E_0}{E_s}$	$\frac{E_{min}}{E_s}$	Field for minimum H / Am^{-1}	Reference
$Fe_{75}P_{15}C_{10}$	0.91	0.56	560	Berry & Pritchet [1975a]
$Fe_{40}Ni_{40}P_{14}B_6$ METGLAS 2826	0.88	0.71	320	Berry & Pritchet [1976a]
$Fe_{78}Si_{10}B_{12}$ ≈METGLAS 2605S2	-	0.34	-	Arai & Tsuya [1978]
$Fe_{71}Co_9B_{20}$	-	0.31	280	Mitchell *et al* [1979]
$Fe_{80}B_{20}$ METGLAS 2605	-	0.61	160	
$Fe_{78}Si_{10}B_{12}$ ≈METGLAS 2605S2	-	0.36	144	
$Fe_{80}Si_5B_{15}$	0.21	0.18	20	Brouha & van der Borst [1979]
$Fe_{81}Si_{3.5}B_{13.5}C_2$	-	0.16	-	Wun-Fogle *et al* [1986] * Smooth surfaced alloy.
METGLAS 2605SC		0.09 *		
$Fe_{78}Si_9B_{13}$	-	0.19	-	
METGLAS 2605S2		0.15 *		
$Fe_{81}Si_{3.5}B_{13.5}C_2$ METGLAS 2605SC	0.82	0.44	500	Kobelev *et al* [1987]
$Fe_{80.2}Cr_2Si_{3.8}B_{14}$ METGLAS 2605S3A	0.65	0.49	100	Duhaj & Kaczkowski [1991]
$Fe_{40}Ni_{40}B_{20}$ VAC0040	0.99	0.74	120	Gibbs [1991]

Table 3.2 Reported values of the engineering magnetostriction for transverse field annealed alloys

Alloy	λ_e ppm	C_Q $10^{-17}(A^{-2}m^2)$	Reference
$Fe_{75}P_{15}C_{10}$	40	-	Berry & Pritchet [1975a]
$Fe_{81}Si_{3.5}B_{13.5}C_2$ METGLAS 2605SC	61.5	4.01	Thomas [1991]
$Fe_{78}Si_9B_{13}$ METGLAS 2605S2	60.9	4.01	
$Fe_{40}Ni_{38}Mo_4B_{18}$ METGLAS 2826MB	23.8	5.86	
$Fe_{40}Ni_{40}B_{20}$ VAC0040	29	5.81	
$Fe_{80.2}Cr_2Si_{3.8}B_{14}$ METGLAS 2605S3A	30	-	Duhaj & Kaczkowski [1991]

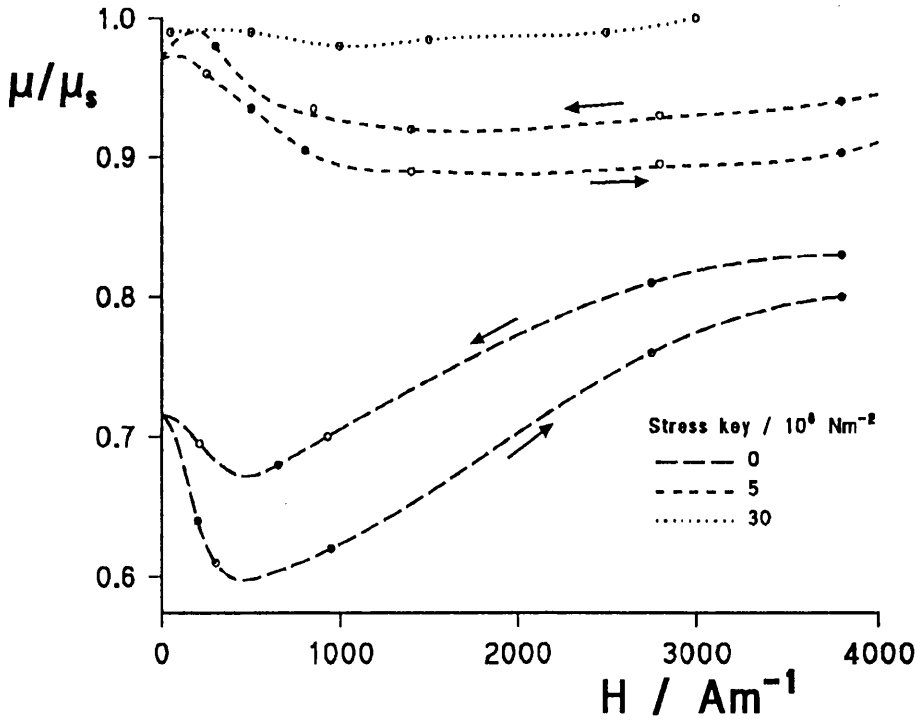

Figure 3.6 Stress dependence of the shear modulus in field annealed $Fe_{78}Si_{10}B_{12}$ amorphous alloy, after Kiss *et al* [1989].

3.5 Magnetomechanical Damping.

The field dependence of the Young's modulus is a direct result of the coupling between the magnetic field and the strain which produces a rotation of the domains within the ribbon. The domain movements are responsible for a further effect, a magnetic contribution to the total internal friction of relaxation and hysteretic types. These can be observed as a damping of either an elastic wave travelling along the amorphous ribbon Kobelev and Soifer [1986], or a decay in the free vibration of a vibrating reed, Berry and Pritchet [1976a]. A measure of the internal friction Q^{-1} can be obtained from the damping decrement δ as defined by Malkinski and Malkinski [1990] provided the damping is not large i.e. $Q^{-1} \ll 1$, equation 3.10.

$$Q^{-1} \approx \frac{\delta}{\pi} \qquad 3.10$$

The damping decrement can be calculated from the ratio of the initial peak amplitude of the oscillation V_0 to the peak height of the n^{th} oscillation V_n as in equation 3.11.

$$\delta = \frac{1}{n}\ln\left(\frac{V_0}{V_n}\right) \qquad 3.11$$

The internal friction has a high degree of correlation with the field dependent elastic moduli. A maximum can be observed in the internal friction at a bias field that corresponds to the minimum in the normalised elastic modulus this is demonstrated in Figure 3.7. Table 3.3 shows reported magnitudes of the main features of the field dependent damping curve for a number of different alloy compositions. Q^{-1}_0 is the damping at zero applied field, Q^{-1}_s that at saturation and Q^{-1}_{max} the maximum observed damping at the bias field H_b.

The usual approach to describing the mechanical damping is to consider the contributions from three mechanisms which have a frequency dependence and would thus be expected to return different magnitudes for the overall damping over a range of frequencies;

Magnetomechanical hysteresis which is associated with the irreversible movement of magnetic domain walls under the action of stress. It is stress amplitude dependent and independent of frequency, Nowick and Berry [1972].

Macroscopic eddy currents are produced by changes in the magnetisation of the sample under the influence of elastic stresses (moment rotation). For low frequencies macro eddy currents are proportional to the frequency of the magnetisation changes whereas for higher frequencies they are dependent on $1/\sqrt{f}$.

Microscopic eddy currents are caused by changes in the local magnetisation which are not identical to the changes in the macroscopic magnetisation. This is a direct result of the magnetic domain structure. Micro eddy currents are proportional to the frequency of magnetisation changes.

These mechanisms have been used to describe the origins of the damping for various measurement techniques. Macroscopic and Microscopic eddy current rely on moment rotation and thus would be expected to be influenced by similar process to that of the Elastic modulus. The Magnetomechanical hysteresis, however, would be more dependent on the pinning of domain walls. Both Atalay and Squire [1991] and Kiss *et al* [1988] carried out measurements utilising a torsional pendulum at low frequencies and have attributed the major loss to magnetomechanical hysteresis. Pulse echo measurements are carried out at high frequencies and are thus dominated by macroscopic and microscopic eddy currents. Kobelev and Soifer [1986] have separated these two effects by considering the zero applied field case in which only micro eddy currents make a contribution. Their results demonstrate that the micro eddy current contribution is dominant not only for the zero field case but also when the elastic wave is propagated in the same direction as the applied field. For an elastic wave propagated perpendicular to the applied field macroscopic eddy currents predominate. The vibrating reed measurements are carried out at intermediate frequencies and contain contributions from all three mechanisms as well as an anomalous hysteretic loss for a zero applied field, Berry and Pritchet [1976b]. In all cases, however, the form of the field dependence follows that of the elastic modulus and all the alloys reviewed irrespective of the measurement technique exhibit comparable changes in the internal friction within the same order of magnitude.

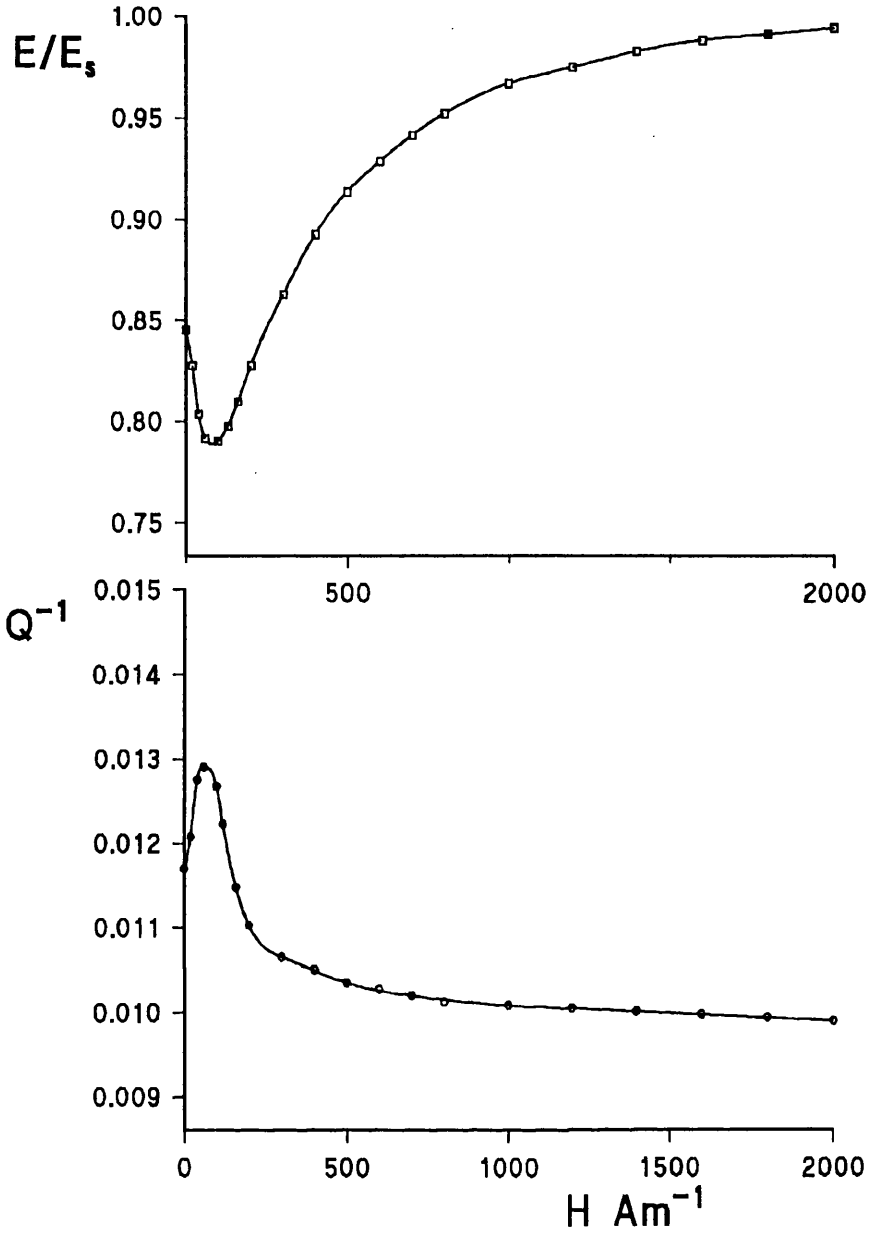

Figure 3.7 Internal friction Q^{-1} and normalised Young's modulus dependences on bias field for as cast $Fe_{81}Si_4B_{15}$, after Kaczkowski and Malkinski [1984].

Table 3.3 Reported magnitudes for magnetomechanical damping

Alloy Composition	Measurement technique	Q^{-1}_0 X10^{-3}	Q^{-1}_s X10^{-3}	Q^{-1}_{max} X10^{-3}	H_b Am^{-1}	Annealed state	Reference
$Fe_{81}Si_{3.5}B_{13.5}C_2$ METGLAS 2605SC	Pulse echo	60 Q^{-1}_0-Q^{-1}_s	-	95 Q^{-1}_{max}-Q^{-1}_s	800	As cast	Kobelev and Soifer [1986]
$Fe_{78}Si_{10}B_{12}$ ≈METGLAS 2605S2	Torsional pendulum	40	8	62	70	Transverse anneal	Kiss *et al* [1988]
$Fe_{75}P_{15}C_{10}$	Vibrating reed	2	3	10	560	Transverse anneal	Berry and Pritchet [1976a]
$Fe_{81}Si_4B_{15}$	Resonance / Antiresonance	10	1	17	70	As cast	Kaczkowski and Malkinski [1984]
$Fe_{77.5}Si_{7.5}B_{15}$ WIRE	Torsional pendulum	12.5	4	33	300	Optimally Annealed	Atalay and Squire [1991]

3.6 Magnetoelastic Coupling Constant.

The magnetoelastic coupling constant **k** is the fractional transfer between magnetic and mechanical energy and is therefore intrinsically linked to the field dependent elastic moduli. The field dependence of the coupling constant once again takes the form of the field dependant modulus with a maximum in coupling less than unity occuring at the same bias field as the minimum in the elastic modulus. If E_0=E_s then with no applied bias field there is no magnetoelastic coupling and the coupling constant is zero. As the applied field magnetically saturates the material the coupling constant falls to a saturation value which is less than the maximum value. Consideration of the moment rotation model

yields an expression for the coupling constant, equation 3.12. This equation is valid for fields less than the anisotropy field and the coupling constant is a maximum when the applied field is equal to the anisotropy field, Livingston [1982].

$$k = \left[1 + \frac{\mu_0 M_s H_a^3}{9\lambda_s^2 E_s H^2}\right]^{-\frac{1}{2}} \leq 1. \qquad 3.12$$

This expression contains identical parameters in a similar functional form to that obtained by Livingston for the field dependent modulus. An optimisation of the field dependent modulus would therefore on this basis be expected to optimise the energy transfer giving maximum coupling constants. Examination of Table 3.4 demonstrates that in the as-cast state values for the coupling constant are typically of a similar order of magnitude to those for crystalline magnetostrictive materials. Crystalline magnetostrictive materials have coupling constants which are typically of the order of **k=0.3**. Transverse field annealing to induce a perpendicular easy axis considerably enhances these values in some cases to values greater than those obtained for piezo-electric transducers where the electromechanical coupling constants are of the order of **k=0.7-0.8**, Berlincourt *et al* [1964]. It should be noted, however, that the indirect measurement of **k** as in those of Wun-Fogle *et al* [1986] will tend to give inflated values for the coupling constant O'Dell [1982].

As would be expected from the measurements of both the Young's modulus and the magnetostriction the coupling constant for Cobalt based alloys are small (**k=0.17**), Baczewski *et al* [1984], whereas Iron based alloys with low Cobalt content can exhibit large coupling constants. By far the largest magnetoelastic coupling is observed after field annealing in a transverse field commercially available METGLAS 2605## alloys.

Where ## denotes a number of different identifiers. This is in line with their large saturation magnetostriction and field dependent elastic modulus observed in Table 3.1 and Table 3.2.

Table 3.4 Reported coupling constants for a range of alloy compositions

Alloy	k_{max}	Field for maximum H / Am^{-1}	Annealed state	Reference
$Fe_{78}Si_{10}B_{12}$ ≈METGLAS 2605S2	0.72	-	Transverse anneal	Arai & Tsuya [1978]
$Fe_{71}Co_9B_{20}$	0.81	270	Transverse anneal	Mitchel *et al* [1979]
$Fe_{80}B_{20}$ METGLAS 2605	0.62	150		
$Fe_{78}Si_{10}B_{12}$ ≈METGLAS 2605S2	0.82	150		
$Fe_{80}Si_5B_{15}$ ≈METGLAS 2605S3	0.85	70	Transverse anneal	Brouha & van der Borst [1979]
	0.47	100	As quenched	
$Fe_{80}Si_{10}B_{10}$	0.54	150	Transverse anneal	
	0.35	400	As quenched	
$Fe_{40}Ni_{38}Mo_4B_{18}$ METGLAS 2826MB	0.5	65	Transverse anneal	Anderson [1982]
$Fe_{78}Si_9B_{13}$ METGLAS 2605S2	>0.9	80		
$Fe_{79}Si_5B_{16}$ METGLAS 2605S3	>0.9	80		
$Fe_{81}Si_{3.5}CB_{13.5}C_2$	0.92	-	Transverse anneal	Wun-Fogle *et al* [1986]
METGLAS 2605SC	0.95 *			* Smooth surfaced alloy.
$Fe_{78}Si_9B_{13}$	0.90	-		
METGLAS 2605S2	0.92 *			
$Fe_{80.2}Cr_2Si_{3.8}B_{14}$ METGLAS 2605S3A	0.52	100	stress relieved	Duhaj and Kaczkowski [1991]

4 MAGNETOELASTIC WAVES IN AMORPHOUS RIBBONS.

4.1 Introduction.

Elastic waves are coupled to the magnetic field through the magnetomechanical coupling constant. When elastic waves are transmitted through an amorphous material the propagation of the waves is influenced by the magnetomechanical properties of the material. In the presence of a magnetic field the elastic waves have a field dependent phase velocity through the elastic modulus dependence and a field dependent attenuation from the magnetomechanical damping. A brief overview of the wave propagation modes in magnetic material is given in order to identify the form of the desired oscillation for the shear wave magnetometer. The magnetic field dependent velocity and attenuation are then considered. Consideration is also given to a technique for modelling the behaviour of magnetoelastic waves. Finally some of the results obtained from the model are compared with the experimentally observed data.

4.2 Propagation Modes of Magnetoelastic Waves.

The solution of the wave equation in elastic media yields many different modes of propagation depending on the geometry and boundary conditions of the medium. A rigourous treatment of elastic waves would be overly complicated and unjustified here. A simple consideration of the various degrees of freedom of a propagation medium yields two distinct groups of modes pertinent to the geometries encountered in magnetoelastic wave devices. Typically magnetoelastic wave device geometries are either of the ribbon form, Imamura & Sasaki [1984], or amorphous magnetic films deposited on non magnetic substrates, Webb *et al* [1979]. Two distinct groups of modes are observed in the two different media. Amorphous ribbons can be considered as plates or slabs of infinite extent with a finite thickness. In the slab like media of the ribbons bulk waves

predominate and are of the Lamb extensional and flexural type modes and the shear modes. These three modes are illustrated in Figure 4.1a. In the case where these modes are coupled to the magnetic field they are commonly referred to as **EMEWs, FMEWs** and **SMEWs** respectively. When a film is deposited on a substrate the substrate thickness in general tends to be far greater than the film thickness. The boundary conditions for the solution of the wave equation are simplified if the substrate is assumed to be of infinite thickness. The device can then be considered as being a half space medium in which surface acoustic waves of the Rayleigh or Love types predominate, Ewing *et al* [1957]. These devices lend themselves to high frequency applications as at high frequencies (f_0>50MHz) the penetration depth is relatively small and most of the elastic energy is concentrated in the magnetoelastic surface layer, Matthews and van de Vaart [1969]. Magnetically coupled surface waves are commonly abbreviated in the literature to **MSAW**. The two types of **MSAW** modes are illustrated in Figure 4.1b.

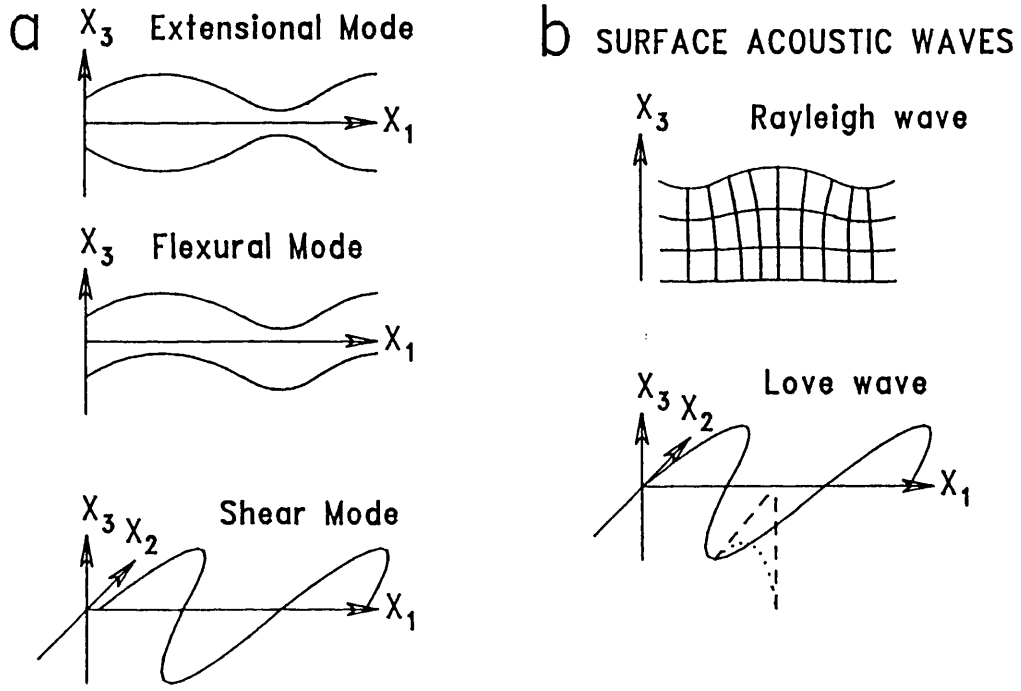

Figure 4.1a Illustration of the particle displacements of elastic waves in a slab.

4.1b Illustration of the fundamental surface acoustic waves.

In general the different magnetoelastic wave modes are dispersive in nature having phase and group velocities which depend on the frequency of propagation. If the waves are being propagated through material with ribbon geometries i.e. thin slabs, there is also a frequency limit below which the phase and group velocities for a particular mode become imaginary. The frequency at which this occurs is known as the cut-off frequency. Oscillation modes at frequencies below their cut-off frequency decay exponentially and are not propagated through the material. A special case occurs however, for the zeroth order shear mode in which the phase and group velocities are independent of frequency and in the absence of magnetoelastic coupling are equal to $\mathbf{V_s}$ the characteristic transverse shear wave velocity. This mode is also related to only one elastic modulus whereas both the flexural and extensional modes depend on two elastic moduli. The zeroth order shear mode is thus non-dispersive and can be propagated through a ribbon down to zero frequency. This is illustrated in Figure 4.2 which shows the frequency spectrum for the lower order shear modes in an infinite plate. ω is the propagation frequency, **d** the thickness of the slab and the product γd the propagation constant for the oscillations from the standard exponential notation for a wave propagated along the z axis depicted in equation 4.1

$$U_z = Ae^{i(\gamma z - \omega t)} \qquad 4.1$$

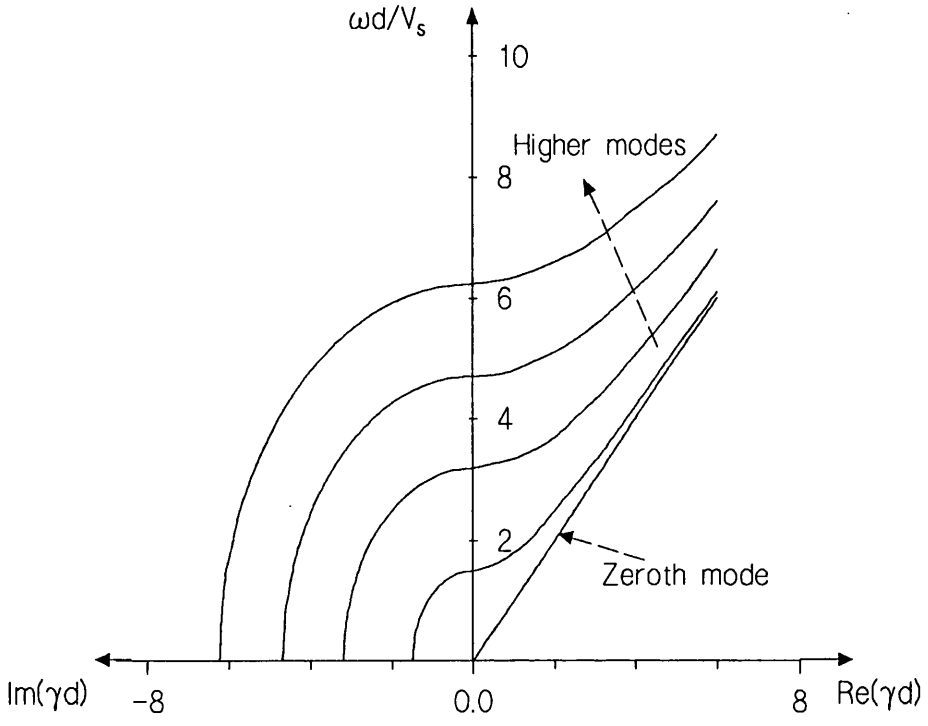

Figure 4.2 Frequency spectrum for shear modes in an infinite plate, after Meeker and Meitzler [1964]

The absense of a cut-off frequency for the zeroth order shear mode means that for the correct choice of ribbon geometry only this mode will be propagated and the ribbon will be free of the unwanted dispersive modes. The cut-off frequencies for shear wave modes propagating in a slab medium are given by equation 4.2, where **n** is an integer related to the order of the shear mode (**n=0,1,2...etc**).

$$\frac{\omega d}{V_s} = n\pi \qquad 4.2$$

In the case of amorphous ribbons of typical thickness 25μm the transverse shear wave velocity is of the order of $3kms^{-1}$ and as a result the zeroth order shear mode can

be propagated without higher modes up to frequencies in the order of 60MHz provided the appropriate transducer arrangement is employed, Berlincourt *et al* [1964] and May [1964]. For very long ribbons however the interactions of the elastic wave with the edges of the ribbon can become appreciable. This results in dispersive modes which are in the zeroth shear mode with respect to the thickness direction travelling along the ribbon reflecting back and forth between the edges, Meitzler [1964].

4.3 Attenuation of Magnetoelastic Waves in Amorphous Alloy.

In order to optimise the signal to noise ratio of the shear wave magnetometer system it is desirable to maximise the frequency of propagation of the elastic waves and at the same time minimise the loss due to attenuation, Squire and Gibbs [1988b]. Therefore, it would appear that two aspects of the attenuation are important in the application of amorphous material to elastic wave devices: the dependence of the attenuation of the elastic waves with propagation frequency and the field dependent attenuation. Tsuya *et al* [1977] and Squire and Gibbs [1988b] have both studied the effects of the propagation frequency in "as received" and field annealed amorphous ribbons. Tsuya *et al* [1977] studied the attenuation properties of longitudinal Love type MEWs in $Fe_{78}Si_{10}B_{12}$ amorphous alloy whereas Squire and Gibbs [1988] concentrated their investigations on pulsed shear wave propagation along METGLAS 2826MB ($Fe_{40}Ni_{38}Mo_4B_{18}$) to obtain data specifically for the shear wave magnetometer application. In both cases the attenuation was seen to increase rapidly above a few mega-Hertz and followed the attenuation relationship shown in equation 4.3 which is commonly found for delay lines using polycrystalline metals, Meitzler [1964].

$$\alpha = af + bf^4 \qquad 4.3$$

α is the attenuation constant and f the frequency. The constant **a** depends on hysteresis losses in the material. For polycrystalline materials **b** is related to scattering at grain boundaries and topological surface features. To explain the attenuation observed in amorphous ribbon where no grain boundaries are present Squire and Gibbs suggested that scattering could occur at domain boundaries. The results obtained by Squire and Gibbs [1988] are shown in terms of the relative amplitudes of successive shear wave pulses in Figure 4.3 and show clearly the detrimental effects of the $1/f^4$ term for high-frequency operation.

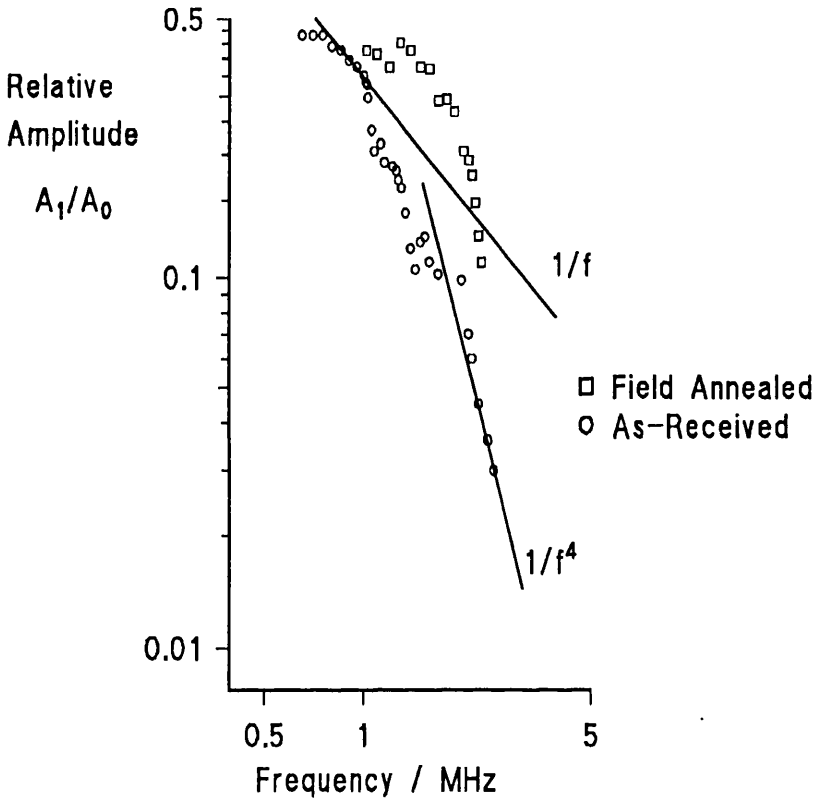

Figure 4.3 The frequency dependence of shear wave transmission along METGLAS 2826MB amorphous ribbon.

Kobelev and Soifer [1986] made experimental observations on the magnetic field dependence of the propagation of both Lamb and shear waves in METGLAS 2605SC ($Fe_{81.5}Si_{3.5}B_{13.5}C_2$) and observed that in both cases for waves transmitted along a ribbon the field dependence was of the same form as the magnetoelastic damping for a magnetic field applied along the ribbon length. The maximum attenuation occurred at the same applied field as the maximum magnetoelastic coupling. Squire and Gibbs [1988] observed a sharp initial increase in the attenuation for the "as received" ribbons compared with the field annealed material. This was possibly due to a large moment distribution in the "as received" ribbon with a much greater percentage of the more easily rotated 45° moments than in the transversely field annealed material. The field annealed material was also observed to exhibit considerably less scattering because of the removal of local stress centres in the accompanying stress relief. However, the stress relief along with the field anneal increases the magnitude of the magnetoelastic coupling and thus the overall attenuation of the magnetoelastic wave, Greenough and Schulze [1990]. Inoue [1985a] has presented a model for predicting the behaviour of MEWs in thin conducting plates which have a uniaxial in-plane anisotropy. This model will be discussed in more detail in chapter 4.5. The model predicts that for the three types of bulk magnetoelastic waves by far the greatest attenuation is observed in the flexural mode, the shear modes being damped the least. A large attenuation of the propagated waves suggest a high degree of magnetomechanical coupling and hence a pronounced field dependence of the velocity. Large coupling and hence large velocity changes are always realised at the expense of losses.

4.4 Velocity Dependence of Magnetoelastic Waves on the Magnetic Field.

As would be expected from the dependence of the elastic moduli on the applied field the magnetoelastic wave velocity is a function of applied field. The maximum change observed in the velocity is also a function of the frequency of the oscillations and depends on the magnetoelastic wave mode being propagated. Arai *et al* [1976] observed that for the longitudinal modes in $Fe_{78}P_{13}C_7$ amorphous ribbon there was a decrease in the observed magnitude from approximately 12% velocity change with applied field at 100kHz to less than 4% at 1MHz. The low frequency response agreed well with their observed change in the magnitude of the elastic modulus. The loss in response can be explained in terms of an increase in the magnetomechanical damping. Examination of the effect of varying the thickness of $Fe_{78}Si_{12}B_{10}$ ribbon on the delay properties between 500kHz and 10MHz was carried out by Arai and Tsuya [1978]. The thicker ribbons i.e. 20μm had a variable delay time which had a maximum change in magnitude of 20% at 500kHz. The delay decreased with increasing frequency and was approximately proportional to $1/f$. This would point towards micro eddy current damping as being the main mechanism contributing to the decrease in the observed velocity changes in amorphous ribbons in this frequency range, Imamura and Sasaki [1984]. Inoue [1989] proposed that this loss in response was actually due to dynamic demagnetising fields. These are caused by gradients in the magnetisation associated with the longitudinal MEWs which increase with increasing frequency. It was suggested that micro eddy current damping only played a part at higher frequencies of the order of a few tens of mega-Hertz.

The field dependence of longitudinal MEWs in the tens of kilo Hertz frequency band along transversely field annealed $Fe_{40}Ni_{40}B_{20}$ (VAC0040) has been studied by Imamura and Sasaki [1984] and Imamura *et al* [1985]. The results agreed closely with

those predicted from consideration of the uniaxial induced anisotropy. A maximum velocity change observed was for longitudinal waves at 60kHz and was of the order of a 20% change at an applied field close to the anisotropy field. Kobelev and Soifer [1986] investigated the longitudinal and shear mode magnetic field dependence at 5MHz. As with the low frequency longitudinal response the shear mode response follows a similar form to that of the field dependent modulus with a maximum velocity change with field of approximately 4%. The longitudinal mode response at this frequency has fallen to below a 2% change in the velocity. Inoue [1989] has indicated that EMEWs are favourable for MEW devices operating at low frequencies and FMEWs and SMEWs for high frequency operation with the constraint that the flexural mode is dispersive. The velocity dependence on applied magnetic field in METGLAS 2605CO ($Fe_{67}Co_{18}Si_{11}B_{14}$) is shown in Figure 4.4 for both the extensional and the shear modes as a function of propagation frequency, Inoue *et al* [1985b]. The results clearly show the similarity of the response to that of the elastic modulus response. The reduction in the extensional mode response with increasing frequency is also evident.

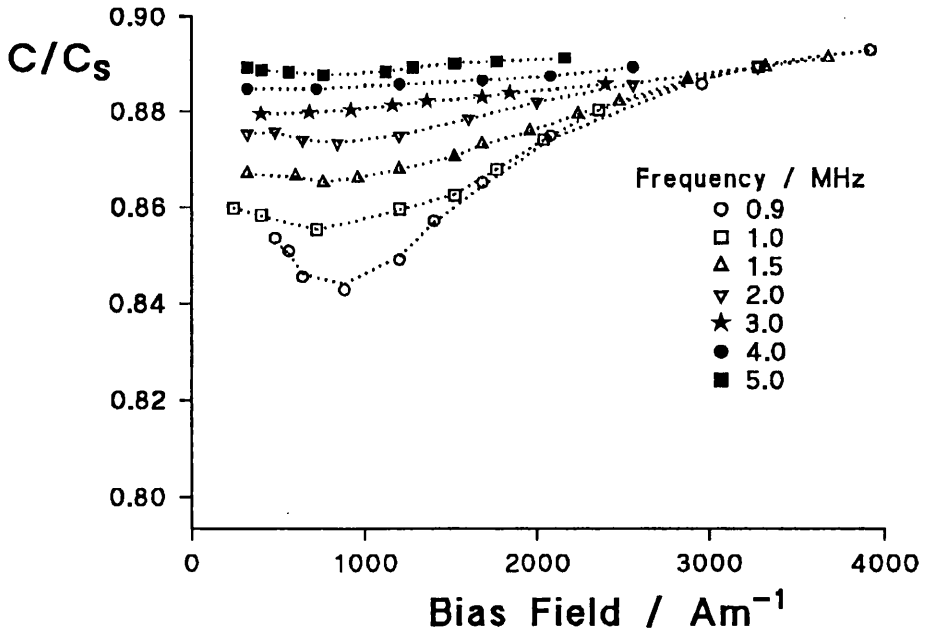

Figure 4.4a Bias field dependence of EMEW velocity along T.F.A. METGLAS 2605SC.

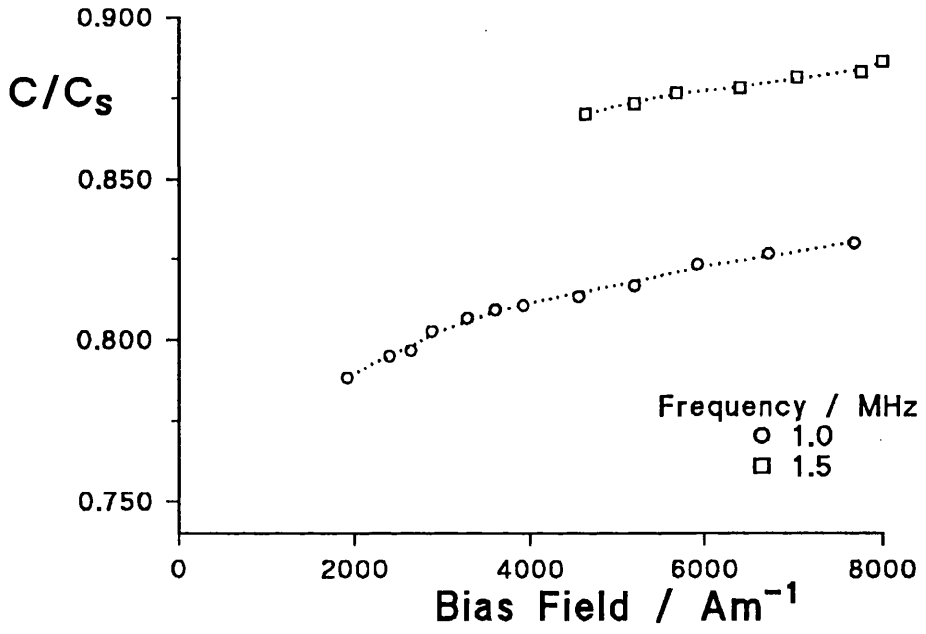

Figure 4.4b Bias field dependence of SMEW velocity for the same sample as in 4.4a, after Inoue *et al* [1985b].

The delay properties of magnetoelastic surface wave devices have been studied by both Webb *et al* [1979] and to a far greater extent by Inoue *et al* [1984], [1986], [1987a], [1987b], [1987c], [1989] & [1990]. Webb *et al* [1979] studied the delay field dependent velocity change in Fe-B electron beam co-evaporated films of the order of a micron in thickness on piezoelectric substrates. A maximum velocity change of 0.03% for a 140MHz MSAW was obtained. A predominant problem with MSAW devices is restricting the MSAW to the magnetic layer and thus achieving the maximum magnetomechanical coupling. An extension of the model for MEWs to account for the behaviour of MSAWs in a half space media, Inoue *et al* [1984] & [1985], demonstrated that to obtain the optimum change in the MSAW velocity two requirements had to be fulfilled: a large oscillation frequency and film thickness to restrict the MSAW to the magnetic layer and a maximum magnetomechanical coupling in the magnetic layer. A maximum velocity change for such a device was observed to be approximately 10% for an Fe-Co-B sputter deposited film with MSAWs propagated at 30MHz, Inoue *et al* [1987a]. Inoue *et al* [1987b] concluded from experimental and theoretical observations that the main limiting factor for such devices was the attenuation of the MSAWs brought about by eddy current damping at these frequencies. On a theoretical basis Inoue *et al* [1985] demonstrated a fall in the response from 24.6% for a nonconducting medium to 5.6% for a conducting medium. A multilayered device consisting of magnetic layers sandwiched between insulating layers was suggested as an alternative device configuration. This reduces eddy currents while maintaining a thick magnetically active layer. Inoue *et al* [1987c] analysed the behaviour of this configuration for an in-plane anisotropy perpendicular to the propagation direction with a further adaptation to his model. The effect of the thickness and number of insulating layers on the field dependence of the propagation velocity and attenuation was examined for a fixed overall film thickness, Inoue *et al* [1990]. The important parameter was found to be the number of

insulating layers, with an optimum of 15 insulating layers of 0.5μm thickness in a total film thickness of 15μm. This was the optimum point for a balance between minimum attenuation and maximum velocity change. A velocity change of 40% was predicted. Experimental observations have demonstrated that on introducing a single insulating layer the attenuation was reduced from 28dB/cm to 13dB/cm although only a 0.85% change in velocity with applied field was seen, Inoue [1989].

4.5 Theoretical Analysis of Magnetoelastic Waves in a Magnetic Slab.

4.5.1 Introduction.

With the current interest in controllable delay lines and acoustic wave devices a great deal of attention has been given to the modelling of magnetoelastic waves in magnetic materials in order to predict the behaviour of such devices. The behaviour of magnetoelastic Love wave propagation was studied by van der Vaart [1971] in metal coated layered substrates whereas Ganguly *et al* [1976] concentrated on surface acoustic waves in a magnetic film piezoelectric substrate configuration. Ganguly *et al* [1978] have also studied magnetoelastic surface waves in highly magnetostrictive cubic crystals. Elastic wave propagation has also been modelled in ribbon type geometries by Tsuya and Arai [1977]. The geometry selected was an infinitely thin ribbon of infinite length but finite width in which they used quasi-static approximations for determining the magnetisation vectors. These approximations become invalid for high frequencies as not only does the wavelength of the MEW approach the thickness of the ribbon but the magnetisation has a dynamic spin nature in the high frequency region. Consideration will therefore be given here to the approach adopted by Inoue and his co-authors. As with Ganguly *et al* [1976] & [1978], Inoue *et al* have employed the matrix technique for solving the wave equations in different media. This technique was proposed by Fahmy and Adler [1973] as a means of simplifying the solution of acoustoelectric waves in

multilayered structures made up of materials of arbitrary anisotropy, piezoelectricity and conductivity. This technique was adopted in order to predict the operating properties of multilayered SAW devices as variable delay media, Inoue *et al* [1987c] & [1990] and Inoue [1989]. Before progressing to the more complicated multilayered structures however, consideration was given to the geometries of greater interest to this work. Initially loss terms were ignored and the MEW propagation in a non conducting magnetic slab of finite thickness and infinite extent was modelled, Fujii *et al* [1982] and Inoue *et al* [1983]. This was then extended to include conducting magnetic material so that the extent of the eddy current damping could be studied, Inoue [1985a]. In its final form the model takes into consideration the behaviour of a conducting magnetic ribbon material which is isotropic apart from a magnetic in-plane uniaxial anisotropy. The magnetisation vector is also coupled to both the applied magnetic field and the elastic waves, further to the work of Tsuya and Arai [1977].

The studies undertaken on the model by Inoue *et al* did not include investigation into the suggested optimum configuration for device performance, an in-plane anistropy perpendicular to the wave propagation vector. Although the model does not take into account any effects from magnetic domain walls the fact that the model could potentially elucidate between eddy current damping and the loss mechanisms suggested by Squire and Gibbs [1988] along with the omission of studies into an in-plane perpendicular anisotropy prompted further investigations in to the model's behaviour to be carried out.

4.5.2 Outline of the Magnetoelastic Wave Model.

An outline is given here of the model proposed by Inoue *et al* [1982]. The starting equations are presented along with boundary conditions and the method adopted for solving the numerical calculations. A more detailed description of the model is best obtained from Inoue *et al* [1983] and Inoue [1989].

The transmission medium can be described using cartesian coordinates (x_1,x_2,x_3) as being of infinite extent in the x_1, x_2 plane but with a finite thickness **d** in the x_3 direction. The infinite slab is positioned about the origin in the x_3 direction such that the material extends from the origin to x_3=**d**. This geometry is shown in Figure 4.5.

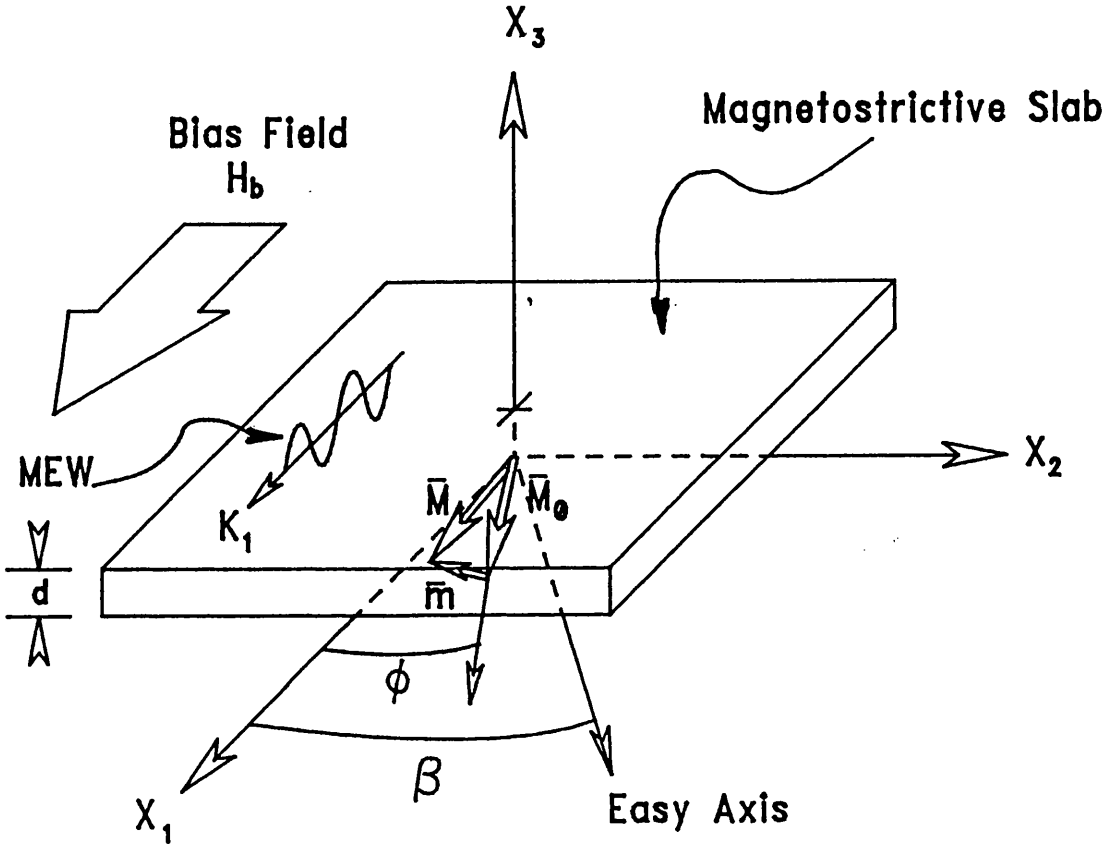

Figure 4.5 Infinite slab geometry used for the analysis of magnetoelastic waves.

The bias field $\mathbf{H_b}$ is applied parallel to the direction of the wave motion denoted by the wave vector $\mathbf{k_1}$ in the x_1 direction. A uniaxial anisotropy within the material is represented by an easy axis direction at an angle β to the wave motion in the x_1, x_2 plane. The direction of the static magnetisation vector $\mathbf{M_0}$ is obtained by considering the

coherent rotation of the magnetic moments in an applied field. The angle defining the direction of the magnetisation in the x_1, x_2 plane ϕ is obtained from the solution of equation 4.4 where $\mathbf{H_k}$ is the anisotropy field, Stoner and Wohlfarth [1947].

$$\frac{1}{2}\sin 2(\phi-\beta)+\frac{H_b}{H_k}\sin\phi \;=\; 0 \qquad 4.4$$

The dynamic precessional motion of the resultant magnetisation $\mathbf{M}=(M_1,M_2,M_3)$ is obtained from considering the spin motion of the dynamic part of the magnetisation vector $\mathbf{m}=(m_1,m_2,m_3)$ given by equation 4.5. γ is the gyromagnetic ratio (the ratio of the magnetic moment of the system to its angular momentum) and $\mathbf{h_{eff}}=(h_1,h_2,h_3)$ is the total effective internal field due to the magnetisation fluctuations caused by the wave motion.

$$\frac{d\mathbf{m}}{dt} \;=\; -\gamma(\mathbf{M}\times\mathbf{h_{eff}}+\mathbf{m}\times\mathbf{H_b}) \qquad 4.5$$

The effective field can be calculated from the differential of the free energy density with respects to the magnetisation vector $\mathbf{m}$ as shown in equation 4.6. The free energy density ε consists of contributing terms from the uniaxial anisotropy energy ε_k, the magnetoelastic energy ε_H due to an externally applied field, the magnetostatic energy due to the demagnetising field ε_d, the magnetoelastic coupling energy ε_{me} and the elastic energy ε_e as shown in equation 4.7.

$$\mu_0\mathbf{h_{eff}} \;=\; -\frac{\partial\varepsilon}{\partial\mathbf{m}} \qquad 4.6$$

$$\varepsilon \;=\; \varepsilon_k+\varepsilon_H+\varepsilon_d+\varepsilon_{me}+\varepsilon_e \qquad 4.7$$

The elastic energy term has no effect on the effective field but must be included as elastic waves are being considered and in this respects must contribute to the solution of the wave equation. Substituting for the individual terms in the free energy equation yields equation 4.8. The i-jth components of the strain tensor $\mathbf{S_{ij}}$ can be obtained from equation 4.9 where $\mathbf{u}=(u_1,u_2,u_3)$ is the particle displacement vector for the elastic waves from their equilibrium sites. λ and μ are the Lamé elastic constants for the medium and B the magnetoelastic coupling coefficient as defined by Kittel [1949]. $\mathbf{h_d}$ is the demagnetising field and is related to the magnetic potential ψ by $\mathbf{h_d}=-\nabla\psi$.

$$\begin{aligned}\varepsilon \;=\; & -K\sin^2(\phi-\beta) \\ & -\mu_0(M_1+m_1)H_b \\ & -\mu_0\,\mathbf{m}\cdot\mathbf{h_d} \\ & +\frac{B}{M^2}\Sigma_{ij}M_iM_jS_{ij} \\ & +\Sigma_{i=j}\left\{\frac{1}{2}(\lambda+2\mu)S_{ii}^2+\lambda S_{ii}S_{jj}+\frac{1}{2}\mu S_{ij}^2\right\}\end{aligned} \qquad 4.8$$

$$S_{ij} \;=\; \frac{1}{2}\left(\frac{\partial u_i}{\partial x_j}+\frac{\partial u_j}{\partial x_i}\right) \qquad 4.9$$

The second equation of motion important to the system describes the particle displacements within the medium and is simply the elastic wave equation , ρ being the density, as shown in equation 4.10.

$$\rho\frac{\partial^2\mathbf{u}}{\partial t^2} \;=\; \nabla\cdot\mathbf{T} \qquad 4.10$$

The stress tensor is related to the free energy through the strain tensor as shown in equation 4.11.

$$T_{ij} = \frac{\partial \varepsilon}{\partial S_{ij}} \qquad 4.11$$

If the magnetoelastic waves are consider as travelling in the x_1 direction then all the variables must be of the standard time dependent wave form $\exp i(k_1x_1 + k_3x_3 - \omega t)$ with ω the angular frequency of the oscillations. The magnetoelastic waves must satisfy both the magnetic and the mechanical boundary conditions at the slab surfaces x_3=0 and x_3=d. At the free surface boundaries the stress vanishes and T_{13}=T_{23}=T_{33}=0. Magnetically the boundary conditions are met by the magnetic potential satisfying the Maxwell equation $\nabla \cdot \mathbf{B} = \mu_0 \nabla \cdot (\mathbf{h}_d + \mathbf{m}) = 0$ and if ψ^{in} is the potential within the slab and ψ^{out} the potential in free space beyond the surfaces then equation 4.12 and equation 4.13 must also be satisfied.

$$-\frac{\partial \psi^{in}}{\partial x_3} + m_3 = -\frac{\partial \psi^{out}}{\partial x_3} \qquad 4.12$$

$$\frac{\partial \psi^{in}}{\partial x_1} = \frac{\partial \psi^{out}}{\partial x_1} \qquad 4.13$$

With the conditions that $\nabla^2\psi^{out} = 0$ and $\psi^{out} \to 0$ for $|x_3| \to \infty$, ψ^{out} is given for x_3<0 and x_3>d by equation 4.14 and equation 4.15.

$$\psi^{out}(x_1, x_3) = \psi^{in}(x_1, d)e^{-k_1(x_3 - d)} \qquad x_3 > d \qquad 4.14$$

$$\psi^{out}(x_1, x_3) = \psi^{in}(x_1, 0)e^{+k_1x_3} \qquad x_3 < 0 \qquad 4.15$$

According to the matrix approach of Fahmy and Adler [1973] the equations of motion for the system can be written as a matrix differential equation of the form shown in equation 4.16.

$$\frac{\partial \tau^j}{\partial x_j} - \mathbf{P}_j \tau^j = 0 \qquad 4.16$$

τ^j is the state vector where the subscript j denotes the plane perpendicular to x_j or the direction of action. τ^j is a ten dimensional vector and in the case of the x_3 direction $\tau^3 \equiv [T_{13}, T_{23}, T_{33}, h_1, h_2, U_1, U_2, U_3, A_1, A_2]^t$. $\mathbf{A}=(A_1,A_2,A_3)$ is the magnetic vector potential given by $\nabla \times \mathbf{h} = i(\omega\sigma/C_L^2)\mathbf{A}$, C_L being the velocity of light and σ the conductivity of the slab. $\mathbf{P}_j$ are the (10X10) state matrices of the system. In general each element of the state matrix is a function of the wave vector **k** and the frequency. The solution of the differential equation to obtain the depth variation of the MEWs through the slab is given by equation 4.17.

$$\tau^3(x_3) = \Phi^3(x_3)\tau^3(0) = e^{P_3 x_3}\tau^3(0) \qquad 4.17$$

According to the matrix approach, with the inclusion of the boundary conditions nontrivial solutions require that the upper right hand quadrant of the matrix $\Phi^3(h)$ is zero. This is written compactly in equation 4.18 as,

$$\left| [\Phi^3(h)]_{ur} \right| = 0 \qquad 4.18$$

The magnetoelastic wave dispersion can be found by constructing $\Phi^3(x_3)$ and solving the determinant numerically via an iterative process to obtain the values of the complex wave number which satisfies the relation.

4.5.3 Prediction of Magnetoelastic Waves Properties for a Perpendicular In-Plane Anisotropy.

The model for magnetoelastic waves in a magnetic slab was implemented from an incomplete listing of the computer code used by Inoue [1989]. The code was written in the FORTRAN computer language. Two routines were missing from the code, a matrix multiplication routine which for hardware reasons was originally written by Inoue specifically for the computer used in his analysis and a determinant evaluation routine readily available in Subroutine software libraries. The results presented here were calculated using a Gould NP1 computer system, a matrix multiplication routine being incorporated into the original code and the determinant evaluation being under taken with a FORTRAN subroutine from the Numerical Algorithms Group Ltd FORTRAN subroutine library (NAG library). The studies undertaken by Inoue [1985a], Inoue *et al* [1985b] and Inoue [1989] comprised an examination of the effect of changing the model parameters for an arbitrary amorphous alloy. The effect of the magnitude of the magnetoelastic coupling coefficient B and of the conductivity σ on the field dependent velocity and attenuation of the magnetoelastic waves for a range of in-plane anisotropy directions were of main interest. Inoue [1985b] did not examine the wave transmission characteristics for an inplane easy axis perpendicular to the propagation direction. This study therefore concentrates on the velocity and attenuation field dependences in an amorphous slab with the material parameters of METGLAS 2605S2 with an easy axis perpendicular to the wave motion. This material and configuration demonstrated exceptional field responses for magnetoelastic responses in the review of experimental data in the previous chapter.

The validity of the amended code was initially checked using the data and results of Inoue *et al* [1985b] and Inoue [1989]. The model parameters used for the evaluation of the transmission characteristics of the METGLAS 2605S2 for the field dependences

are shown in Table 4.1 and are readily available in the literature. The magnetisation direction ϕ was calculated from the magnitude of the applied field $\mathbf{H_b}$ and the easy axis direction β using a program written separately in order to solve equation 4.4. The easy axis direction was chosen as 89.9° in order to avoid possible computational instabilities in the solution indicated by Inoue *et al* [1986].

Table 4.1 Parameters adopted for the modelling of magnetoelastic waves in METGLAS 2605S2.

Parameter		Value	Units
Anisotropy energy	K_u	50	Jm^{-3}
Magnetoelastic Coupling coefficient	B	$1.7X10^6$	Jm^{-3}
Film Thickness	d	25	μm
Saturation Magnetisation	M_s	$1.26X10^6$	Am^{-1}
Density	ρ	7180	Kgm^{-3}
Conductivity	σ	$7.7X10^5$	$\Omega^{-1}m^{-1}$
Transverse Phase velocity	C_t	$3X10^3$	ms^{-1}
Longitudinal Phase velocity	C_l	$5.6X10^3$	ms^{-1}
Easy Axis direction	β	89.9	Degrees
Oscillation Frequency	f	1.0	MHz

The dispersion relation for the magnetoelastic waves in the infinite slab using the parameters shown in Table 4.1 with $H_b/H_K=0.1$ is shown in Figure 4.6. The normalised propagation velocity is plotted against the oscillation frequency. Two easy axis directions are shown, the perpendicular easy axis and one at 45° to the wave propagation direction.

In both cases the three observed modes are plotted EMEW, FMEW and SMEW. The FMEW is dispersive in nature along with the EMEW at high frequencies whereas the SMEW is nondispersive and has a velocity equal to the transverse shear wave velocity. Figure 4.7 shows the calculated velocity against field response for the shear magnetoelastic waves of interest to this study. The responses for both the perpendicular easy axis and an easy axis at 85° to the propagation direction are shown. Figure 4.8 is the attenuation constant or the complex part of the wave vector against applied field for the perpendicular anisotropy. The dotted lines in both Figure 4.7 and Figure 4.8 represent an extrapolation of the limited data and as a result there is some uncertainty of the exact relationships in these regions. Two important features concerning the model can be observed from these figures. In the case of the velocity response, although of a similar form to the elastic modulus variations discussed earlier, the main change occurs at the anisotropy field and not between zero applied field and the anisotropy field. This observation disagrees with the experimental evidence of Kobelev and Soifer [1986] and Inoue [1985b] for shear waves in amorphous ribbons. This also disagrees with the field responses seen for the other propagation modes, Imamura and Sasaki [1984] and Imamura *et al* [1985] for extensional modes and Webb *et al* [1979] for magneto surface acoustic waves which also have a field dependence similar to the elastic modulus dependence. The attenuation constant also disagrees with the experimental data with the attenuation tending rapidly towards zero for fields less than the anisotropy field. This disagreement with the experimental observations means that without further detailed examination into the limiting effects on the model, the model was of little use for investigating the effects outlined in chapter 4.4.1. The implementation of the model was not pursued further due to time constraints.

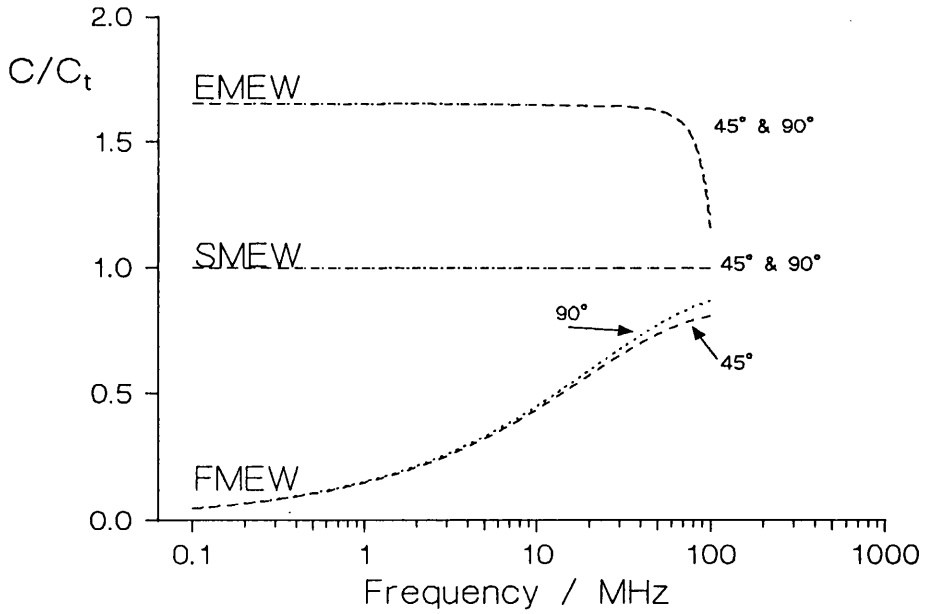

Figure 4.6 Magnetoelastic wave dispersion calculated from the slab model of METGLAS 2605S2 after Inoue [1989].

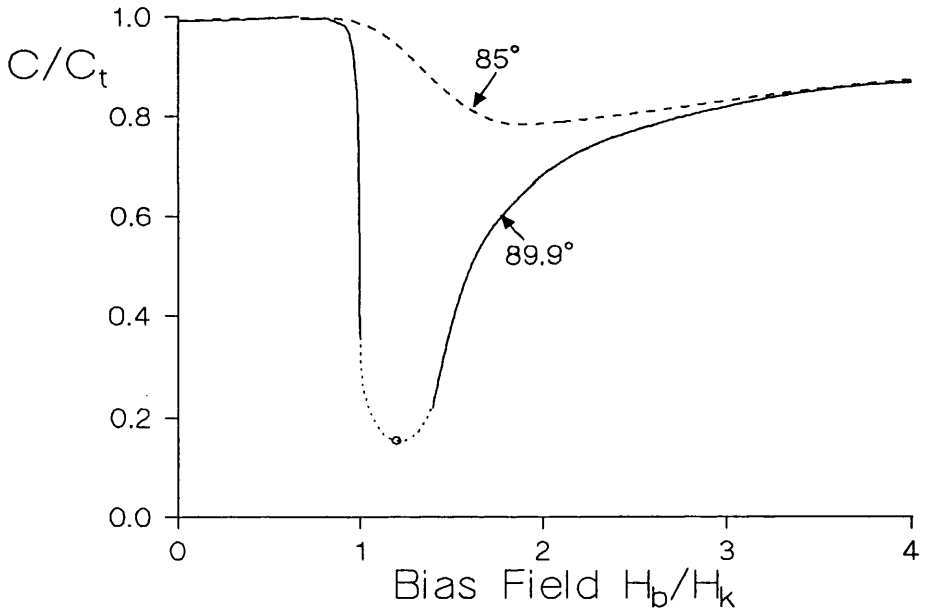

Figure 4.7 Velocity against field response of shear waves calculated from the slab model of METGLAS 2605S2 after Inoue [1989].

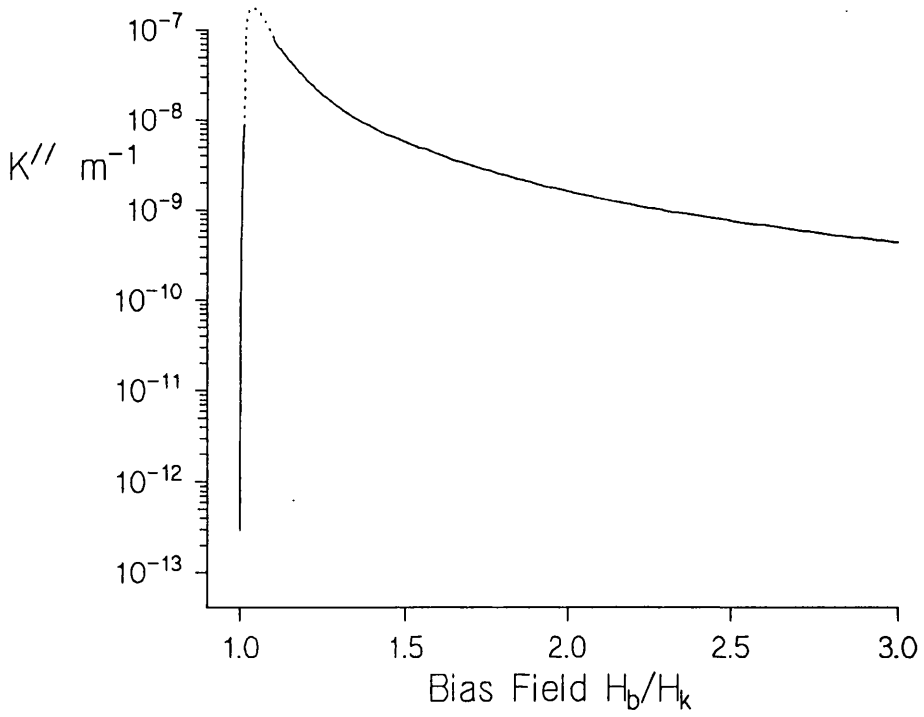

Figure 4.8 Attenuation against field response of magnetoelastic shear waves calculated from the slab model of METGLAS 2605S2 after Inoue [1989].

5 AMORPHOUS ALLOY MAGNETIC TRANSDUCERS.

5.1 Introduction.

This chapter presents and discusses the results of the assessment of the amorphous alloy magnetic transducers used throughout the study of the shear wave magnetometer. The studies described here were carried out on notionally 'as-cast' amorphous ribbons, as a concurrent study of the transducer properties of field annealed amorphous alloys was undertaken by Bassir [1991a]. The construction of the amorphous alloy shear wave magnetic transducers is initially described. This is followed by a brief summary of the work carried out by Bassir [1991a]. The measurements undertaken on the 'as-received' alloy magnetic transducers are finally presented and discussed.

5.2 Magnetic Field Sensor Assemblies.

The continuous wave (CW) shear wave magnetic transducer arrangement employed in the operation of the shear wave magnetometer was introduced in chapter 1. The magnetic transducer consists essentially of a length of amorphous ribbon along which the shear waves are propagated and are influenced by the applied magnetic field through the magnetoelastic coupling. The shear waves are propagated along the ribbon and received using piezoelectric transducers in the length expanded bar configuration of Berlincourt *et al* [1964] with the polarisation direction along the x axis with a length **l** and width and thickness dimensions of **w** and **t** respectively as shown in Figure 5.1. The transducers are bonded onto the surface of the ribbon and the mechanical shearing processes of the transducer is coupled to the ribbon. This produces shear waves which propagate with a wave vector in the z direction along the ribbon and is widely accepted as a means of propagating shear waves in shear mode strip delay lines, May [1964].

The mechanical resonance of the piezoelectric transducer depicted in Figure 5.1

can be represented in terms of an equivalent electrical resonance circuit as shown in Figure 5.2. This is the equivalent circuit for the unloaded piezoelectric resonator as described by Berlincourt [1964]. The capacitance C_0 is the fixed capacitance between the upper and lower electrode faces. **C** and **L** are the resonant components of the circuit and **R** represents a combination of the loss and the radiation resistance of the transducer.

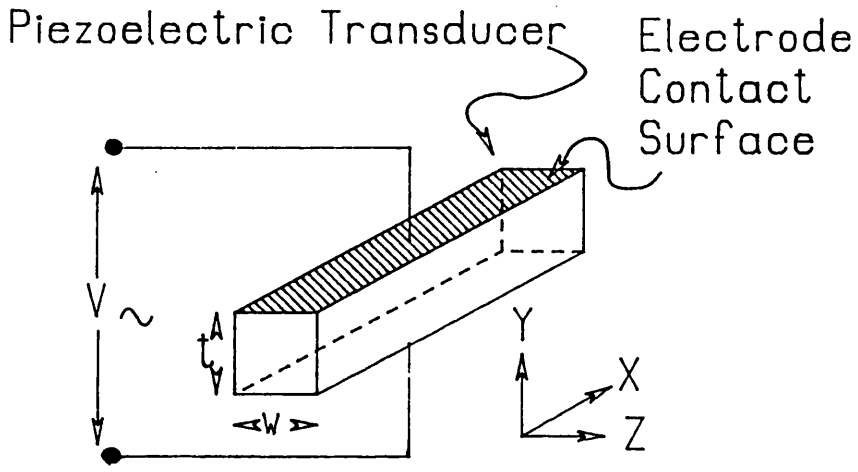

Figure 5.1 Piezoelectric length expanded bar with the electric field perpendicular to the length.

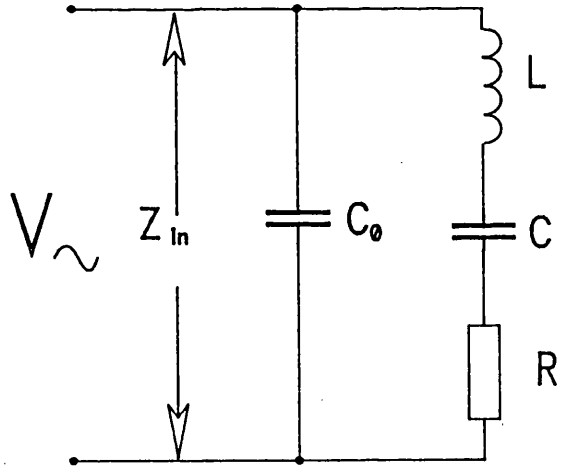

Figure 5.2 Approximate equivalent circuit for an unloaded piezoelectric resonator.

Although the equivalent circuit shown in Figure 5.2 is of the simplest form and does not take account of any mass loading effects from the mounting of the transducer to the amorphous ribbon it is useful in illustrating the necessary properties for optimising the transducer operation. Of most importance to the optimisation of the transducer are the resonant frequency and also the impedance of the transducer at the resonant frequency. This information is most readily available from examination of the real and imaginary parts of the impedance plots against frequency. Consideration of the real and imaginary parts of the equivalent circuit gives the following expressions for the impedance. The real part is given in equation 5.1 and the imaginary part in equation 5.2.

$$Z_{\Re} = \frac{R}{\left(1+\frac{C_0}{C}-\omega^2 C_0 L\right)^2+(\omega C_0 R)^2} \qquad 5.1$$

$$Z_{\Im} = j\frac{\left\{\frac{1}{\omega C}(\omega^2 LC-1)\left(1+\frac{C_0}{C}-\omega^2 C_0 L\right)-R^2\omega C_0\right\}}{\left(1+\frac{C_0}{C}-\omega^2 C_0 L\right)^2+(\omega C_0 R)^2} \qquad 5.2$$

Graphs of the real and imaginary components of the impedance against angular frequency are shown in Figure 5.3a and Figure 5.3b respectively. The conditions plotted are for $\mathbf{C_0=C=R=L=1}$. The graphs show clearly the circuit resonance. This occurs for the parallel configuration of the piezoelectric resonator at a maximum in the real component of the impedance. In order to maximise the amplitude of the received signal and essentially reduce the insertion loss the two transducers should be as closely matched in their resonances as possible. The main contribution to the insertion loss is then that due to the transmission along the ribbon. The insertion loss is the ratio of the signal obtained at the output to that applied at the input of a delay line.

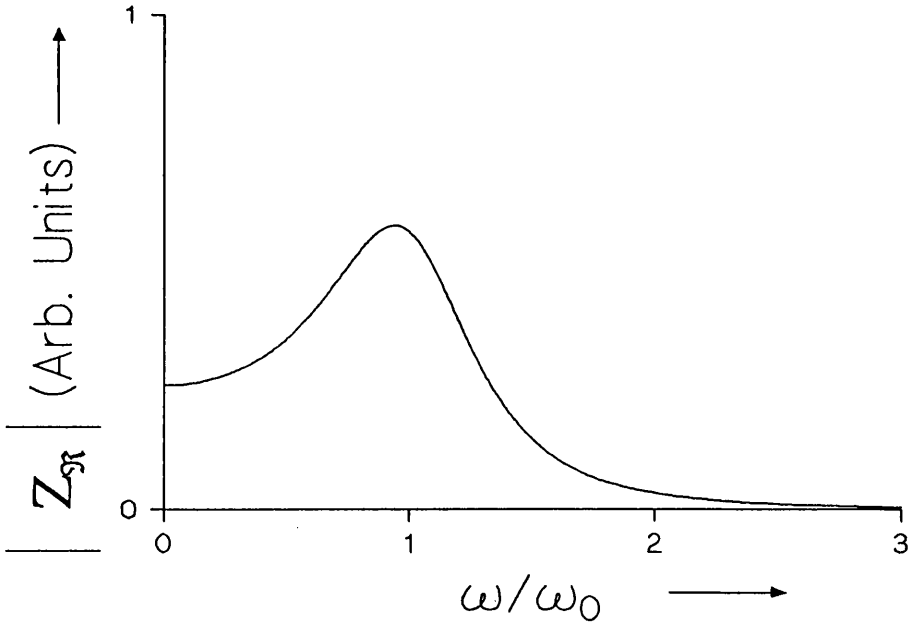

Figure 5.3a

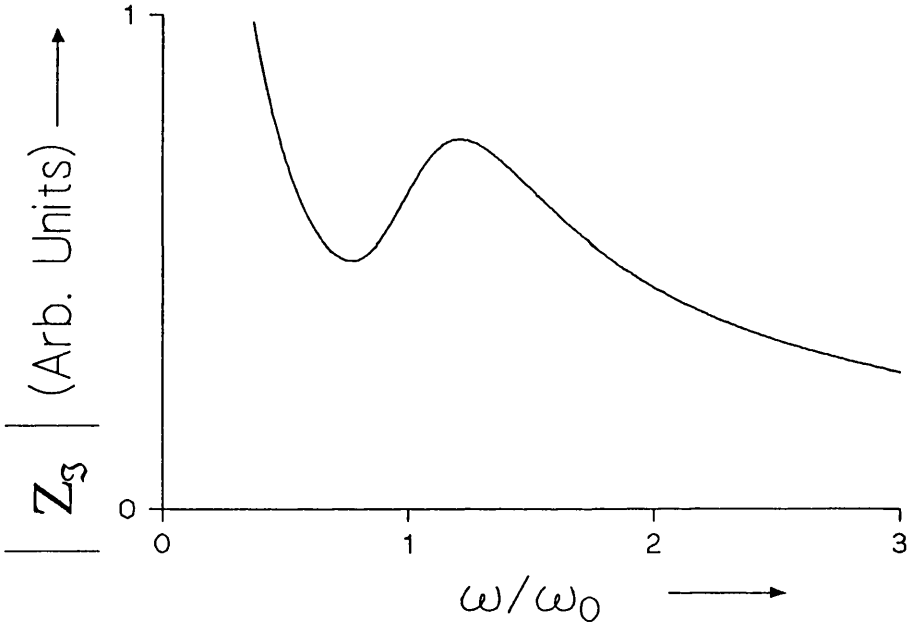

Figure 5.3b Representation of the real 5.3a and the imaginary 5.3b component of the impedance against angular frequency for the piezoelectric resonator.

A further consideration for the optimisation of the transducers is matching the impedance of the transmitter transducer to the drive oscillator so that maximum power is transferred to the transducer. In the case of the receiver a maximum signal amplitude is required and so matching to the real component of impedance is undesirable. Important to the receiver operation, however, is the matching of the imaginary component of the impedance to the load connected to the transducer. A rough matching to the load was achieved using an inductive termination. The two components of transmitter transducer impedance at resonance can be readily extracted from the measured impedance against frequency plots. The matching of the transducer impedance to the drive impedance can then be achieved by employing a transformer as depicted in Figure 5.4. In Figure 5.4 the capacitance **C** and the resistance **R** represent the real and imaginary component of the impedance respectively. The transformer is used to cancel out the capacitive imaginary part of the impedance by tuning the magnitude of the reactance of the inductive secondary winding of the transformer to be equal to the magnitude of the reactance of the capacitive transducer at the resonance frequency of the transducer to satisfy the condition in equation 5.3. This produces a solely real impedance which from classical optimum power transfer considerations must then be matched so that it is equal to the purely real output impedance of the drive oscillator. The matching of the source and load resistances can be achieved by performing an impedance transform by adjusting the turns ratio of the transformer primary coil to that of the secondary coil. Provided the reactance of the primary coil of the transformer is far greater than its resistance at the resonance frequency of the transducer, the impedance matching condition is given by equation 5.4 where **N** is the turns ratio of the secondary winding to that of the primary winding. The optimum matching condition for any particular transmitter depends on its resonant frequency and the value of the two components of impedance at this frequency and for this reason the matching can differ vastly from one transducer to another.

Optimum matching of the transmitter has not been undertaken throughout this study although rough matching of the receiver to the load was always carried out. In the cases where transmitter matching has been undertaken this will be stated.

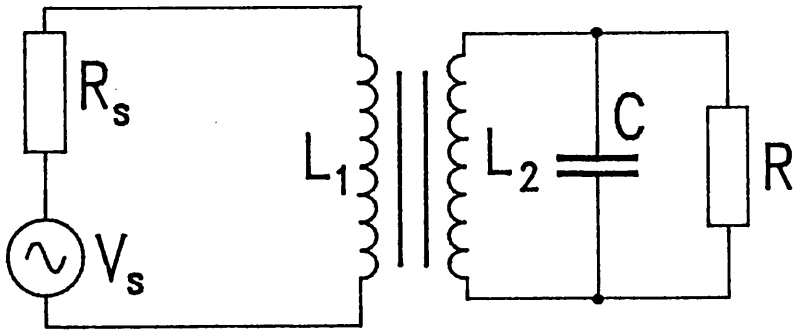

Figure 5.4 Source to drive transducer optimum power matching circuit.

$$L_2 = \frac{1}{C\omega_0^2} \qquad 5.3$$

$$N = \sqrt{\frac{R}{R_S}} \qquad 5.4$$

Two different types of transducer material have been employed to propagate the shear waves a lead titanate-lead zirconate solid solution, specifically PZT5A and PZT7A, and lithium niobate ($LiNbO_3$). The two materials both have high piezoelectric coupling

factors for the shear mode, k_{15}=0.61 for the $LiNbO_3$ and k_{15}=0.68 for PZT5A (Quartz $k \approx 0.1$). Lithium niobate also has a smaller piezoelectric strain constant than PZT5A although both are comparatively large compared to other piezoelectric materials (d_{15}=68pCN^{-1} for $LiNbO_3$, d_{15}=584pCN^{-1} for PZT5A and d=2.3pCN^{-1} for Quartz), Berlincourt [1971]. The piezoelectric strain constant relates the shearing strain of the transducer to the electric field applied across it. The resonant frequency of the materials is dictated by the thickness **t** of the transducers and is inversely proportional to the thickness. The less important dimensions of the transducers are the length **l** and the width **w**. For high transducer efficiency $l \geq \lambda \gg w$ where λ is wavelength of the shear waves and $w \geq 2t$. For all cases l=12.5mm and the width condition was fulfilled, Bassir [1991a]. Lithium niobate and PZT differ most in that their resonant frequencies for an equivalent thickness of material are not the same. Lithium niobate resonates at a higher frequency than the same sized PZT transducer. PZT was used for investigations carried out at frequencies about and below 1MHz. At these frequencies the thickness of the PZT is small enough to present a minimal mass loading to the ribbon. At higher frequencies where the PZT transducers would be fragile as well as difficult to manufacture because of their thickness, lithium niobate was used. The PZT transducers used in this study were the same as used by Bassir [1991a] whereas the lithium niobate transducers used were "matched pairs" precision cut to have identical free unloaded resonances. These transducers were supplied by Gooch and Housego Ltd with silvered electrodes deposited on the opposing faces y=0 and y=t in Figure 5.1. This differs from Bassir [1991a] who manufactured his own lithium niobate transducers. Figure 5.5 shows the thickness dependence of the free resonance of the two different types of material, Bassir [1991a], and also includes the lithium niobate transducer data supplied by Gooch and Housego Ltd.

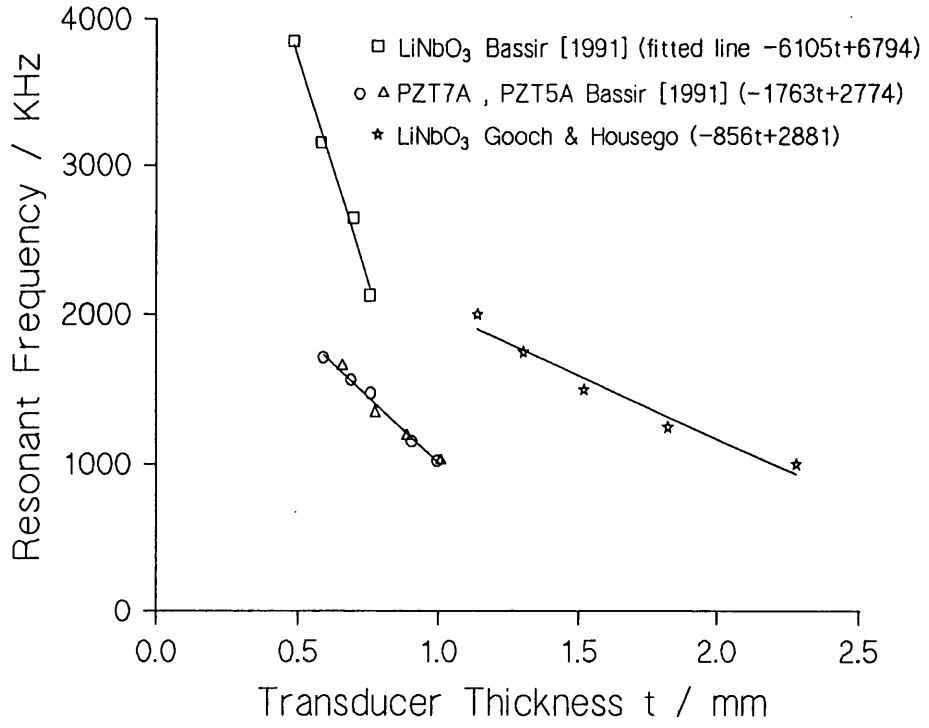

Figure 5.5 Free resonance dependence on the transducer thickness for PZT and lithium niobate transducers.

The transducers were bonded to the amorphous ribbon using either silver loaded epoxy resin or cyanoacrylate adhesive at a separation **L** between the transducers. When referring to a transducer arrangement the quoted length will be the separation between the transducers. In general the magnetic material extended less than 1cm beyond the transducers for bonding to the Tico pad™. For the non silvered transducers a top electrode was also constructed by applying a thin film of silver loaded epoxy. The epoxy is also used to bond the electrode lead wire to the surface. The bottom electrode surface was the surface in contact with the amorphous ribbon and in this case the covered area of the ribbon itself makes up the bottom electrode. The electrode lead wire for the bottom electrode was directly soldered to the amorphous ribbon so that the ribbon became the

ground plane for both the transmitting and receiving electrodes. For all the cases to be considered here the non silvered transducers were bonded to the ribbon using silver epoxy, whereas, for the silvered transducers cyanoacrylate was used. This also included the attachment of the lead wire to the top electrode. Figure 5.6a and Figure 5.6b show the impedance variations with frequency for a PZT5A transducer bonded to amorphous ribbon using silver epoxy and is notionally taken as the shear wave transmitter $\mathbf{T_1}$. Figure 5.6c and Figure 5.6d show a different PZT5A transducer that has been cut to equivalent dimensions as that of Figure 5.6a in order to have an equivalent resonance frequency so as to act as a receiver $\mathbf{T_2}$ in the magnetic transducer arrangement. Figure 5.6c and Figure 5.6d also clearly show the non-reproducability of the silver epoxy bond in remounting the transducers. The reproducibility of the cyanoacrylate bond for the Gooch and Housego lithium niobate transducers would be expected to be superior to that of the silver epoxy bond because of the reduced complexity in achieving the bond, however, Figure 5.7a and Figure 5.7b show this not to be the case. Figures 5.7 also demonstrate a poor match between the resonant frequencies of the receiver and transmitter as well as a shift from the specified resonant frequencies of 1MHz. Obviously the bond is not as reproducible as would be expected and the mechanical loading of the mounted transducers disrupts the free resonance frequency. (The accuracy of the specifications supplied by Gooch and Housego Ltd was not checked). The PZT5A transducers of Figures 5.6 are of an exceptional match and more typically resonance frequency matching similar to those of Figures 5.7 were observed. In general the non matched resonance frequencies of the transducers made it essential to test the operation of the whole magnetic transducer assembly in situ to obtain a minimum insertion loss. This examination allowed the received signal to be maximised by experimentally selecting the transmitter and its operating frequency from comparisons of the operation of both the premounted transducers. The impedance plots could then be used to match the transmitter impedance

to the source at the selected frequency. In general the optimum transmitter was the transducer with the sharpest and most pronounced resonance peak and the receiver the transducer with a broader band resonance

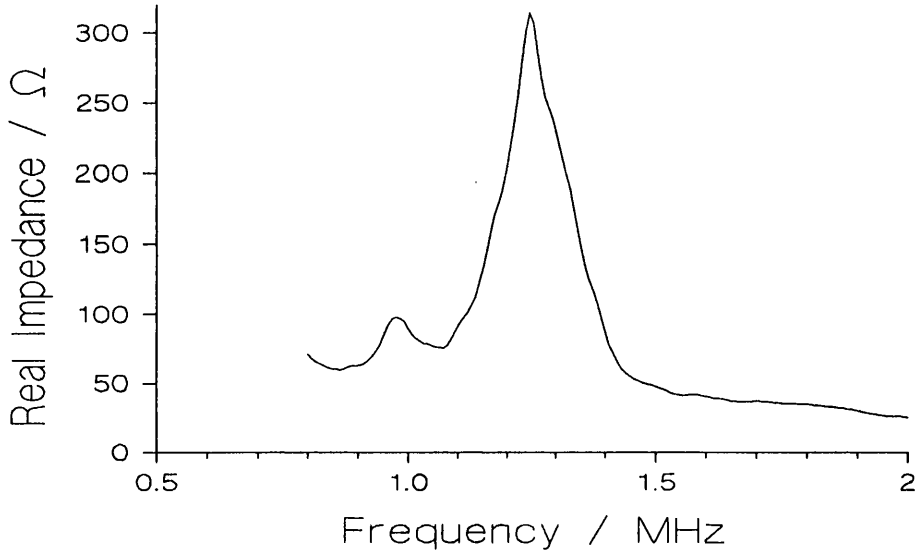

Figure 5.6a

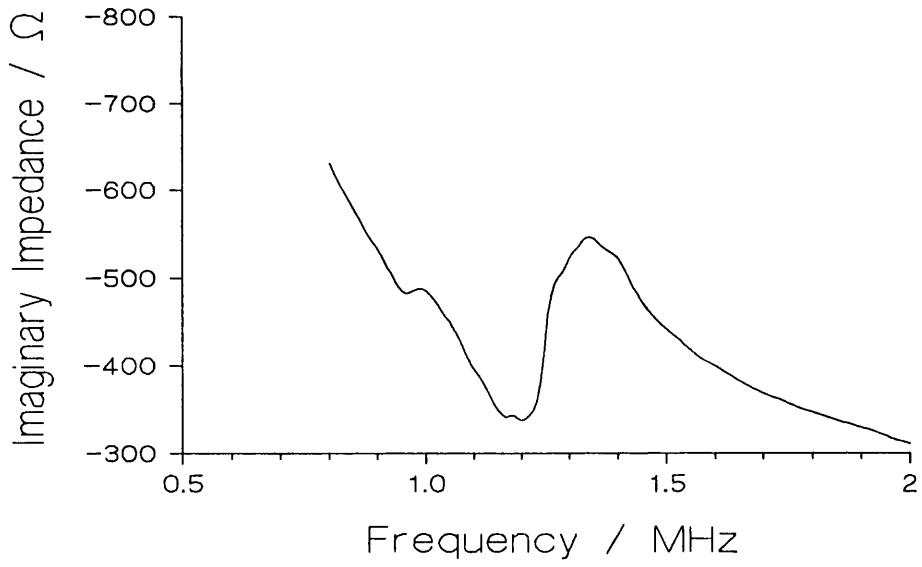

Figure 5.6b Real **a)** and Imaginary **b)** components of Impedance against frequency for a PZT5A transmitter $\mathbf{T_1}$.

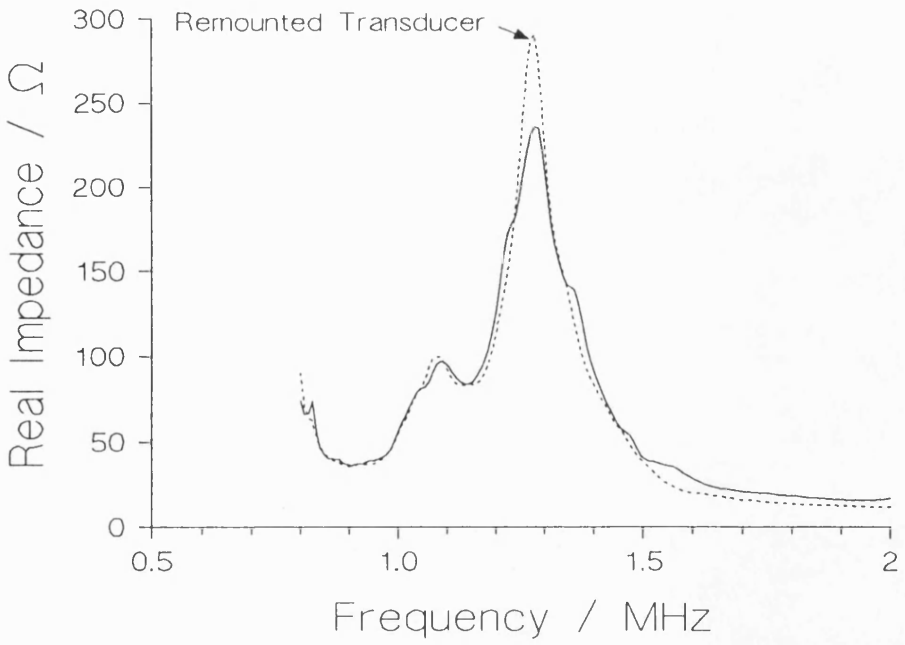

Figure 5.6c

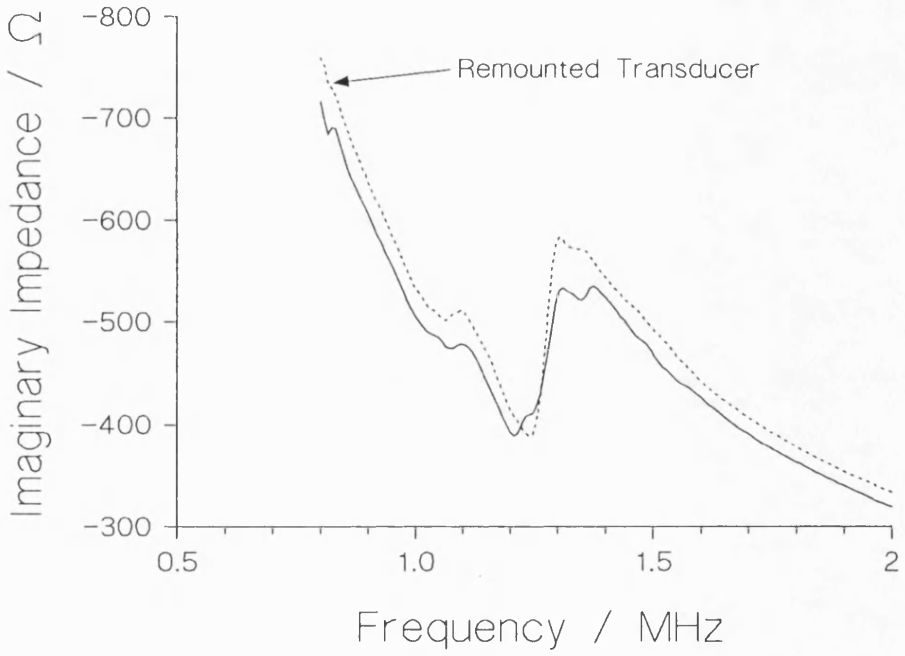

Figure 5.6d Real **a)** and Imaginary **b)** components of Impedance against frequency for a PZT5A receiver $\mathbf{T_2}$.

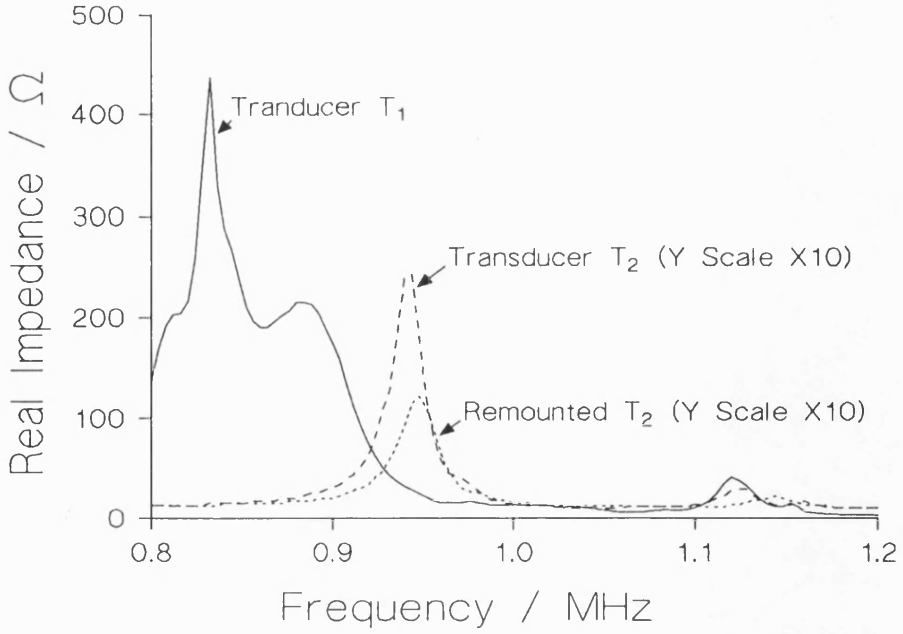

Figure 5.7a

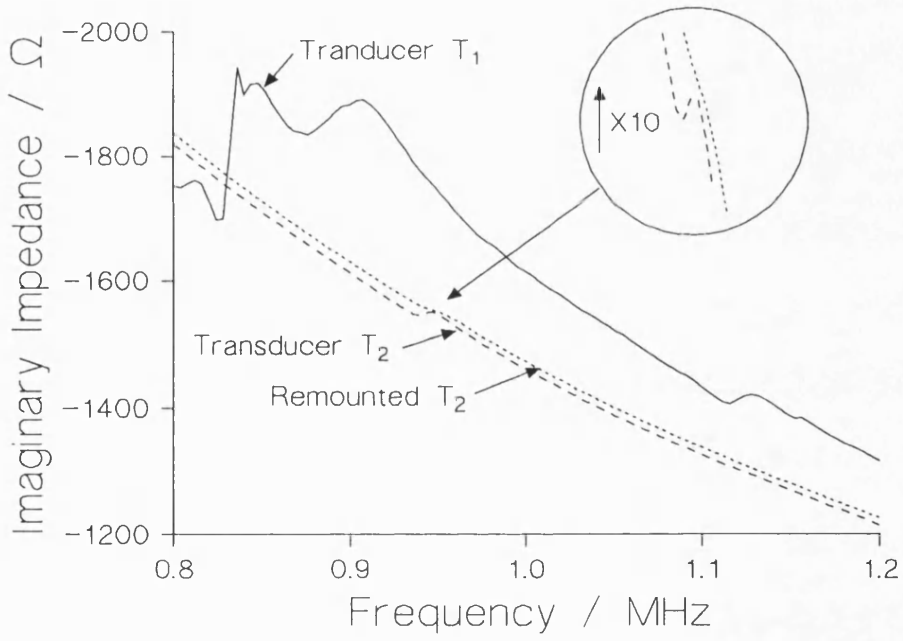

Figure 5.7b Real **a)** and Imaginary **b)** components of impedance against frequency for a "matched" pair of 1MHz specified lithium niobate transducers.

The continuous wave magnetic transducer element of amorphous ribbon and piezoelectric transducers was supported by a transducer mount as shown in Figure 5.8. The amorphous ribbon was bonded to the Tico pad™, which was cut to an approximate thickness of 5mm, using an impact adhesive. The pads supported the amorphous ribbon above the transducer support arm and also acted as shear wave absorbers preventing undesirable reflection from the ribbon ends. The lead wires from the piezoelectric transducers were connected to aluminium core coaxial cable cables and the earth lead was attached to the amorphous ribbon behind the transducers on the area bonded to the Tico pad™.

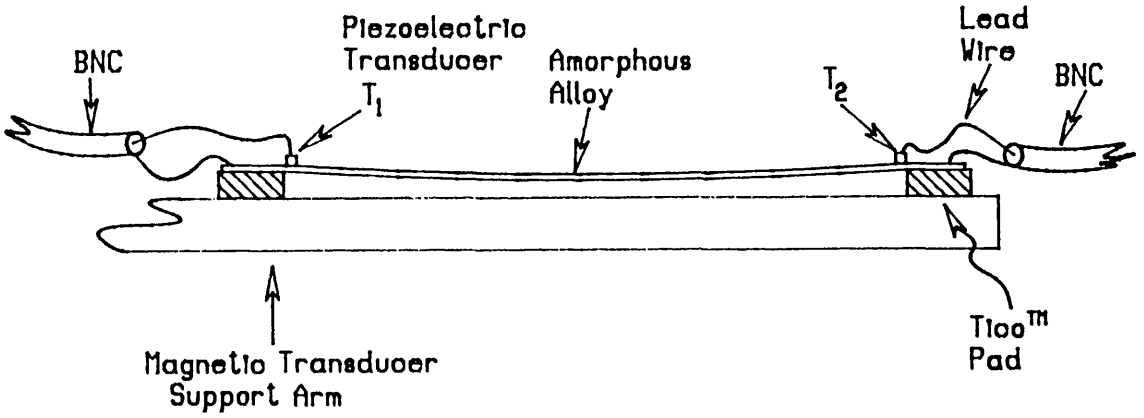

Figure 5.8 Magnetic transducer head sensor assembly.

When examining the properties of long lengths of ribbon with transducer separations greater than 10cm the ribbon was allowed to sag between the end supports so that at its centre it was supported just above the support arm. Allowing the longer ribbons to sag minimised the axial stress experienced by the ribbon. An axial stress tends

to align the magnetic moments along the length of the ribbon and essentially place the ribbon in a state of high magnetomechanical damping. This affect was not as prevalent in the shorter ribbons as they are essentially self-supporting between the end supports. The insertion loss was seen to decrease for large applied stresses as would be expected, although a reduction in the shear modulus response was then observed, see chapter 3.

5.3 Investigations on Field Annealed Amorphous Ribbon Transducers.

The field annealing studies undertaken by Bassir [1991a] & [1991b] concentrated on the study of transversly annealed and stressed relieved materials. The material of main interest was METGLAS 2605S2 ($Fe_{78}Si_9B_{13}$) because of the large Young's modulus dependence on field observed for the transverse field annealed materials, see chapter 3. Other materials examined included METGLAS 2826MB and VAC 0040. The annealing process was carried out using a process similar to that of Thomas [1991]. The apparatus consisted of a large water cooled electromagnet capable of producing a magnetic flux density of the order of 0.17T perpendicular to two rectangular pole pieces 46cm long separated by an air gap of 5.5cm. The measurement of the flux density was carried out at a position along the long axis halfway between the ends of the pole pieces. This flux density falls to 0.145T 18cm in either direction along the long axis from this position i.e. 5cm from each end perpendicular to the pole faces. The ribbon to be annealed was sandwiched between two rectangular bars of aluminium to which a chromel-alumel thermocouple was attached to monitor the temperature. This arrangement was then placed in a Pyrex tube positioned between the magnet pole pieces and hot air blown along the tube to heat the sample. The ribbons were annealed just below their Curie temperature (T_c=415°C for 2605S2 T_a=410°C) for a time long enough for a well defined in-plane anisotropy to be induced (usually 1hr), see Thomas [1991]. The anneal time was taken as the time between achieving a stable anneal temperature and switching off

the heater element. The whole arrangement was allowed to cool in a stream of cool air.

The introduction of an in-plane anisotropy enhances not only the field dependence of the elastic moduli but also the magnetomechanical coupling and the field dependent magnetomechanical damping. Bassir [1991b] discovered early on that field annealed materials did not perform well in the continuous wave mode transducers described in chapter 5.2. Although the field annealing process reduces the base line noise of the magnetoelastic waves through the removal of cast in local inhomogeneities, the increased sensitivity to mounting stresses and reflection and attenuation at 90° domain walls severely degraded the output signal of the magnetic field transducer. Bassir [1991a], therefore, concentrated his work on optimising the received amplitude and the increased amplitude response to magnetic field of the shear waves for field annealed material first observed by Squire and Gibbs [1988b]. This was investigated for both a continuous and a pulsed mode of operation along the field annealed amorphous ribbons. Stress relieved amorphous ribbon did not display the initial sharp fall in amplitude observed in the field annealed materials by Squire and Gibbs [1988b].

Bassir [1991a] proposed that domain walls act upon ultrasonic waves in a similar way to grain boundaries in polycrystalline materials. Reflection and scattering at domain walls can be observed as noise, however, the direction of the applied field anneal with respects to the direction of the particle displacement is the factor which strongly affects the attenuation by absorption. Figure 5.9 shows the general propagation configuration for the shear waves with a particle displacement $\mathbf{V}_i$ in the plane with a wave vector $\mathbf{k}$ at an angle α to the direction of the field anneal.

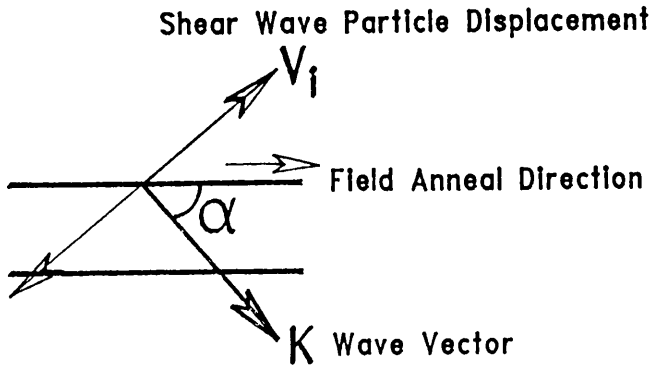

Figure 5.9 General configuration for shear waves interacting with domain walls.

The optimum value for the angle α comes from a number of considerations. For α=90° the attenuation is high due to scattering and reflection; this is the normal configuration considered. For α=0° the attenuation from scattering and reflection is severely reduced but the wave front will be perforated by the domain walls and will have regions of low and high pressure. If the domains are considered as being rectangular the tensile stresses from the shear wave will have the greatest effect at an incident angle of α=45° to the domain wall. Also of importance are the creation of the induced anisotropy perpendicular to the applied field direction to facilitate the largest overall field response and also the minimising of demagnetising affects by retaining favourable ribbon dimensions. Figure 5.10a and Figure 5.10b show the pulse response and continuous wave transducer arrangements respectively that were adopted by Bassir [1991a]. The incident angle of 45° onto the ribbon edge also has the advantage of minimising the possibility

of losses through mode conversion of the shear waves as the angle is greater than the total internal reflection angle of approximately 33°. The ribbons were transversely field annealed and the applied field acted along the long axis of the ribbons.

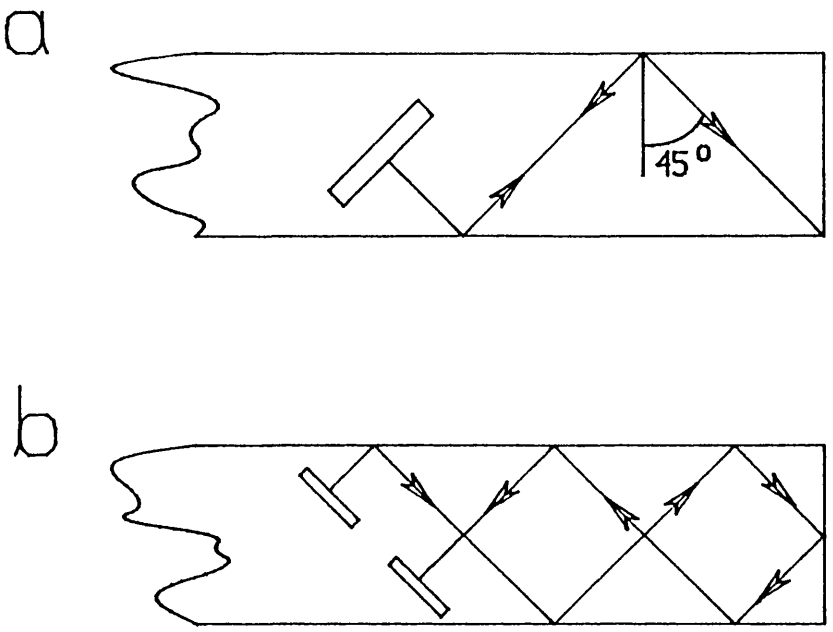

Figure 5.10a Pulse mode magnetic transducer arrangement.

5.10b Continuous mode magnetic transducer arrangement.

The characteristics of the various transducer arrangements were studied using the pulse echo technique as well as examination of the continuous wave mode using a digital storage oscilloscope to examine the output signal from the transducer. The magnetic transducer was held between Tico pad™ absorbers placed behind the piezoelectric transducers in the non ultrasonically active region of the ribbon and allowed to hang vertically to minimise the stresses in the material. A magnetic field was applied by placing

the transducer arrangement within a pair of Helmholtz coils. The magnetic transducer was also surrounded by a perspex tube to minimise mechanical vibrations from air currents.

In the pulse mode the 45° configured magnetic transducers were found to return primary echos up to an order of magnitude greater in amplitude than the normal transducer configuration. The response to magnetic fields was also seen to improve and was explained in terms of the reflective corner at the end of the magnetic transducer acting as a stress raiser. Removal of the corner to present a perpendicular reflective edge reduced both the amplitude and the amplitude response. When constructing the magnetic transducers a compromise in the path length of the shear waves and ultimately the dimensions of the amorphous ribbon had to be made. Maximum interaction with the magnetic material , minimum demagnetisation and minimum interference from side lobes generated by the piezoelectric transducers require long lengths of ribbon, whereas, minimum attenuation demands shorter ribbon. Figure 5.11a and Figure 5.11b show the pulse and continuous wave responses respectively, this is for a transversely field annealed METGLAS 2605S2 two transducer arrangement as depicted in Figure 5.10b for a range of excitation frequencies. The active ribbon was 10cm long by 2.5cm in width. The pulse response was the amplitude of the first received pulse against magnetic field and the continuous wave response was the received amplitude of the continuous wave as a function of applied field. In both cases the amplitudes are normalised to the zero field amplitudes for comparison purposes. The maximum received amplitude for the pulse response was of the order of 800mV and the response in general was comparable to that of the single transducer arrangement shown in Figure 5.10a. The maximum amplitude response was observed at approximately 900kHz for the pulse response and 800kHz for the continuous wave. The responses decrease for higher and lower frequencies.

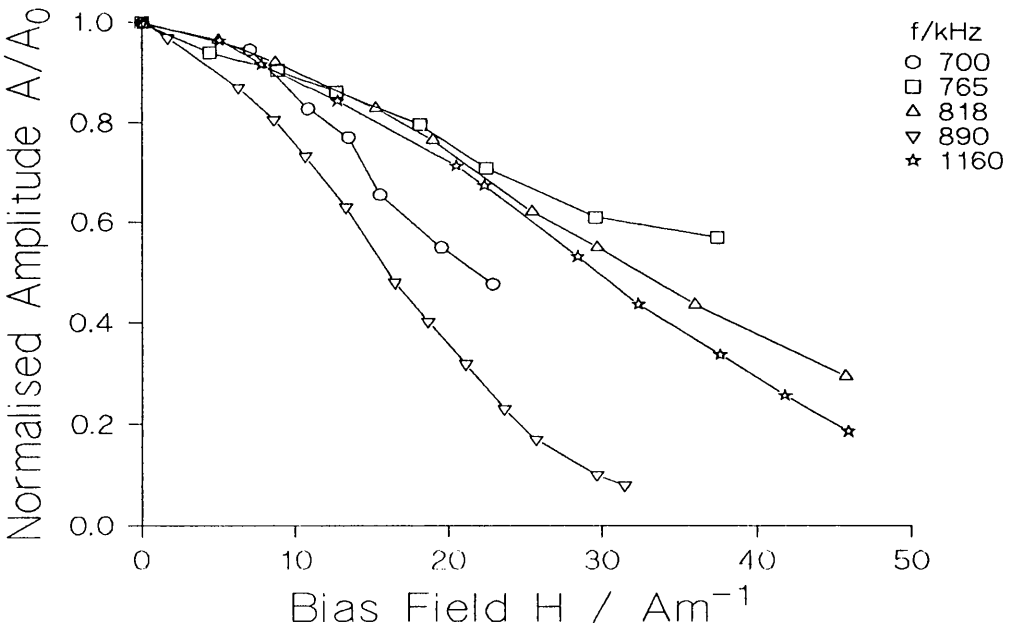

Figure 5.11a Pulse response for field annealed METGLAS 2605S2 with two piezoelectric transducer configuration shown in Figure 5.10b

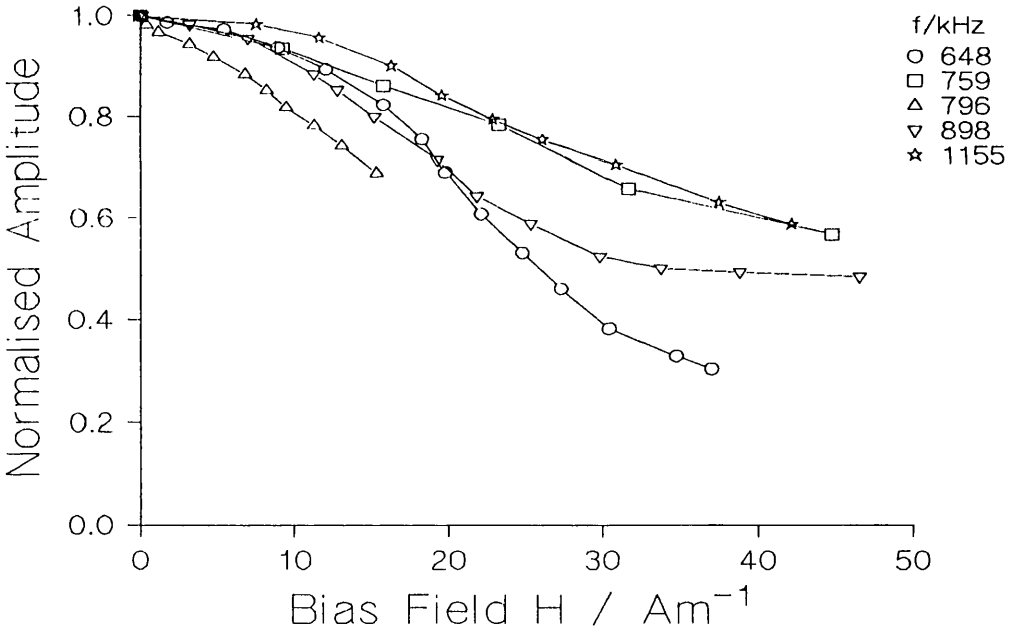

Figure 5.11b Continuous wave response for field annealed METGLAS 2605S2 with two piezoelectric transducer configuration shown in Figure 5.10b

5.4 Investigations on "as-received" Amorphous Ribbons.

5.4.1 Selection of a Suitable Alloy Composition

The operation of the shear wave magnetometer system described in chapter 1 relies on the magnetic response of a continuous wave transducer as described in chapter 5.2. The concurrent investigations on field annealed materials, specifically METGLAS 2605S2, undertaken by Bassir [1991b] demonstrated the unsuitability of this treatment for the continuous wave magnetic transducers. The studies on the "as-received" amorphous ribbon were carried out with the objective of identifying a suitable transducer material for the construction of the continuous wave transducers which would allow the characterisation and the development of the magnetometer system. For any transducer application the main desirable criterion is a large signal with a large signal response to the quantity to be measured. The selection of the transducer material for the shear wave magnetometer was therefore carried out in terms of the insertion loss and the amplitude response of the magnetic transducer arrangements for low fields about zero applied field, as the proposed system operates in a closed loop configuration. For the different materials investigated piezoelectric transducers resonating at approximately equivalent frequencies were employed.

The general arrangement used for studying both the amplitude and phase responses of the magnetoelastic shear waves in the continuous wave magnetic transducer is shown in Figure 5.12. Shear waves were excited in the magnetic transducer using a Philips PM5193 programmable function generator which was capable of operating over a frequency range of 0.1mHz to 50MHz and was always operated at its maximum output of $20V_{p\text{-}p}$. The bias field was applied to the transducer using a one metre long solenoid with 1311 turns/m. The solenoid was driven by a Feedback PFG605 power function generator which could drive a maximum current of 200mA through the solenoid and

was operated with a triangular wave output with a total sweep time of the order of one minute. The amplitude of the received wave was measured using a Philips PM2554 AC millivoltmeter (2Hz-12MHz) and the phase change by a PSI 4011 phasemeter referenced to the drive oscillator. Both outputs were recorded on two Philips PM8143 X-Y recorders against the solenoid current which was measured using a Keithley 177 DMM . On the occasions when larger applied field were required the solenoid was driven by a Farnell AP100-90 regulated power supply. Each sample was demagnetised by applying a large decaying a.c. current before commencing with the measurements. The results presented in this chapter were digitised using a Cherry digitiser and retain all the salient features of the X-Y plots. This method of investigating the low field responses of the amorphous ribbons presents a more detailed picture than the point measurements of Bassir [1991a].

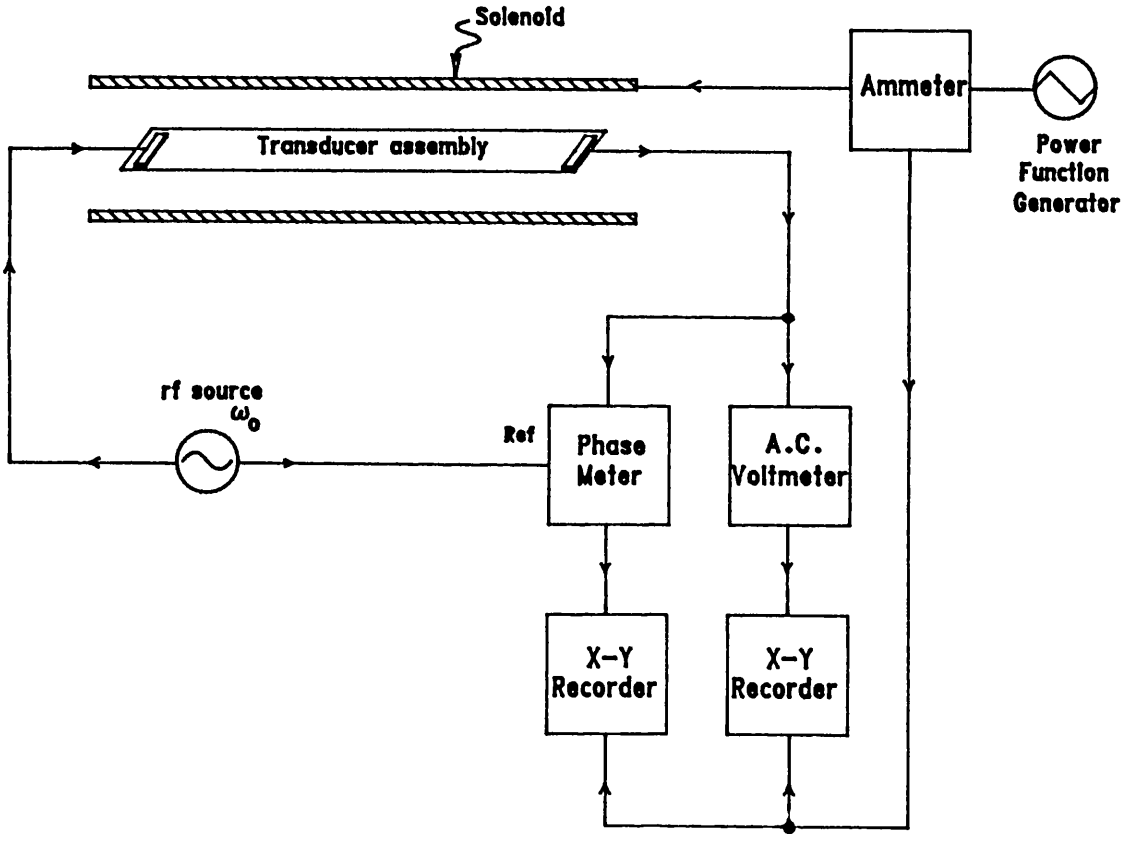

Figure 5.12 Magnetic transducer characterisation system

The previous success with iron-nickel based alloy VAC 4040 in Squire and Gibbs [1987a] & [1988a] directed the investigations towards a comparison between these alloys and the iron-silicon-boron alloys which exhibit large changes in the elastic moduli in the annealed state, see chapter 3. The composition and some important parameters of the alloys of main concern to the study are listed in Table 5.1. For all but the METGLAS 2826MB only one batch or casting run of alloy was available. For METGLAS 2826MB initially only one batch of material was available (REEL 1) although later in the investigations a second sample was acquired (REEL 2) from which comparative studies were carried out and are discussed in chapter 5.4.2.

Table 5.1 Amorphous alloys of concern to the studies on the shear wave magnetometer.

Trade Name	Composition	Curie Temp / °C	Crystallisation Temp / °C	λ_s ppm	Resistivity / μΩ.m	Coefficient of expansion ppm / °C	Saturation induction B_s / T
METGLAS 2826MB	$Fe_{40}Ni_{38}Mo_4B_{18}$	353	410	12	1.6	-	0.88
METGLAS 2605S2	$Fe_{78}Si_9B_{13}$	415	550	27	1.3	-	1.58
VAC 0040	$Fe_{40}Ni_{40}B_{20}$	400	400	20*	1.25	12	1.0
VAC 4040	$Fe_{39}Ni_{39}Mo_4Si_6B_{12}$	260	450	8	1.35	12	0.75
VAC 7505	$Fe_{78}Si_9B_{11}C_2$	420	500	30	1.3	8	1.5

* Data from Thomas [1991], otherwise manufacturers' data.
VAC is a registered trade mark of Vacuumschmelze GmbH of Germany.
METGLAS is a registered trade mark of Allied-Signal of the USA.

The normalised amplitude responses for 10cm transducers made from the "as-received" alloys VAC 7505 METGLAS 2605S2 and METGLAS 2826MB (REEL 1) are shown in Figure 5.13. The normalised amplitude is shown as a function of the internal field, demagnetising fields being taken into consideration. The approach to the

correction for the demagnetising fields is discussed in chapter 5.4.2. The VAC 7505 demonstrates a minimal response to magnetic field and had a peak to peak receiver transducer output of 187mV at zero applied field at a resonant drive frequency of 1133kHz. The magnetic transducer constructed from the METGLAS 2605S2 displays an increase in its output amplitude and the greatest attenuation of the three materials having a peak to peak amplitude of only 1.6mV at zero applied field for a resonant drive frequency of 1025kHz. The amplitude was observed to fall off for much greater applied fields with a form similar to that of the METGLAS 2826MB. By far the greatest response was observed for the METGLAS 2826MB with a peak amplitude of 324mV at a frequency of 1256kHz. The METGLAS 2826MB was also found to work most satisfactorily within the magnetometer system. No results for magnetometer performance are presented in this chapter but suffice it to say that the magnetometer was found to operate with the METGLAS 2826MB transducer, whereas, great difficulty was encountered in achieving any form of operation with the other materials. In the case of the VAC7505 this was most probably due to the minimal response, whereas, with the METGLAS 2605S2 the large magnitude of the attenuation was responsible.

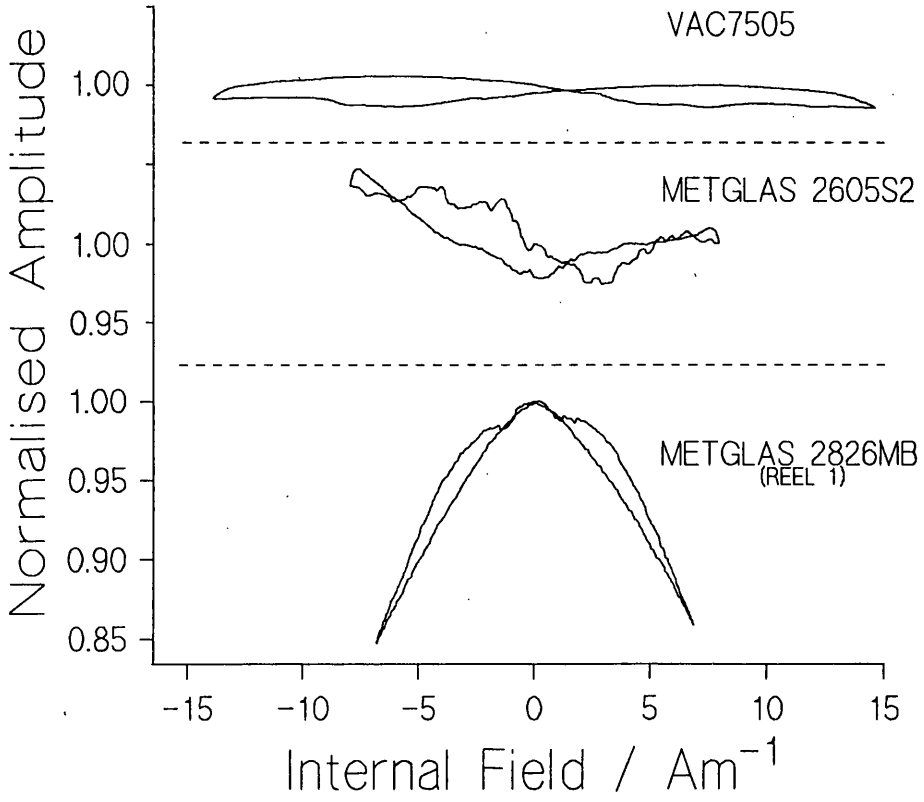

Figure 5.13 Comparison of low field amplitude responses for three magnetic transducers utilising different alloy compositions.

Two further METGLAS 2826MB (REEL 1) transducers were constructed specifically for use in the characterisation of the magnetometer system itself which will be covered in chapter 7. These magnetic transducers had a transmitter-receiver separation of 20cm and will be referred to as MT1 (magnetic transducer 1) which had an optimum operating frequency of the order of 1067kHz and MT2 (magnetic transducer 2) with an operating frequency 1362kHz. Figure 5.14a and Figure 5.15a are the low field amplitude and phase responses for MT1. Figure 5.14b and 5.15b represent the same quantities for MT2.

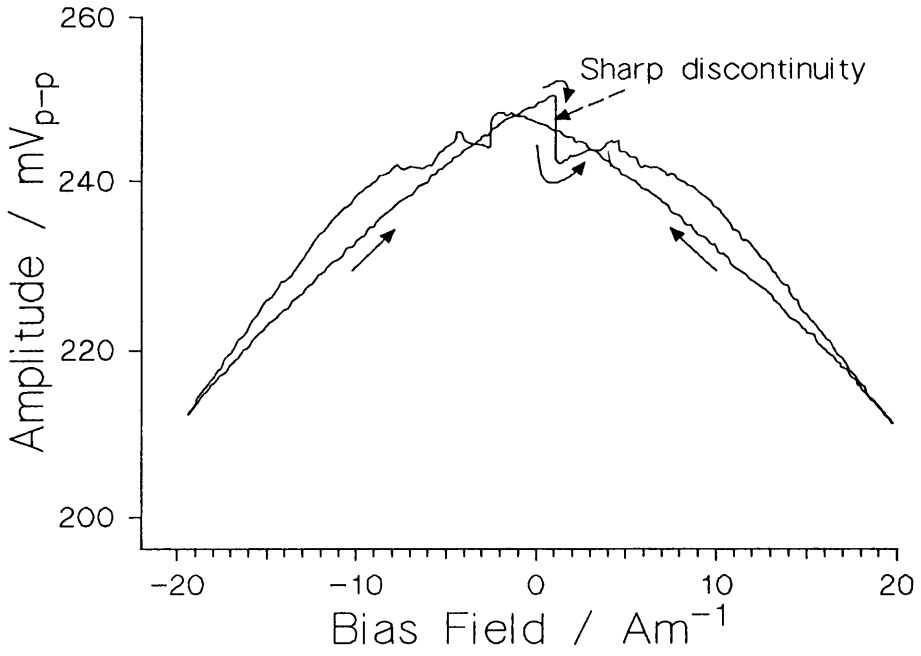

Figure 5.14a Low field amplitude response for magnetic transducer MT1.

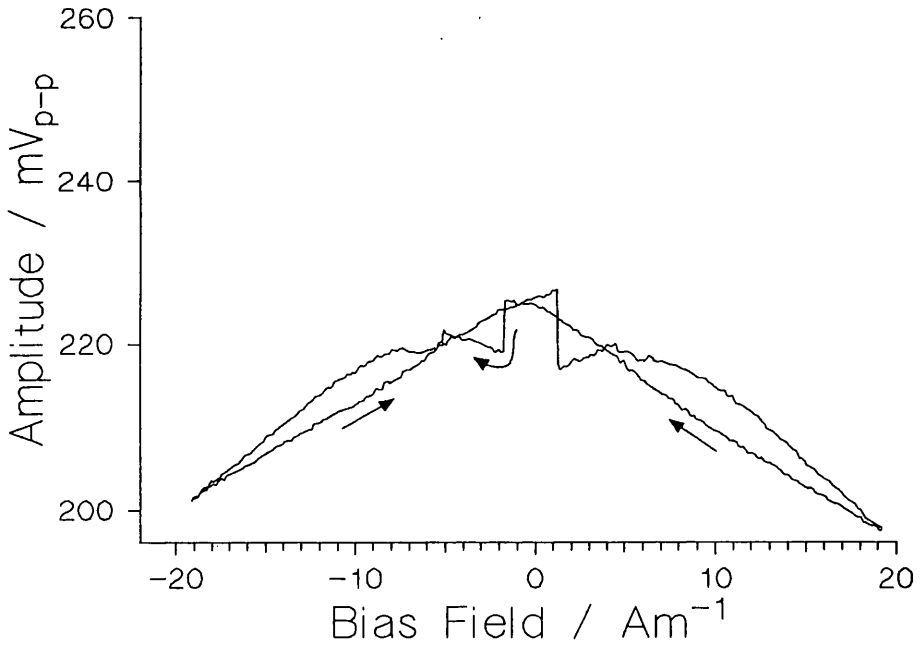

Figure 5.14b Low field amplitude response for magnetic transducer MT2.

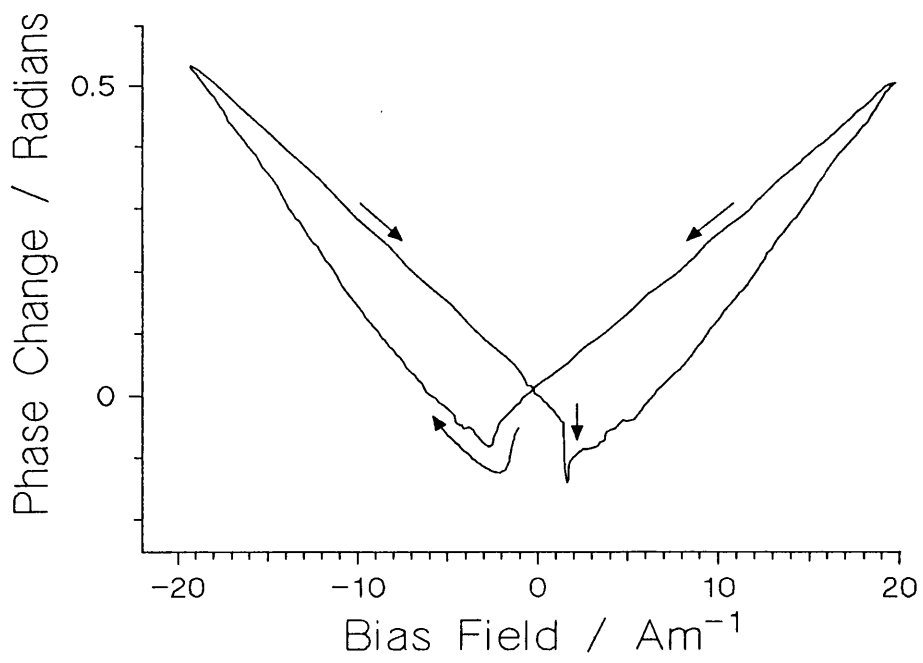

Figure 5.15a Low field phase response for magnetic transducer MT1.

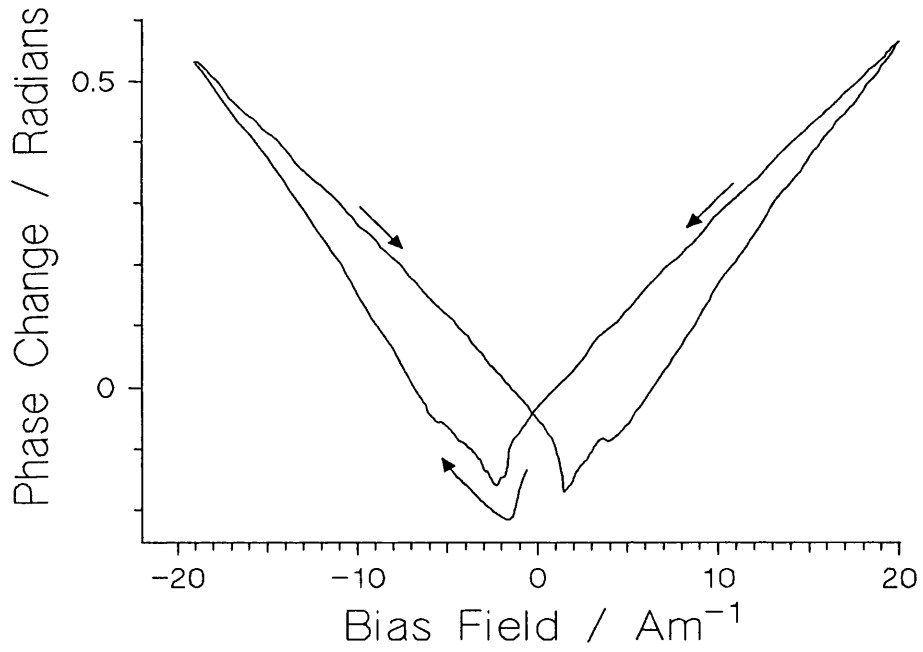

Figure 5.15b Low field phase response for magnetic transducer MT2.

The two transducers display the same gross changes in the amplitudes of both quantities measured as well as showing a distinct correlation in features. Both transducers exhibit discontinuities in the amplitude and the phase at fields equivalent to the approximate expected coercive field for these as received materials of a few Am^{-1}. These discontinuities although less prominent can also be observed in the 10cm magnetic transducer of Figure 5.13. The overall amplitude of the output of MT2 was observed to be smaller than that of MT1. This is probably due more to a difference in piezoelectric transducer efficiency than any marked increase in attenuation with the increased operating frequency of MT2.

The amplitude response and the change in the shear wave velocity for applied fields with magnitudes approaching the saturation field for the transducer MT1 are shown in Figure 5.16 and Figure 5.17 respectively. The field in this case was generated using the Farnell regulated power supply and as a result the graphs are made up of point measurements rather than the continuous traces presented previously. These measurements were carried out with both the input and output piezoelectric transducers optimally matched as described in chapter 5.2 and hence explains the large overall amplitude observed in Figure 5.16. The phase response was not seen to be effected by the matching process. The velocity dependence of Figure 5.17 was derived from the phase dependence of the magnetic transducer. The absolute velocity was calculated from equation 5.5, where $\mathbf{f_1}$-$\mathbf{f_2}$ is the frequency adjustment necessary to produce an additional phase change along the transducer of 180°. **C** is the absolute velocity and **L** the separation between the piezoelectric transducers.

$$C = 2L(f_1 - f_2) \qquad 5.5$$

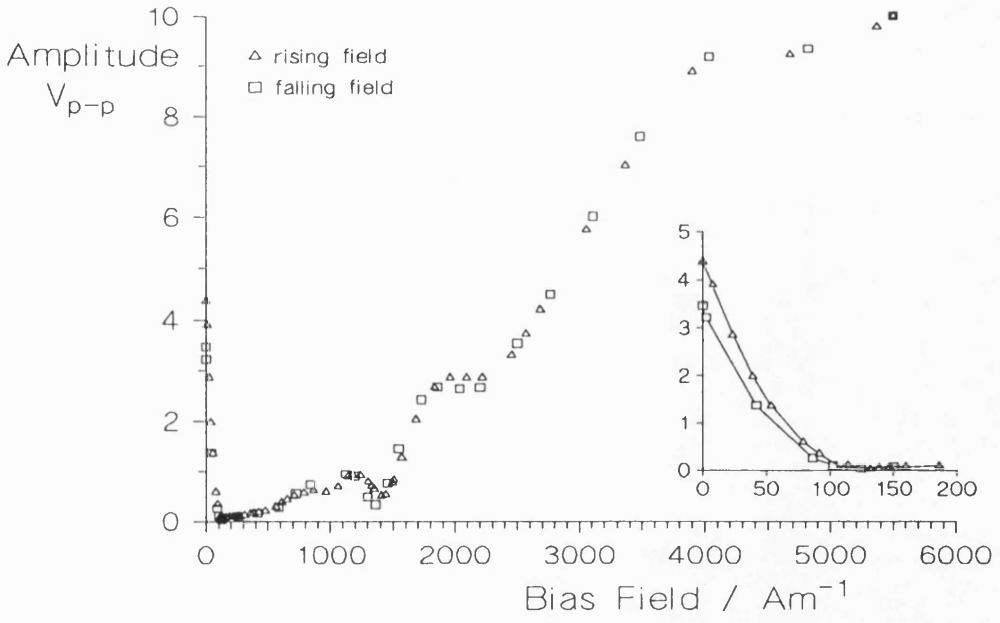

Figure 5.16 High field amplitude response for MT1. Inset shows expanded low field data.

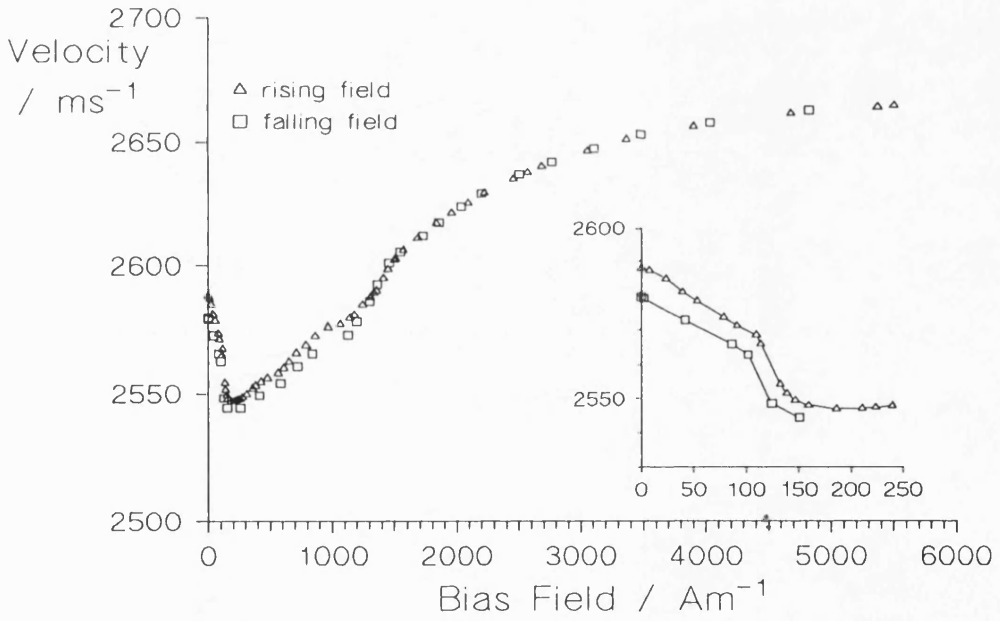

Figure 5.17 High field velocity dependence for MT1. Inset shows expanded low field data.

The phase shift was observed on a CRO with the trigger referenced to the drive oscillator. The frequency shift could be easily ascertained to within ±0.1kHz whereas the piezoelectric transducer separation could realistically only be estimated to within ±1mm. These uncertainties introduce an error into the calculation of the absolute velocity far greater than the overall field dependence which retains negligible errors occurring from the various instrumentation components. The absolute velocity was calculated to be 2600±170ms^{-1} accounting for the two aforementioned errors. This velocity corresponds to an approximate wavelength of 2.5x10^{-3}m and a frequency shift of 6.5kHz for a phase shift of 180°.

The amplitude response of Figure 5.16 exhibits unusual features above a bias field of the order of 1000Am^{-1}. These should not appear in terms of the coherent rotation model but can be explained, however, in terms of constructive and destructive interference of the shear wave travelling along the ribbon with reflected waves from the imperfect Tico pad™ end absorbers. Replotting the field dependent amplitude against the field dependent phase with an arbitrary origin as shown in Figure 5.18 demonstrates this effect clearly with maxima in the received amplitude occurring at 0°, 360° and 720°, minima occur at 180° and 540°. This is shown more clearly in the inset figure in which the magnetic effect has been removed by fitting an exponential curve to the data of Figure 5.18.

The interference phenomenon can also be observed in an amplitude against drive frequency plot. Figure 5.19 shows a frequency sweep of the received shear wave amplitude for a transducer arrangement employing the 2MHz specified lithium niobate transducers 10cm apart along a ribbon of METGLAS 2826MB (REEL 2). As well as demonstrating that the mounting of the piezoelectric transducers has perturbed the specified resonance frequency the figure also demonstrates that the transducers can be

forced to oscillate with considerable amplitude off resonance. Also apparent are constructive interference peaks occurring at frequency intervals of approximately 26kHz which corresponds once again to a phase difference of 360° for the 10cm transducer.

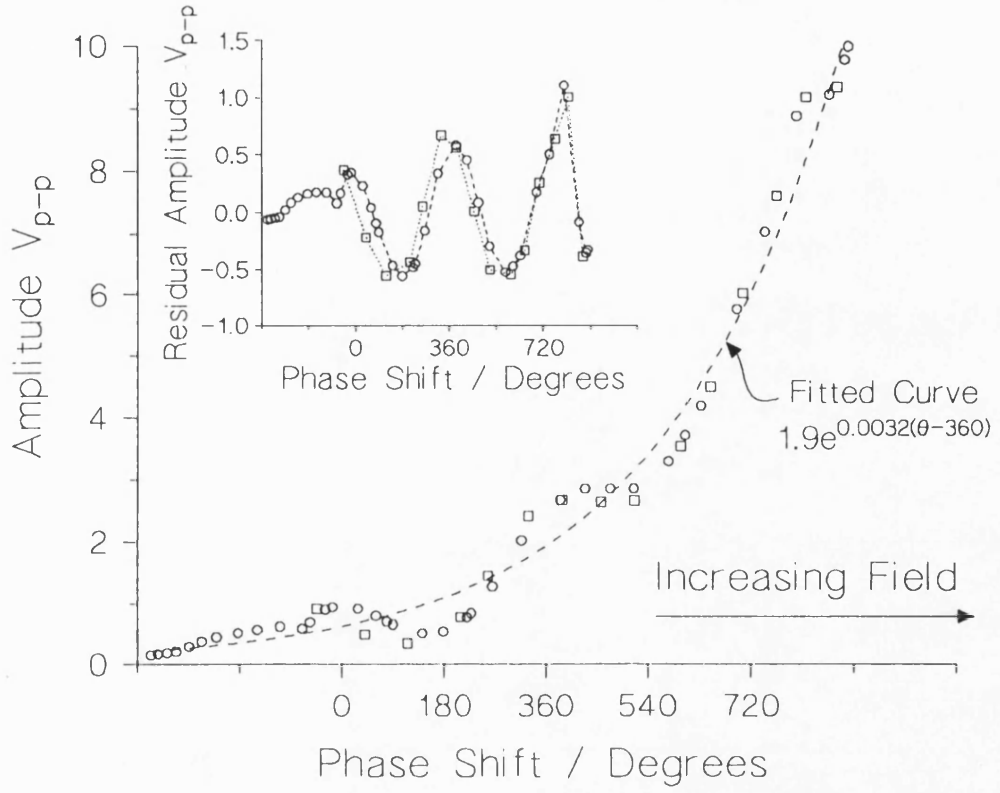

Figure 5.18 Field dependent amplitude plotted as a function of field dependent phase. Inset shows residual amplitude after subtraction of the magnetic affect.

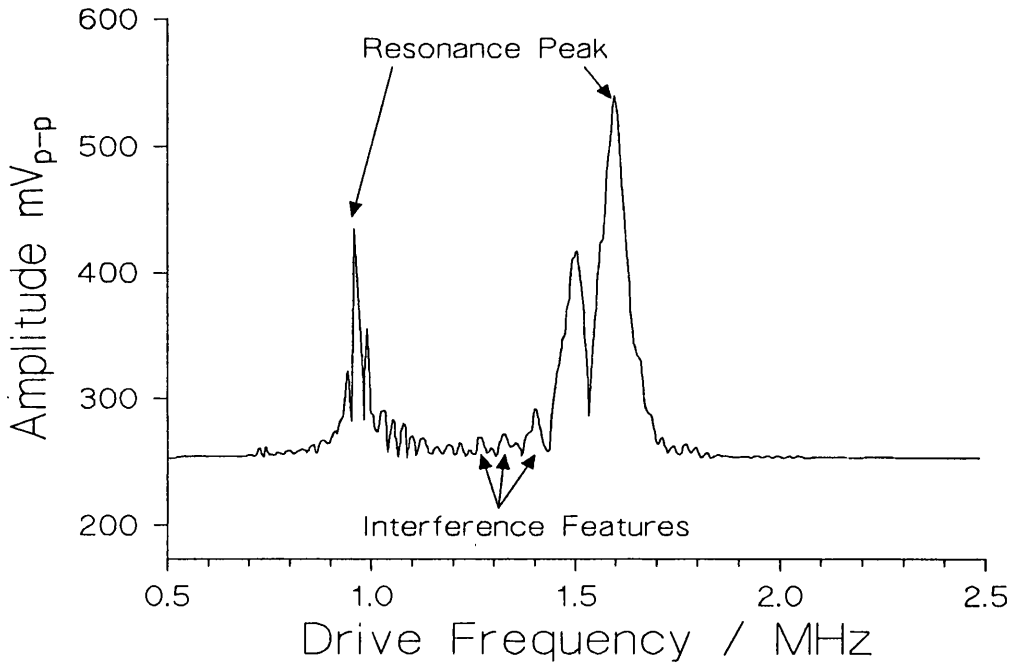

Figure 5.19 Magnetic transducer output amplitude as a function of drive frequency.

Both Figure 5.16 and Figure 5.17 exhibit features typically expected from the coherent rotation model. The two responses fall rapidly to minima before once again rising as the applied magnetic fields become of sufficient magnitude for the ribbon to approach saturation. From the classical description the minima occur in the region of the material's anisotropy field. Figure 5.20 and Figure 5.21 show the amplitude and the response respectively for the transducer MT1. Once again the figures were produced using a continuous field sweep but in this case up to a field in the region of the anisotropy field. Figures 5.14 - 5.15 inclusive, Figure 5.20 and Figure 5.21 demonstrate that in general for the low to intermediate magnetic field ranges up to the anisotropy field, taking into account the hysteresis, the responses are a combination of a linear and a quadratic function about zero applied field. This observation can be used as an aid for comparing responses and is discussed in chapter 5.4.2.

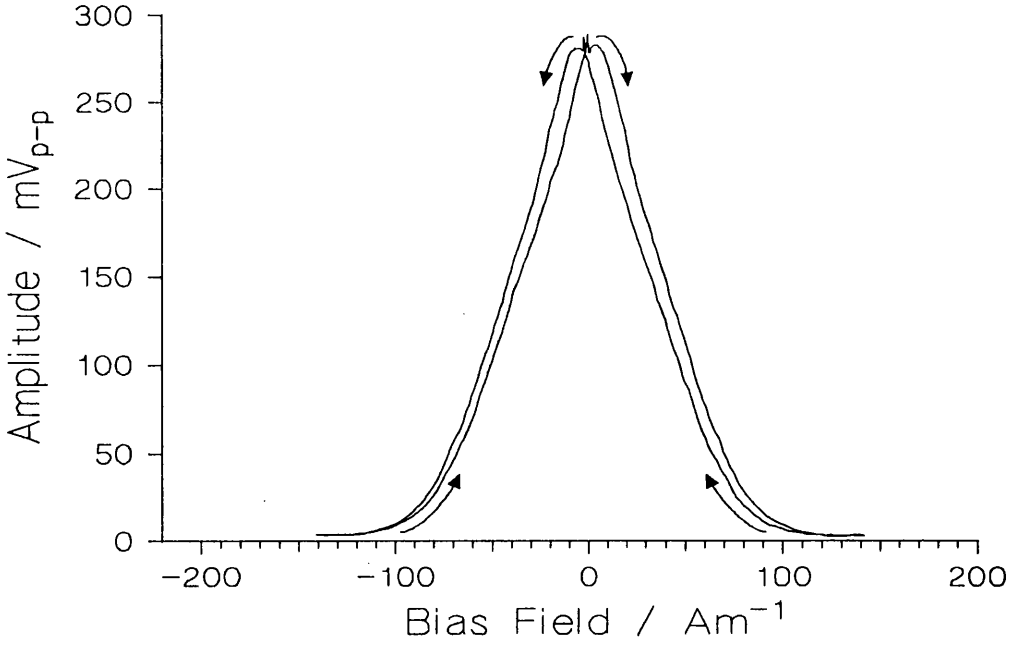

Figure 5.20 Amplitude response for MT1 for fields approaching the anisotropy field.

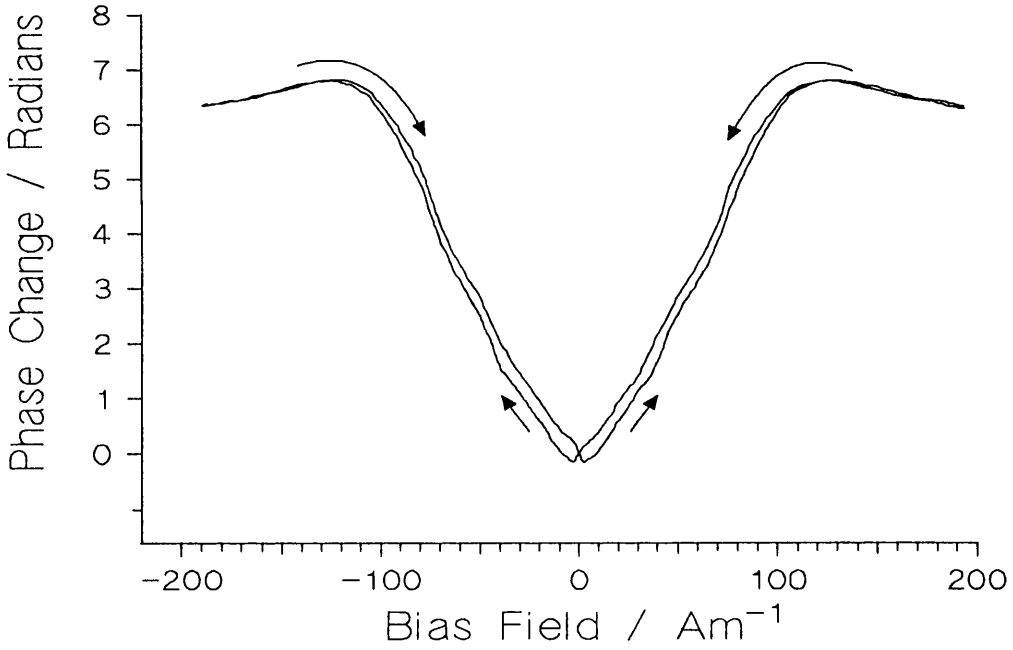

Figure 5.21 Phase response for MT1 for fields approaching the anisotropy field.

Figure 5.22 shows the extremes of the continuous wave amplitude response data of Bassir [1991a] from Figure 5.11b plotted alongside the amplitude response of Figure 5.20. The response is given as a function of applied bias field rather than Internal field as this more clearly compares the operation of the whole magnetic transducer arrangement, whereas, the internal field is useful for comparing material properties. On this basis the amplitude response of MT1 was comparable to the field annealed magnetic transducers constructed by Bassir [1991a]. If internal fields are considered the response of the field annealed transducers would be comparatively larger.

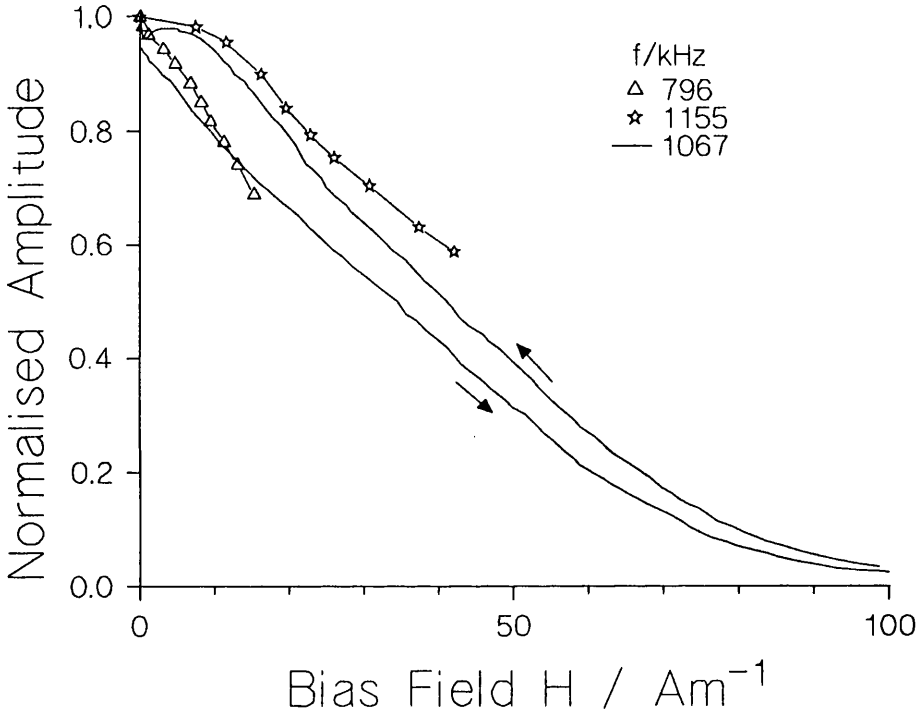

Figure 5.22 Comparison of "as-received" and field annealed transducer amplitude responses. Points - Bassir [1991a], continuous trace - this study

5.4.2 The Magnetic Response as a Function of Active Material Length.

The dependence of the magnetic response on the active material length i.e. the transducer separation **L**, for both supplies of the METGLAS 2826MB (REEL 1 & 2) was investigated. Starting with a 30cm separation the low field amplitude and the phase responses were recorded using the arrangement described in the previous chapter. The piezoelectric transducer which was selected as the receiver for the transducer arrangement was removed from the ribbon after recording the response, the ribbon shortened by 5cm and the receiver remounted for the next measurement. Responses were thus obtained for transducer separations **L**=30,25,...,5cm. For the METGLAS 2826MB (REEL 1) PZT5A transducers were employed bonded with silver loaded epoxy and the measurement process repeated twice using the same transducers so as to obtain a more complete data set. Both data sets produced similar overall results. The PZT5A transducers used resonated at a frequency of 1200kHz which had to be fine tuned within a frequency band of ±30kHz to obtain a maximum received amplitude for each transducer remount. The data collection for the lithium niobate transducers ,operating around 950kHz, used with the METGLAS 2826MB (REEL 2) was repeated six times because of the greater ease with which these transducers could be remounted and once again the six data sets were essentially internally consistent apart from some spurious results which did not follow through the data sets.

To facilitate a direct comparison between the different magnetic transducer lengths the response as a function of internal field was studied. An important point to note, however, is that when operated in the magnetometer system the external field and not the internal field is the important quantity and thus in this mode of operation the demagnetising field would reduce the responses more for the shorter magnetic transducers. The internal field was obtained by calculating the demagnetising field for a general ellipsoid from the method of Osborn [1945]. The internal field $\mathbf{H}_i$ can be found

from equation 5.6, where C_D is a constant for a particular length of material calculated from χ the materials intrinsic susceptibility, **D** the demagnetisation factor, and $\mathbf{H_a}$ the external applied field.

$$H_i = C_D H_a = \frac{H_a}{1 + D\chi} \qquad 5.6$$

The initial susceptibility of the material was calculated by fitting a standard cubic expression about the coercive field for the measured magnetisation curves of the two material batches over an approximate field range of $20Am^{-1}$. The length of material for which the susceptibility was measured was 0.5m. The demagnetisation factor for this length of ribbon was calculated and the intrinsic susceptibility obtained from equation 5.7, where χ_m is the measured susceptibility. The procedure for obtaining the magnetisation curves is outlined in the following chapter and relies on a quasi d.c. method described fully by Squire *et al* [1988c].

$$\frac{1}{\chi} = \frac{1}{\chi_m} - D \qquad 5.7$$

The measured and calculated susceptibilities for the two batches of material are given in Table 5.2, whereas the constants C_D relating the internal field to the external applied field for the lengths of ribbon investigated are given in Table 5.3. The demagnetising factors calculated were for the total length of the ribbon and so included the clamped material of approximately 1cm in length at each end. The greatest contribution to errors in C_D come from the approximation to an ellipsoid made for the geometry of the ribbon.

Table 5.2 Measured and intrinsic susceptibility of the two METGLAS 2826MB ribbons.

	χ_m(50cm ribbons)	χ
REEL 1	13000	14800
REEL 2	14500	16800

Table 5.3 Internal field to applied field relational constants.

Transducer separation L / cm	REEL 1 C_D (for L+2cm)	REEL 2 C_D (for L+2cm)
5	0.214	0.193
10	0.395	0.366
15	0.542	0.505
20	0.640	0.611
25	0.715	0.689
30	0.770	0.747

The amplitude and phase responses for one of the two data sets collected for the METGLAS 2826MB (REEL 1) are shown in Figure 5.23 and Figure 5.24 respectively. The 30cm data continued the trends that can be observed from the data given in the figures and so was not shown in the figures purely so as to aid clarity. Similarly the phase responses have been shifted so as not to overlay one another. For the measurements taken on the material from (REEL 1) apart from the response for the 5cm transducer separation the same external applied field was used. A larger external field was used for the 5cm magnetic transducer as for this geometry the demagnetising field had by far the greatest effect and it was desirable to compare the responses over equivalent internal

field ranges. When carrying out the measurements on the material of (REEL 2) identical internal fields were applied in all cases.

All the amplitude response data demonstrated the expected result of a general decrease in the received zero applied field amplitude with increasing piezoelectric transducer separation. There also appeared to be a trend towards a reduced response with increasing length. The data for the (REEL 1) material shown in Figure 5.23, however, demonstrated the irregular features observed earlier in Figure 5.14. These became more prominent with increasing length causing an increased sharpness in the response for fields near the expected coercive field. The irregularities were not observed in the (REEL 2) data, an example of a 15cm magnetic transducer amplitude response from this material being shown in Figure 5.25. This can be compared with the equivalent response for the material of (REEL 1) which is shown on an expanded scale in Figure 5.27. The overall fractional change in the amplitude can also be seen to be smaller for Figure 5.25 ($\approx$16%) compared to that of Figure 5.27 ($\approx$21%).

From consideration of equation 1.14 the phase response of the material would be expected to increase with increasing length. This would appear to be the case from examination of Figure 5.24 although the grosser change in the response appears to come about once more from an increase in the sharpness of the response with increasing length. Again this occurs for small fields equivalent to those observed in the amplitude response and does not occur for the (REEL 2) material. Almost identical phase responses were obtained for the representative 15cm and 25cm magnetic transducer shown in Figure 5.26 with a marginally smaller overall phase change especially for the 25cm transducer than the equivalent (REEL 1) transducer.

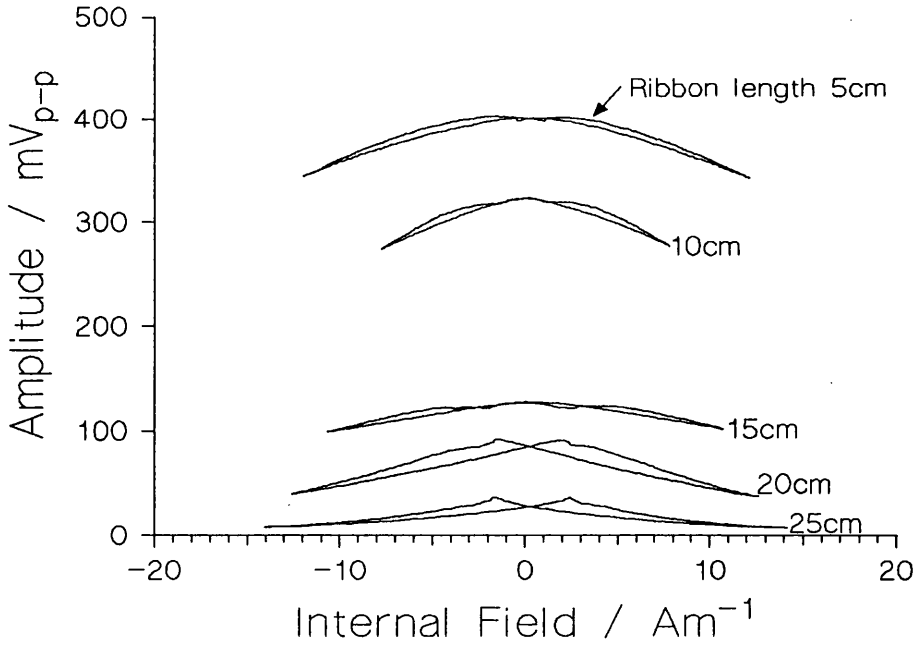

Figure 5.23 Amplitude response set for REEL 1 magnetic transducers.

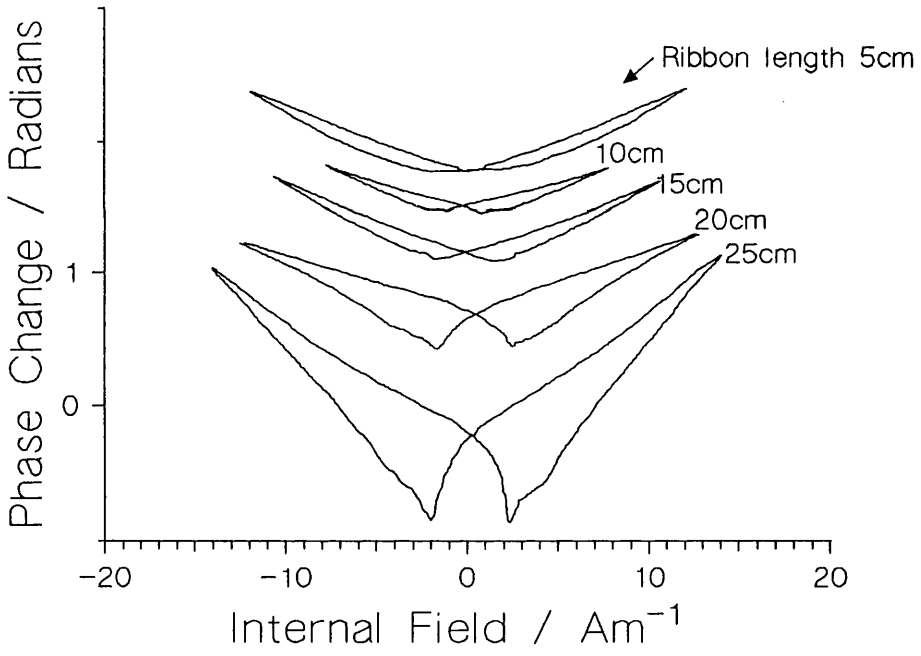

Figure 5.24 Phase response set for REEL 1 magnetic transducers.

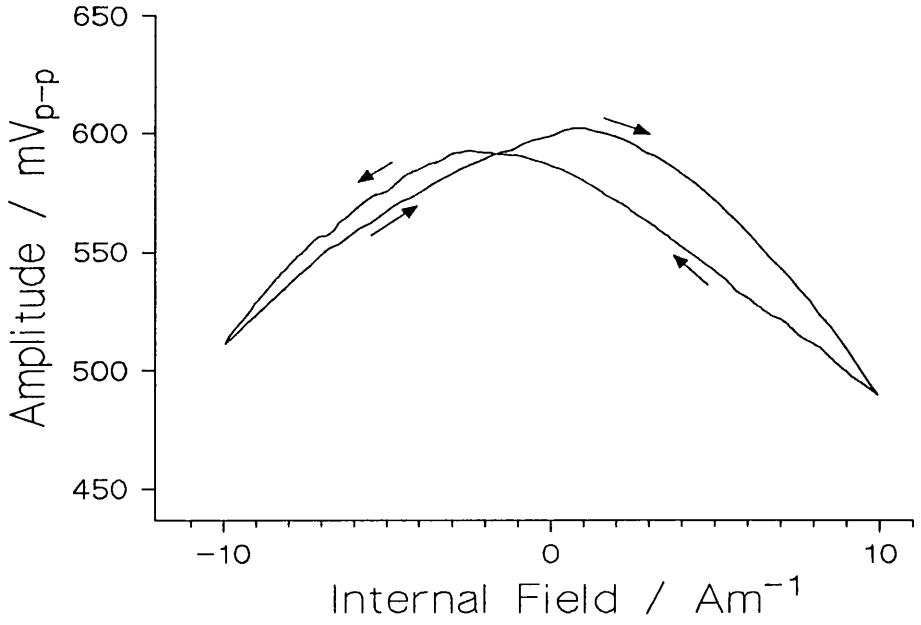

Figure 5.25 Amplitude response for 15cm magnetic transducer using REEL 2 material.

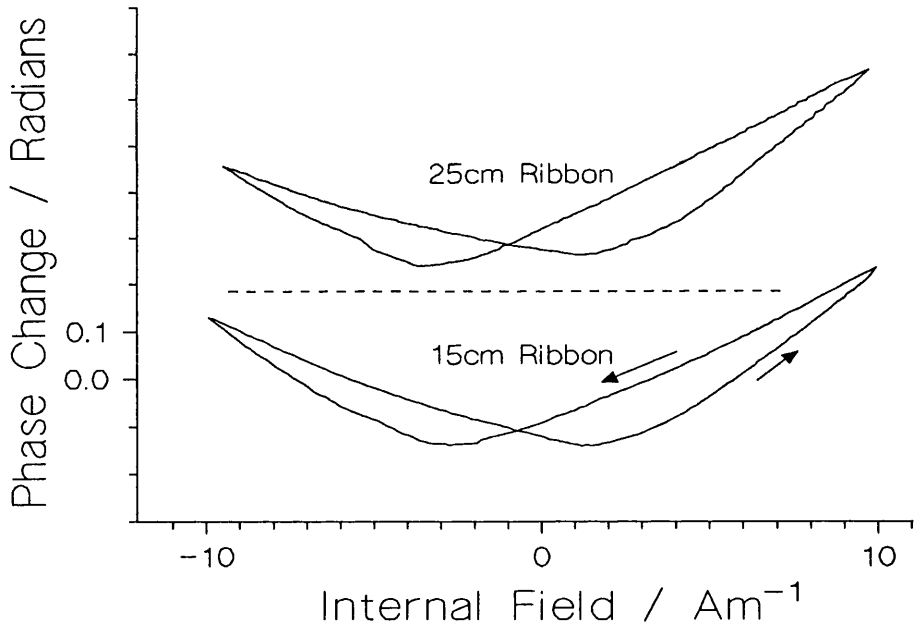

Figure 5.26 Comparison of the phase responses for 15cm and 25cm REEL 2 magnetic transducers.

A more quantitive examination was undertaken of the magnetic responses by performing curve fitting to the response data. As was observed earlier the responses contain a substantial linear component as well as a quadratic component with a hysteresis about zero applied field. A realistic approximation to the responses could, therefore, be made by fitting equation 5.8 and equation 5.9 separately to the rising field and the falling field shear wave amplitude, A_2 and phase change, $\Delta\phi$ respectively. **H** is the internal field and the coefficients $\mathbf{a_1}$,$\mathbf{b_1}$ and $\mathbf{d_1}$ in the amplitude response equation are the peak zero field amplitude, the normalised linear amplitude response and the normalised quadratic amplitude response respectively. An important consequence of the modulus sign around the linear term which should not be lost sight of is that this term is essentially an even powered series which contains a quadratic term in itself. The coefficients $\mathbf{a_2}$, $\mathbf{b_2}$ and $\mathbf{d_2}$ in the phase response equation are a d.c. instrumentation phase shift of no importance to this study and the linear and the quadratic phase responses respectively. The coefficients **c** and **e** in both equations would be expected to reflect the field positions of the response features discussed previously.

$$A_{2(H)} = a_1 \{ 1 - b_1 | H - c_1 | - d_1 (H - e_1)^2 \} \qquad 5.8$$

$$\Delta\phi_{(H)} = a_2 + b_2 | H - c_2 | + d_2 (H - e_2)^2 \qquad 5.9$$

The curve fitting was implemented using a commercially available graphics software package (FIG.P - Publ; Biosoft, 22 Hills Road, Cambridge) to fit the curves to the digitised response data. Typical fits of the equations to the amplitude and phase response data are shown in Figure 5.27 and Figure 5.28. Two values of the coefficients were obtained from each data set and the average and standard errors calculated from the sum total of the obtained parameters.

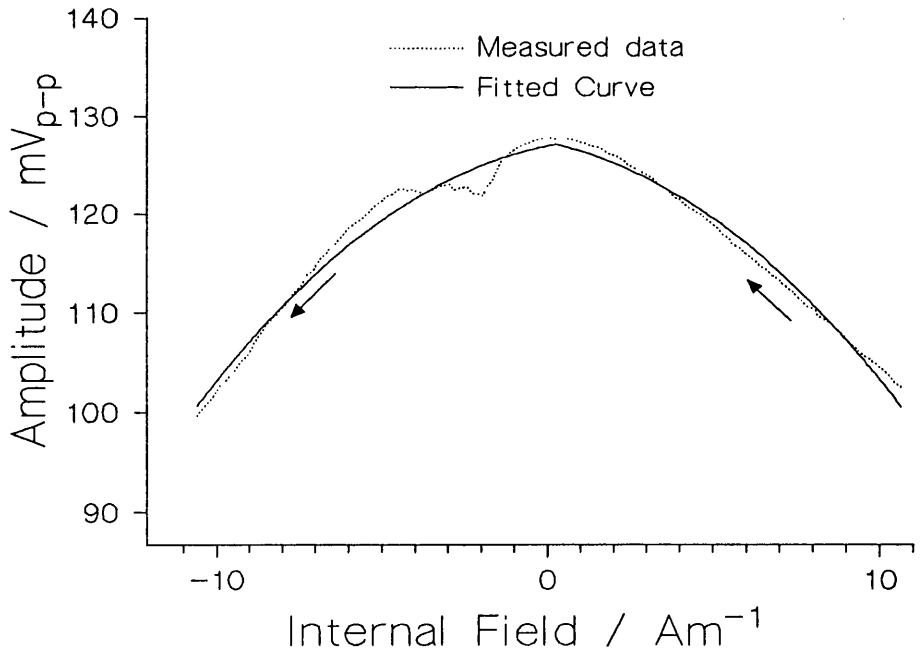

Figure 5.27 Typical fit to the amplitude response data of the (REEL 1) material.

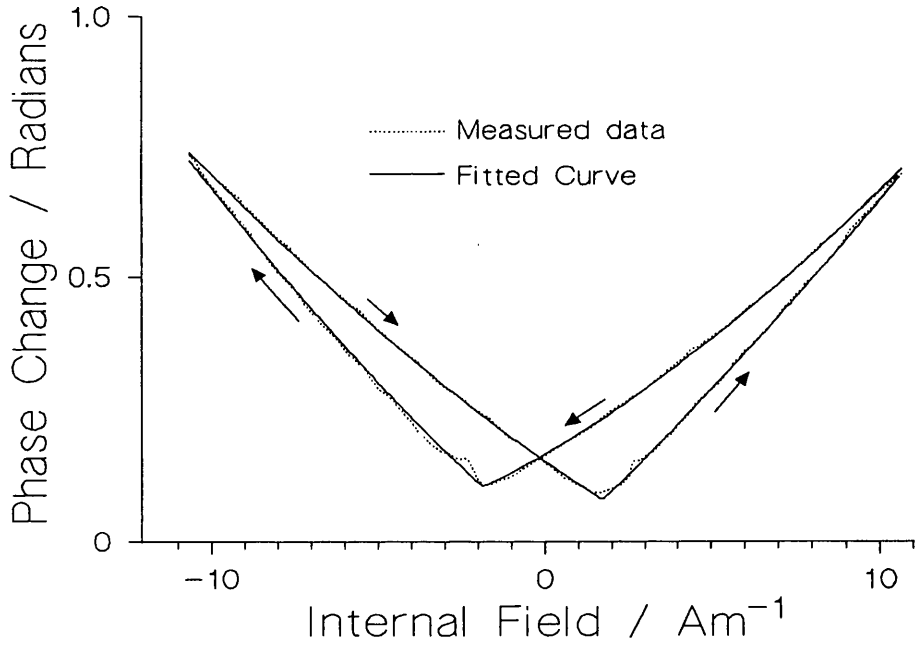

Figure 5.28 Typical fit to the phase response data of the (REEL 1) material

Curve fitting was not undertaken on the phase response data of the (REEL 2) magnetic transducers as the spurious results observed in each data set made it impossible to get a complete set of results. Satisfactory fits were obtained for all the data in the (REEL 1) sets as well as acceptable fits being obtained for the (REEL 2) amplitude response data. The phase responses in the (REEL 2) sets all displayed similar gross overall changes which demonstrated a reduced overall change in phase compared to the phase responses of the (REEL 1) data, see Figure 5.26. The (REEL 1) data demonstrated the more interesting trends and this was the more intensively studied material. The overall quality of the fits tended to be reflected in the size of the error bars.

Figure 5.29 a,b,c shows the coefficients for the amplitude response data as functions of piezoelectric transducer separation. Figure 5.29a shows the zero field peak amplitude of the received signal and in both cases the length dependence was found to be exponential in nature the fitted straight lines being exponential fits to the logarithmic plotted Y-ordinate. The normalised amplitude responses for the two materials are shown in Figure 5.29b. The (REEL 2) material shows a constant response independent of length whereas the (REEL 1) material shows an increased response for the longer lengths essentially reflecting the increase in the prominence of the low field features. The quadratic response shown in Figure 5.29c also demonstrates similar trends.

Figure 5.30 a,b shows the coefficients for the phase response data as functions of piezoelectric transducer separation. It is suggested that the increase in the phase response seen for the four shorter transducers in Figure 5.30a demonstrates the expected increase in the phase response with an increase in length, whereas, the increase in response for the two longest lengths comes from the increase in the prominence of the low field features. Figure 5.30b demonstrates a similar quadratic dependence to that of the amplitude response.

The coefficients **c** and **e** where found to have a large spread of values approximately

equating to the field positions of the response features. Typical values quoted here for the rising field data of Figure 5.23 are $\mathbf{c}=1.9\pm1.5Am^{-1}$ and $\mathbf{e}=0.4\pm5.0Am^{-1}$.

The increase in the responses for the longer lengths of material were studied further by constructing magnetic transducers from the 5cm lengths cut from the original transducers in the process of reducing the transducer lengths in the initial studies. These transducers produced similar results to the 5cm transducers from the initial study and thus the increase in response was concluded to be due to a bulk effect rather than localised to the removed length of material. There was also no gross overall difference in the measured magnetisation curves for the removed material from those of the remaining material. It was important to discriminate between the two materials as the transducers constructed from (REEL 1) performed far more satisfactorily in the magnetometer system than those made from (REEL 2). The exact nature of the distinguishing property between the compositionally identical materials is discussed in chapter 5.4.4.

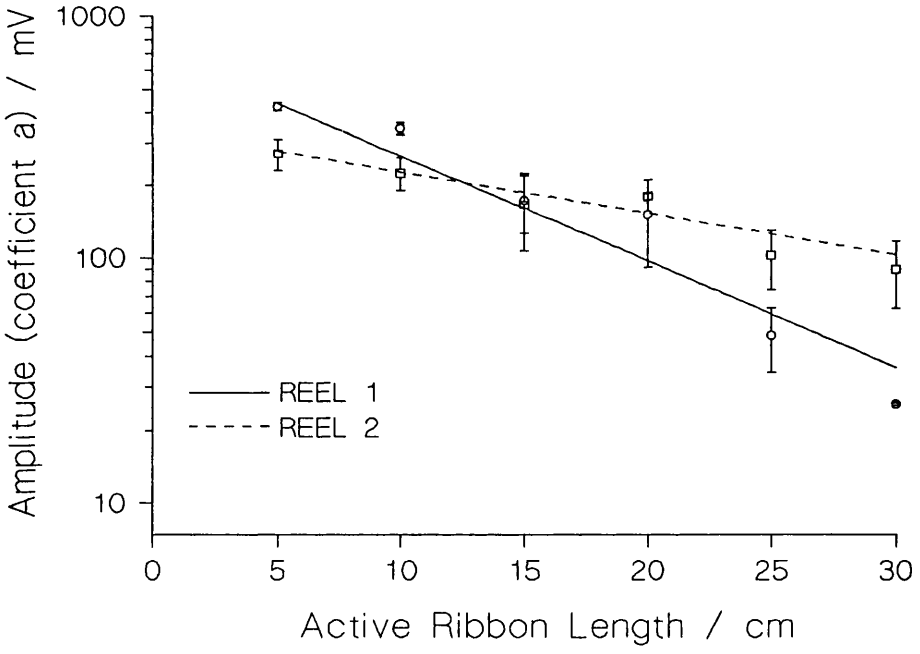

Figure 5.29a Amplitude response peak amplitude, coefficient $\mathbf{a_1}$.

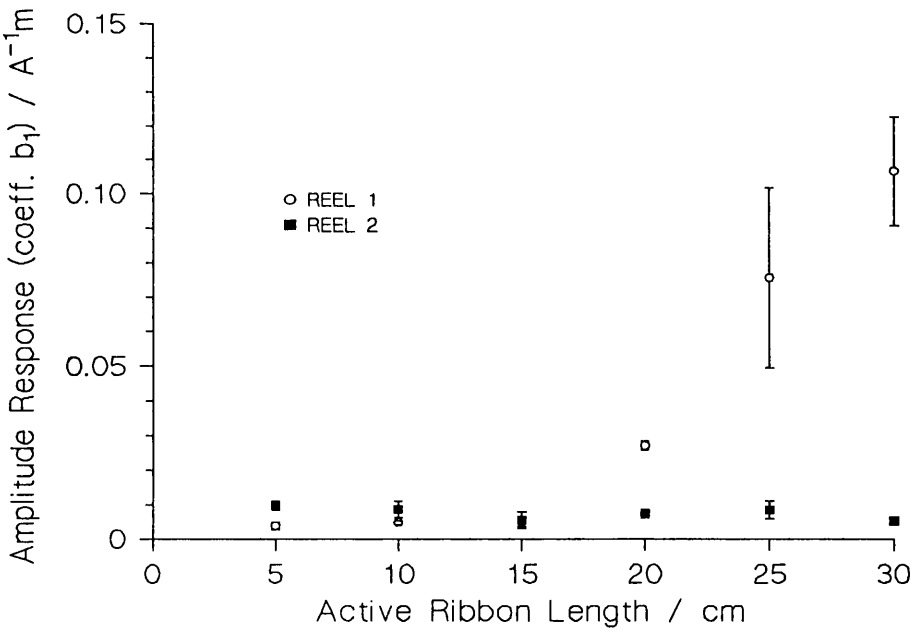

Figure 5.29b Normalised linear amplitude response, coefficients $\mathbf{b_1}$.

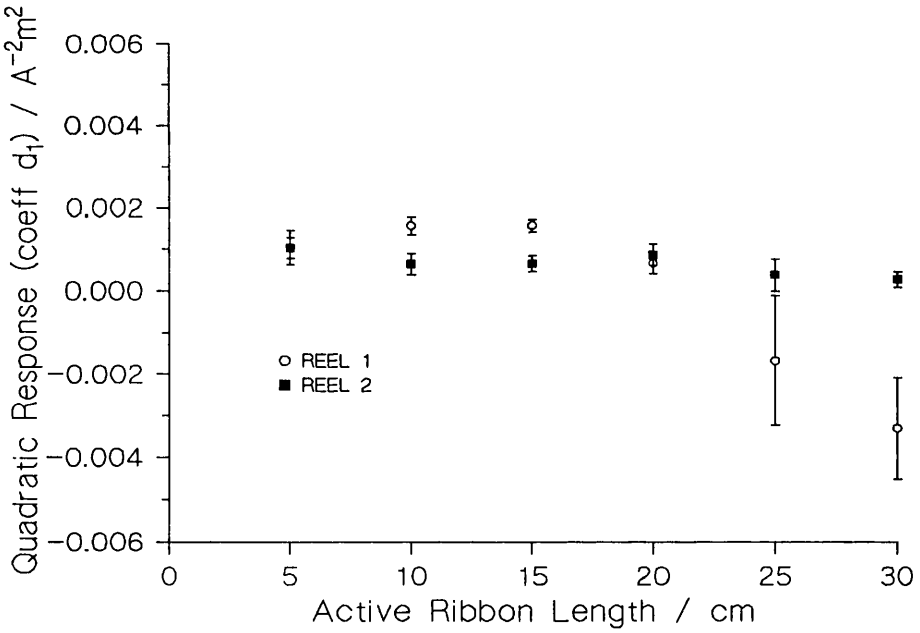

Figure 5.29c Normalised quadratic amplitude response, coefficient $\mathbf{d_1}$.

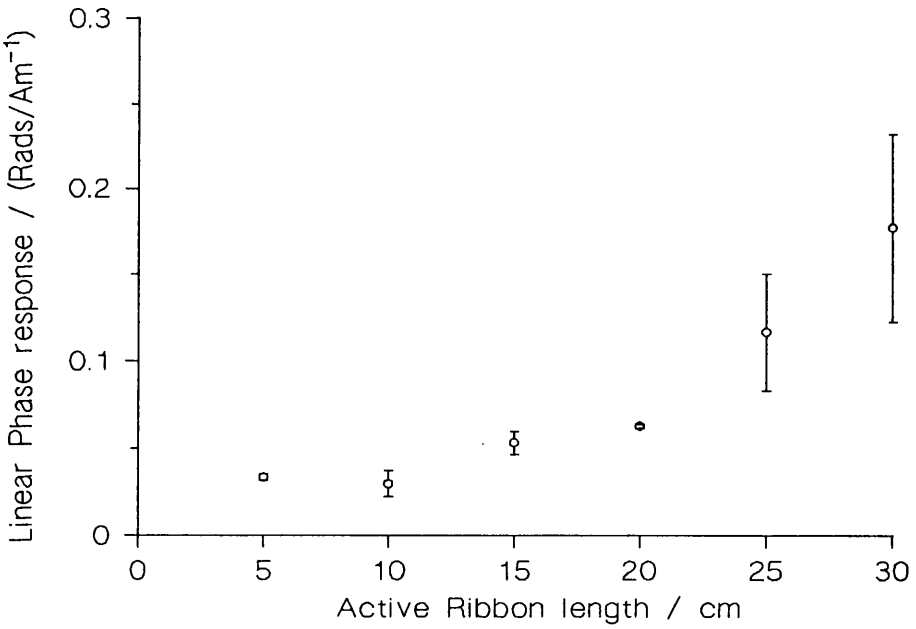

Figure 5.30a Linear phase response, coefficient $\mathbf{b_2}$.

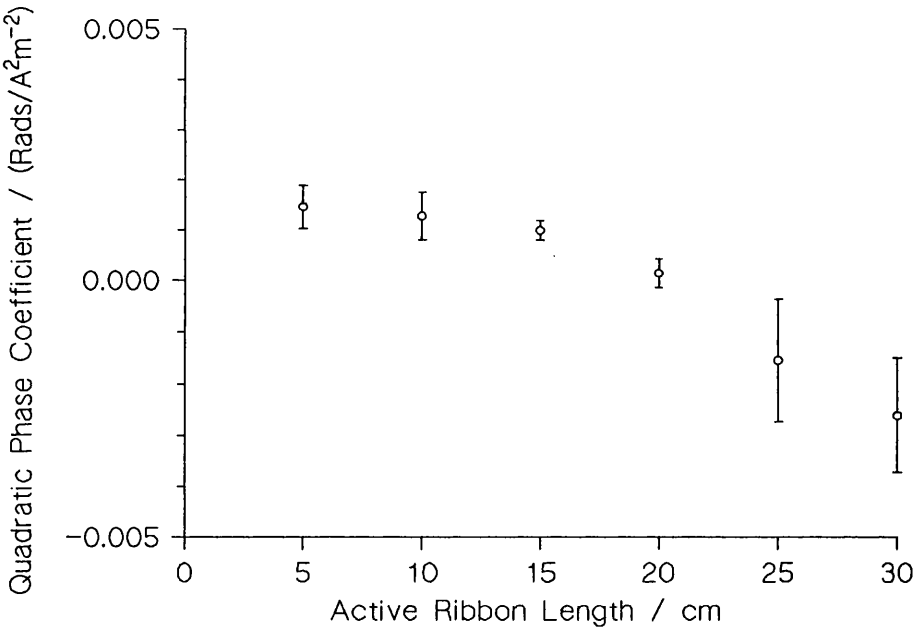

Figure 5.30b Quadratic phase response, coefficient $\mathbf{d_2}$.

5.4.3 The Magnetic Response as a Function of Propagation Frequency.

The amplitude and phase response as a function of frequency were studied for the magnetic transducers. The amplitude and phase responses were measured and the data manipulated as in the previous chapter. The transducer configuration investigated was the 20cm lithium niobate (REEL 2) transducer. The lithium niobate transducers were selected, as a number of matched pair transducers were available over a frequency range at individually specified frequencies. Unfortunately the loading of the transducer induced by the bonding to the ribbon surface perturbed the resonance frequencies of the transducers to the point where the higher frequency transducers (1.5, 1.75 & 2.0MHz) all resonated at approximately equivalent frequencies (≈1.6MHz), see Figure 5.19 which shows the transducer output amplitude for a 2MHz transducer. Fortunately the transducers could be driven off resonance and still provide comparatively large signals. The investigation was carried out utilising only one pair of 2MHz transducers driven at selected frequencies off resonance apart from the lowest frequency, for which the 1MHz transducers were used. The transducers were mounted sequentially onto three different lengths of material to obtain a range of data sets. The use of this off-resonance technique makes it impossible to compare absolute amplitudes of the received signals; however, there should be no problems comparing the frequency effects on the linear amplitude and phase responses. The results for the normalised linear amplitude response and the linear phase response are shown in Figure 5.31a and Figure 5.31b respectively. Figure 5.31a shows that in general there was no change in the amplitude response with frequency. The slightly larger response around 1MHz could possibly be due to the response being adversely effected by the far greater received amplitude about the resonance frequency. Figure 5.31b shows a perceptible change in the phase response with frequency. The expected dependence from equation 1.14 would be a linear increase with frequency and a free hand line has been drawn on the graph for guidance. Again the spurious points

about 1.6MHz could possibly be due to a resonance effect, similarly for the slightly high value at 0.8MHz. A further influencing factor is the frequency dependence of the shear modulus field dependence. This would be expected to reduce with increasing frequency through magnetomechanical damping consideration and from examination of equation 1.14, can be seen to directly effect the magnitude of the response.

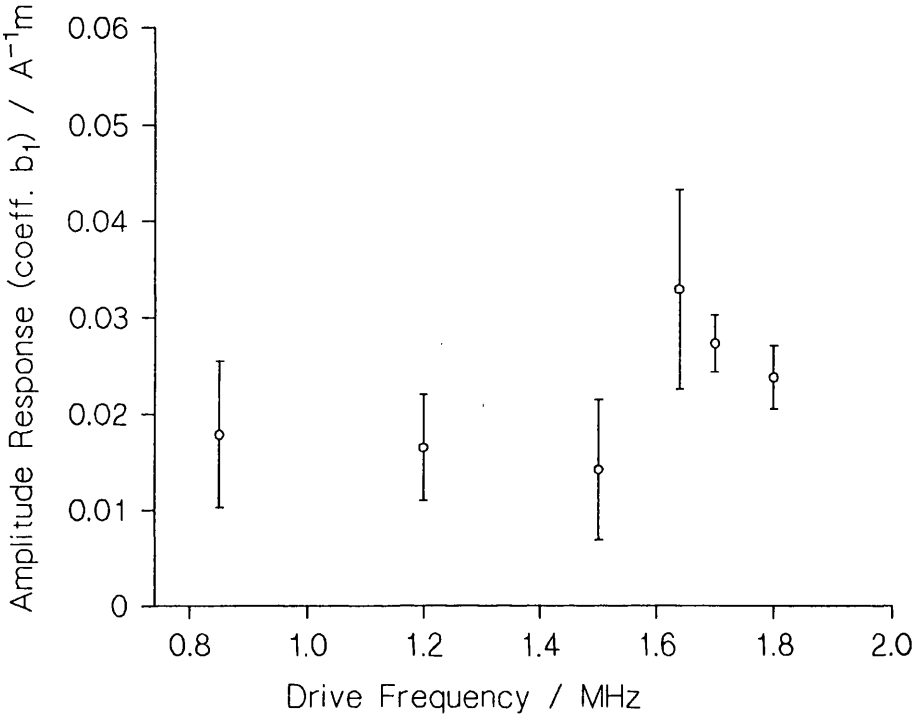

Figure 5.31a Normalised linear amplitude response as a function of frequency.

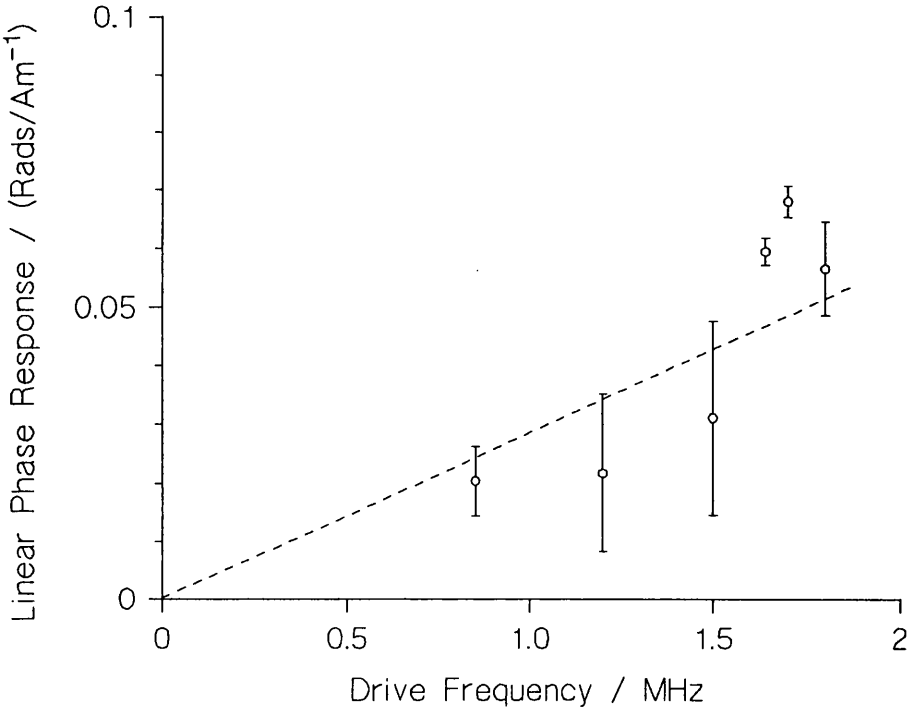

Figure 5.31b Linear phase response as a function of frequency. Dotted line shows expected form.

5.4.4 Distinguishing Properties of the Two METGLAS 2826MB Batches.

In order to isolate the distinguishing properties of the two METGLAS 2826MB ribbon supplies the magnetisation curves for the two materials were examined. The magnetisation curve of a material provides the most fundamental insight into the materials magnetic properties. The magnetisation curves for the two materials were measured using a quasi d.c. method described fully by Squire *et al* [1988c].

The apparatus consisted essentially of a long solenoid 1.5m long used to provide the applied field to the sample to be measured. The sample was placed within one of two accurately wound search coils 82mm in length wound with 20,000 turns around a flat rectangular coil former. The remaining search coil was placed 470mm from the

sample coil, the two coils being equidistant from the centre of the solenoid so as to be within the uniform applied field of the field solenoid. The applied field was stepped through a user defined field range with a step size which varied according to the function shown in equation 5.10, where **t** is the current step number, **T** the total number of steps in the cycle and **0<b<1** a user selected shape parameter, that allowed the data collection to be concentrated within the low field region of most interest.

$$H = \frac{\tan\left(\frac{2b\pi t}{T}\right)}{\tan\left(\frac{b\pi}{2}\right)} H_{max} \qquad 5.10$$

The stepping of the applied field produced *emf* spikes in the search coils which on the application of Faradays induction law gave a measure of the change in induction. The two search coils were arranged so that the induction of free space was subtracted from the signal and only the magnetisation of the sample measured, equation 5.11. The constant of proportionality was obtained by normalising the magnetisation at saturation to published data.

$$\int V dt \propto \mu_0(H+M) - \mu_0 H \propto \mu_0 M \qquad 5.11$$

The signal from the balanced coils was integrated using an analogue integrator for each field step. The integrated signal was summed over the full measurement time by the controlling microcomputer and thus reduced drift problems associated with long term analogue integrators. The microcomputer was also used to drive the applied field through a power amplifier. The duration between each field step was of the order of one hundred milliseconds the total time for the data collection taking of the order of **60s** depending on the number of steps. This "quasi d.c." method allows gross eddy current affects to be

ignored.

Figure 5.32 shows the saturation magnetisation curves for both the METGLAS 2826MB (REEL 1) and (REEL 2) materials with an inset figure so that the minor differences in the two curves can be more easily perceived. The initial susceptibility for the (REEL 2) material was marginally greater than that for (REEL 1) the values being quoted previously in Table 5.2. The inset figure would also suggest a marginally smaller anisotropy energy for the (REEL 2) material. Both materials have an approximate coercivity of $10Am^{-1}$.

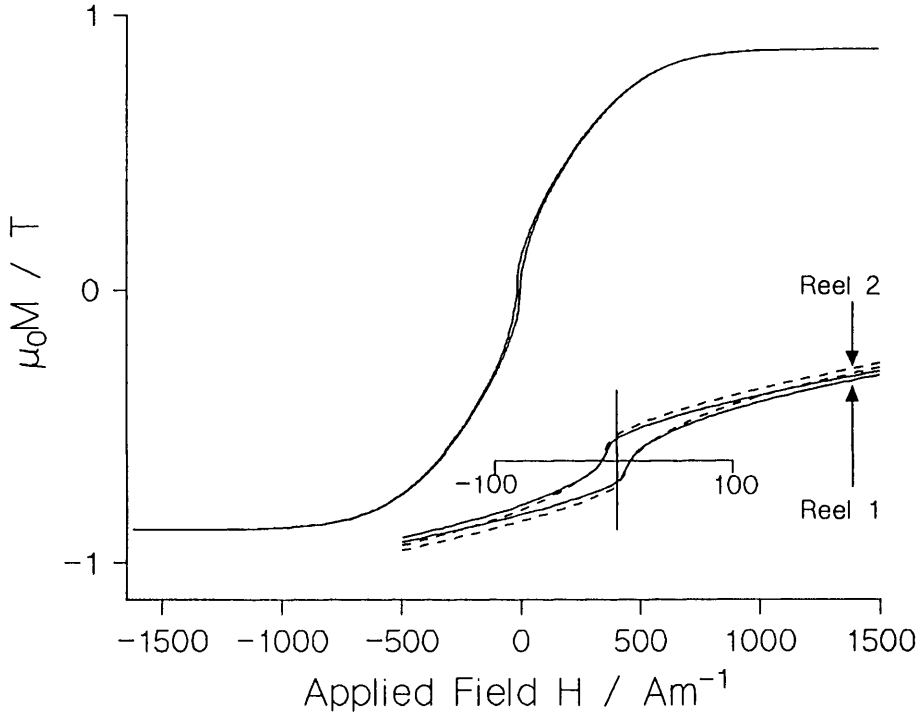

Figure 5.32 Saturation magnetisation curves for both METGLAS 2826MB batches. The sample lengths were 50cm.

Minor loop curves about zero applied field, for an equivalent field range to that used in Figure 5.14, were also measured and are shown in Figure 5.33a and Figure 5.33b. Figure 5.33a demonstrates large discontinuities or Barkhausen jumps in the magnetisation which, for both the rising and falling field sweeps, can be seen to correspond approximately to the field values for the discontinuities in both the amplitude and the phase responses of Figure 5.14 and Figure 5.15. Figure 5.33b also demonstrates a considerable number of Barkhausen jumps which have no corresponding discontinuities in Figure 5.25 or Figure 5.26. Although the magnetisation discontinuities could provide an explanation for the features observed in the (REEL 1) material the evidence of Figure 5.33b suggests that of more concern is to explain the lack of low field features in the response of Figure 5.25 and Figure 5.26 in order to ascertain the fundamental difference between the two samples.

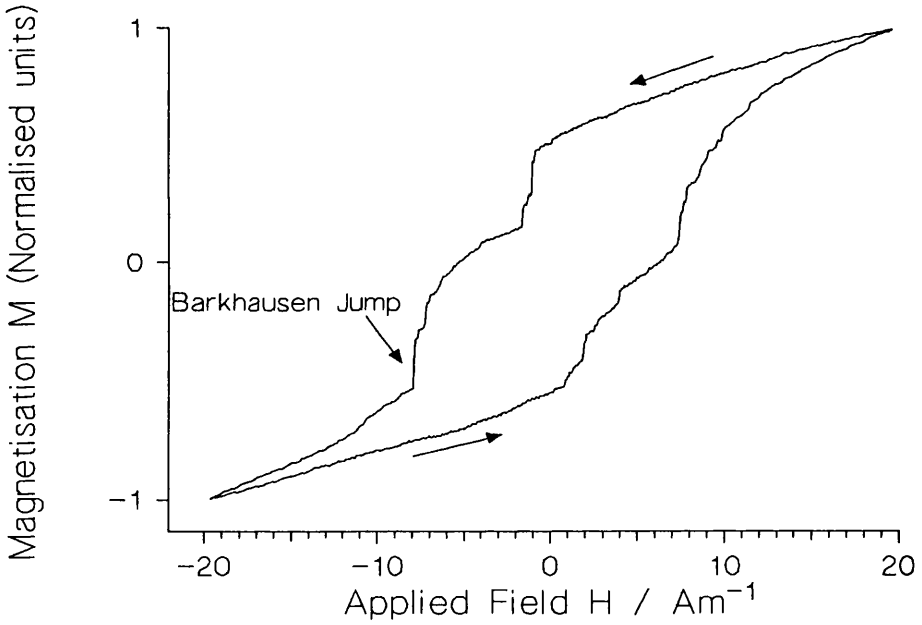

Figure 5.33a Minor magnetisation loop for METGLAS 2826MB (REEL 1).

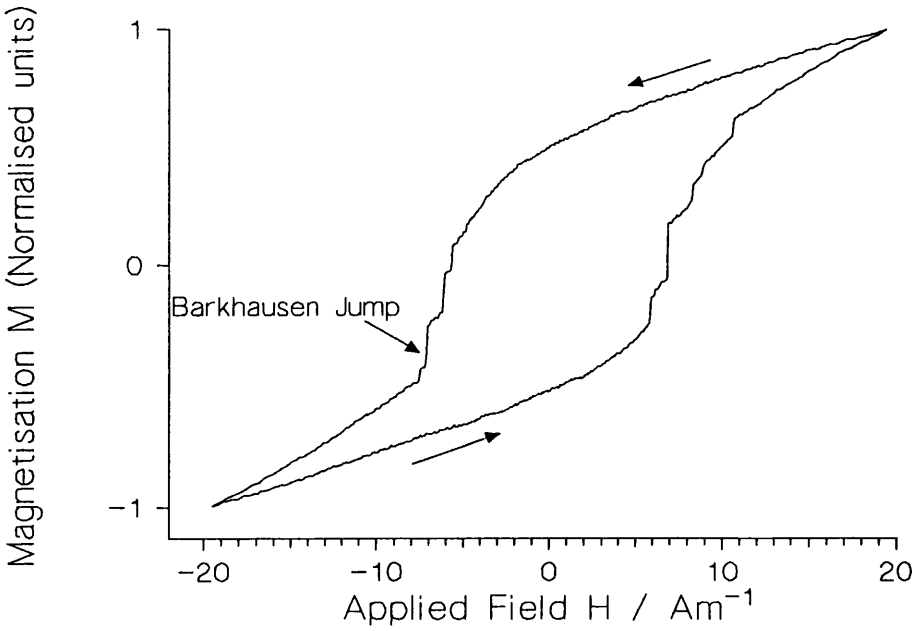

Figure 5.33b Minor magnetisation loop for METGLAS 2826MB (REEL 2).

Further information on the material properties was obtained from X-ray diffraction studies of the two materials. The measurements were carried out on a Philips X-ray diffraction system utilising a 4kW X-ray generator with a 2kW copper target and a computer controlled diffractometer goniometer on which was mounted a proportional counter. The output of the counter could be recorded on either a chart recorder or by the computer. The measurements were taken over angles of 2θ=5-60°. Two separate wavelengths of radiation are emitted from the copper target $K\alpha_1$=0.15405nm and $K\alpha_2$=0.15443nm which have a weighted mean of λ_{Cu}=0.15418nm. From this value and the Bragg equation, given in equation 5.12, diffraction angles for the <110> and <200> lattice planes for crystalline α-Fe can be calculated to be 44.7° and 65.0° at which diffraction peaks would be expected to be observed. Although the short range order of

the amorphous phase has a similar mean nearest neighbour distance a bump would be expected to be observed rather than a peak because of the inherent random nature of the structure.

$$\lambda_{Cu} = \frac{2a\sin\theta}{\sqrt{(h^2+k^2+l^2)}} \qquad 5.12$$

The X-ray diffraction results were taken for both the wheel side and the free side of the casting process and are shown in Figure 5.34a for the (REEL 1) material and in Figure 5.34b for the (REEL 2) material. The (REEL 2) material exhibits the classically expected amorphous bump for both sides of the material, whereas, the (REEL 1) material demonstrates a clearly crystalline free side. This would appear to be strictly a surface crystallisation, as the coercivities and susceptibilities of the two materials do not differ significantly, suggesting that the crystallites do not extend to any degree into the bulk of the material, Sheard *et al* [1989]. The crystallisation would appear to have occurred during the casting process due to poor control rather than in some post production process as the dull wheel side would be expected to display the greatest crystallisation in this case, Herzer and Hilzinger [1986]. It has been suggested by Thomas *et al* [1991] that controlled surface crystallisation is a viable method for controlling and optimising magnetic parameters specifically the magnetostriction. This occurs because of a bulk induced perpendicular anisotropy due to compression from the crystalline surface with an in-plane surface anisotropy from tensile effects proposed by Ok and Morrish [1981a]. Although this does not explain the lack of low field features in Figure 5.25 it potentially explains the improved response observed with the (REEL 1) material and emphasises an important difference between the two materials.

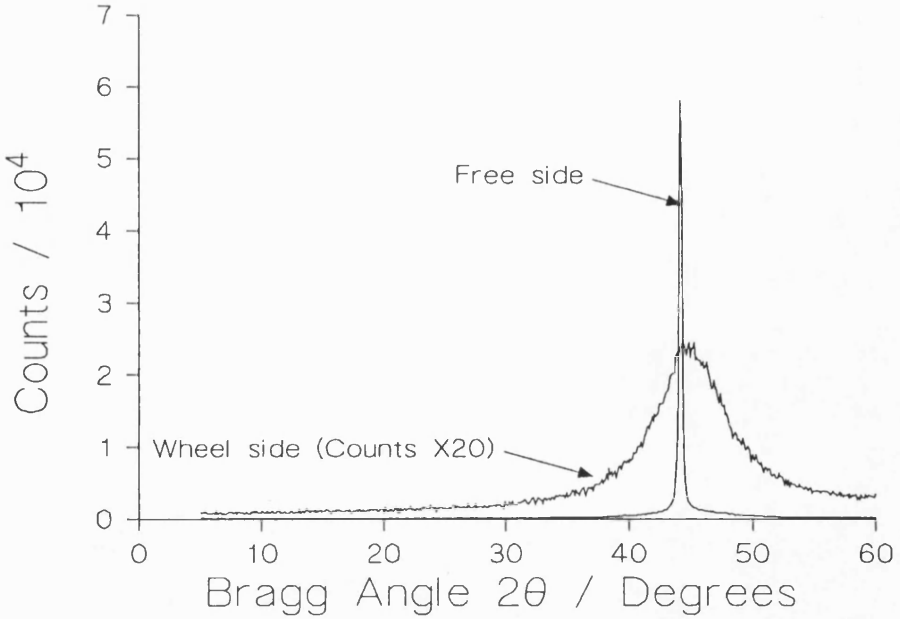

Figure 5.34a X-ray diffraction results for (REEL 1) material.

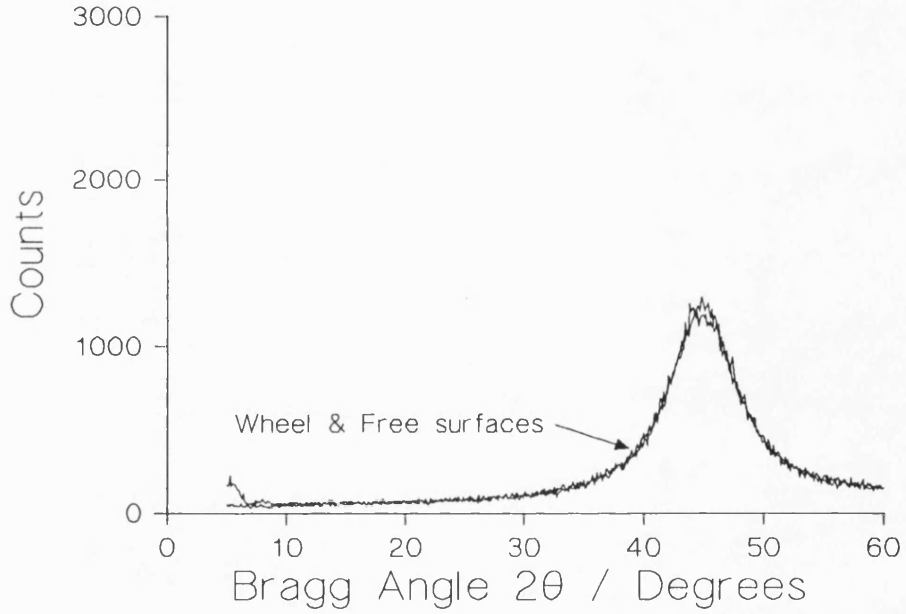

Figure 5.34b X-ray diffraction results for (REEL 2) material.

6 SHEAR WAVE MAGNETOMETER SYSTEM RESPONSE MODEL.

6.1 Introduction.

The Shear-wave Magnetometer, as described in the system overview in chapter 1, employed a mixer element for the detection of the modulated phase change of the shear waves travelling along the magnetic transducer. The shear waves have both a field dependent amplitude and a field dependent phase change and were discussed in the previous chapter. On the application of a modulation field the shear wave thus underwent both a phase and an amplitude modulation because of the two responses. Mixer elements are in general sensitive to both an amplitude modulation and a phase modulation and produce an output signal which is a combination of both these affects. The idealised mixer output function is shown in equation 6.1, where **k** is the mixer gain, $\mathbf{A_1}$ the amplitude of the reference signal, θ_0 the total phase change along the transducer and ω the shear wave excitation frequency.

$$V_{mix} = \frac{kA_1 A_{2(H)}}{2}[\cos(2\omega t + \phi_0 + \Delta\phi_{(H)}) + \cos(\phi_0 + \Delta\phi_{(H)})] \qquad 6.1$$

$\mathbf{A_2}$ and $\Delta\phi$ are the field dependent magnetic transducer output amplitude and the field dependent phase change along the ribbon. The applied magnetic field **H** consists of the modulation field at a frequency ω_m with a modulation depth **h** and an external d.c. field $\mathbf{H_0}$ in this case the field to be measured by the instrument, equation 6.2.

$$H = H_0 + h\sin\omega_m t \qquad 6.2$$

The output signal from the mixer was, therefore, oscillatory in nature consisting of Fourier components at the modulation frequency and its multiples as well as a much

higher frequency term at twice the shear wave excitation frequency all having a functional dependence on the applied field **H**. The Shear-wave Magnetometer employs a measurement of the Fourier component at the modulation frequency for the measurement of $\mathbf{H_0}$. The high frequency term at 2ω can be ignored and can be easily filtered out because of the large frequency differential between the modulation signal and the shear wave excitation frequency, see chapter 7. The effect, however, of the magnitude of the amplitude and phase responses of the magnetic transducer, the magnitude of the modulation depth and the overall phase change along the ribbon on the mixer output signal for an applied magnetic field for the low frequency harmonic terms is of immediate interest to the operation of the system. This could not be studied systematically on an experimental basis because of the lack of success in tailoring the properties of the ribbons to produce an operational magnetic transducer through field annealing. This chapter presents a simple linear model for predicting the output of the mixer element. This model was examined in terms of the low frequency harmonics of the modulation frequency. This was carried out in order to interpret the behaviour of modifying the model parameters representing the physical effects which influence the performance of the magnetometer system. Finally an alternative approach to the interpretation is also presented using digitised fits to the amplitude and phase response data in an attempt to explain the observed response. The fitting of the response data does, however remove most of the model's flexibility.

6.2 The Linear Response Model.

The output of the mixer element can be investigated by studying the ideal mixer output function given in equation 5.1 with physically meaningful functions substituted for the field dependent variables $V_{2(II)}$ and $\Delta\phi_{(II)}$. In chapter 5 it was demonstrated that a form of quadratic equation could be used to model the magnetic field response behaviour

of both the shear wave amplitude and the phase change, equation 5.8 and equation 5.9. These fits, however, each contained five coefficients including the field shifting coefficients which allow for the hysteresis in the responses. A far more basic description of the response was required for the system response model so that the number of coefficients describing a particular response would be a minimum. The effect of altering any particular system variable or field response on the total system response could then be studied simply by varying a single coefficient. For the low applied magnetic field case of interest here a reduced form of the quadratic functions were employed in which the field shifting coefficients and the second order quadratic terms were dropped to give equation 6.3 and equation 6.4 for the amplitude response and the phase response respectively. The d.c. term in the phase response was also dropped. This was essentially an instrumentation offset in the fitting process and could be taken up in the total d.c. phase shift along the transducer, ϕ_0. The coefficients of the equations represent the same quantities as defined previously in chapter 5 although they will obviously be of different magnitudes if the coefficients dropped had significant values. $\mathbf{a_1}$ and $\mathbf{b_1}$ are the peak zero field amplitude and the linear amplitude response and $\mathbf{b_2}$ is the linear phase response. A maximum mathematical limit of $1 > b_1|H|$ can be ascribed for the validity of the equations by considering the amplitude response function which in the context described cannot be less than zero as it represents the amplitude of the received shear wave. In practice the functions were only approximations which become deficient long before this limit was reached. The functions did ,however, have some validity over the range of fields considered which were well within both of these limits.

$$A_{2(H)} = a_1\{1 - b_1|H|\} \qquad 6.3$$

$$\Delta\phi_{(H)} = b_2|H| \qquad 6.4$$

Figure 6.1a shows the measured amplitude response for the magnetic transducer MT1 along with the fitted curve for the full quadratic function of equation 5.8 and the fitted curve after the quadratic term was dropped. Figure 6.1b shows the fitted curves to the transducer phase response. In both the figures the fitted functions retained the field shifting coefficients and the results were shifted vertically before plotting for clarity. The fits in Figures 6.1a & b were carried out using the software package introduced in chapter 5 (FIG.P). The values of the important coefficients obtained from the software package are given in Table 6.1a and Table 6.1b for the amplitude and the phase responses respectively. For both responses an additional set of values are given and represent the estimated values for the coefficients of equation 6.3 and equation 6.4. These are the values used where appropriate for the coefficients throughout this chapter. The software package values were not used for the calculations as the software was not available at the time of undertaking these studies. The values obtained, however, were close to those obtained from the later FIG.P fits and as a result the work was not repeated.

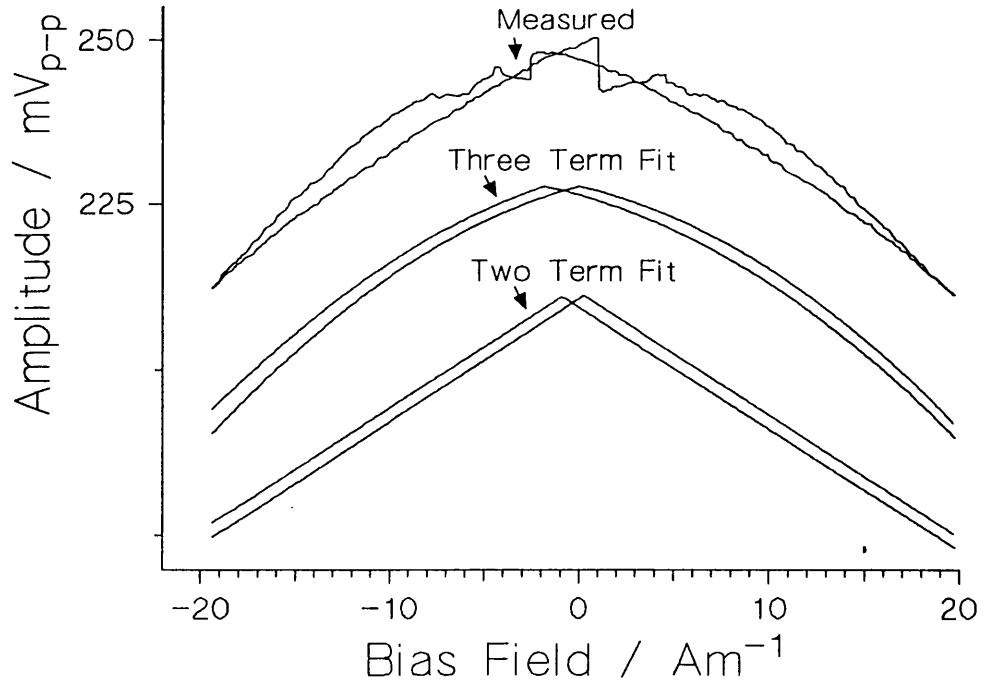

Figure 6.1a Fitted curves to MT1 amplitude response.

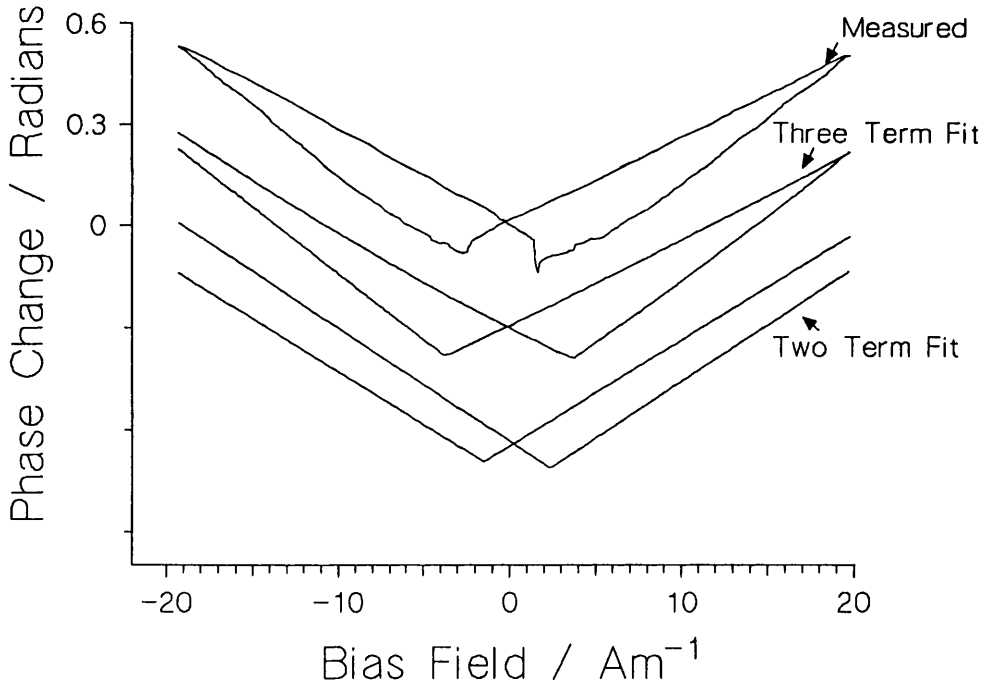

Figure 6.1b Fitted curves to MT1 phase response.

Table 6.1a Coefficients obtained for the functions fitted in Figure 6.1a

Description	Reference Equation	Field sweep direction	a_1 / mV	b_1 / $10^{-3}A^{-1}m$	d_1 / $10^{-3}A^{-2}m^2$
Three Term quadratic	5.8	Rising	248	2.9	0.23
		Falling	248	3.2	0.21
Two Term linear	5.8	Rising	251	7.4	-
		Falling	251	7.3	-
Estimated Linear	6.3	-	250	8.1	-

Table 6.1b Coefficients obtained for the functions fitted in Figure 6.1b

Description	Reference Equation	Field sweep direction	b_2 / 10^{-2}(Rads/Am^{-1})	d_2 / 10^{-4}(Rads/A^2m^{-2})
Three Term quadratic	5.9	Rising	2.9	2.3
		Falling	3.0	0.9
Two Term linear	5.9	Rising	3.3	-
		Falling	3.1	-
Estimated Linear	6.4	-	3.1	-

6.3 Analytical Solution of the Linear Response Model.

The linear system response model was constructed by substituting the linear amplitude and phase response functions into the ideal mixer output equation given in equation 6.1. Only the low frequency mixer output signal was of interest to the operation of the magnetometer. This consisted of terms at the modulation frequency and its

multiples and as a result the much higher frequency signals in the frequency band around twice the shear wave drive frequency could be ignored. The Linear Response Model equation is, therefore, given by equation 6.5.

$$V_{mix} = \frac{\beta a_1}{2}\{1 - b_1|H_0 + h\sin\omega_m t|\}\cos\{\phi_0 + b_2|H_0 + h\sin\omega_m t|\} \qquad 6.5$$

V_{mix}	Mixer output signal.
β	Mixer gain including local oscillator signal amplitude $\beta=kA_1$.
a_1	Zero field amplitude coefficient.
b_1	Normalised linear amplitude response coefficient.
b_2	Linear phase response coefficient.
H_0	Applied bias field, the field to be measured by the system.
h	Modulation field amplitude.
ϕ_0	Total phase change along the transducer referenced to the input wave.
ω_m	Modulation frequency (Radians/s)
t	Time.

This is an oscillatory function with a d.c. term and terms at multiples of the modulation frequency. The function, therefore, can be decomposed into a Fourier series by calculating the Fourier coefficient for the equation. The Fourier series for the system response was most easily constructed by firstly calculating the Fourier series for the function **f(t)** given in equation 6.6. The function **f(t)** is depicted graphically in Figure 6.2 which shows the two separate cases which have to be considered to obtain a full solution for $H_0 \geq 0$. For $H_0 < 0$ the solution resembles the positive applied field solution but with a phase shift of 180°. From consideration of Figure 6.2 it can be seen that the high field solution for $H_0 \geq h$ consists simply of a d.c. Fourier term and a term at the fundamental of the modulation frequency. The low field case of $H_0 < h$ will only be

considered in any detail here as the behaviour of low field signals was of more interest to the operation of the closed loop magnetometer system. Stipulating a low bias field also lends itself to a less involved solution of the Fourier series.

$$f(t) = |H_0 + h \sin \omega_m t| \qquad 6.6$$

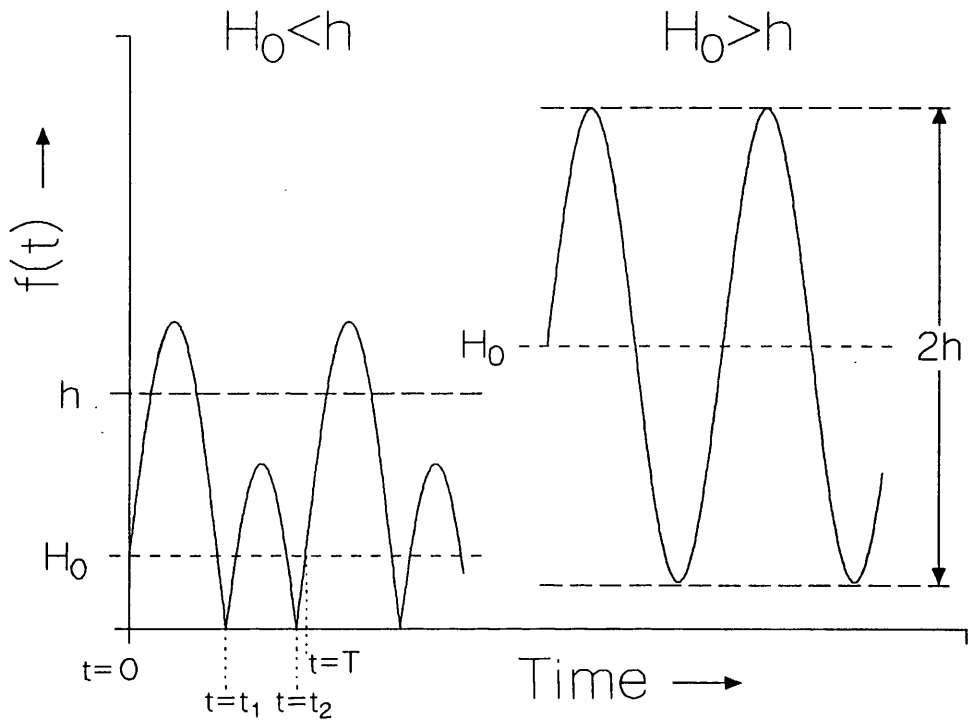

Figure 6.2 Graphical representation of the function **f(t)** for the two important cases to be considered.

For the applied field case of $0 \leq H_0 < h$ the function **f(t)** can be written as two separate equations valid within the limits specified, equation 6.7 and equation 6.8, where **T** is the period of oscillation. The time limits t_1 and t_2 are given by equation 6.9 and equation 6.10 where $x = H_0/h$ the normalised applied field.

$$f'(t) = H_0 + h\sin\omega_m t \qquad (t_2 - T) \le t < t_1 \qquad 6.7$$

$$f''(t) = -(H_0 + h\sin\omega_m t) \qquad t_1 \le t < t_2 \qquad 6.8$$

$$\omega_m t_1 = \pi + \sin^{-1} x \qquad 6.9$$

$$\omega_m t_2 = 2\pi - \sin^{-1} x \qquad 6.10$$

From the functions $f'(t)$ and $f''(t)$ and the limits for t_1 and t_2 the Fourier coefficients for the function $f(t)$ can be calculated by substitution into the Fourier integrals. It was assumed that for the case of most interest that x was small such that $0 \le x \ll 1$ and $\omega_m t_1 = \pi + x$ and $\omega_m t_1 = 2\pi - x$. The linear response coefficients b_1 and b_2 could also be assumed to be small as shown in Table 6.1a and Table 6.1b so that second order terms containing these two coefficients could be ignored. The calculated Fourier coefficients X_n and Y_n for $f(t)$ can, therefore, be shown to be given by equations 6.11, 6.12 and 6.13 for the first three terms i.e. the d.c., fundamental and second harmonic of the modulation frequency. Equation 6.14 shows the Fourier series up to the second harmonic term for the function $f(t)$.

$$\frac{1}{2}X_0 \approx \frac{2h}{\pi} \qquad 6.11$$

$$X_1 = 0 \qquad Y_1 \approx \frac{4hx}{\pi} \qquad 6.12$$

$$X_2 \approx -\frac{4h}{3\pi} \qquad Y_2 = 0 \qquad 6.13$$

$$f(t) = |H_0 + h\sin\omega_m t| \approx \frac{1}{2}X_0 + Y_1\sin\omega_m t + X_2\cos 2\omega_m t + \ldots.$$

$$\approx \frac{2h}{\pi} + \frac{4hx}{\pi}\sin\omega_m t - \frac{4h}{3\pi}\cos 2\omega_m t + \ldots. \qquad 6.14$$

Of paramount interest to the operation of the shear wave magnetometer system was the response to the applied magnetic field of the signal component at the modulation frequency of the mixer output. Also potentially of interest were the signal components at d.c. and the second harmonic of the modulation frequency. The Fourier coefficients for the mixer output response model can be calculated without resorting to further Fourier integrals by the substitution of the Fourier series for **f(t)** into equation 6.5. Retaining the approximations of **x**, $\mathbf{b_1}$ and $\mathbf{b_2}$ being small as in the previous analysis it was only necessary to substitute for the function **f(t)** up to the second harmonic term of the Fourier series as shown in equation 6.14. Substitution of the higher frequency terms of **f(t)** only produced second order small terms in the coefficients of the Fourier series of the mixer output of interest in this analysis. Expansion of the mixer response equation and the dropping of second order small terms yields the Fourier coefficients $\mathbf{X_n}$ and $\mathbf{Y_n}$ for the mixer output signal given in equation 6.15, 6.16 and 6.17. The resultant mixer output function is given by the substitution of these coefficients into equation 6.18.

$$\frac{X_0}{2} = \beta a_1 \cos\left(\phi_0 + \frac{2hb_2}{\pi}\right)\left[\frac{1}{2} - \frac{hb_1}{\pi}\right] \qquad 6.15$$

$$Y_1 = -\beta a_1 \frac{2hx}{\pi}\left[b_1 \cos\left(\phi_0 + \frac{2hb_2}{\pi}\right) + b_2 \sin\left(\phi_0 + \frac{2hb_2}{\pi}\right)\right] \qquad 6.16$$

$$X_2 = \beta a_1 \frac{2h}{3\pi}\left[b_1 \cos\left(\phi_0 + \frac{2hb_2}{\pi}\right) + b_2 \sin\left(\phi_0 + \frac{2hb_2}{\pi}\right)\right] \qquad 6.17$$

$$(X_1 = Y_2 = 0)$$

$$V_{mix} \approx \frac{X_0}{2} + Y_1 \sin \omega_m t + X_2 \cos 2\omega_m t + \ldots. \qquad 6.18$$

The response of the signal at the modulation frequency obtained from the analysis of the system response equation can be seen to be directly proportional to the applied magnetic bias field $\mathbf{H_0}$ through the normalised field variable **x**. The d.c. output of the mixer and the amplitude of the signal at the second harmonic of the modulation frequency are independent of the applied magnetic field within the bounds of the low field constraint. The sensitivity of the magnetometer system depends on the sharpness of slope of the output signal of the mixer to the applied bias field to be measured. The greater this slope the larger the mixer output signal changes for a given applied field. The magnitude of the bias field response of equation 6.16 depends on the mixer gain β, the received shear wave amplitude $\mathbf{a_1}$ and both the linear response coefficients for the amplitude and phase responses $\mathbf{b_1}$ and $\mathbf{b_2}$ respectively as well as the total phase change of the shear waves along the transducer ϕ_0. The magnitude of the response was not directly affected by the magnitude of the modulation field amplitude **h** because of the definition of **x**. This does, however, effect the optimum value of the phase change ϕ_0 which has to be tuned to optimise the separate affects of $\mathbf{b_1}$ and $\mathbf{b_2}$. The optimum phase shift for ϕ_0 can be found by differentiating equation 6.16 with respects to ϕ_0 such that $(1/x)(dY_1/d\phi_0) = 0$. This returns the relation for the optimum phase change in radians and is given in equation 6.19. The optimum phase is repeated at multiples of 180°.

$$\phi_{0_{opt}} = \tan^{-1}\left(\frac{b_2}{b_1}\right) - \frac{2hb_2}{\pi} \qquad 6.19$$

The tuning of the phase change ϕ_0 can also be employed to null either the d.c. signal term or the second harmonic term. The d.c. term can be made zero by tuning ϕ_0 to the condition shown in equation 6.20. This also has the effect of removing the dependence of the fundamental response on the linear amplitude response $\mathbf{b_1}$ and maximising the effect of the phase response $\mathbf{b_2}$. Conversely an additional phase shift 90° maximises the

effect of the amplitude response and removes the phase response dependence on the fundamental signal response. In both cases, however, the response would be less than the optimum response. The condition for a zero second harmonic signal is given by equation 6.21 and is repeated at multiples of 180°.

$$\phi_{0_{phase}} = (2n+1)\frac{\pi}{2} - \frac{2hb_2}{\pi} \qquad n = 0, 1, 2, .. \qquad 6.20$$

$$\phi_{0_{amp}} = -\tan^{-1}\left(\frac{b_1}{b_2}\right) - \frac{2hb_2}{\pi} \qquad 6.21$$

6.4 Numerical Solution of the Linear Response Model

The linear response model was also solved numerically as an alternative to the analytical solution. A numerical solution had the advantage over the analytical in that no small order approximations were necessary for the response coefficient and the applied bias magnetic field. In this respects the solution was more exact apart from potential calculation errors in the implementation of the solution. The numerical analysis was based on the summation form of the Fourier integrals with the summation series for the $\mathbf{n^{th}}$ Fourier coefficient $\mathbf{X_n}$ and $\mathbf{Y_n}$ for the function **F(t)** being given by equation 6.22 and equation 6.23 respectively.

$$X_n = \frac{2}{N}\sum_{t_i=\frac{T}{N}}^{T} F(t_i)\cos\left(\frac{2\pi n}{T}t_i\right) \qquad 6.22$$

$$Y_n = \frac{2}{N}\sum_{t_i=\frac{T}{N}}^{T} F(t_i)\sin\left(\frac{2\pi n}{T}t_i\right) \qquad 6.23$$

T is the oscillation period of the waveform and **N** the number of divisions over which the single period was summed. The function **F(t)** in the analysis was the full

linear response function for the signal at the mixer output given in equation 6.5. The calculation of the coefficients was accomplished within computer code written to allow an analysis of the magnitude of the coefficients as a function of any of the parameters contained within the model.

The numerical accuracy of the result was obviously a trade off between calculation time and a large enough value of the period division **N** such that the summation approached the limit of the Fourier integral. The optimum value for the number of divisions was investigated by comparing the normalised amplitude of the second harmonic coefficient of the analysis for increasing **N**. The amplitude was normalised against the coefficient's amplitude for large **N**, i.e. approaching the limit of the integral. The parameters employed for this study were within the physically meaningful limits of the ensuing investigations to be undertaken. The coefficients for the linear response model were those given in Table 6.1a and Table 6.1b and an applied bias field of $\mathbf{H_0=2Am^{-1}}$ and a modulation amplitude of $\mathbf{h\approx 4Am^{-1}}$. The mixer gain β was taken from the measured value obtained for the mixer component in chapter 7 and the phase change along the ribbon ϕ_0 as the value which returned a zero d.c. signal term from the model for no applied magnetic field. Figure 6.3 shows the normalised second harmonic term against the number of summation divisions per period. The figure clearly shows that the desired result was rapidly achieved for **N** approaching fifty. An acceptable process time could be achieved, however, with **N=500** and for this reason was carried through throughout the investigations giving an increased confidence in the result.

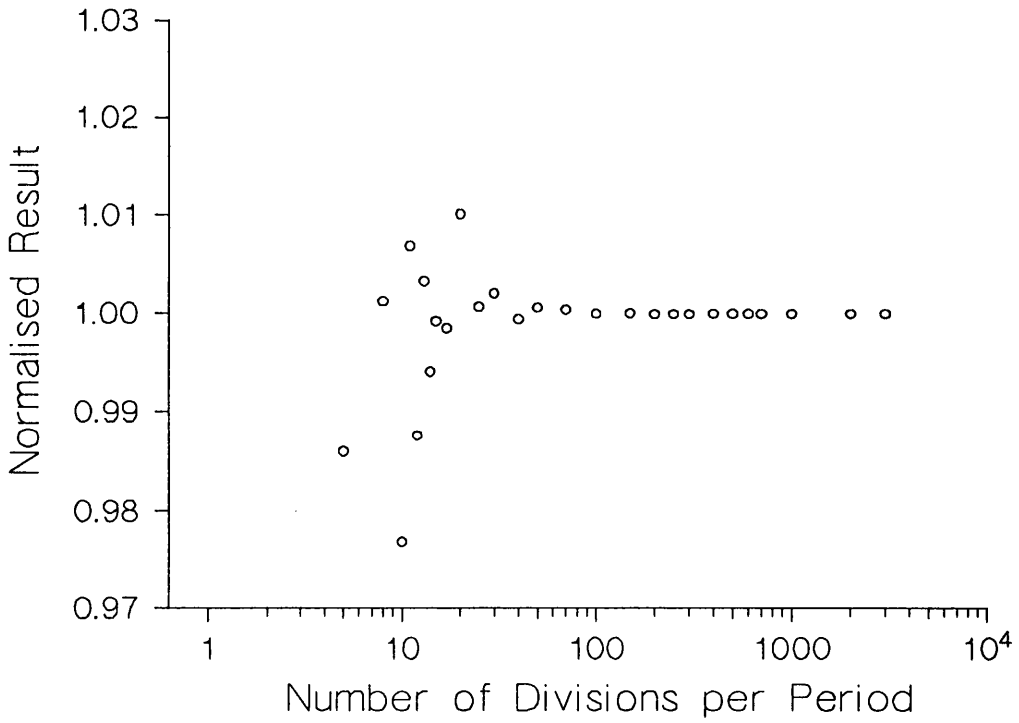

Figure 6.3 Amplitude of the second harmonic term normalised against the value of the term for large **N** plotted against the number of divisions per period **N**.

6.5 Investigation of the Magnetometer System Response.

The response to the applied magnetic bias field was studied experimentally for the two "as-received" transducers MT1 and MT2 characterised in chapter 5. The general arrangement used for studying the amplitude of the harmonic terms of immediate interest to the operation of the magnetometer was an extension of the system described in Figure 5.12 and was essentially the shear wave magnetometer system introduced in chapter 1 but in the open loop mode of operation as shown in Figure 6.4.

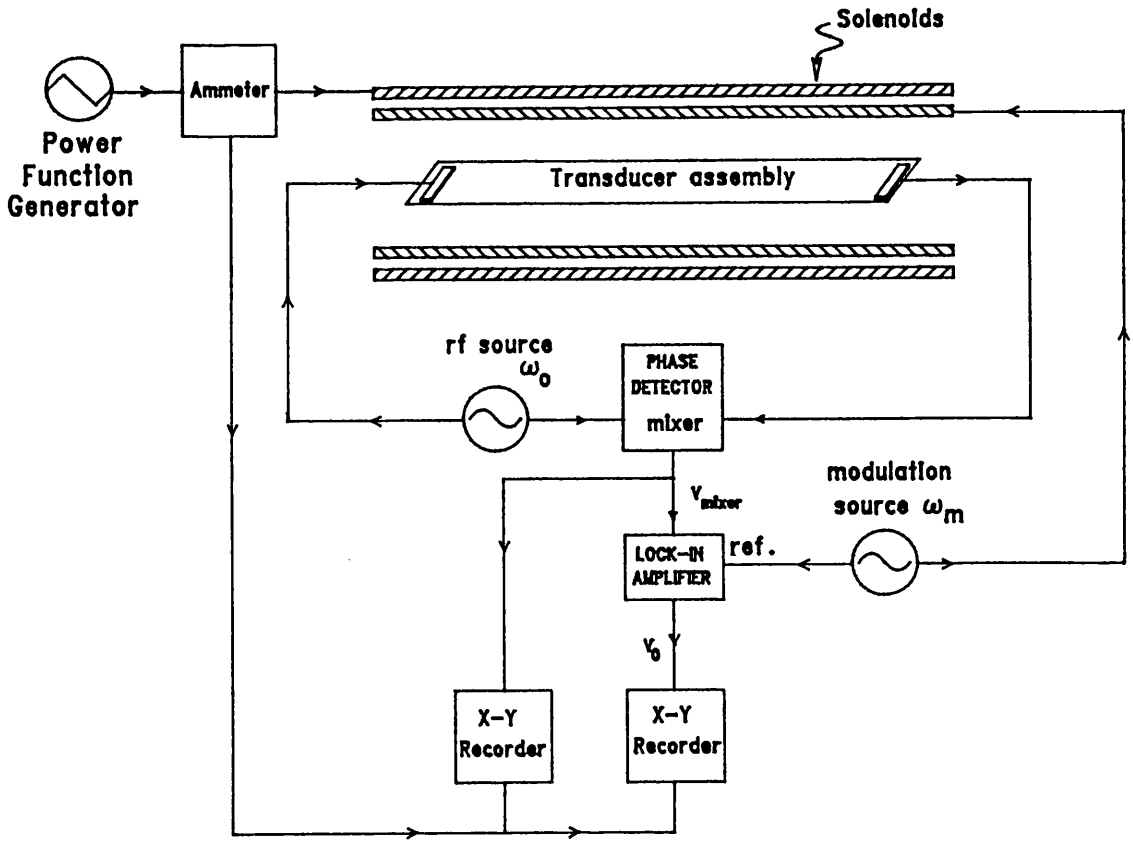

Figure 6.4 Magnetometer system response characterisation system.

A second solenoid coil with 910 turns/m was added to the arrangement of Figure 5.12 in order to apply a modulation field to the magnetic transducer arrangement. The solenoid was driven using a Philips PM5190 LF Synthesizer and the RMS modulation current measured by a Philips PM2517E multimeter which had a measurement bandwidth well within the modulation frequency range to be studied. The amplitude of the modulation field was estimated from equation 6.24, where i_m was the measured RMS solenoid current in millamperes.

$$h \approx nI \approx 0.91\sqrt{2}\, i_m \qquad 6.24$$

The output of the magnetic transducer was connected to the mixer element along with a reference signal from the shear wave drive oscillator. The mixer element employed was a Mini-Circuits SRA-3 Schottky diode double balanced mixer with a gain as defined previously of $\beta = 0.65$. The mixer in terms of device performance is considered in greater detail in chapter 7. The d.c. signal output of the mixer over a range of applied fields was recorded using a Philips PM8143 X-Y recorder. The amplitude of the signal components at the modulation frequency and its second harmonic were measured using a Stanford Research SR510 Lock-in Amplifier which was referenced to either the modulation frequency or its second harmonic using an internal frequency doubler. The output of the Lock-in amplifier was recorded as a function of applied magnetic field on a Philips X-Y recorder. The optimum setting for the reference phase was found by nulling the Lock-in amplifier output signal for a given applied d.c. field followed by a phase shift of 90° to maximise the output. The applied magnetic field was generated as in chapter 5 with a slow enough sweep rate so that the rate of change of the recorded signal was not limited by the time constants of the measurement instrumentation.

6.5.1 Comparison of the Measured and the Calculated System Response

The magnetometer system response for an applied field range of -20 to 20Am^{-1} was measured for the magnetic transducers MT1 and MT2. Both transducers were observed to behave similarly as would be expected. The measurements were carried out for a modulation current $\mathbf{i_m}$**=3mA** and the total phase change set through fine tuning of the frequency of the shear wave drive oscillator such that the d.c. mixer output signal was approximately zero for no applied field. Figures 6.5a, b & c show the measured d.c., fundamental and second harmonic signals against applied field for the magnetic transducer MT1. These are compared with the harmonic terms calculated from the numerical solution of the linear response model. All the model results are shown as

discreet points joined with straight lines for clarity whereas, the measured results are shown as continuous traces. The parameters used in the model were those stated previously for the estimated linear fits to the amplitude and phase responses of the transducer, $\mathbf{a_1=250mV}$, $\mathbf{b_1=8.1x10^{-3}A^{-1}m}$ and $\mathbf{b_2=3.1x10^{-2}Rads/Am^{-1}}$. The modulation amplitude was calculated internally within the software from an entered modulation current using equation 6.24 and was the same as that for the measured response of $\mathbf{i_m=3mA}$. The total phase change ϕ_0 was selected to match the condition for the measured response of zero d.c. output for no applied field. The value for ϕ_0 was obtained from the response model by plotting the amplitude of the d.c. term against ϕ_0 for zero applied field and noting the value of the phase at the zero crossing point, $\phi_0=\mathbf{1.495}$. This value for ϕ_0 also agrees with that calculated from equation 6.20 which is identical to three decimal places.

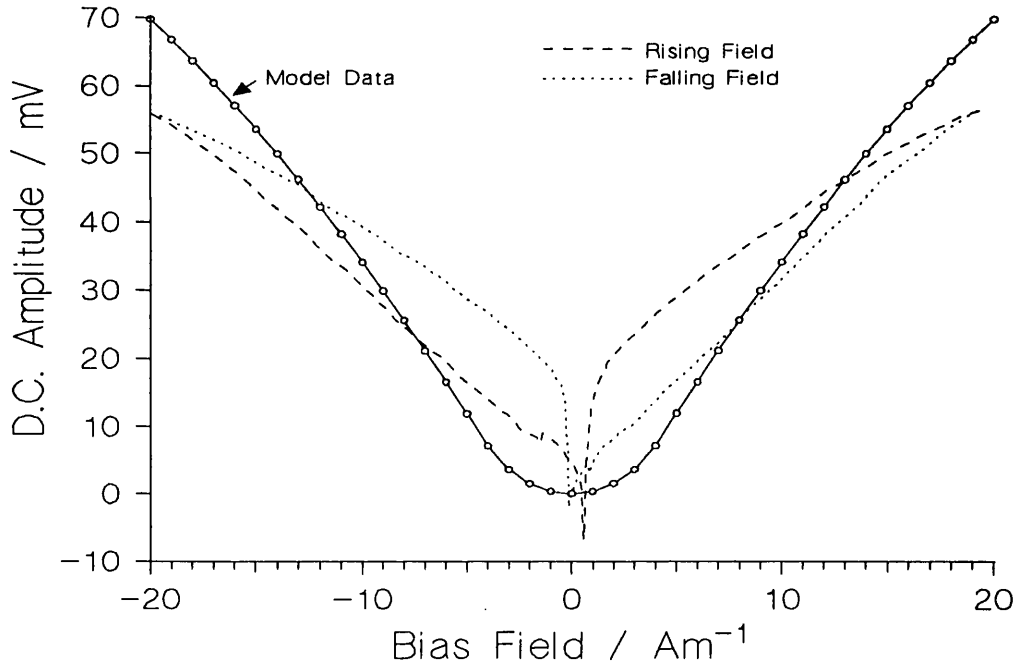

Figure 6.5a Comparison of the measured and the calculated d.c. response.

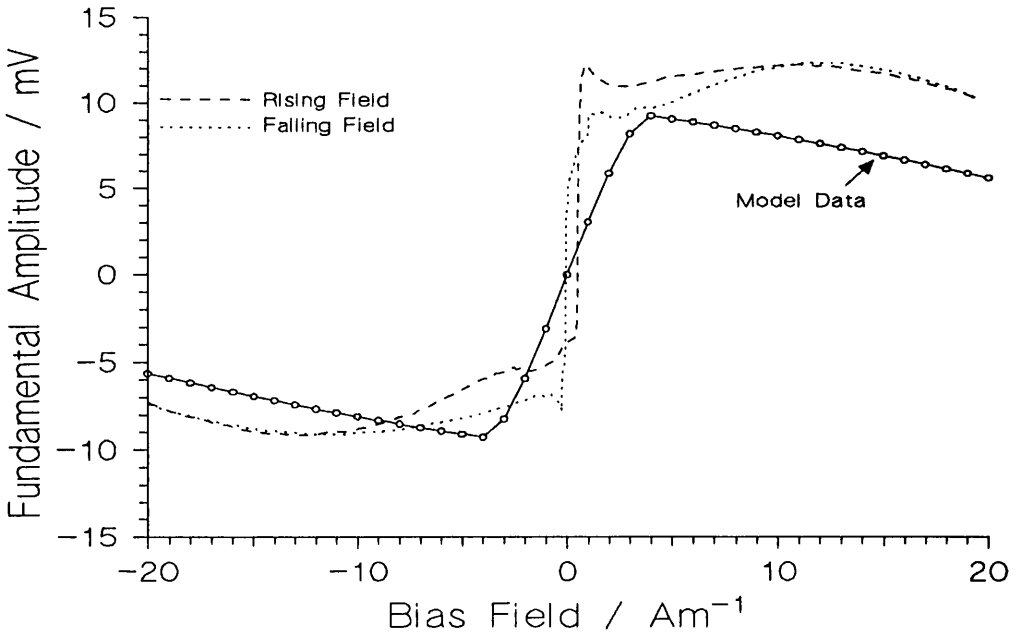

Figure 6.5b Comparison of the measured and the calculated fundamental response.

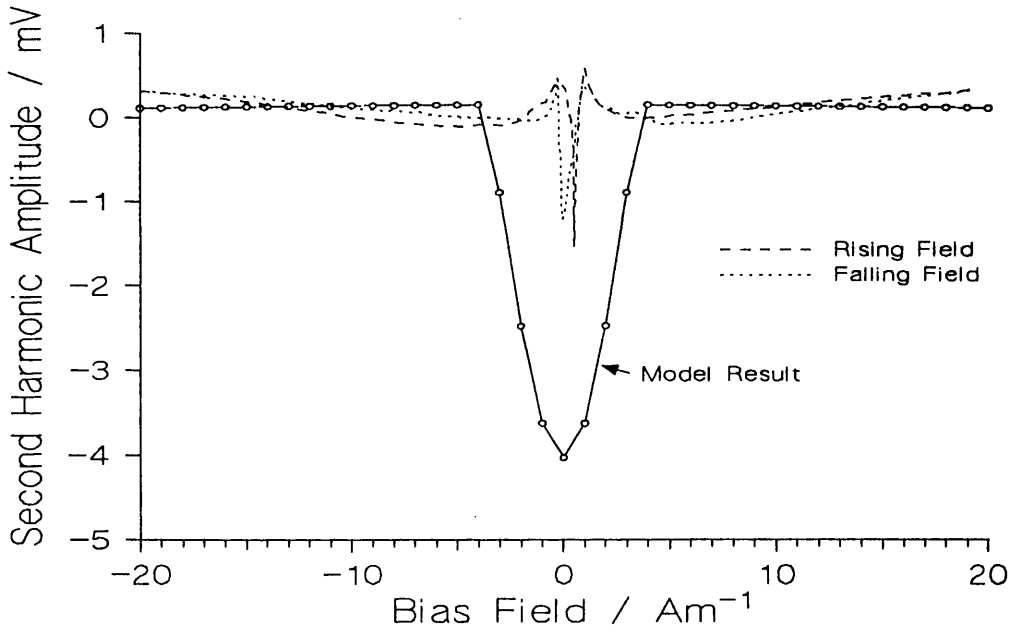

Figure 6.5c Comparison of the measured and the calculated second harmonic response.

6.5.2 Effect of the Phase ϕ_0 on the System Response.

Using the values for the model coefficients stated in chapter 6.5.1 the three harmonic responses were calculated over a field range -20 to 20 Am^{-1} for a range of the fixed phase change ϕ_0. The results were calculated at fixed increments of the phase change starting at a phase for which the d.c. component was zero for no applied field. A total range of 2πradians was encompassed. The results are shown in Figures 6.6a, b & c for the d.c., fundamental and second harmonic terms respectively. The d.c. response can be seen to have two zero points for no applied field as predicted by equation 6.20. Figure 6.6b shows that for these two phases the responses are equivalent but reflected in the x-axis. Also the optimum response does not occur at either of these phases. For the response coefficients used, however, the response was approaching the optimum at these phases suggesting a major contribution to the overall response from the phase response term $\mathbf{b_2}$. Figure 6.6c demonstrates that the second harmonic term approaches a maximum for small fields at the optimum response phase $\phi_{0_{opt}}$ as suggested by equation 6.17. The second column of phases for both the as plotted and the reflected in the x-axis gave values of the second harmonic amplitude with field only marginally different from the phases in the first column and for this reason were not plotted for clarity. They were not, however, identical and the difference only became noticeable for the low amplitude second harmonic term and is reflected in the absence of a second column phase for this case.

For low applied fields about the zero field origin all three terms appear to follow the applied field responses predicted by the analytical model in equations 6.15, 6.16 & 6.17.

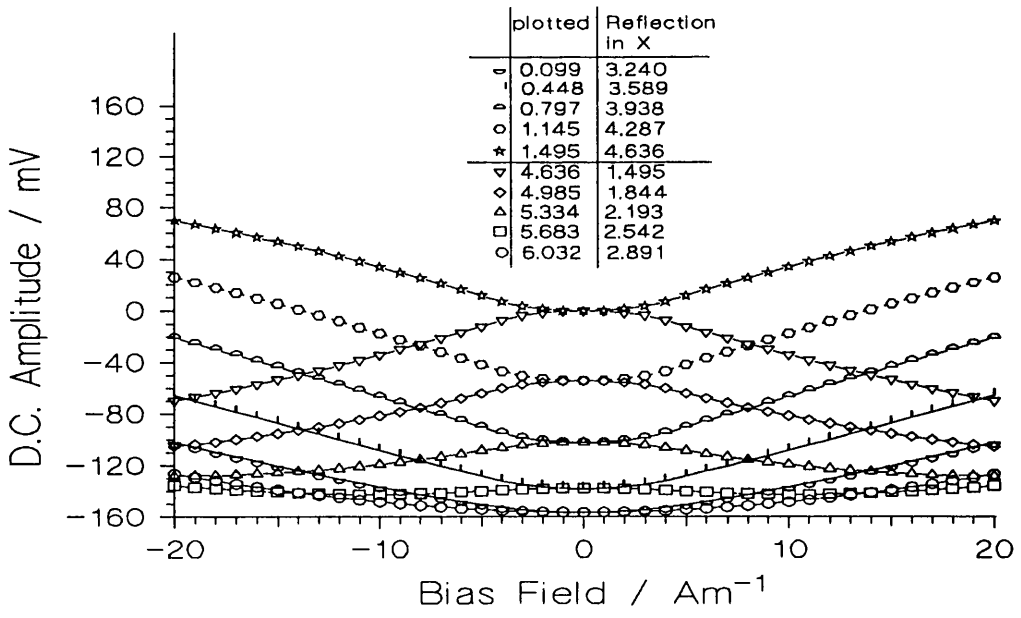

Figure 6.6a The d.c. signal response as a function of bias field with ϕ_0 as a parameter.

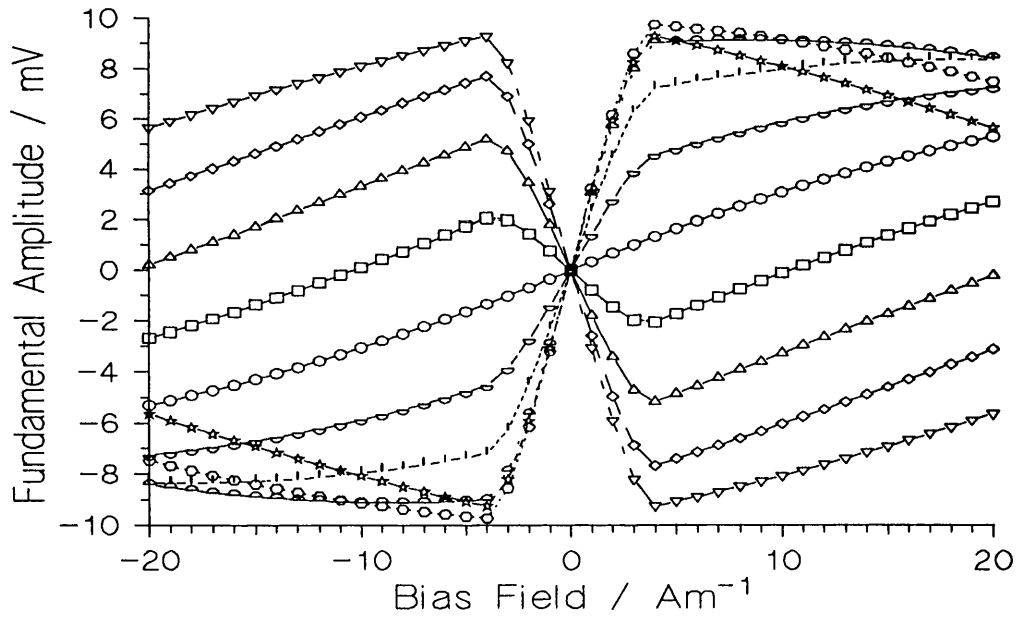

Figure 6.6b The fundamental signal response as a function of bias field with ϕ_0 as a parameter.
(Key for phase change same as Figure 6.6a.)

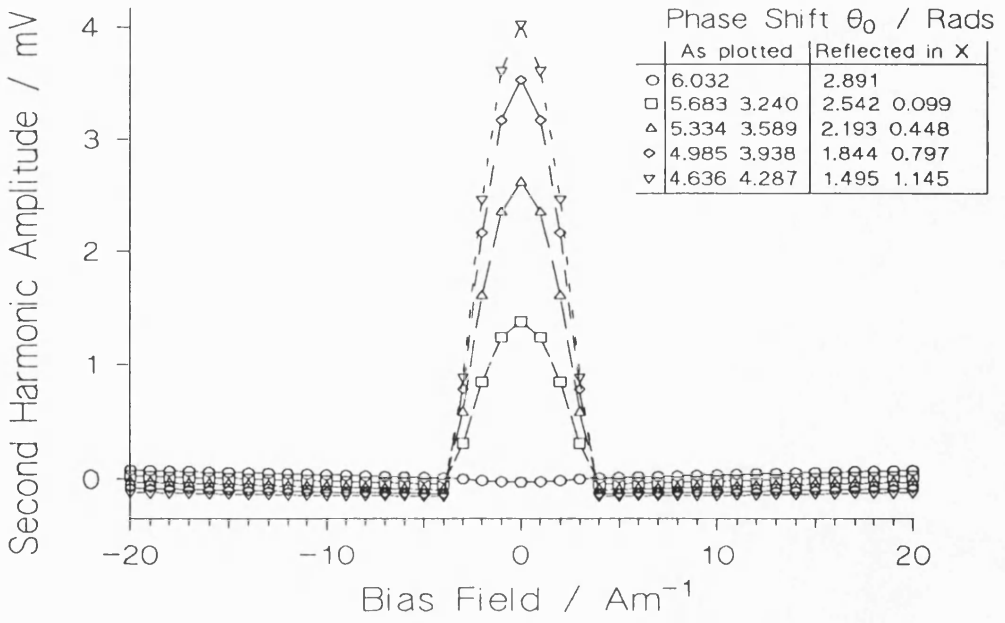

Figure 6.6c The second harmonic signal response as a function of bias field with ϕ_0 as a parameter.

6.5.3 Effect of the Modulation Amplitude on the System Response.

The effect of varying the modulation amplitude was studied in terms of varying the modulation current. The model response parameters used were those given in chapter 6.5.1. The responses were examined for the phase ϕ_0 such that the d.c. term was always zero for no applied field no matter what the modulation amplitude. A different phase, therefore, had to be employed for each modulation amplitude interval. The results are shown in Figures 6.7a, b & c for the d.c., fundamental and second harmonic terms respectively. Figure 6.7a demonstrates a decrease in the amplitude of the d.c. term at any given applied field for an increasing modulation amplitude as would be expected from equation 6.15. In the analytical solution of the linear response model it was stated that a change in character of the harmonic response should be observed when $\mathbf{H_0}$=**h**. This can be seen as a modulation amplitude dependent change in the response curves

shown in Figures 6.7b & c. As expected from equation 6.16 the actual slope of the response curve immediately about the field origin was independent of the modulation amplitude.

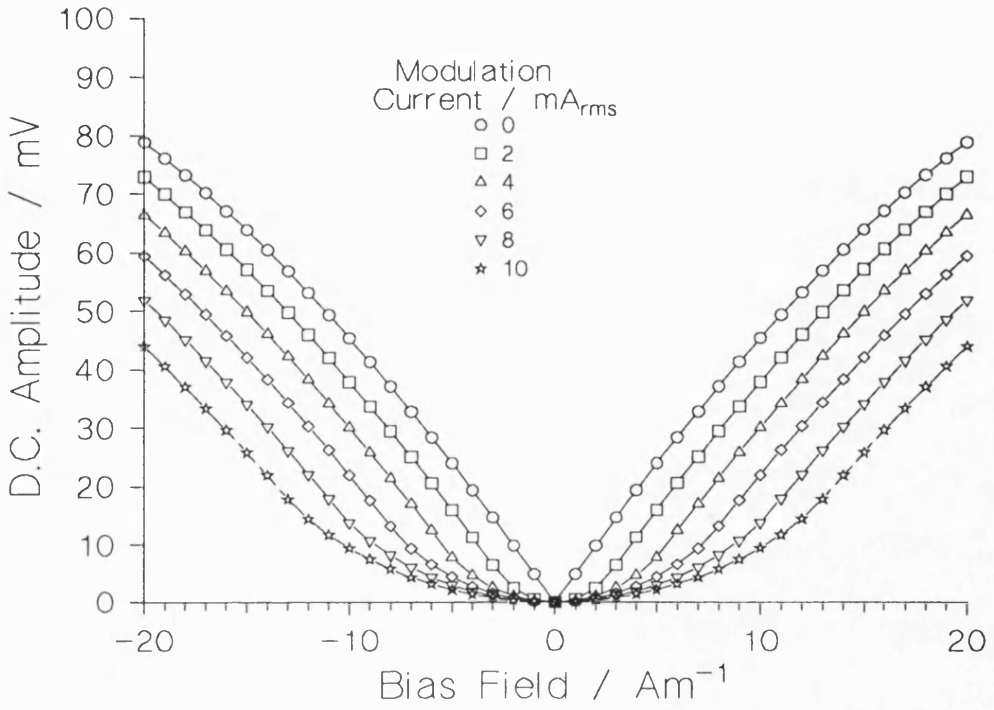

Figure 6.7a The d.c. signal response as a function of bias field with $\mathbf{i}_m$ as a parameter.

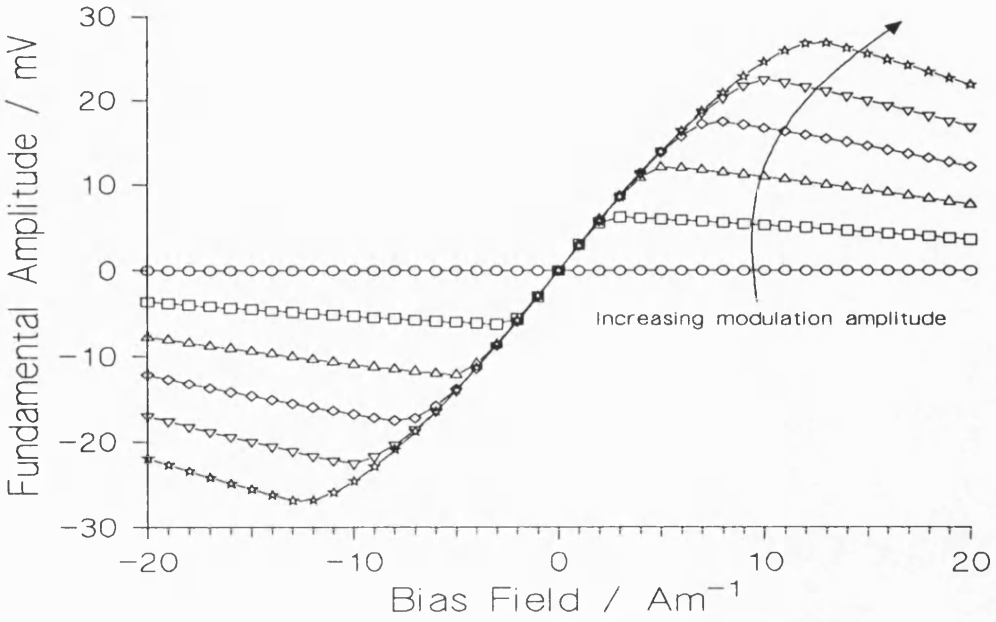

Figure 6.7b The fundamental signal response with $\mathbf{i}_m$ as a parameter.
(Key for modulation amplitude same as Figure 6.7a.)

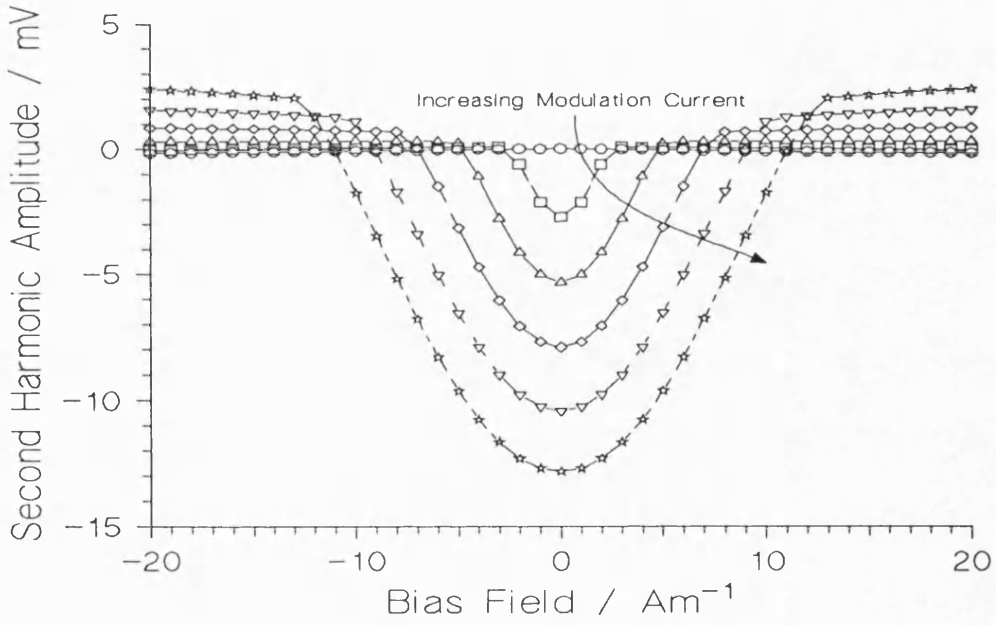

Figure 6.7c The second harmonic signal response with $\mathbf{i}_m$ as a parameter.
(Key for modulation amplitude same as Figure 6.7a.)

6.5.4 Effect of the Linear Response Coefficients on the System Response.

The effect on the harmonic amplitudes of the mixer output signal for a range of both the linear amplitude response coefficient and the linear phase response coefficient was studied encompassing the values measured for the two magnetic transducers in chapter 6.2. Each response was studied separately with the value of the other response coefficient set to the measured value. Apart from the total phase change the remaining model parameters were those given in chapter 6.5.1. As with the previous investigations the phase ϕ_0 was chosen such that the d.c. signal term was zero for no applied field for all the response coefficients investigated. Figures 6.8a, b & c and Figures 6.9a, b & c show the responses to an applied magnetic field on varying the amplitude response coefficient $\mathbf{b_1}$ and the phase response coefficient $\mathbf{b_2}$ for the d.c., fundamental and second harmonic terms respectively. According to the analytical solution of equation 6.16 with ϕ_0 set to the condition given in equation 6.20 there should be no change in the response on varying the amplitude response coefficient $\mathbf{b_1}$. Figure 6.8b, however shows a decrease in the slope of the system response about the zero field origin on increasing $\mathbf{b_1}$ suggesting a significant second order term missing from equation 6.16. This was also reinforced by the second harmonic dependence shown in Figure 6.8c. Increasing the phase response coefficient $\mathbf{b_2}$ for the given d.c. phase condition greatly enhances the magnitude of the fundamental response curve about the field origin as shown in Figure 6.9b. The second harmonic amplitude term was also seen to increase in amplitude both affect being expected from equations 6.16 & 6.17. It would be expected from these result that the converse would also be true for the d.c. phase set such that the amplitude response was optimised.

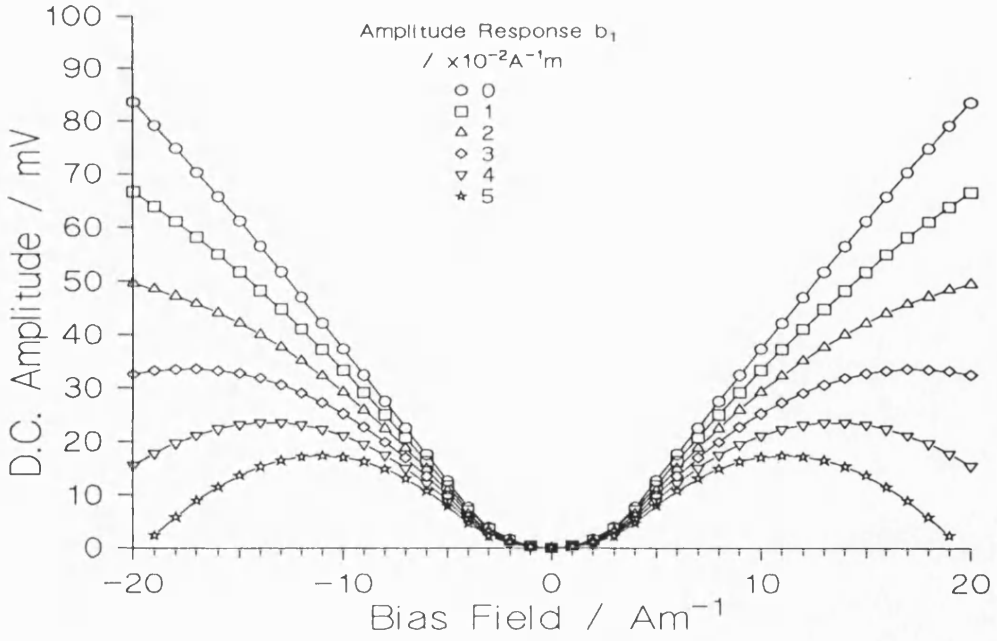

Figure 6.8a The d.c. signal response with $\mathbf{b_1}$ as a parameter.

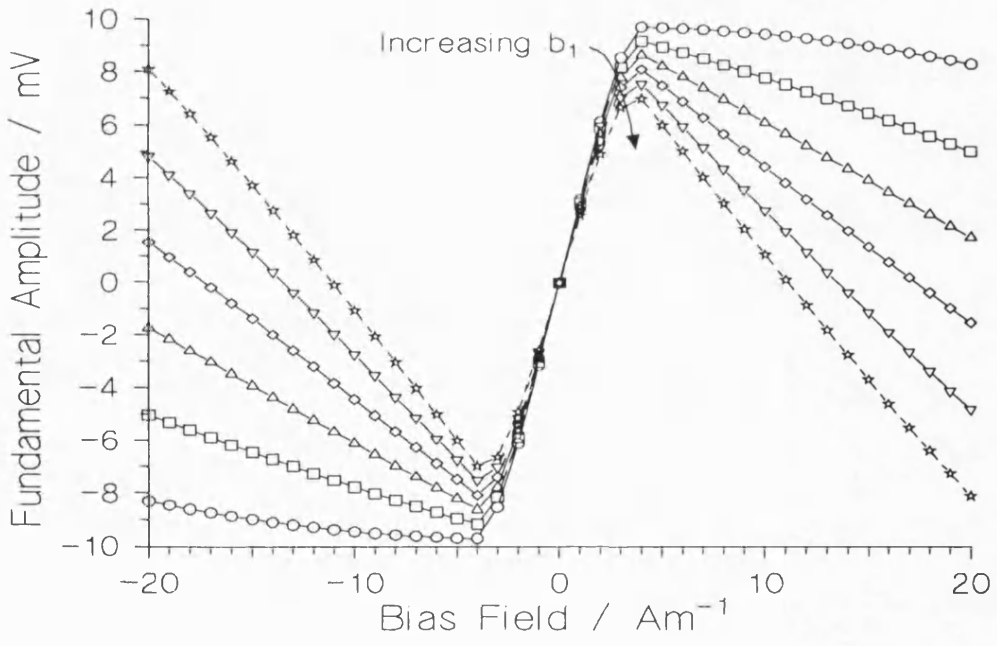

Figure 6.8b The fundamental signal with $\mathbf{b_1}$ as a parameter.
(Key for amplitude response same as in Figure 6.8a.)

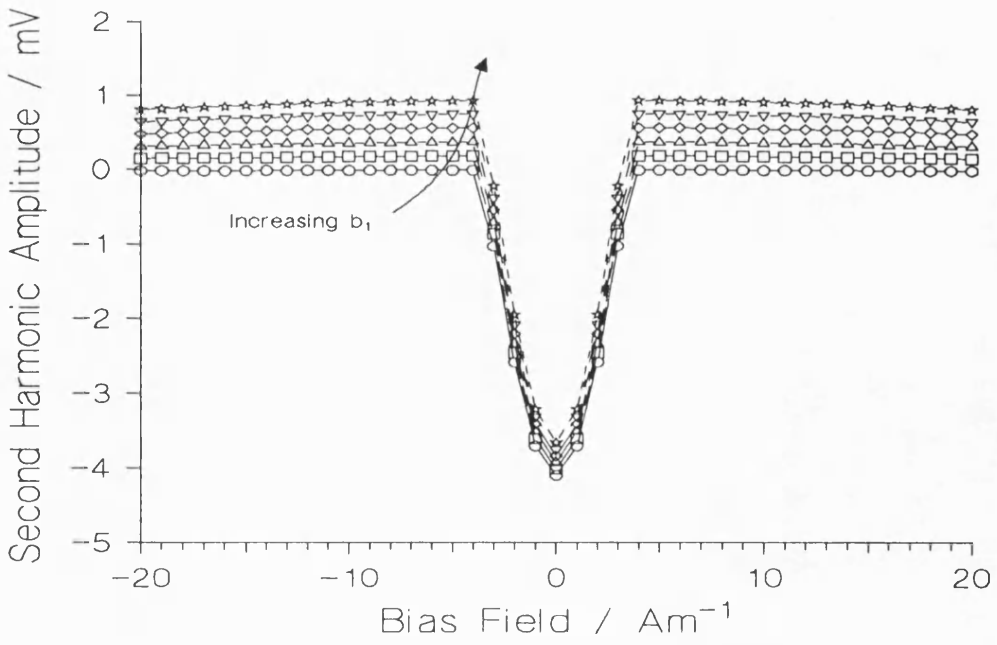

Figure 6.8c The second harmonic signal response with $\mathbf{b_1}$ as a parameter. (Key for amplitude response same as in Figure 6.8a.)

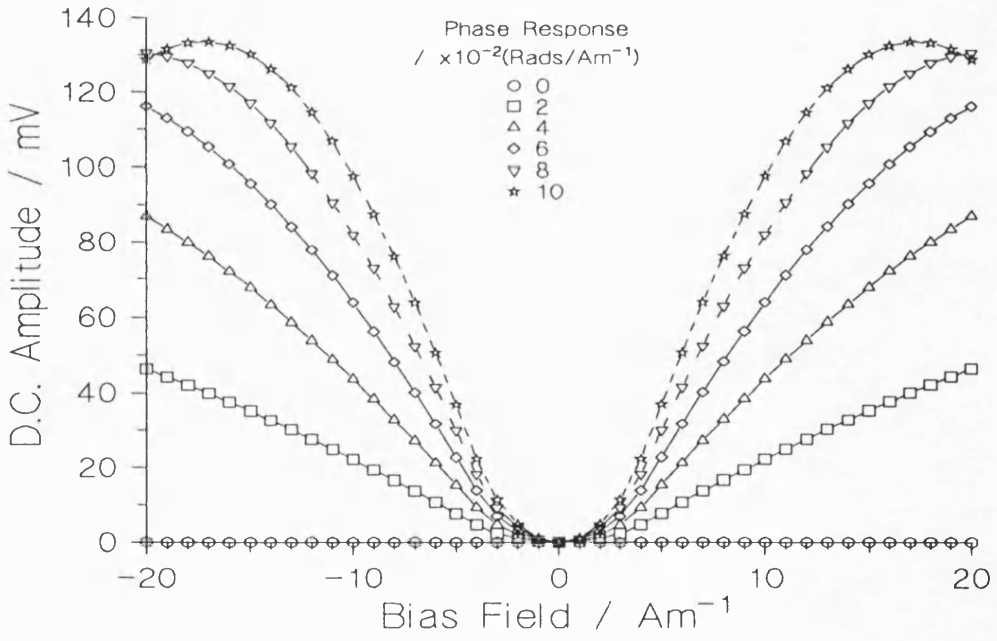

Figure 6.9a The d.c. signal response with $\mathbf{b_2}$ as a parameter.

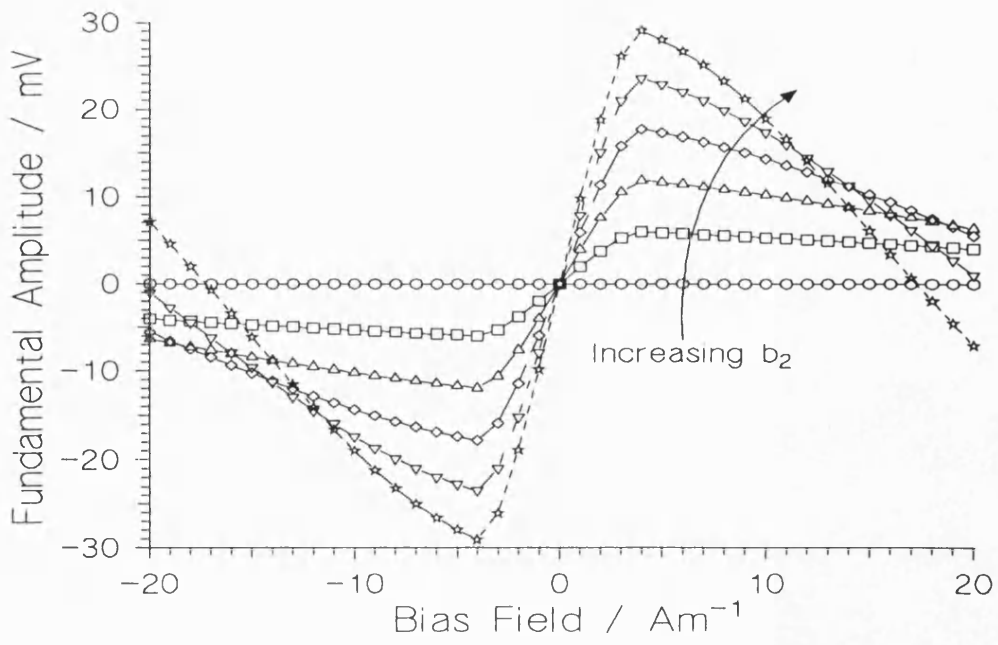

Figure 6.9b The fundamental signal response with $\mathbf{b_2}$ as a parameter. (Key for phase response same as in Figure 6.9a.)

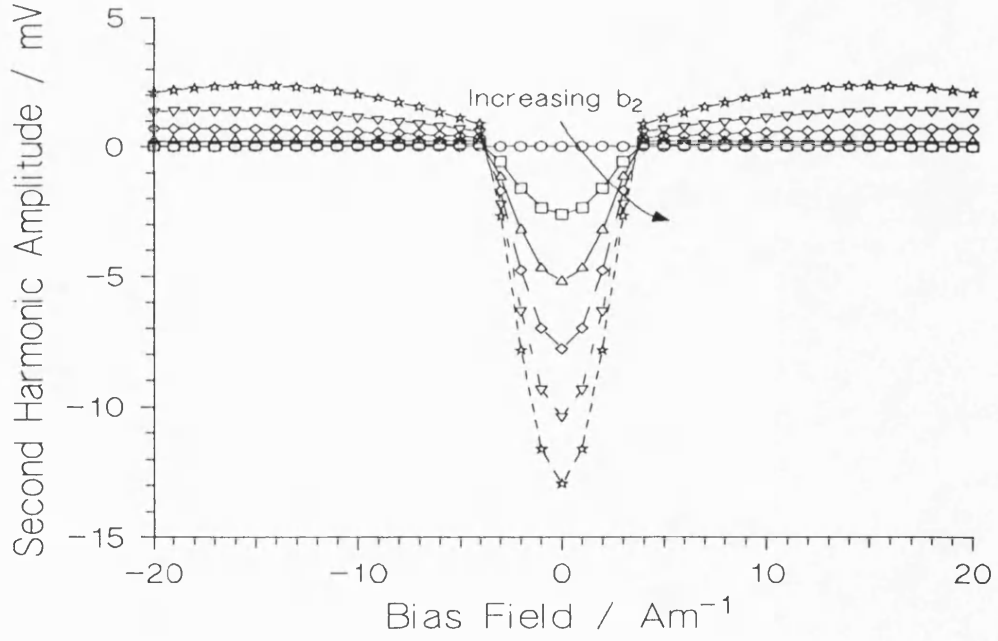

Figure 6.9c The second harmonic signal response with $\mathbf{b_2}$ as a parameter. (Key for phase response same as in Figure 6.9a.)

The effect of the magnitudes of the amplitude and phase responses on the system response can best be summarised by plotting the slope of the fundamental harmonic term about the applied field origin as a function of either of the response. These are shown in Figures 6.10a & b which show the fundamental response slope as a function of the amplitude response and the phase response respectively. The response slopes were calculated from a linear fit to the fundamental signal magnetic field response for the three point about the zero field origin. The figures demonstrate the trend for a decrease in the system response for an increase in the amplitude response coefficient $\mathbf{b}_1$ for a fixed phase response at the zero d.c. for no applied field condition. The zero d.c. phase over the range investigated for the two coefficients is shown in Figure 6.11. As predicted by equation 6.20 the d.c. zero phase was essentially independent of $\mathbf{b}_1$ apart from high values of both $\mathbf{b}_1$ and $\mathbf{b}_2$ where the second order terms become significant.

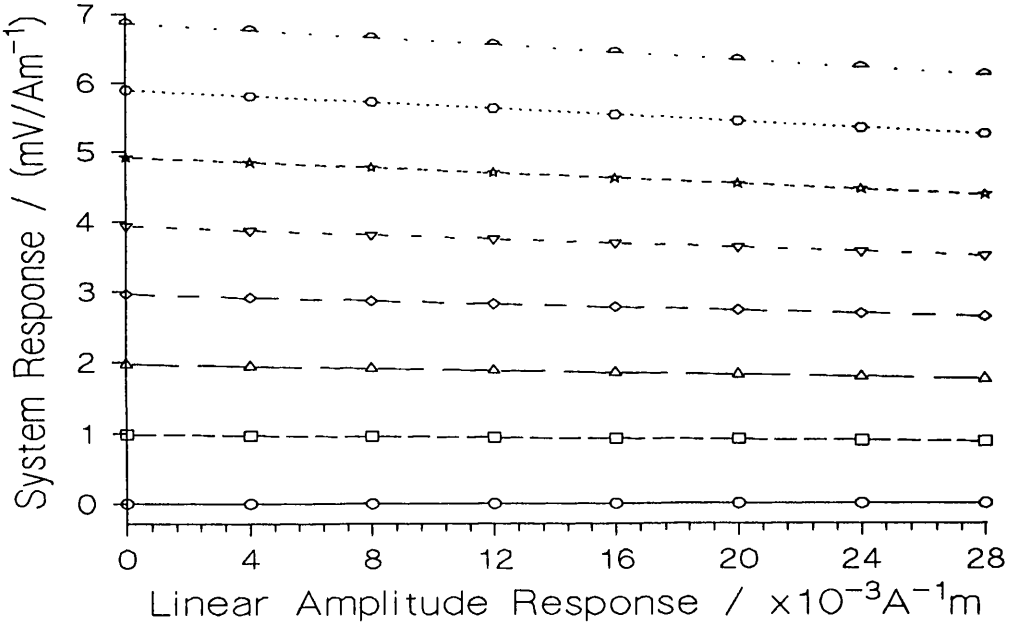

Figure 6.10a The system response plotted as a function of the amplitude response and the phase response.
(Key for phase response same as Figure 6.9a.)

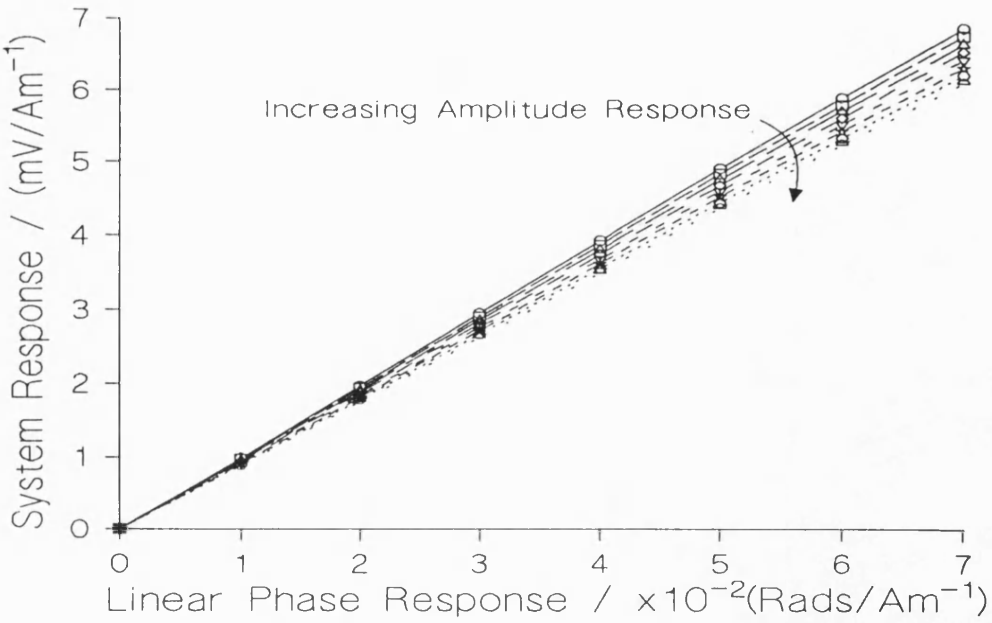

Figure 6.10b The system response plotted as a function of the phase response and the amplitude response.
(Key for amplitude response same as Figure 6.8a.)

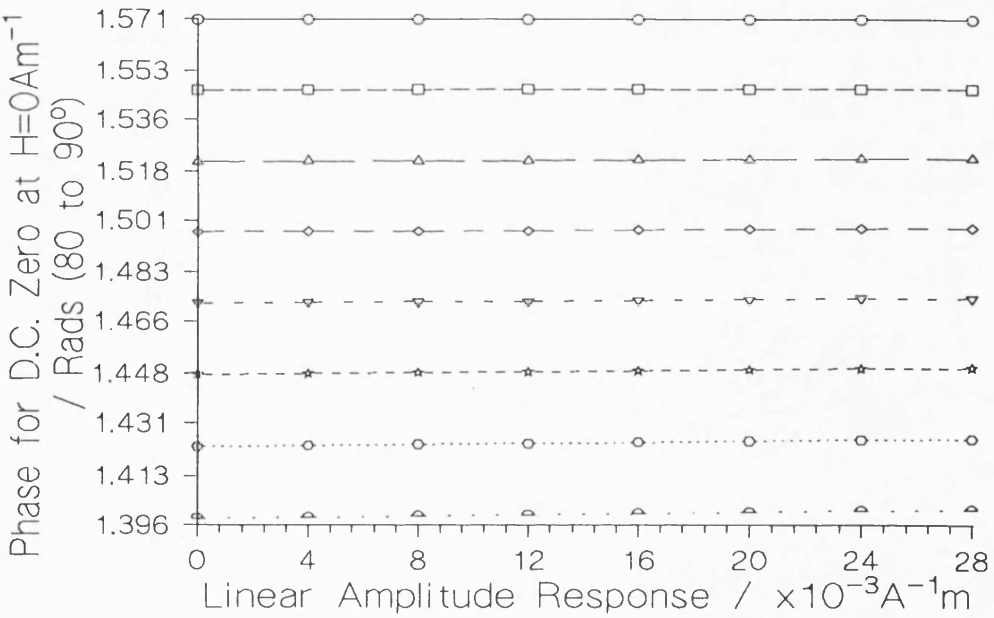

Figure 6.11 The zero d.c. term phase condition for the matrix of $\mathbf{b}_1$ and $\mathbf{b}_2$.
(Key for phase response same as Figure 6.9a.)

6.5.5 Optimum System Response as a Function of the Linear Responses.

The maximum slope of the fundamental signal response to magnetic field was obtained from an investigation of the slope of fundamental response as a function of the d.c. phase ϕ_0. The slope of the response was calculated as in chapter 6.5.4. Figures 6.12a & b show the fundamental system response slopes as a function of the matrix of the response coefficients investigated. The figures show that, unless the amplitude response can be increased considerably, increasing the phase response has the greatest overall effect on the total system response. Figure 6.12a also demonstrates that for a large phase response coefficient $\mathbf{b}_2$, increasing $\mathbf{b}_1$ has little overall effect on the optimum response. Figure 6.12c shows the response slope obtained from the analytical solution of the model for the matrix of response coefficients, equation 6.16. For the lower values of the coefficients $\mathbf{b}_1$ and $\mathbf{b}_2$ studied the analytical model agreed closely with the results for the numerical model. The solution does, however, breaks down for the higher values reflecting the increased importance of the second order terms.

Figure 6.13 shows the phase $\phi_{0_{opt}}$ at which the optimum response was achieved. The plotted points were the values used to obtain the optimum responses plotted in Figures 6.12a & b. The fitted curves are for the function given in equation 6.19 for the parameters employed in the study. Within the margin of error of the optimum phase there was very good agreement between the analytical and the numerical solution. The large errors comes about from the size of the phase increment used in the study. This does not produce large errors in the optimum response as it was fairly insensitive to phase changes of this order.

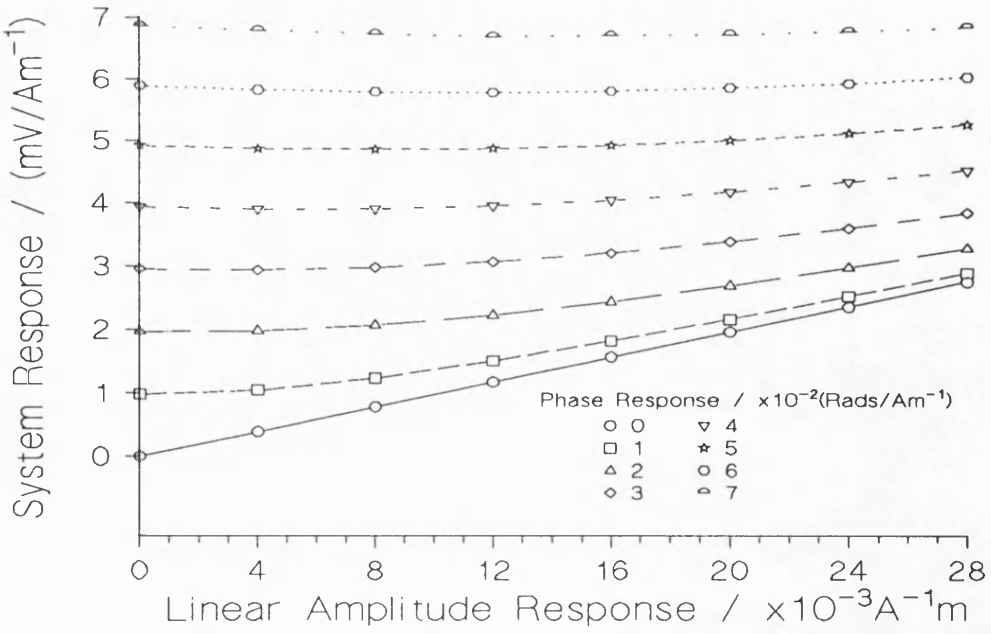

Figure 6.12a The optimum system response as a function of $\mathbf{b}_1$ and with $\mathbf{b}_2$ as a parameter.

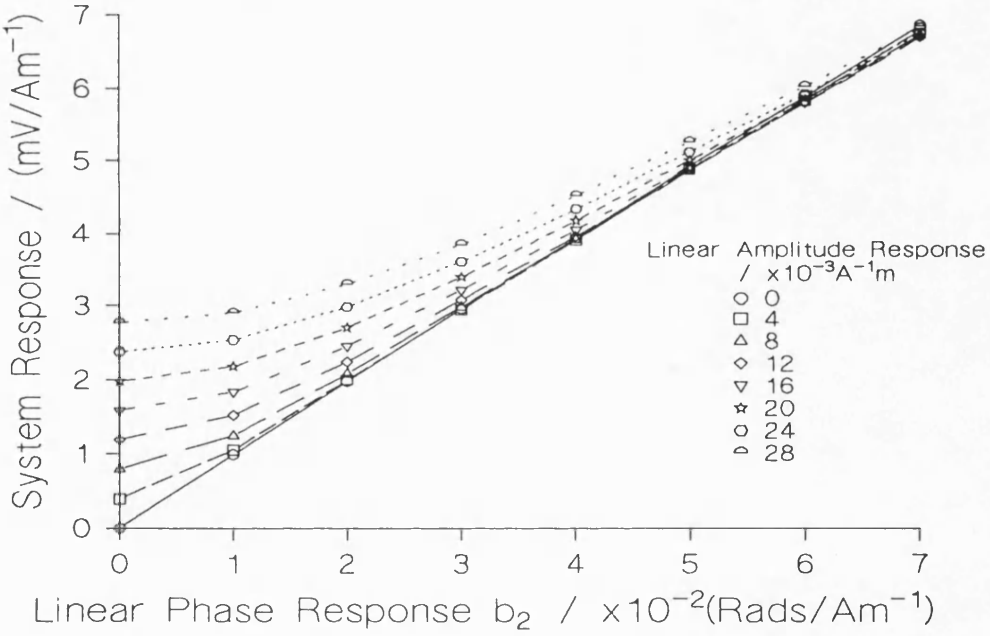

Figure 6.12b The optimum system response as a function of $\mathbf{b}_2$ and with $\mathbf{b}_1$ as a parameter.

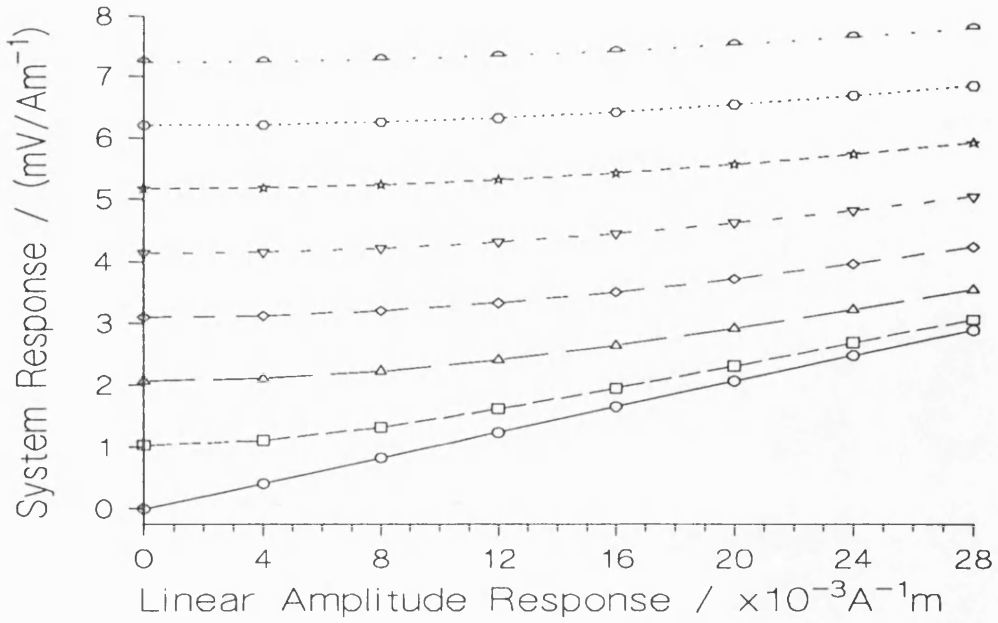

Figure 6.12c The optimum system response predicted from the analytical solution.
(Key for phase response same as Figure 6.12a.)

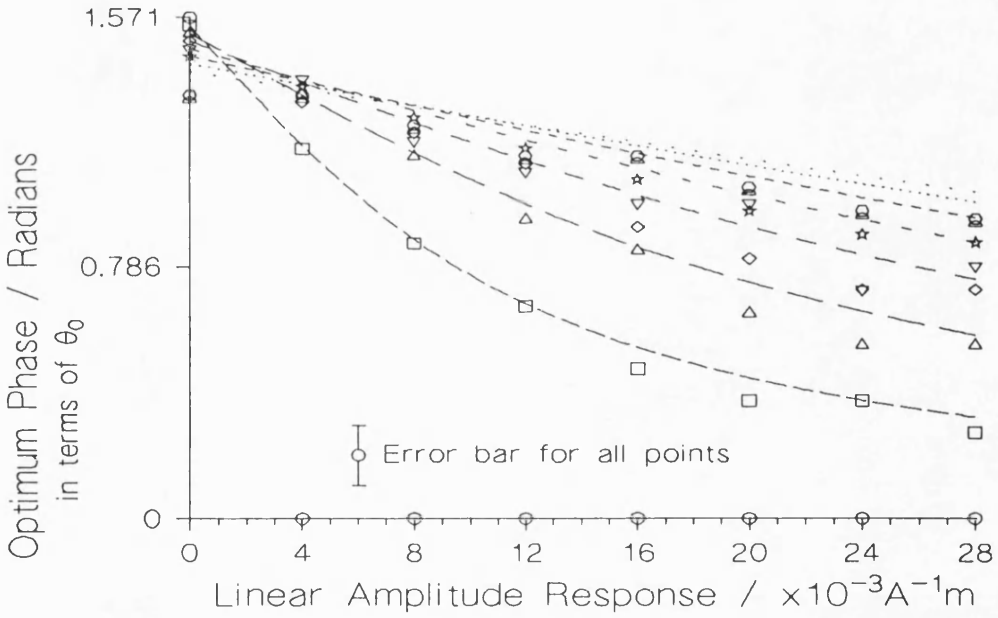

Figure 6.13 Optimum system response phase values as predicted from the two solutions.
(Key for phase response same as Figure 6.12a.)

6.5.6 Summary and Further Interpretation of the Results.

The Linear System Response Model was studied in great detail for realistically attainable amplitude and phase responses in order to ascertain the interaction between the two effects in the magnetometer system. It was found that for the magnitudes of the linear response coefficient $\mathbf{b_1}$ and $\mathbf{b_2}$ measured for the transducers MT1 and MT2 the optimum response of the system was not far removed from the pure linear phase response obtained by setting $\phi_0 = \phi_{0_{phase}}$ in the analytical solution of the model, see Figure 6.10a and Figure 6.12a. The setting for the phase $\phi_{0_{phase}}$ was also not far removed from $\phi_{0_{opt}}$, see Figure 6.11 and Figure 6.13. Increasing the coefficient $\mathbf{b_2}$ above the measured value also had a far greater effect on the system response than increasing $\mathbf{b_1}$. The increase of $\mathbf{b_1}$ in fact decreased the system response if $\phi_0 = \phi_{0_{phase}}$, see Figure 6.10b. If $\mathbf{b_1}$ was of an order of magnitude greater than $\mathbf{b_2}$ then the converse of this argument would be expected to be true and $\phi_{0_{opt}}$ would approach $\phi_{0_{amp}}$. In either case equation 6.5 indicates that an increase in either β or $\mathbf{a_1}$ would produce a proportional increase in the slope of the fundamental system response. The slope of the fundamental system response predicted from this simplistic model was found to be independent of the modulation amplitude and, although no results have been shown, the modulation frequency.

For low values of $\mathbf{b_1}$ and $\mathbf{b_2}$ over the range of values investigated the analytical solution returned results to within a good approximation of the numerical solution. This, however, broke down for higher values of the coefficients, see Figure 6.12a and Figure 6.12c. Over the full range of coefficients studied the phase equations obtained from the analytical solution, equations 6.19, 6.20 & 6.21, gave good agreement with the numerical model, see Figure 6.11 and Figure 6.13.

6.6 The Fitted Amplitude and Phase Response Model.

As an alternative to the Linear System Response Model the phase and amplitude responses measured from the magnetic transducers MT1 and MT2 were digitised at a fixed field interval of $0.5Am^{-1}$ to provide a more exact value for the amplitude and phase shift for any given applied field. These were then used in a numerical solution of the function given in equation 6.25, where $A_{2(II)}$ and $\Delta\phi_{(II)}$ were obtained for any given field from a linear interpolation between the digitised points. The applied field studied was once again a d.c. offset field and a modulation field as shown in equation 6.2.

$$V_{mix} = \frac{\beta A_{(H)}}{2}\cos\{\phi_0 + \Delta\phi_{(H)}\} \qquad 6.25$$

The digitised curves are shown in Figure 6.14a & b and represent the amplitude and phase response for the magnetic transducer MT1. The data was extended with an estimated straight line beyond the measured data in order to account for the additional field presented by the modulation at the investigated bias field maxima.

When calculating the Fourier coefficients within the numerical analysis the hysteresis in the responses was crudely taken into account by using the rising field curves during the period of the modulation oscillation for which the field was rising and the falling field curve for the falling field cycle.

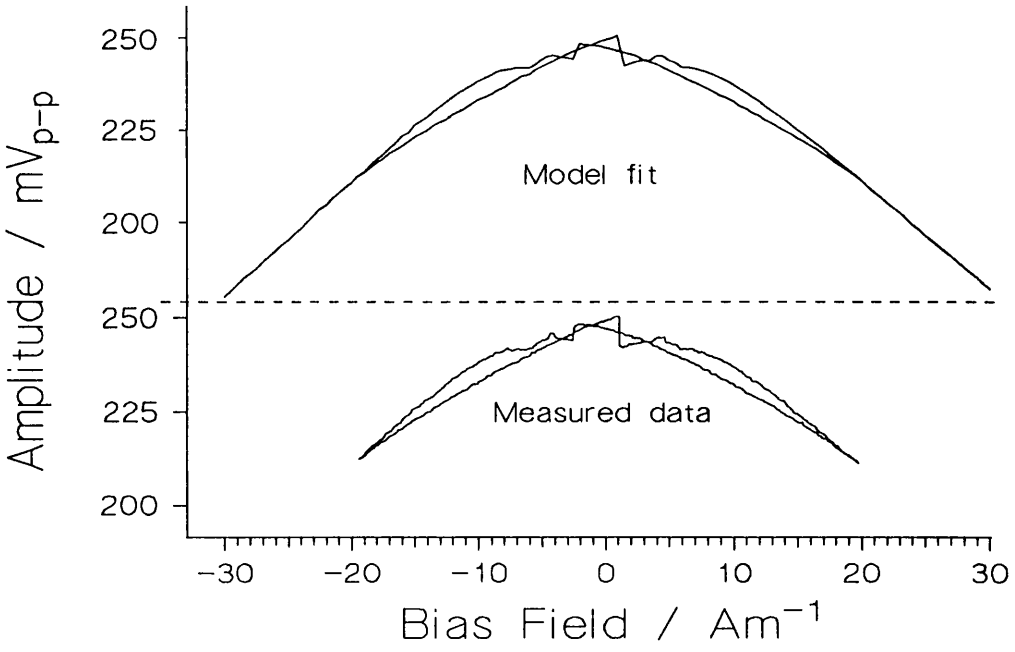

Figure 6.14a Amplitude response fit for alternative model.

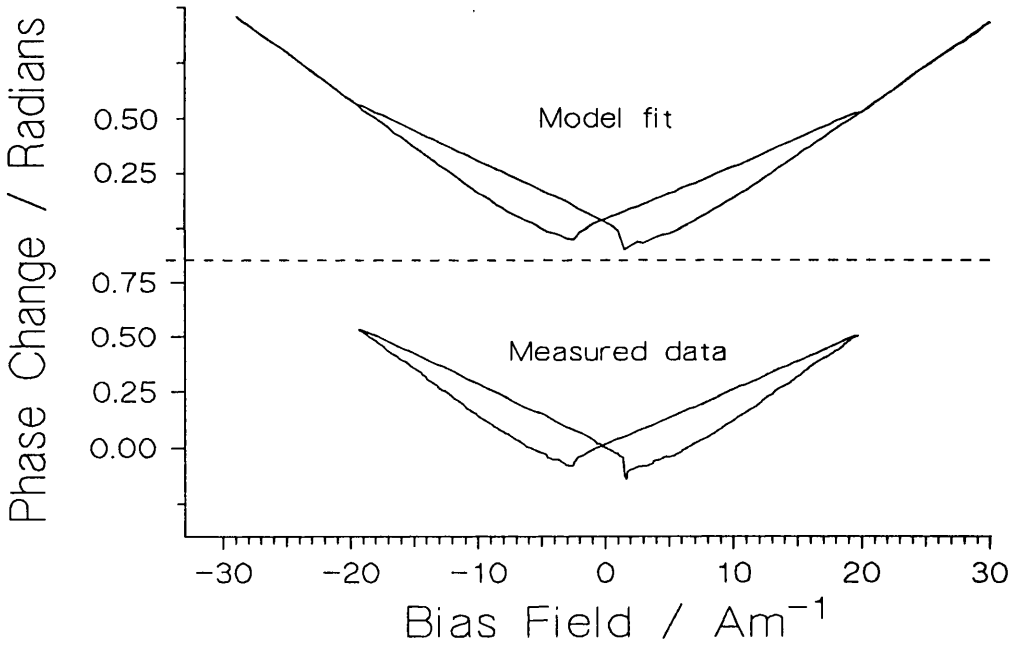

Figure 6.14b Phase response fit for alternative model.

The d.c. signal term and the fundamental term obtained from the model are shown in Figures 6.15a & b respectively and are compared against the measured results obtained in chapter 6.5. The phase ϕ_0 was set to the condition $\phi_{0_{phase}}$ to give a zero d.c. signal for no applied field from a preliminary investigation. The d.c. response appears little different from the linear response model solution. The fundamental signal, however, demonstrates a marginal increase in its slope for low applied bias fields. Also observed was the movement of the turning points in the response which are linked to the modulation field amplitude to greater field amplitudes than for the linear model. Further to this a reduction in the modulation amplitude was seen to marginally increase the response slope. It is suggested that the increase in the slope of the response comes about due to the sharp change in the amplitude and phase responses brought about by the low field discontinuities and that in the limit as the fitted curve approaches the measured curve the response curve measured would be produced. Decreasing the modulation current results in the discontinuities having a more prominant effect on the response, the total response being an average over the modulation field amplitude.

A further contradictory point to note is that the sharp changes in the measured fundamental response do not occur at the same bias field values as the discontinuities in the amplitude and phase response. If, however, the amplitude and phase responses are re-measured using the system described in chapter 5.4.1 but with a modulation field applied the responses shown in Figures 6.16a & b can be measured. These demonstrate a shifting of the response discontinuities brought about by the modulation field to the point where they would appear to coincide with those of both the d.c. and fundamental system responses.

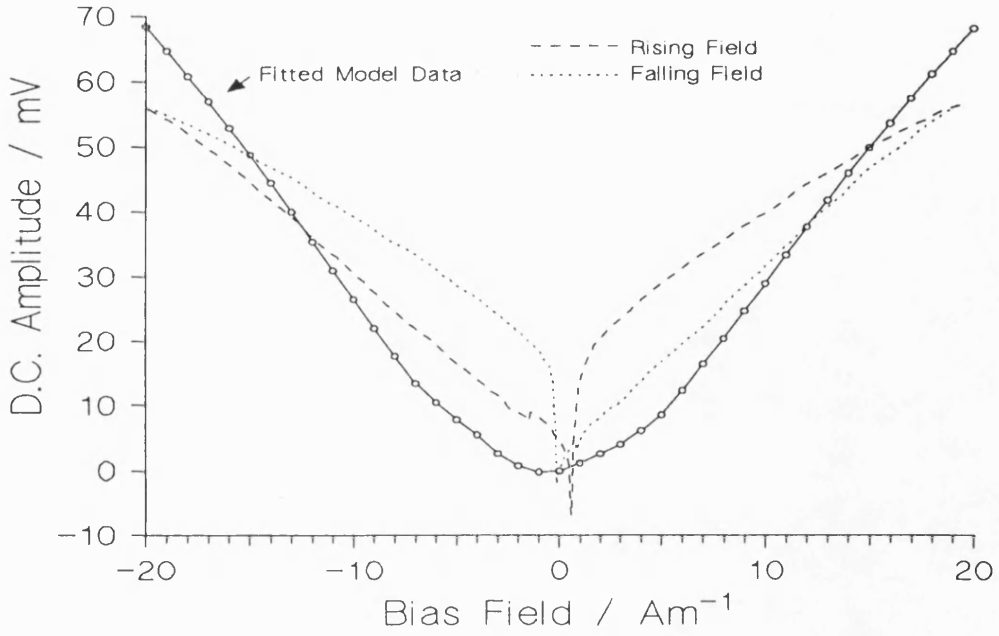

Figure 6.15a Comparison of the measured and the calculated d.c. response.

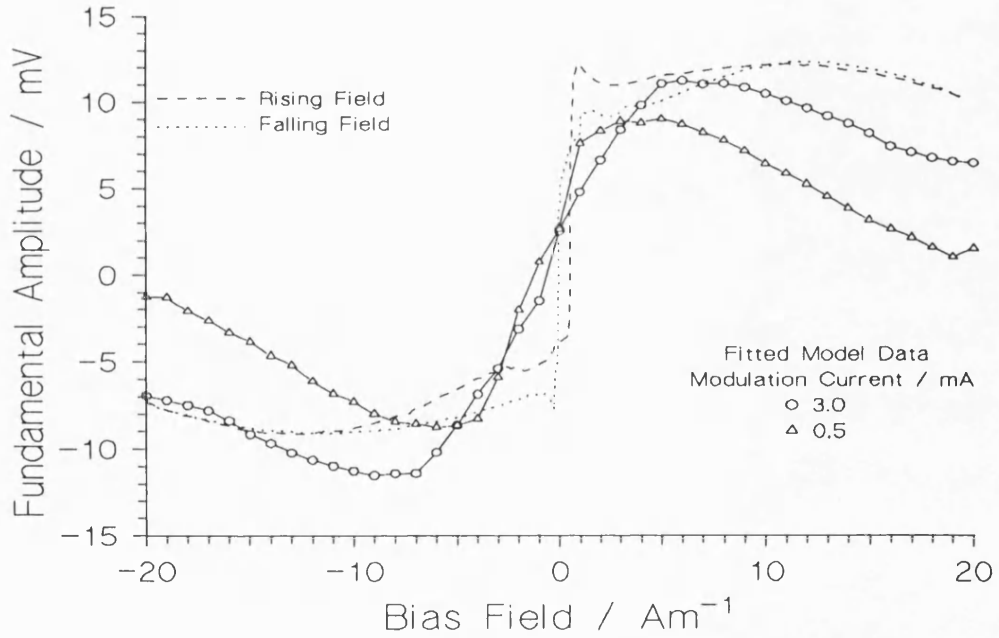

Figure 6.15b Comparison of the measured and the calculated fundamental response.

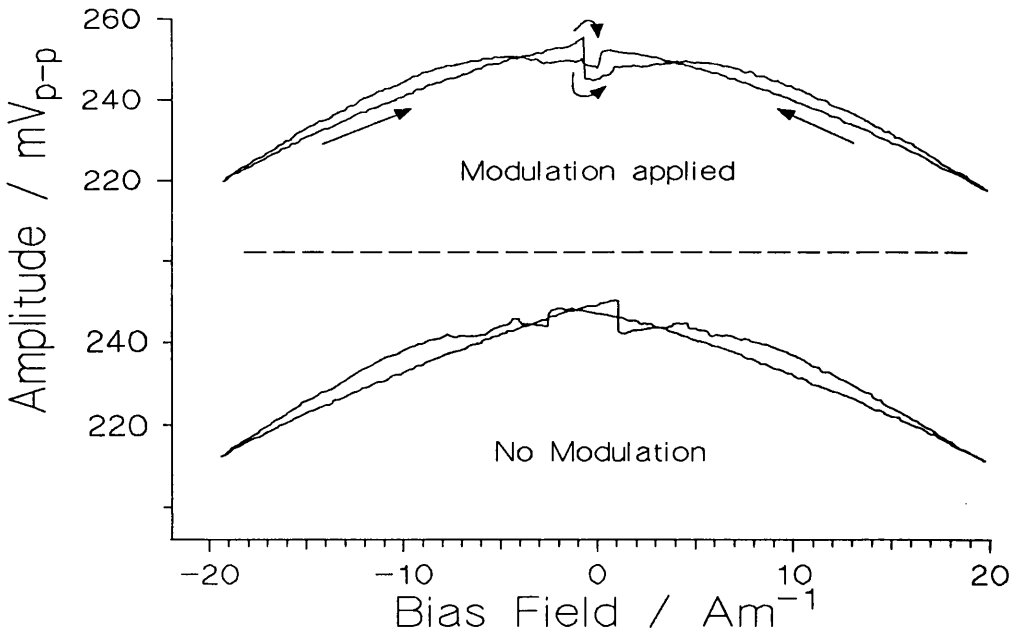

Figure 6.16a Comparison of the measured amplitude response with and without an applied modulation field.

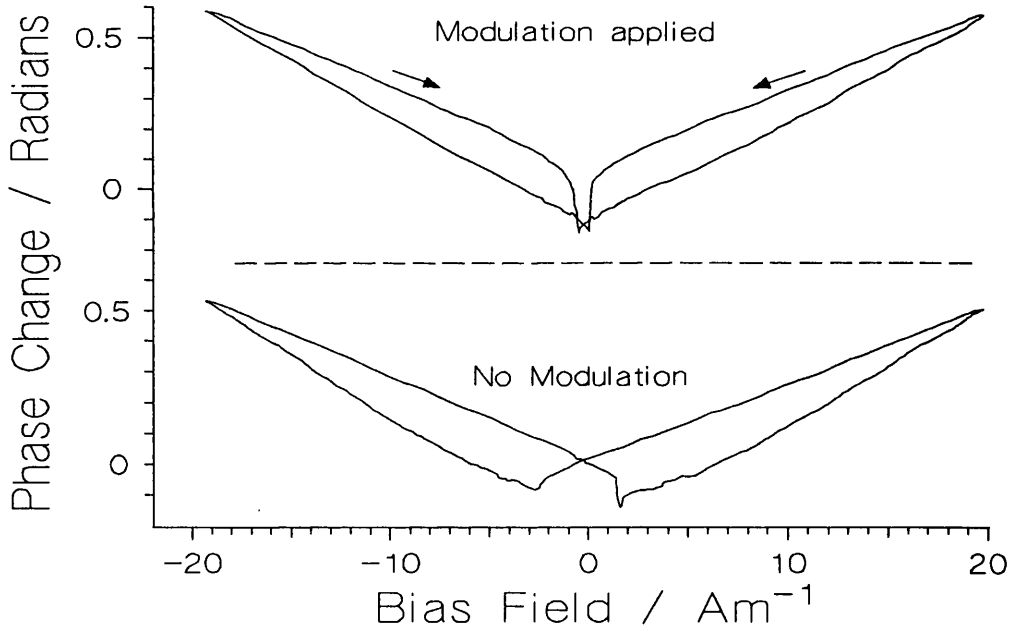

Figure 6.16b Comparison of the measured phase response with and without an applied modulation field.

7 PERFORMANCE OF THE SHEAR WAVE MAGNETOMETER SYSTEM.

7.1 Introduction.

The magnetic transducer element and the electronic components which make up the shear wave magnetometer all generate an associated noise signal which combine to produce an overall system noise. The overall system noise limits the minimum absolute field change that can be reliably detected by the magnetometer. From equation 1.14 the field noise $\mathbf{H}_n$ can be related to the phase noise ϕ_n through equation 7.1, where μ is the shear modulus and $\mathbf{H}$ the applied field.

$$H_n = 2\left(\frac{\phi_n}{\phi}\right)\left[\frac{1}{\mu}\frac{\partial\mu}{\partial H}\right]^{-1} \qquad 7.1$$

The fractional phase noise of the system would be expected to be determined largely by the electronic noise, whereas, the fractional change in the shear modulus with applied field is a material dependent parameter and in principle the larger the value the lower will be the value of the overall field noise.

This chapter investigates the noise contributions throughout the magnetometer system along with their minimisation. An analysis of the operation of the feedback loop arrangement as well as the results of an investigation carried out to optimise the modulation parameter for the operation of the shear wave magnetometer are firstly examined. The performance of the individual electronic components making up the shear wave magnetometer system are then discussed in terms of their gains and output noise signals. The overall magnetometer performance is then formalised. The chapter

concludes with a brief introduction to an alternative pulse mode shear wave magnetometer especially suited to the potentially large amplitude response seen in the single ended pulsed shear wave magnetic transducers described in chapter 5.

7.2 Analysis of the Magnetometer Feedback Loop.

7.2.1 Introduction.

The basic principle of the operation of the shear wave magnetometer is to measure the phase change of the shear waves travelling along the amorphous ribbon magnetic field transducer, the phase change being related to the applied magnetic field. A magnetic modulation signal was applied to the magnetic transducer in order to modulate the phase change along the ribbon to reduce mechanical and electrical noise in the measured signal. The measurement of the phase change was achieved by measuring the amplitude of the modulated phase by demodulating the transducer signal with a mixer element. The output of the mixer element consisted of primarily a signal at the modulation frequency with a signal amplitude related to the applied magnetic field. The signal from the mixer element at the modulation frequency was measured using a lock-in amplifier which in principle gives a d.c. signal output proportional to the amplitude of the input signal at the reference frequency applied to the instrument. The operation of the lock-in amplifier is discussed in more detail in chapter 7.6. The output of the lock-in amplifier, therefore, was a voltage proportional to the magnetic field to be measured. This signal was used in a feedback loop with the phase correctly adjusted relative to the measured magnetic field so as to null the magnetic field measured by the transducer arrangement and thus produce a "locked" system with a linear response limited in dynamic range purely by the output range of the lock-in amplifier. The feedback magnetometer system also has a direct calibration to the measured field by the number of turns on the feedback solenoid. The feedback current supplied by the lock-in amplifier was directly proportional to the

measured magnetic field. The output of the lock-in amplifier has a low-pass filter with a time constant τ. This time constant would be expected to govern the overall time constant and hence the measurement bandwidth of the complete magnetometer system. The relation between the lock-in time constant and the magnetometer time constant, however, is not immediately obvious. To understand fully the operation of the feedback loop it was necessary to develop the response function for the magnetometer in a similar manner to the analysis undertaken by Koo *et al* [1987] for the fibre optic magnetometer.

7.2.2 The Magnetometer Response Function.

The entire shear wave magnetometer feedback loop can be most conveniently represented by a signal flow diagram for the frequency domain as depicted in Figure 7.1. The magnetometer response in the time domain is also considered so as to obtain the response of the magnetometer to external fields and is covered in greater detail regarding other aspects in chapter 8.

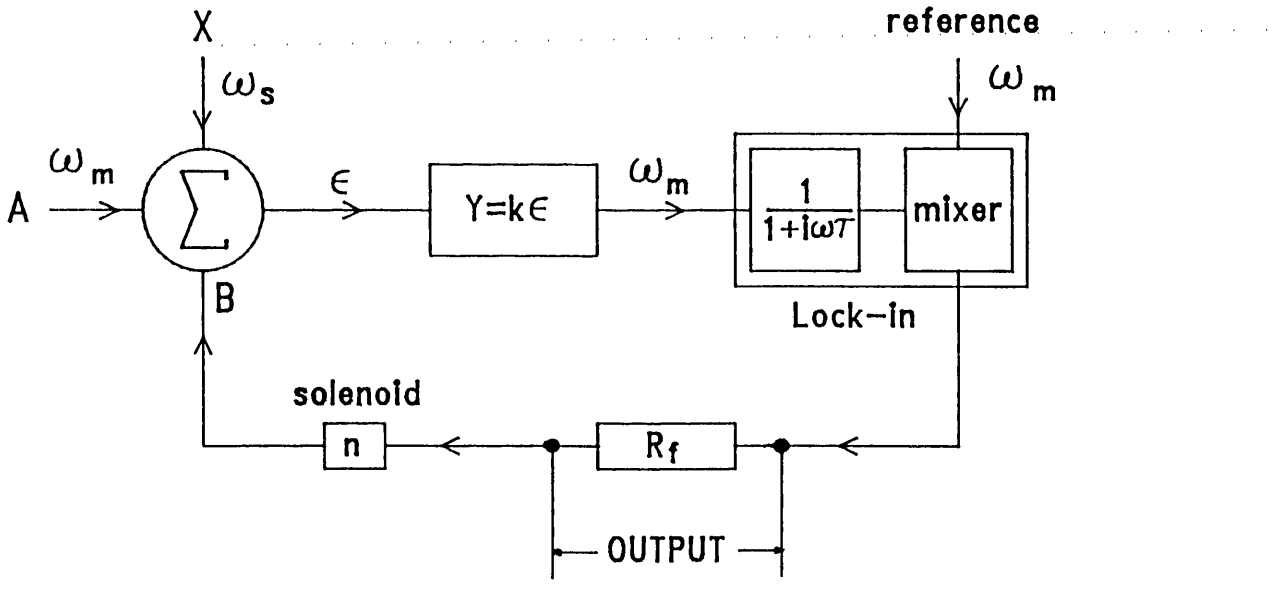

Figure 7.1 The shear wave magnetometer signal flow diagram.

The signal X(ω) in Figure 7.1 represents the external magnetic signal field to be measured by the magnetometer at a frequency ω_s, whereas, A(ω) is the modulation signal at ω_m and B(ω) the feedback magnetic field. These magnetic fields are superposed within the modulation and feedback solenoids to produce a total magnetic signal ε(ω) which is applied to the magnetic transducer. The signal Y(ω) represents the magnetic field dependent signal at the output of the mixer element with **k** being the combined gain for the magnetic field to signal amplitude conversion of the magnetic transducer and mixer element. The constant **k** can be written as a differential as in equation 7.2, where $\mathbf{V_m}$ is the output amplitude of the mixer element.

$$k = \frac{\partial V_m}{\partial H} \qquad 7.2$$

k can be thought of as consisting of a number of gain components from the magnetic transducer and the mixer element. For a simple linear phase response there is the phase change ϕ with applied field **H** for the magnetic transducer related by the constant **a** and can be expressed as in equation 7.3.

$$a = \frac{\partial \phi}{\partial H} \qquad 7.3$$

This phase change then undergoes a transformation within the mixer to a signal amplitude related by a constant **b** and expressed in equation 7.4.

$$b = \frac{\partial V_m}{\partial \phi} \qquad 7.4$$

The constant **k** cannot, however, be assumed to be a direct multiple of these two gains because of the field dependence of the amplitude of the shear waves along the

magnetic transducer as described in chapter 5. The mixer output was also sensitive to variations in the input signal amplitude as discussed in chapter 6 and so the gain **k** is also a combination of the transducer amplitude response **c**, equation 7.5, and the mixer amplitude response **d**, equation 7.6. A_2 is the amplitude of the received shear wave as defined in chapter 1.

$$c = \frac{\partial A_2}{\partial H} \qquad 7.5$$

$$d = \frac{\partial V_m}{\partial A_2} \qquad 7.6$$

An estimate for the combined transducer and mixer gain **k** can be obtained in terms of the Linear Response Model discussed in chapter 6 by applying equation 7.1 to the result obtained for the mixer output signal at the modulation frequency in chapter 6, equation 6.16. If measured values for the linear response coefficients from Table 6.1a and Table 6.1b are considered then from equations 6.16, 6.19 & 6.20 the optimum field response approaches the purely phase response as concluded in chapter 6. The magnitude of the gain **k** is then given by equation 7.7 for a total phase change along the magnetic transducer of $\phi_{0_{phase}}$ given by equation 6.20. β is the mixer gain as defined in chapter 6.3 and is covered in detail in chapter 7.4. $\mathbf{a_1}$ and $\mathbf{b_2}$ are the received shear wave amplitude and the linear phase response respectively.

$$k = \frac{2\beta a_1 b_2}{\pi} \qquad 7.7$$

The signal $Y(\omega)$ at the modulation frequency ω_m is measured by the lock-in amplifier and undergoes low pass filtering as represented by the low-pass filter function

with a time constant τ in Figure 7.1. The output of the lock-in amplifier is proportional to the amplitude of the input signal and can be represented by a lock-in amplifier gain **g** as shown in equation 7.8, where V_o is the lock-in amplifier output signal.

$$g = \frac{V_o}{V_m} \qquad 7.8$$

The lock-in amplifier output signal drives the feedback solenoid of **n** turns per metre through a feedback resistance R_f across which the feedback current I_f can be measured and is proportional to the feedback field. The feedback resistor and the solenoid contribute further to the total gain of the loop with gains **e** and **f** given by equation 7.9 and equation 7.10 respectively.

$$e = \frac{\partial I_f}{\partial V_o} = \frac{1}{R_f} \qquad 7.9$$

$$f = \frac{\partial B(\omega)}{\partial I_f} = n \qquad 7.10$$

The total loop gain **K** obtained from the flow diagram is then given by the product of these gains as shown in equation 7.11, where s is the lock-in amplifier sensitivity in millivolts calibrated to RMS signals with a full scale output of ±10V.

$$K = kefg = \frac{2\beta a_1 b_2 n\, g}{\pi R_f} = \frac{10^4 \beta a_1 b_2 n}{\sqrt{2}\pi R_f s} \qquad 7.11$$

Further consideration of Figure 7.1 yields the coupled equations describing the operation of the feedback loop and are shown in equation 7.12 and equation 7.13, where τ is the time constant of the output filter of the lock-in amplifier represented by the response for a single pole low-pass filter.

$$\varepsilon(\omega) = A(\omega_m) + X(\omega) + B(\omega) \qquad 7.12$$

$$B(\omega) = \frac{-K}{1 + i\omega\tau}[X(\omega) + B(\omega)] \qquad 7.13$$

The above expression for $\mathbf{B}(\omega)$ can be rearranged to give the feedback signal, $\mathbf{B}(\omega)$ in terms of the magnetic signal to be measured, $\mathbf{X}(\omega)$ as shown in equation 7.14.

$$B(\omega) = \frac{\left[-\frac{K}{1+K}\right]}{1 + i\omega\left[\frac{\tau}{1+K}\right]} X(\omega) \qquad 7.14$$

$$B(\omega) = \frac{-K}{1 + i\omega\tau} X(\omega) \qquad K \ll 1 \qquad 7.15$$

$$B(\omega) = \frac{-1}{1 + \frac{i\omega\tau}{K}} X(\omega) \qquad K \gg 1 \qquad 7.16$$

It can be seen from equation 7.15 and equation 7.16 that for sufficiently high feedback loop gain the magnitude of the feedback signal $\mathbf{B}(\omega)$ approaches that of the external field $\mathbf{X}(\omega)$ and that the frequency domain experiences a low-pass filtering with an effective time constant $\tau/(1+K)$. The bandwidth of the closed loop system is, therefore, determined not as a whole by the time constant of the lock-in amplifier but also by the loop gain of the system producing an effective system time constant.

Further to the above analysis the effect of applying a field step to the magnetometer system can be investigated. A field step in the frequency domain can be represented by equation 7.17, where $\mathbf{X_0}$ represents the magnitude of the field step for $\mathbf{x(t)=X_0}$ for $\mathbf{t>0}$ and $\mathbf{x(t)=0}$ for $\mathbf{t\leq 0}$.

$$X(\omega) = \frac{X_0}{i\omega} \qquad 7.17$$

Substituting this into equation 7.13 and taking the inverse Laplace transform yields the result shown in equation 7.18 for the feedback signal **b(t)** in the time domain.

$$b(t) = \frac{K}{(1+K)} X_0 \left\{ 1 - \exp\left[-\frac{t}{\left[\frac{\tau}{(1+K)}\right]} \right] \right\} \qquad 7.18$$

The feedback signal can be seen to follow the input signal with an exponential approach to the magnitude of the applied signal with the effective time constant defined previously. A measure of how closely the feedback signal follows the applied signal can be obtained by defining a "tracking efficiency". The tracking efficiency describes how closely **b(t)** approaches **x(t)** in the steady state condition $t \gg \tau/(1+K)$. The tracking efficiency is, therefore, given by equation 7.19.

$$\frac{b(t)}{X_0} \times 100\% = \frac{K}{1+K} \times 100\% \qquad 7.19$$

The repercussions of this feedback analysis are that to obtain a "locked" system a suitably high loop gain is required as shown by equation 7.18. The signal-to-noise ratio of the signal at the modulation frequency can be improved, however, by increasing the lock-in amplifier time constant with out any loss in system bandwidth simply by increasing the loop gain to compensate for the change in the effective time constant.

7.2.3 The Feedback System Response Time and Tracking Efficiency.

The response time and the tracking efficiency defined in chapter 7.2.2 were measured for the shear wave magnetometer system using the magnetic transducer **MT1**. A magnetic field pulse of **163nT** was applied to the sensor using a PM5134 function

generator driving a signal solenoid of 1311 turns per metre. The response of the magnetometer to this signal was measured across the feedback resistor $\mathbf{R_f}$. The dynamic results were recorded using a Thurlby DSA524 digital storage adaptor and the results displayed on a Tektronix 2246 oscilloscope and hard copies obtained using an X-Y recorder connected to the storage adaptor. A modulation current of $\mathbf{i_m=3mA}$ was applied at a frequency of **870Hz** with a feedback resistance of $\mathbf{R_f=2K\Omega}$. The tracking efficiency was measured for a range of loop gains by measuring the ratio of the applied field step current to the feedback current measured across $\mathbf{R_f}$ with a correction made for the difference in the solenoid calibrations. The response time was also measured for a range of gains for a lock-in amplifier time constant of τ=**3s**. The response time was taken as the time taken to reach 90% of the final value of the magnetometer output. This response time is equal to 2.3τ of a first-order filter with time constant τ. The tracking efficiency and response time were obtained from measurements on the captured magnetometer outputs for a range of feedback loop gains obtained by changing the sensitivity of the lock-in amplifier. Figure 7.1 shows a typical response to a magnetic field step of 163nT for a lock-in amplifier sensitivity of 100μV. The response time is indicated by τ.

The tracking efficiency and the response times of the magnetometer system for a range of loop gains are shown in Figure 7.2 and Figure 7.3 respectively. The errors in the quantities are those estimated from examination of the full set of pulse response data. The spurious results obtained for both quantities at very low gains probably come about due to insufficient loop gain to retain the "locked" operation.

The loop gains in both cases were calculated by applying equation 7.10 to the values for the transducer coefficients given in Table 6.1a and Table 6.1b for the magnetic transducer **MT1**. The loop gain given in equation 7.10 was derived directly from the linear response model and Figures 7.2 & 7.3 clearly show the underestimate of the gain **k** defined in equation 7.6 compared with that shown for the transducer in chapter 6.5.1,

Figure 6.5b. The exact magnitude of the gain cannot be obtained from Figure 6.5b because of the sharp discontinuous nature of the response, however, the gain would appear to be some average of the response curve over the modulation field range. The gain **k** would, therefore, be expected to have some dependence on the modulation amplitude.

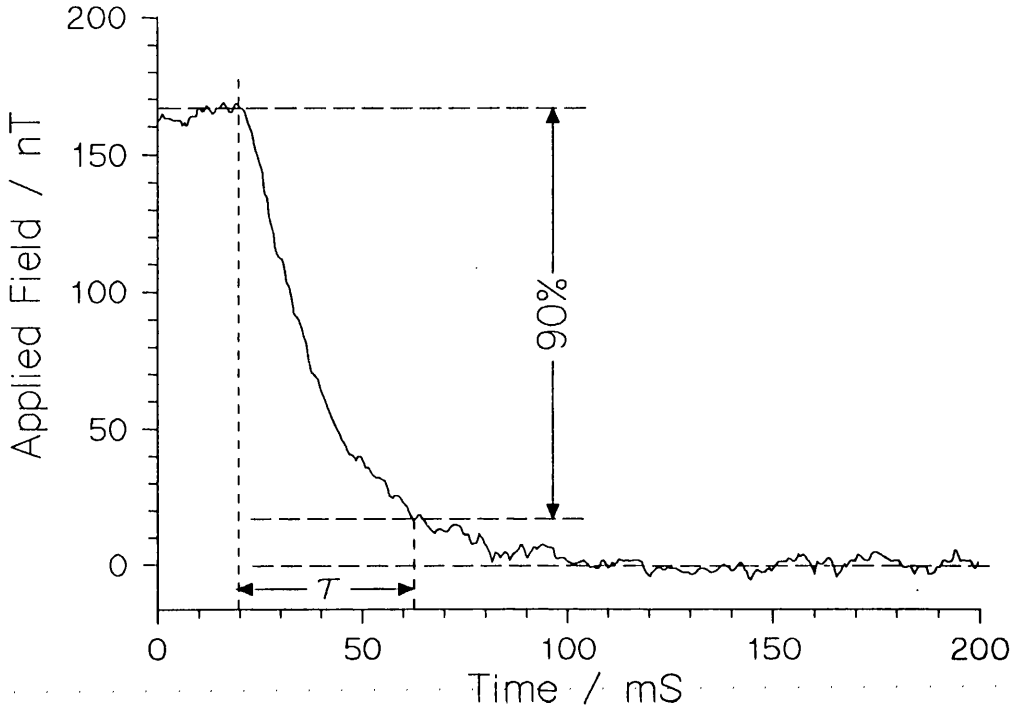

Figure 7.1 Typical magnetometer response to removing a d.c. field of 163nT. The lock-in time constant was 3s and the sensitivity 100μV. The feedback resistor was 2KΩ.

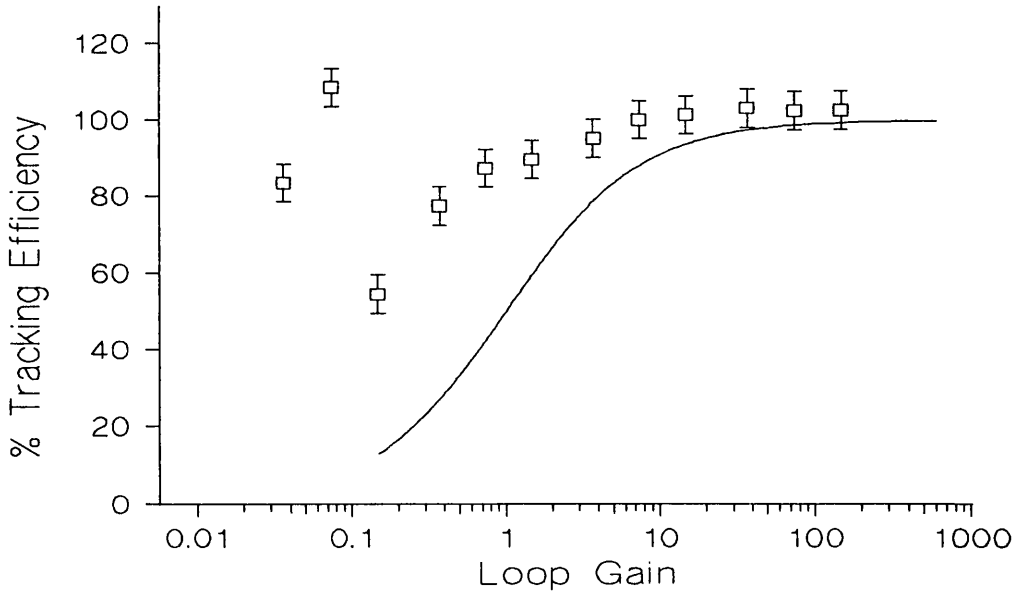

Figure 7.2 Measured system tracking efficiency as a function of loop gain calculated from equation 7.10. The theoretical curve is also shown.

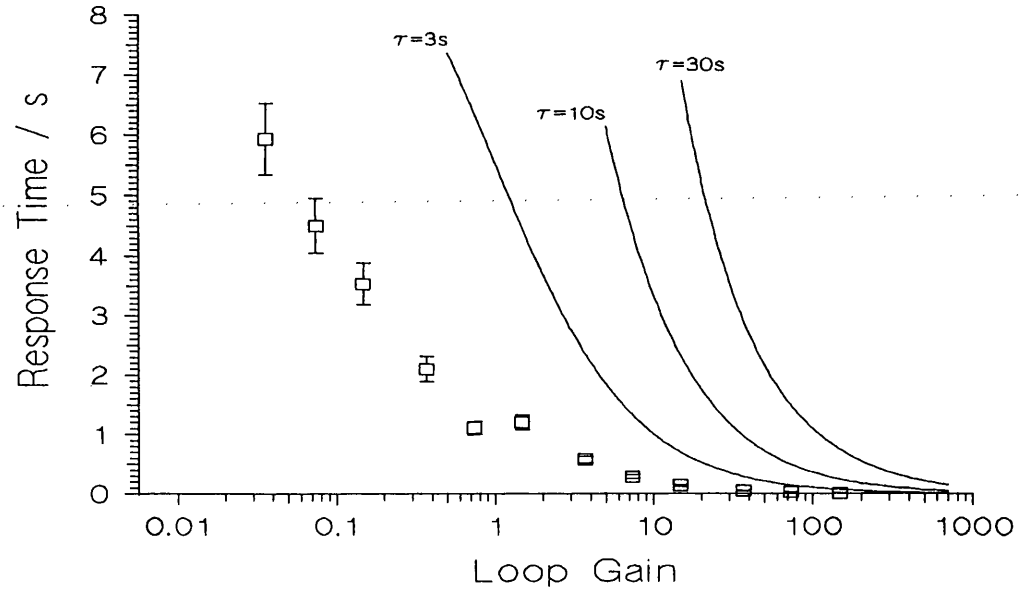

Figure 7.3 Measured system response time as a function of loop gain calculated from equation 7.10 for a lock-in amplifier time constant of τ=3s. Theoretical curves for a range of time constants are also shown.

The loop gain for both the tracking efficiency and the response time can be adjusted by an extra gain factor so that the tracking efficiency data fits the theoretical curve given by equation 7.18. The tracking efficiency was fitted, as it is theoretically purely gain dependent, unlike the response time which contains the lock-in amplifier time constant. The modified data is shown in Figure 7.4 the fit being accomplished by applying an additional correction factor eight to the loop gain. The response time data can be seen to have minor discrepancies. The lower gain data is probably a closer fit than it would immediately suggest as the error bars in the logarithmic gain axis would be more prominant at lower gains. The higher gain values for which gain errors are not as prominent would suggest a higher measured time constant, which could possibly be due to the calibration or definition of the lock-in amplifier time constant, but is more likely due to the approximation to a single-pole response of the lock-in amplifier output.

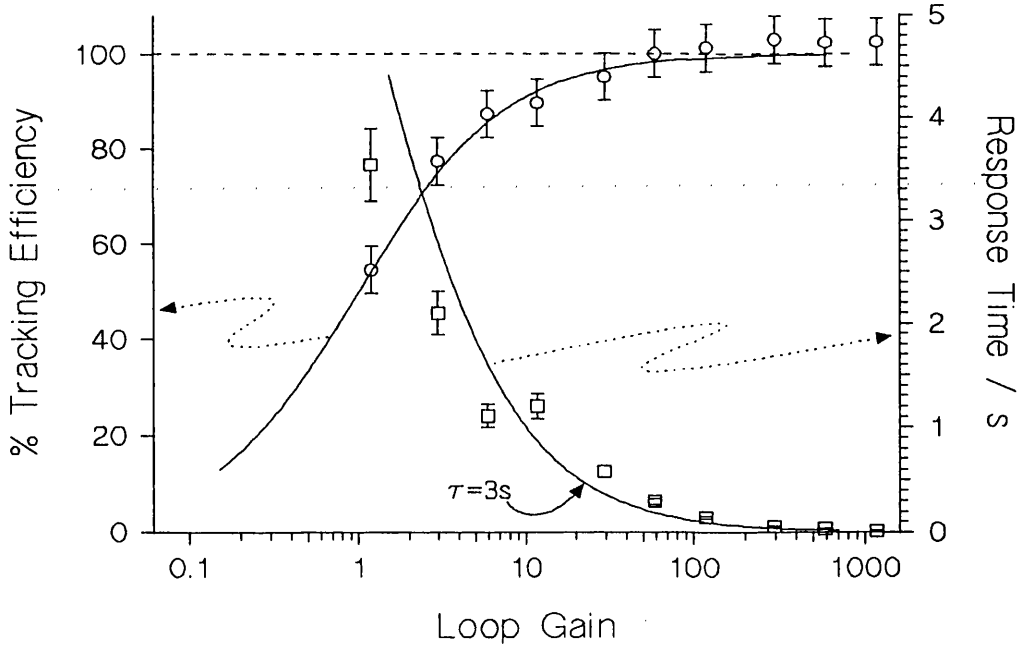

Figure 7.4 Tracking efficiency and response time modified to fit the theoretical data for the tracking efficiency.

7.3 Optimisation of the Modulation Signal.

The Linear Response Model discussed in chapter 6 suggested that the response of the fundamental signal at the modulation frequency measured by the lock-in amplifier had a slope about the origin that was independent of the modulation signal amplitude and frequency. The lack of any frequency dependent hysteresis considerations such as eddy current loss in the model as well as the proposal made in chapter 7.2.3 regarding the modulation current magnitude along with further consideration which are discussed in chapter 8 suggest that the response curve depends on both the modulation frequency and the modulation amplitude. The dependence of the magnetometer response on the modulation parameters was first observed by Squire and Gibbs [1988a]. The results presented here are further to their observations and were carried out in order to pin-point more accurately the optimum operating conditions and possibly support the proposal made in chapter 7.2.3

The optimum operating conditions for the modulation signal were found by investigating the magnetometer system response using the method described in chapter 6.5. This gives the lock-in amplifier output as a function of applied bias field and is a direct measure of the magnitude of the signal from the mixer element at the modulation frequency. The effect of varying both the modulation amplitude and frequency were studied. The lock-in amplifier output against field curves were directly comparable with that of Figure 6.5b, as the same magnetic transducer, **MT1**, was employed. In the closed loop configuration introduced in chapter 1.2.4 and discussed further in chapter 7.2 the magnetometer system operates about the zero field position on the response curve and for maximum sensitivity the slope of the curve about zero field or the gain **k** as defined in equation 7.6 should be a maximum.

Figure 7.5 shows the lock-in amplifier output for a range of modulation frequencies. The lock-in amplifier sensitivity was **s=10mV** and the time constant τ**=100ms**. The

modulation current was $\mathbf{i_m=6.5mA}$ this corresponds to a peak modulation field amplitude of $\mathbf{8.4Am^{-1}}$ from equation 6.24 and the total bias field sweep range was $\mathbf{\pm 25Am^{-1}}$. Figure 7.5 would suggest an optimum modulation frequency of the order of $\mathbf{f_m=870Hz}$. Above this frequency eddy current damping would appear to produce an increase in the hysteresis observed while at lower frequencies there is a marked fall off in the response slope possibly due to predominant magnetomechanical damping, although a degradation in the lock-in amplifier performance at low frequencies could also contribute, Wang [1989].

Figure 7.6 demonstrates the effect of varying the modulation amplitude on the response curve. The lock-in amplifier sensitivity was $\mathbf{s=500mV}$ and the time constant $\mathbf{\tau=100ms}$. The modulation frequency was $\mathbf{f_m=870Hz}$ and the total bias field sweep range was $\mathbf{\pm 6.5Am^{-1}}$. Figure 7.6 shows that the slope of the response curve about zero field increases for decreasing modulation amplitude, although an increase in the hysteresis of the loop was observed from that of the high modulation amplitudes. This observation would appear to support the proposals made in chapter 6.6 and chapter 7.2.3. It was suggested that the sharp response about zero field is partially due to the discontinuities observed in the amplitude and phase response of the magnetic transducer. These discontinuities are averaged over the range of the modulation amplitude with the whole response. Reducing the modulation amplitude gives a more predominant contribution to the system response from these discontinuities.

Figure 7.5 Magnetometer system response curves for a range of modulation frequencies. The lock-in amplifier sensitivity was **s=10mV** and the time constant **τ=100ms**. The peak modulation field amplitude was **8.4Am^{-1}** with a total bias field sweep range **±25Am^{-1}**.

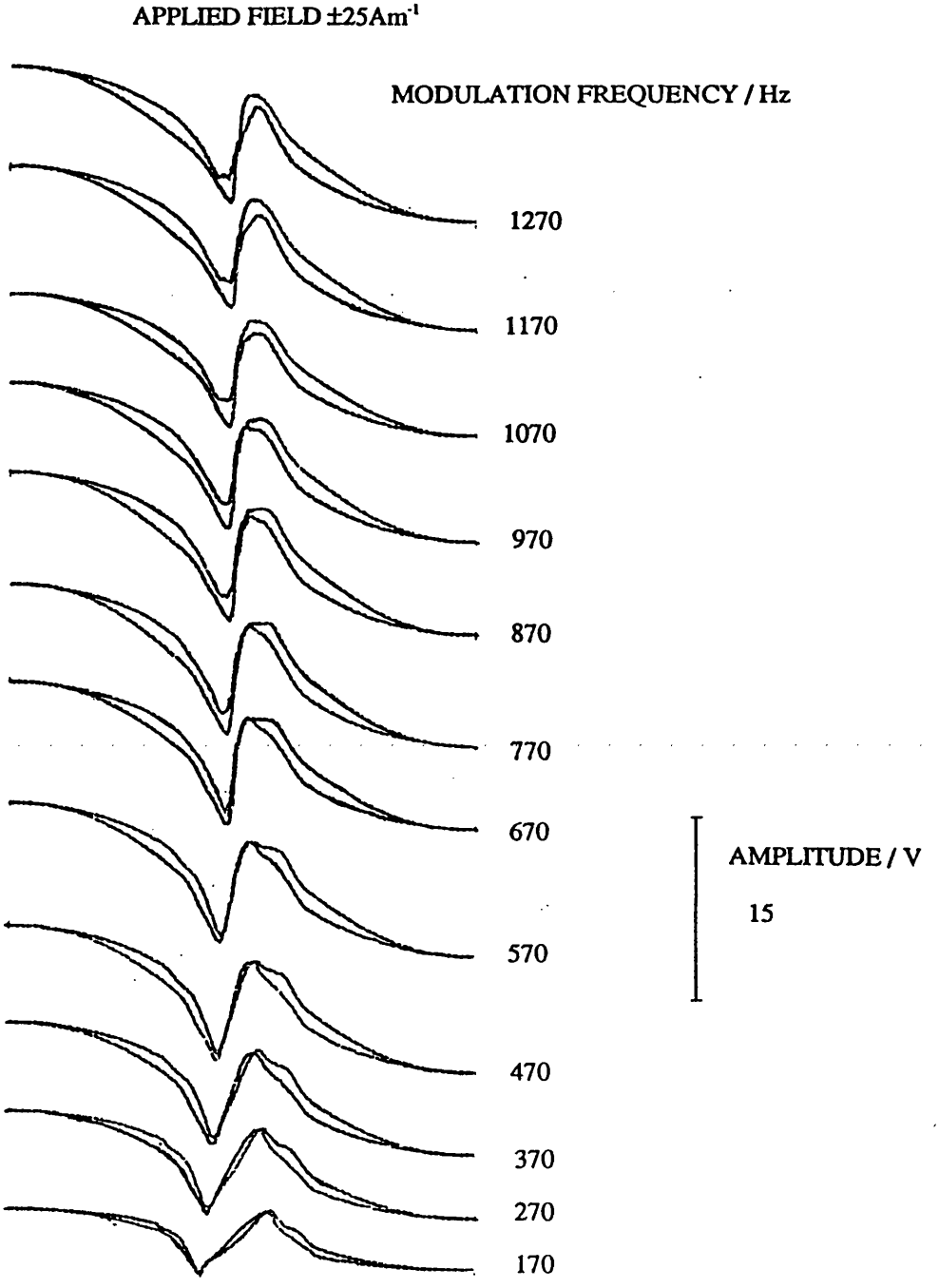

Figure 7.6 Magnetometer system response curves for a range of modulation amplitudes. The lock-in amplifier sensitivity was **s=500mV** and the time constant **τ=100ms**. The modulation frequency was **f_m=870Hz** and the total bias field sweep range **$\pm$6.5Am^{-1}**.

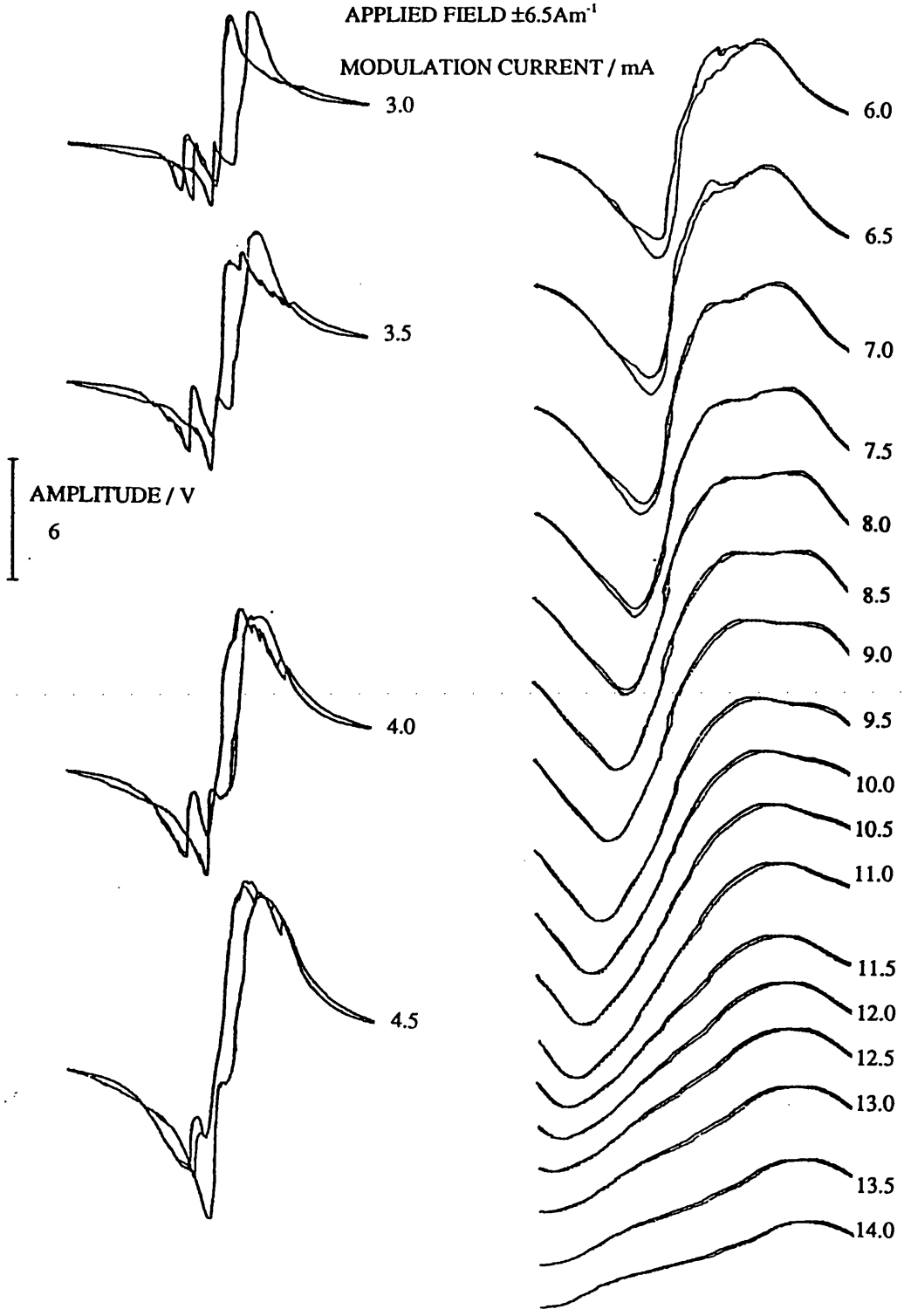

7.4 Performance of the Mixer Element.

7.4.1 Introduction.

Three different mixer elements were investigated in order to find the most suitable element as well as the optimum operating conditions for the device. Any limitations on the system operation from the mixer element could potentially be solved by introducing a higher specified device or designing a dedicated unit. The three mixers investigated, however, were high performance devices and the results for two of the mixers are presented. The two devices discussed are a passive device, the Mini Circuits SRA-3 and an active device, the Analog Devices 429A.

7.4.2 Mixer Gain.

The output signal of both mixers was measured as a function of the input signal for a range of local oscillator signals. The local oscillator signal and the input signal were supplied by two Philips PM5190 LF Synthesizers. The frequency of operation of the synthesizers was chosen as $\mathbf{f_0}$**=1MHz** in order to simulate the expected magnetic transducer output signal ($\mathbf{f_0}$**=2MHz** was also investigated; however, the results were comparable). The signal frequency was set **1kHz** higher than the local oscillator signal to produce a mixer output signal at a frequency comparable to the optimum modulation frequency. The magnitude of the mixer output signal was measured either on a Tektronix 2246 oscilloscope or a Hewlett Packard 3561A Spectrum Analyser.

Figure 7.7a and Figure 7.7b show the results obtained for the SRA-3 Schottky diode mixer and the active 429A mixer respectively.

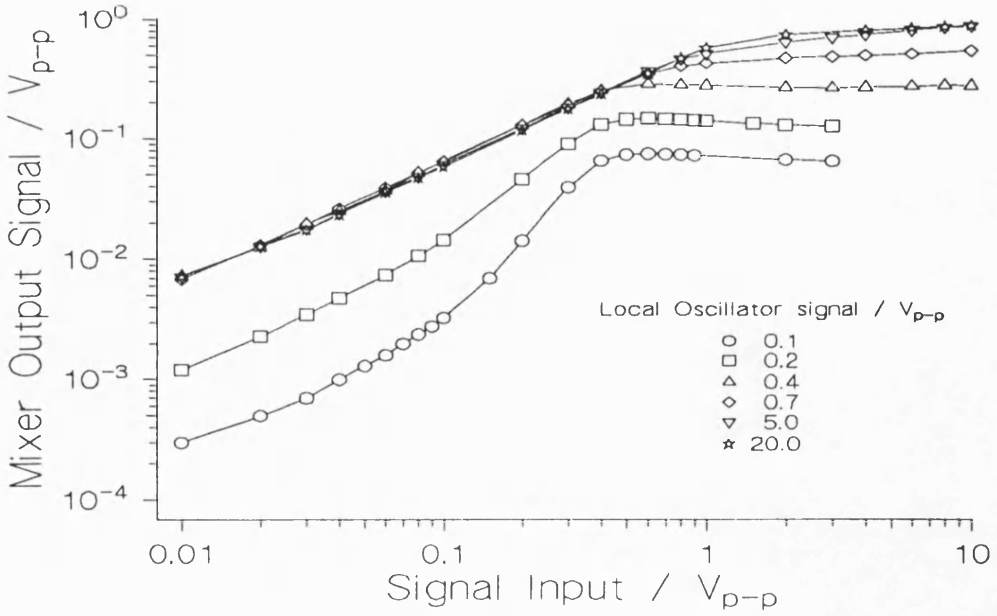

Figure 7.7a SRA-3 mixer output as a function of signal input and local oscillator level.

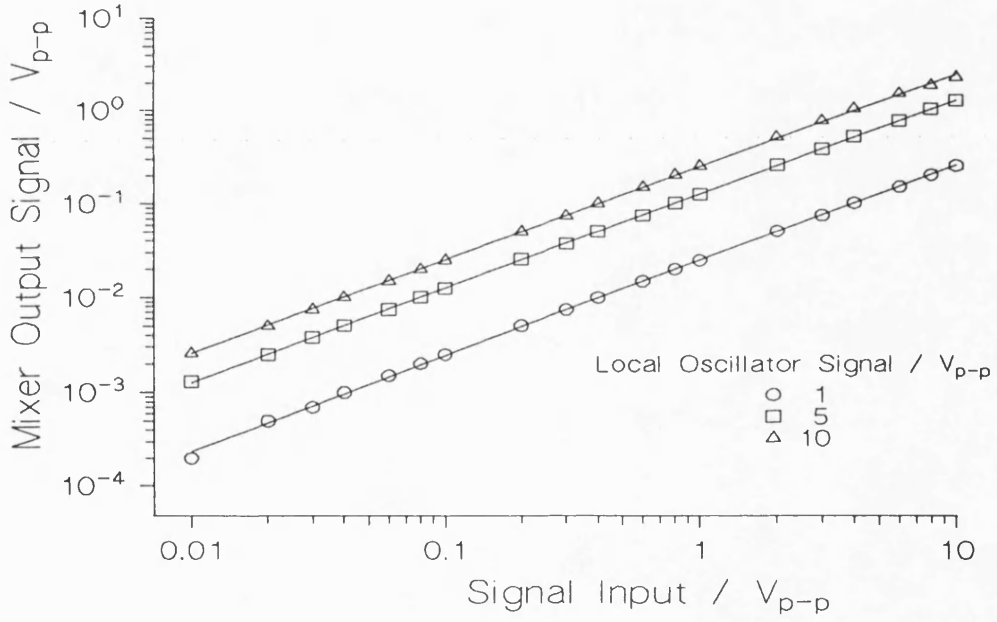

Figure 7.7b 429A mixer output as a function of signal input and local oscillator level.

The features observed in Figure 7.7a can be explained in terms of the saturation of the mixer input brought about by the diode bridge configuration of the mixer. For a fixed local oscillator voltage the mixer output amplitude increases in a linear fashion with increasing signal input magnitude up to a signal input amplitude of the order of **0.5V**. Above this level increasing the signal amplitude has little effect on the output signal. The input essentially saturates above this level and for a source with a poor drive capability such as the piezoelectric transducers used in the magnetic transducer arrangement considerable loading of the signal was observed. Below this level no loading was observed. For a fixed signal input and varying the local oscillator level a similar behaviour was observed. Loading of the drive oscillator was not as pronounced due to the drive capability of the oscillator and for this reason the same signal output could still be used to drive the magnetic transducer without buffering of the signal. Increasing the local oscillator level above the saturation point, however, still has little effect on the output signal magnitude. The optimum local oscillator amplitude would appear to be at or above this saturation level as above this level the mixer output to signal input is linear over a greater range of input signals. The slope of this linear region for any given local oscillator level is the gain β defined in equation 6.5. The mixer gain β for a range of local oscillator levels above the saturation amplitude is listed in Table 7.1.

Figure 7.7b demonstrates the linear nature of the active mixer over a range signal and local oscillator levels. Again the gain β for the device is listed in Table 7.1. A local oscillator level greater that $\mathbf{10V_{p\text{-}p}}$ was impractical for either of the mixers as on connection of the magnetic transducer input matching discussed in chapter 5.2 to the synthesizer output the maximum signal obtainable was $\mathbf{10V_{p\text{-}p}}$.

Table 7.1 Mixer gains for the two devices considered for a range of local oscillator input amplitudes.

Local Oscillator amplitude / V_{p-p}	SRA-3 Gain $\beta \times 10^3$	429A Gain $\beta \times 10^3$
0.4	640	-
0.7	628	-
1.0	-	25
5.0	606	129
10.0	-	237
20.0	590	-

7.4.3 Mixer Output Noise.

The output noise voltage for the two mixers was measured as a function of local oscillator amplitude with the signal input being terminated with an input impedance $\mathbf{R_{in}=50\Omega}$. The local oscillator signal was provided by a Philips PM5193 Programmable Synthesizer and the output noise measured over a 20Hz frequency bandwidth centred about 1kHz using a Hewlett Packard 3651A Spectrum Analyser. A 9452 Brookdeal Precision a.c. amplifier was employed between the mixer and analyser in order to amplify the noise of the considerably quieter SRA-3 device so that the noise signal fell within the measurement range of the spectrum analyser. The Brookdeal amplifier had a specified noise voltage referenced to its input of $\mathbf{5.7nV/Hz^{1/2}}$.

Figure 7.8 shows the SRA-3 output noise as a function of the magnitude of a **1MHz**

local oscillator signal. There was little variation in the results at a frequency of **2MHz.** The minimum mixer output noise was achieved for local oscillator signals between approximately **0.4 - 4.0V**. the exact magnitude of the noise signal could not be measured due to the limitations imposed by the Brookdeal Precision amplifier. The output noise of the active 429A mixer was found to be independent of local oscillator amplitude with a magnitude of v_n=**1.23±0.08μV/Hz$^{1/2}$**.

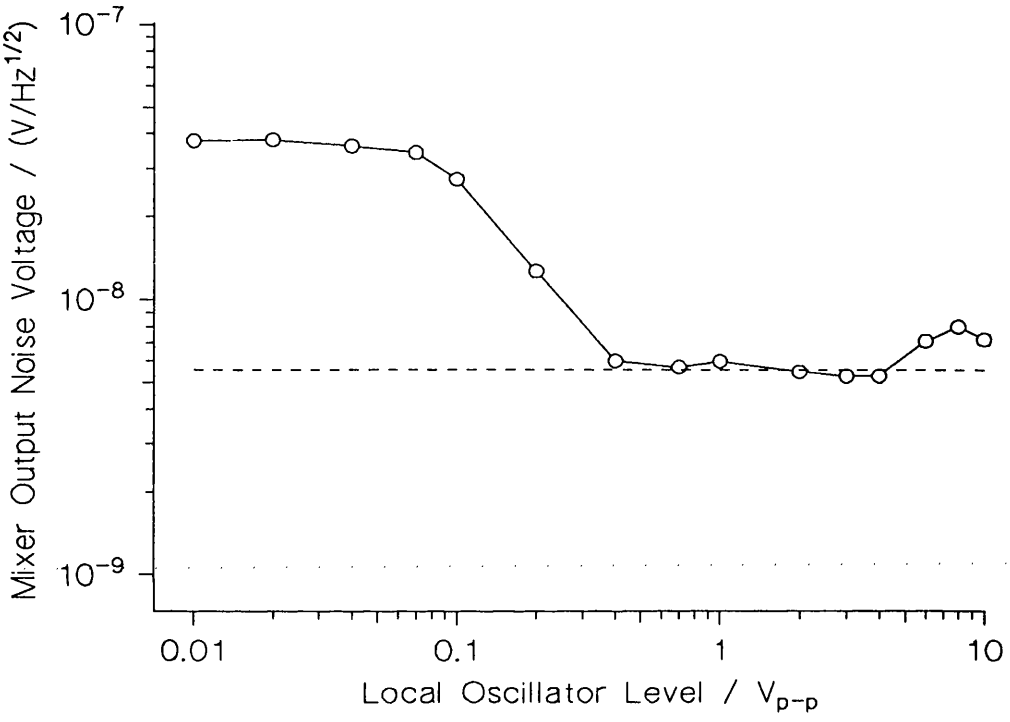

Figure 7.8 Output noise of the SRA-3 mixer as a function of local oscillator level. The dashed line shows the noise level of the Brookdeal Precision pre-amplifier.

7.4.4 Output Impedance of the Mixers Investigated.

The output impedance of the two mixers was measured simply by applying signals to the local oscillator and the signal input as described in chapter 7.4.2. The magnitude

of the open circuit output signal was then measured. The amplitude was then measured across a shorting resistance across the output and the magnitude of the resistance necessary to reduce this amplitude to half that of the open circuit amplitude noted. Taking the mixer output impedance as being in series with the shorting resistance from simple potential divider considerations this can be taken as the output impedance of the mixer.

The output impedance of the SRA-3 was measured to be $\mathbf{R_{out}}\approx\mathbf{1k\Omega}$.

The output impedance of the 429A was measured to be $\mathbf{R_{out}}\approx\mathbf{32\Omega}$.

7.4.5 Signal-to-Noise Ratio of the Magnetic Transducer.

The signal to noise ratio of the modulated signal from the magnetic transducer was measured using the 429A active mixer and the Hewlett Packard signal analyser. The active mixer was employed, as the signal from the mixer was only minimally loaded. The signal to noise ratio was measured by measuring the signal at the modulation frequency and the side band noise just away from the modulation frequency by a few Hertz over a range of local oscillator amplitudes. The magnetic transducer **MT1** was used with a modulation of $\mathbf{i_m}=\mathbf{3mA}$ at a frequency $\mathbf{f_m}=\mathbf{870Hz}$ supplied by the modulation arrangement described in chapter 6.5. The output of the matched magnetic transducer was almost $\mathbf{3V_{p\text{-}p}}$.

The expected result can be observed in Figure 7.9. Initially for small local oscillator levels the mixer essentially has a very low gain and the noise measured was that of the mixer and marginally increasing the oscillator level produces an increase in the signal to noise level. This is because the mixer output noise was unaffected by increasing the gain. Eventually for large local oscillator levels the transducer noise will be greater than the mixer noise and any increase in local oscillator level would not produce an increase in the signal to noise ratio. This occurs at a local oscillator level in the region of one to two volts in Figure 7.9. The gradual increase in the signal to noise ratio above this level

comes about probably due to the fact that the total mixer gain is only just sufficient to bring the magnetic transducer noise above that of the mixer so there was still a considerable contribution to the overall noise from the mixer. This can be seen to be decreasing as the local oscillator level increases.

The result obtained from Figure 7.9 would suggest that the mixer output noise for the present transducers would not be a limiting factor in the overall system performance as it was far out weighed by the transducer noise at the local oscillator levels employed. This would be especially true for the SRA-3 mixer which has a lower output noise than the 429A. An estimate of the ultimate noise floor cannot be made until the lock-in amplifier has been examined in more detail, as the above signal to noise ratio can be improved when measuring the signal with the lock-in amplifier by selecting a longer time constant τ with the ramifications outlined in chapter 7.2.

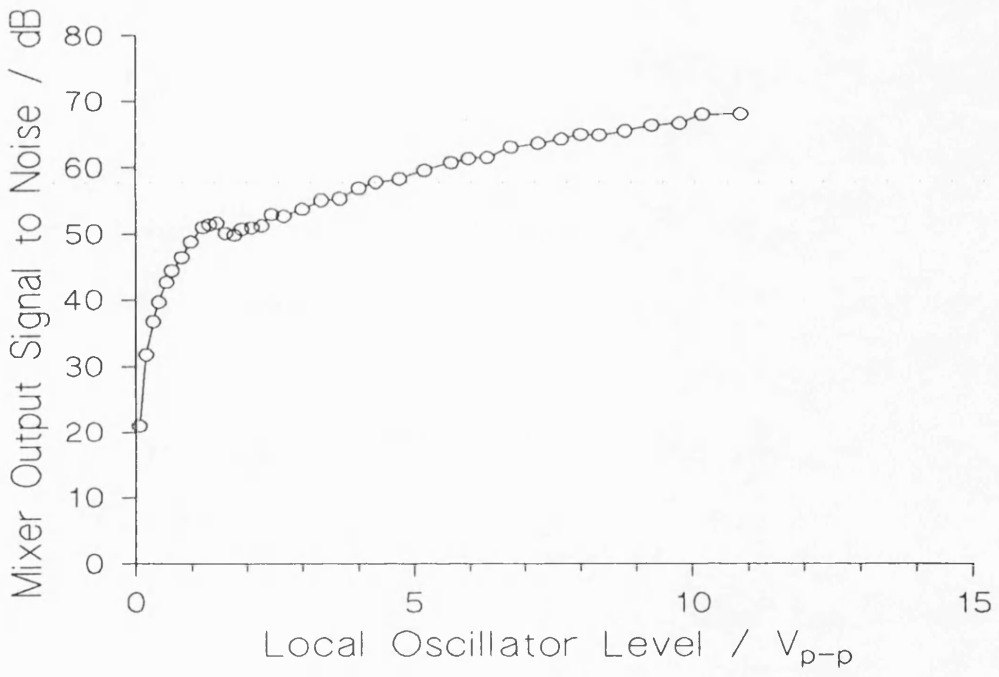

Figure 7.9 Signal to noise ratio of the 429A mixer output for an input signal from the fully matched magnetic transducer **MT1**.

7.5 Performance of the Lock-in Amplifier

7.5.1 Introduction.

Lock-in amplifiers have been described as both sensitive a.c. voltmeters as well as high-Q electronic filters, Wang [1989]. The function of a lock-in amplifier is to measure a discrete a.c. signal at a frequency determined by a reference frequency supplied to the lock-in amplifier. This can also be generated internally within the instrument. The output of the lock-in amplifier is then a d.c. signal with a magnitude proportional to the a.c. input signal amplitude. A schematic functional diagram of a typical lock-in amplifier is shown in Figure 7.10.

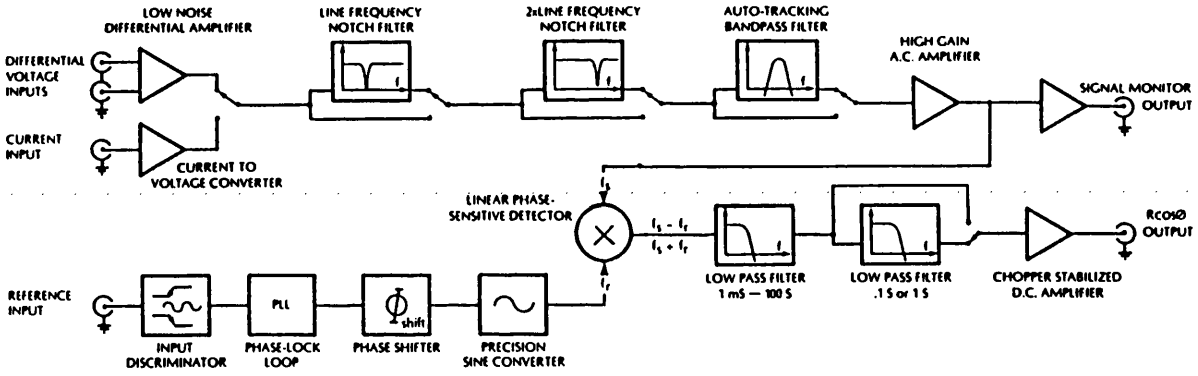

Figure 7.10 Schematic of a typical lock-in amplifier, after Wang [1989].

A lock-in amplifier consists of a number of input filters the important function being a band-pass filter which discriminates the signal frequency to be measured before undergoing high gain a.c. amplification and mixing with a variable phase reference signal. This produces a d.c. output which is filtered by a series of variable time constant low-pass filters and undergoes a d.c. gain. The gain is usually calibrated such that the output amplitude can be referred back to the magnitude of the a.c. signal measured. The reference has a variable phase so that the reference signal can be adjusted to be in phase with the signal to be measured. This is usually achieved by adjusting the phase so that no output signal is observed; the phase is then in quadrature. A fixed phase shift of 90° is then introduced making the reference either in phase or 180° out of phase. The d.c. output signal is then a maximum being positive or negative in sign depending on the fixed phase shift introduced.

If the magnitude of the input signal to be measured varies then there will be an associated frequency spectrum for the output signal containing components at the frequencies of these variation. These components are attenuated by the low pass output filter and thus for a large time constant an average of the input signal magnitude can be attained and a subsequent increase in the signal to noise ratio. The output, however, will not track the high frequency input magnitude variations. In the closed loop feedback operation discussed in chapter 7.2 the effective time constant was governed not only by the lock-in amplifier time constant but also by the loop gain. The signal to noise ratio of the input signal at the output of the lock-in amplifier can, therefore, be improved by increasing the lock-in amplifier time constant provided sufficient loop gain can be achieved to compensate for the subsequent decrease in the magnetometer systems measurement bandwidth. The limiting noise contribution to the magnetometer system would then potentially come about due to the output noise of the lock-in amplifier. This

contribution is discussed in detail in this chapter for two different lock-in amplifiers although four instruments were investigated and employed during the magnetometer development. All performance figures quoted are RMS unless stated otherwise.

7.5.2 Lock-in Amplifier Output Noise.

The output noise of the lock-in amplifier in the magnetometer system generates a noise current in the feedback resistor and the feedback coil and a subsequent magnetic noise field in the feedback coil. This noise field in the feedback coil dictates the minimum field fluctuations that can be detected by the magnetometer system. Four lock-in amplifiers were investigated. Two E. G. & G. Princeton Applied Research instruments the 5210 and 5207 lock-in amplifiers, the higher performance 5210 only being discussed here. A Brookdeal Phase Sensitive Detector 9412A used to obtain the results of Squire and Gibbs [1988a] which will be covered briefly, and a Stanford Research Systems SR510 Lock-in Amplifier which will also be covered in detail.

Figure 7.11 shows comparative time domain output traces showing the output noise measured on a chart recorder for both the Brookdeal 9412A and the Stanford SR510. In both cases a reference signal of $\mathbf{f_m}$**=970Hz** was applied and the time constant selected as τ**=100ms**. The inputs of the lock-in amplifiers were terminated with an input resistance $\mathbf{R_{in}}$**=50Ω**. The 9412A had two outputs and the trace shows the more stable "B" output which had a fixed gain of seven. The sensitivity of the SR510 was **100mV** equating to an RMS gain of 500. In the case of the SR510 the gain was selected so that only output noise was measured, the gain being low enough so that no input noise was observed and so reducing the gain further would not produce any gross change in the noise magnitude. The Dynamic Reserve on the SR510 was set to the low setting giving the greatest output stability. An attempt was made to reduce this noise in the SR510 output by replacing the output amplifier of the instrument with a high stability commutating auto-zero d.c.

amplifier as in Edgar [1989]. No improvement was attained and it was concluded that the major source of output noise came about from phase noise in the lock-in amplifier reference unit.

The output noise was also measured in 1-17Hz bandwidth under the same conditions using the Hewlett Packard 3561A Spectrum Analyser. The RMS noise voltages and the equivalent field noise in the **1311** turns per metre feedback coils for a feedback resistor of $\mathbf{R_f}$**=2kΩ** are shown in Table 7.2. The estimated field noise can be seen to be substantially larger than the minimum detectable field of 2.5pT proposed in chapter 1.2.4.3 and potentially a considerable contribution to the figure measured for the system by Squire and Gibbs [1988a]. The contribution to the field noise from the lock-in amplifier output noise can be reduced by either increasing the feedback resistance $\mathbf{R_f}$ or decreasing the number of turns per metre on the feedback solenoid **n**. This, however, has the effect of reducing the loop gain **K**, equation 7.10. The Johnson noise contribution from the feedback resistor at ambient temperature can be estimated from the standard expression given in equation 7.20. This is insignificant for feedback resistors much less than $\mathbf{R_f}$**=1MΩ** being of the order of $\mathbf{12fT/(\Omega Hz)^{1/2}}$.

$$V_{noise_{RMS}} = \sqrt{4kTR_f} \qquad V/Hz^{1/2} \qquad 7.20$$

Table 7.2 Lock-in amplifier output noise measured using spectrum analyser

Lock-in amplifier model.		RMS Noise voltage $\mu V/Hz^{1/2}$	Estimated RMS field noise $pT/Hz^{1/2}$ (R_f=2kΩ)
SR510		183.2	150
9412A	"A"	145.5	120
	"B"	4.4	4

Figure 7.11 Comparison of two lock-in amplifier output noise voltages measured on a chart recorder for both the Brookdeal 9412A and the Stanford SR510. The reference signal was at a frequency of f_m=**970Hz** and the time constant selected as τ=**100ms**. The inputs of the lock-in amplifiers were terminated with an input resistance R_{in}=**50Ω**.

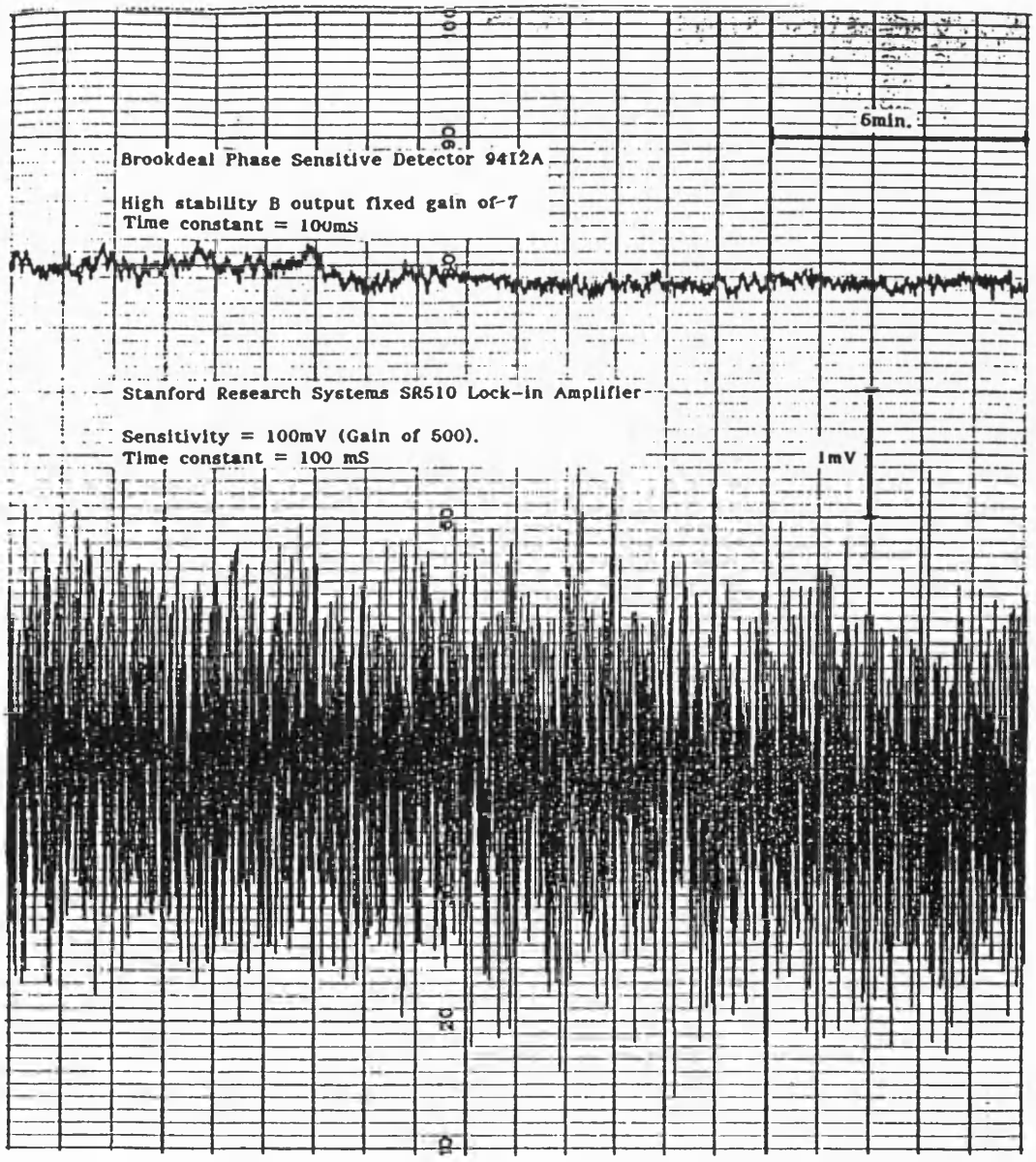

Although the 9412A demonstrated a considerably lower noise floor than the SR510, reliability problems as well as the instrument being generally less flexible led to an alternative low noise instrument being identified: the E. G. & G. 5210. The noise specification of this instrument along with the Stanford SR510 purchased as a dedicated unit for the shear wave magnetometer project will be discussed in terms of estimating an instrument limited, minimum attainable noise floor.

Figure 7.12 shows the effect on the measured noise voltage for the SR510 on increasing the lock-in amplifier time constant. The lock-in amplifier sensitivity used was **1mV** and was chosen such that only output amplifier noise was measured. The input was left open circuit. The output amplifier demonstrates a frequency dependence of the output noise which approaches the classic **1/f** noise for amplifiers. The spectra demonstrate a decrease in the output noise with increasing time constant.

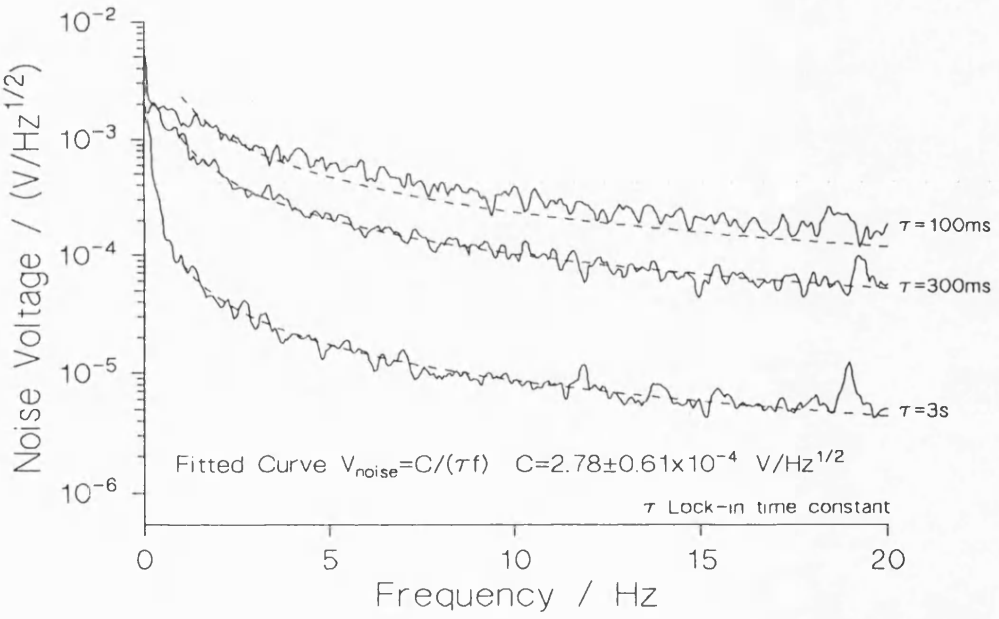

Figure 7.12 Time constant dependence of the output noise of the Stanford Research SR510 Lock-in Amplifier. The fitted curves are shown by dashed lines.

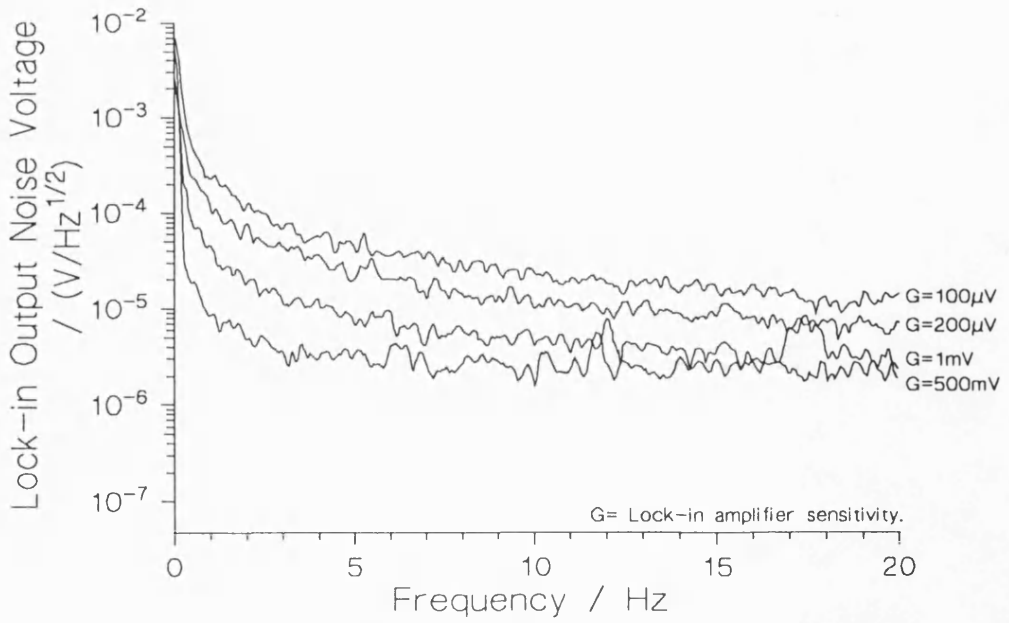

Figure 7.13a Measured output noise spectra for a range of lock-in amplifier sensitivities for the Stanford Research SR510 lock-in amplifier.

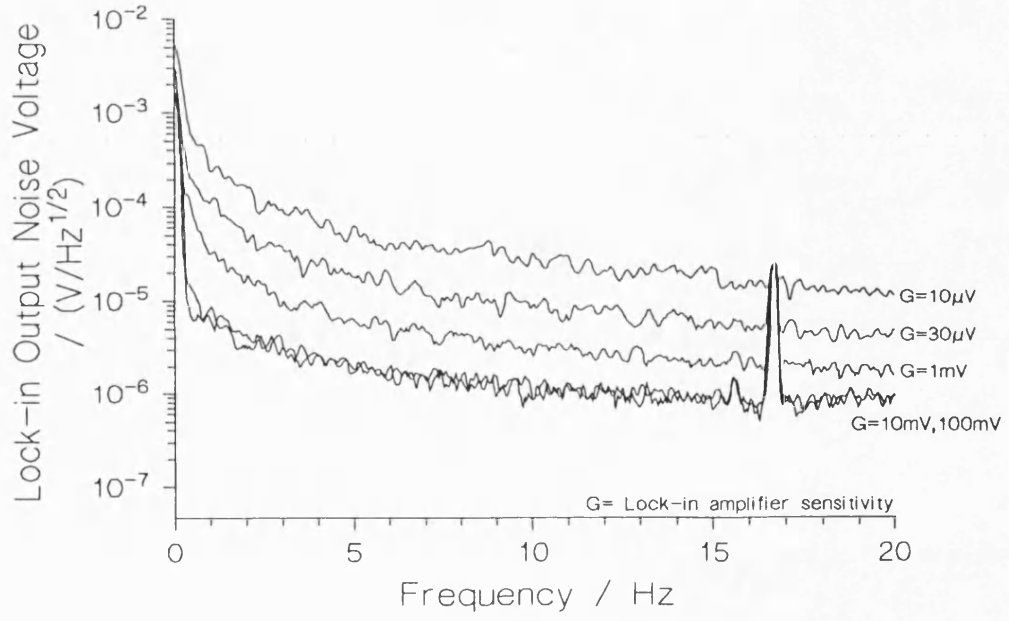

Figure 7.13b Measured output noise spectra for a range of lock-in amplifier sensitivities for the E. G. & G 5210 lock-in amplifier.

Figure 7.13a and Figure 7.13b show the noise spectra over a range of lock-in amplifier sensitivities for both the SR510 and the 5210 lock-in amplifiers respectively. The figures show an RMS average of the measured spectrum over sixteen measurement. An input resistance of $\mathbf{R_{in}=110k\Omega}$ was selected as being an optimum from the amplifier noise contours from the Stanford Research Systems lock-in handbook. This gives an optimum noise performance for the input amplifier of the lock-in amplifier although substantially increasing the Johnson noise which then dominates the input noise. The time constants selected on both instruments were τ**=3s** and the dynamic reserve was set low. Both lock-in amplifiers demonstrated a sensitivity region for which there was no change in the measured noise with lock-in amplifier gain. The quantity measured in this region was taken as the lock-in amplifier output amplifier noise. For higher gains the noise was a combination of output amplifier noise, input amplifier noise and Johnson noise from the source resistance $\mathbf{R_{in}}$. This gain region for the 5210 was for sensitivities above **10mV**, whereas, for the SR510 this occurred in a sensitivity region between **1mV** and **100mV**. Above a sensitivity of **100mV** a further decrease in the output noise was observed. The signal observed at 16.5Hz in Figure 7.13b can be ignored as it is outside the bandwidth of interest.

The output noise of the two lock-in amplifiers can be summarised as shown in Figure 7.14 by plotting the result of an integration of the noise spectrum over a fixed bandwidth and dividing the results by the root of the bandwidth. As mentioned in chapter 2 - concerning magnetometer performances this does not give a technically complete result ignoring the non-white noise nature of the spectrums. This does, however, enable easy comparisons to be made. Examination of Figure 7.14 shows that for peak to peak gains of between $\mathbf{10^3}$ and $\mathbf{10^2}$ the 5210 returns a noise voltage an order of magnitude less than that of the SR510. If a feedback resistor $\mathbf{R_f=2k\Omega}$ is used then this corresponds to a noise field of approximately $\mathbf{3pT/Hz^{1/2}}$ in the 1311 turns per metre feedback solenoid.

In practice for the current magnetic field sensor elements this does not represent sufficient gain for a magnetometer system with reasonable measurement bandwidth. For a sensitivity of **1mV** the noise measured from the 5210 was only marginally lower than the SR510. The noise for the 5210, however, does not increase further for a gain increase of an order of magnitude. The potential, therefore exists to increase the feedback resistance by an order of magnitude and compensating for the loss in loop gain by an increase in lock-in amplifier gain giving a minimum potential field noise of $\mathbf{2pT/Hz^{1/2}}$ for a feedback resistor $\mathbf{R_f=20k\Omega}$ at a lock-in sensitivity of **1mV**. It should be noted at this point that the output impedance of the 5210 was specified and has been measured using the method described in chapter 7.4.4 as $\mathbf{R_o=1k\Omega}$, whereas, that of the SR510 was claimed to be $\mathbf{R_o<1\Omega}$ and was measured to be of the order of $\mathbf{R_o\approx100\Omega}$. The output impedance effectively produces a potential divider network with the feedback solenoid and resistor reducing the perceived field noise and also the loop gain for small feedback resistors. This was more prominent for the 5210 lock-in amplifier.

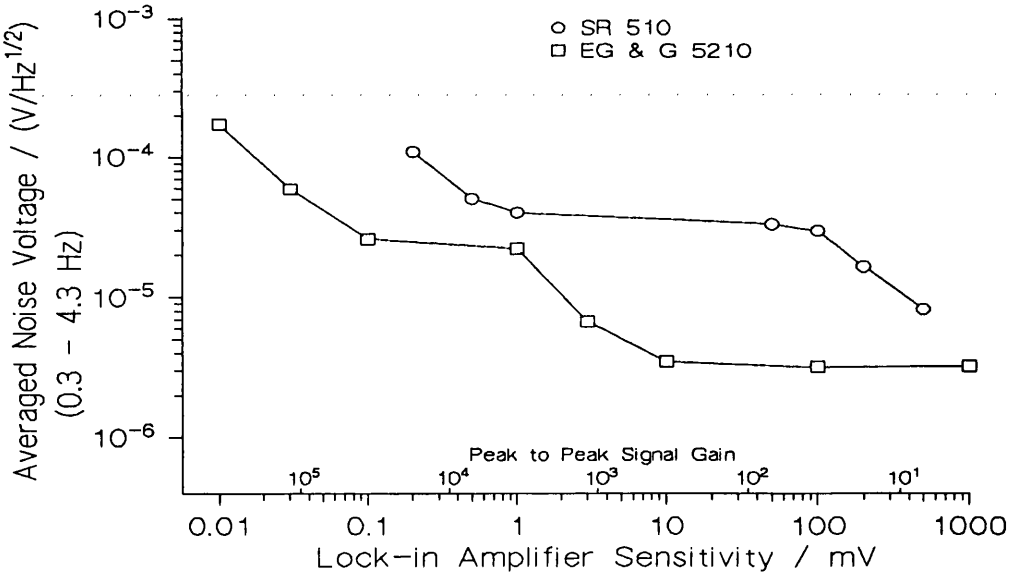

Figure 7.14 Comparison of the two lock-in amplifier output noise voltages for a range of lock-in amplifier sensitivities.

Figure 7.15 demonstrates the estimated magnetic field noise as a function of lock-in amplifier gain for a variety of input terminations to the SR510 lock-in amplifier and for the passive SRA-3 mixer connected to the 5210 lock-in amplifier. In all the cases shown the feedback network of solenoid and resistor was connected to the output and the noise averaged over a **0.3 - 4.3 Hz** bandwidth measured across both the solenoid and the feedback resistor of $\mathbf{R_f=2k\Omega}$. The lock-in amplifier time constant was τ**=3s**. Both the inputs of the two mixers were supplied with identical input signals of frequency $\mathbf{f_o=1MHz}$ with amplitudes so as to place the operation of the SRA-3 mixer within the low noise region demonstrated by Figure 7.8. Under this new set of conditions the magnetic field noise demonstrated a similar form to that expected from Figure 7.15 with some minor variations.

In general over a range of gains the noise measured from the SR510 was seen to be insensitive to changes in gain and it was concluded that this was purely output amplifier noise. Similar to Figure 7.14 an improvement in performance was observed for low gains above a sensitivity of **100mV**. Depending on the input termination the pick-up point for which the gain was large enough to make the input noise dominant was seen to change. This was at higher gains for an input impedance $\mathbf{R_{in}=110k\Omega}$ than for open circuit. For an open circuit input amplifier current noise dominates, whereas, for $\mathbf{R_{in}=110k\Omega}$ the input amplifier was optimised and the input resistor Johnson noise dominated and was smaller in magnitude than the open circuit current noise. For a much lower input impedance and thus lower resistor Johnson noise, the pick-up was seen to move to yet higher gains suggesting that the major contribution to the input amplifier noise came from current noise and not from input amplifier voltage noise.

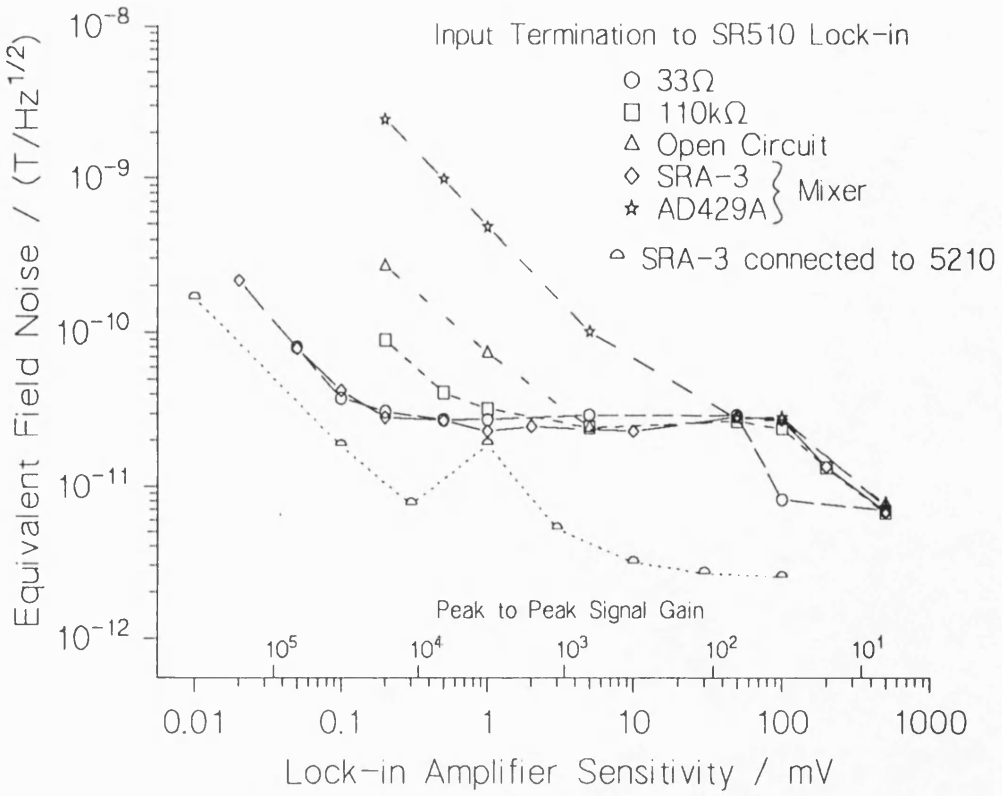

Figure 7.15 Measured output noise for the SR510 lock-in amplifier over a range of sensitivities for different input impedances

As would be expected the higher output noise of the AD429A mixer as measured in chapter 7.4.3 results in a considerable contribution to the total field noise for far lower lock-in amplifier gains than the SRA-3. Although the 429A does not present the same load restrictions on the input signals as the SRA-3 the maximum signal amplitude currently attainable after fine tuning from the **MT1** transducer was of the order of $\mathbf{4V_{p\text{-}p}}$. This only represents at maximum an improvement of one order of magnitude in the mixer output signals if both mixers had identical gains. To justify replacing the SRA-3 with the 429A to attain the same minimum noise floor the lock-in amplifier sensitivity when operating the magnetometer in the closed loop mode with the SRA-3 mixer would have to be of the order of **10mV**. Comparison of the field noise brought about from what

would appear to be mixer output noise in Figure 7.15 gave close agreement to the mixer output noise voltages measured in chapter 7.4.3.

The results for the combination of SRA-3 mixer and 5210 lock-in amplifier would suggest a optimum operating point at a sensitivity of **300μV** or at much lower gains. The arrangement did not preform substantially better at a sensitivity of **1mV** than the SR510 arrangement as would be expected from Figure 7.14. For both arrangement an increase in feedback resistance should increase the performance of the magnetometer provided sufficient lock-in amplifier gain is available to compensate for the loss in total loop gain without amplifying the lock-in amplifier input noise.

7.5.3 Comparison of the Estimated and Measured Equivalent Field Noise.

The equivalent field noise discussed in chapter 7.5.2 was estimated from voltage noise measurement from which current noise through the feedback resistor was calculated. From the current noise the magnetic field noise in the feedback solenoid was calculated from the equation for an infinitely long solenoid. To confirm the validity of these results the magnetic field noise in the feedback solenoid with the lock-in amplifier was measured directly using a very low noise fluxgate magnetometer supplied by Thorn EMI Naval Systems, Rugeley, Staffordshire. The magnetometer had a specified noise floor of $\mathbf{50pT_{p-p}/Hz^{1/2}}$ and a **2Hz** bandwidth. The magnetic field noise was measured halfway along the length of the feedback solenoid with the solenoid placed in a two layer Permalloy can to shield against environmental magnetic noise. The environmental magnetic noise within the shield is discussed in chapter 7.6.

Figure 7.16 shows the magnetic field noise spectrum measured using the fluxgate magnetometer and the spectrum analyser. The spectrum was a single measurement no averaging of successive spectrums being undertaken. The spectrum shows the magnetic

field noise in the feedback solenoid connected to the SR510 lock-in amplifier with an input termination of $\mathbf{R_{in}=33\Omega}$. The lock-in amplifier sensitivity was **1mV** and the time constant τ=**3s**. The figure of $\mathbf{49pT_{RMS}/Hz^{1/2}}$ agrees closely with that predicted in Figure 7.15. A marginally higher noise would be expected as the measurement was taken over a narrower band at a lower frequency. Similar agreement was obtained for other gain settings.

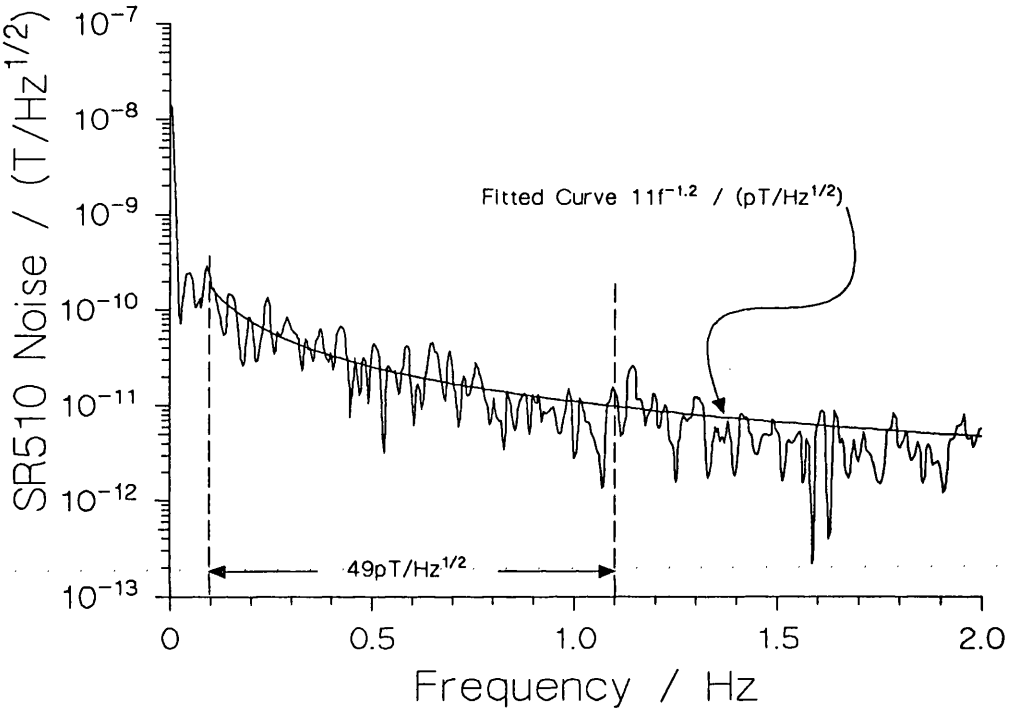

Figure 7.16 Magnetic Field noise measured within the feedback solenoid using a very low noise fluxgate magnetometer. The SR510 lock-in amplifier was connected to the solenoid.

7.5.4 Effect of Large Amplitude Second Harmonic Input Signals.

In chapter 6 the output of the mixer element was investigated in terms of the harmonics of the signal at the modulation frequency. When operating the magnetometer

system in the closed loop mode the fundamental signal is nulled so that the system operates at a zero field point. The second harmonic signal is then the dominant signal applied to the lock-in amplifier input and can be of considerable magnitude. The effect of this signal on the lock-in amplifier output noise depends on how effective the lock-in amplifier input filtering discriminates the signal at the fundamental frequency from that at the second harmonic of the modulation frequency. This was investigated for the SR510 lock-in amplifier by examining the dependence on the output noise of the instrument for a range of second harmonic input amplitudes. A reference signal at a frequency of $\mathbf{f_m=970Hz}$ was supplied to the lock-in amplifier from a Philips PM5190 synthesizer. A second Philips synthesizer was used to supply an input signal to the lock-in amplifier at a frequency $\mathbf{f_2=1922Hz}$. A frequency **18Hz** away from the true second harmonic was chosen to prevent beating of the two incoherent signals observed when a frequency $\mathbf{f_2=1940Hz}$ was selected. The frequency shift removed the effect from the low frequency band of interest. The lock-in amplifier output noise power in a bandwidth of **0 - 15 Hz** was measured using the 3561A spectrum analyser for a range of second harmonic amplitudes at different lock-in amplifier gains. Figure 7.17 shows the output noise power averaged over ten readings against the amplitude of the second harmonic signal. In all the cases the output noise power remained approximately constant until a critical second harmonic amplitude was reached at which point a sharp rise was seen in the noise power.

An approximate value for the critical second harmonic amplitude can be extracted from Figure 7.17 by estimating the base noise level and the gradient of the noise power rise. Figure 7.18 shows the maximum second harmonic input amplitude for which there was no increase in the output noise power against the lock-in amplifier sensitivity.

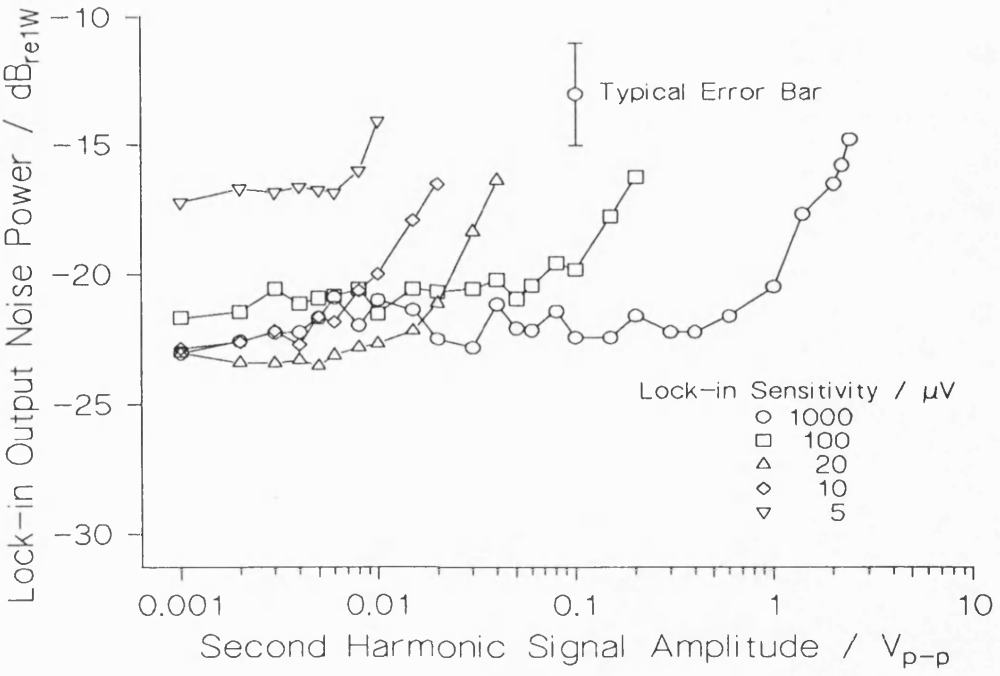

Figure 7.17 SR510 lock-in amplifier output noise power as a function of the amplitude of the second harmonic.

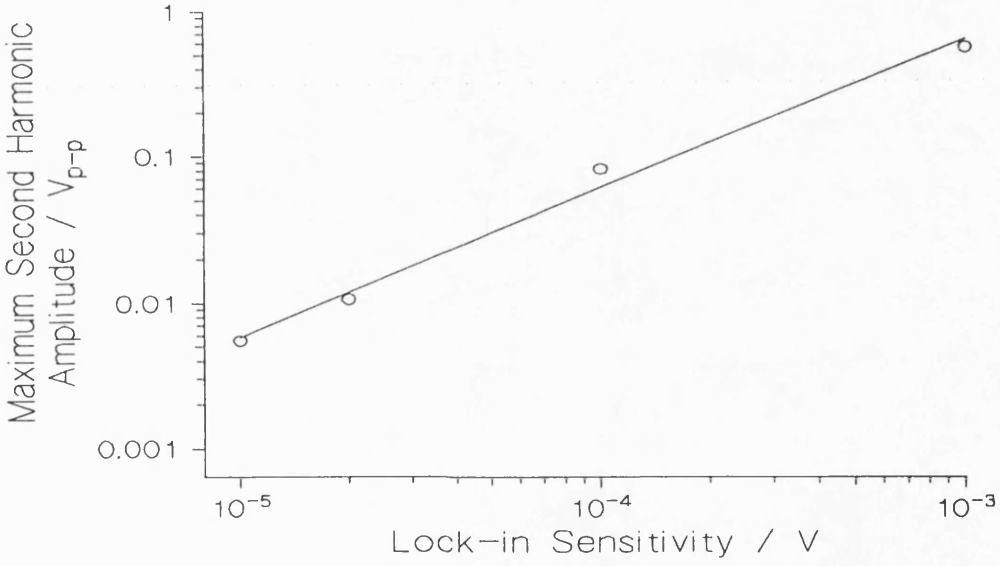

Figure 7.18 Maximum second harmonic amplitude against lock-in amplifier sensitivity.

Any potential increase in the amplifier noise was reduced by the construction of a low noise amplifier designed specifically to filter the second harmonic component of the mixer output signal before passing the signal to the lock-in amplifier. Figure 7.19 shows the functional form of the filter amplifier. A TTL reference signal was obtained from the modulation signal generator. The phase of this signal was compared with the signal from a voltage controlled oscillator after dividing the frequency of the signal by two. The output of the phase detector after filtering and amplification then produces a correction signal which adjusts the free running frequency of the VCO so that the input from the frequency divider was locked to the reference frequency. The output of the VCO was, therefore, at twice the reference frequency. This signal then underwent a manual phase shift and amplitude adjustment as well as passive filtering before being applied to a low noise differential amplifier. For a correct phase and amplitude adjustment the output signal from the amplifier at the second harmonic to the reference can be vastly attenuated. This is essentially a very selective notch filter.

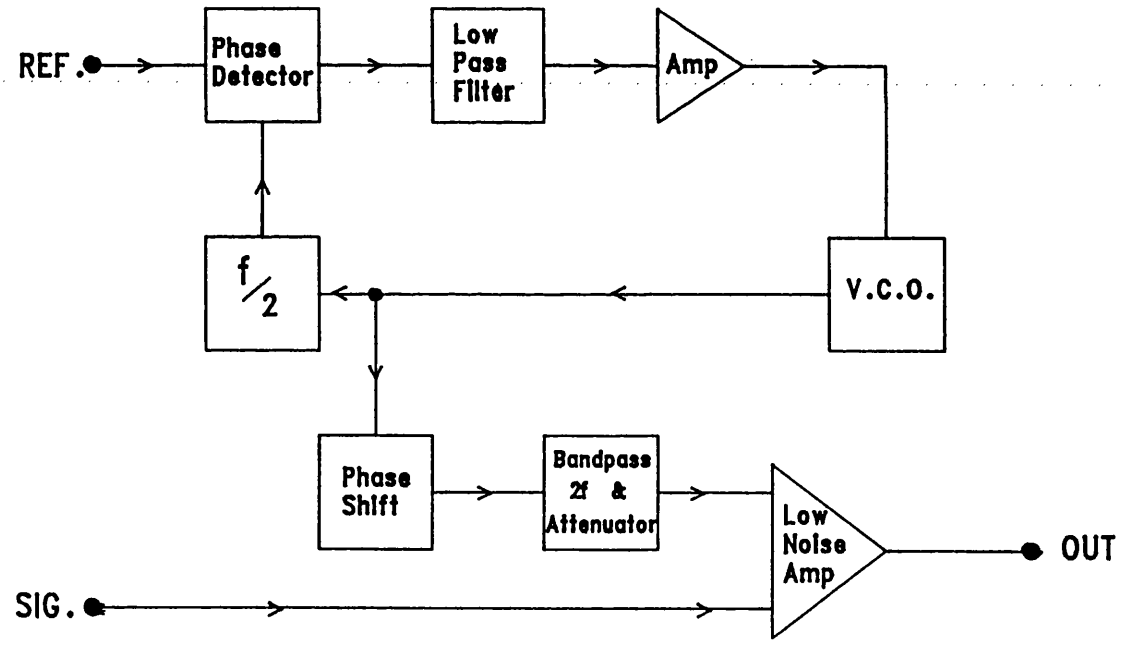

Figure 7.19 Functional diagram of active second harmonic filter

Figure 7.20 shows the circuit diagram for the filter/amplifier circuit. The amplifier employed was an ultra low noise audio preamplifier the SSM-2015. This had a specified noise performance of **1.3nV/Hz$^{1/2}$** and full d.c. coupling. The second harmonic signal was generated using a 565 phase locked loop. The system was designed to operate at a fundamental frequency of **f_m=870Hz** and provided a variable signal gain **G=7.5 to 1080.** The second harmonic rejection attainable when connected as part of the magnetometer system was **18dB** and the amplifier noise referenced to the input was measured as **3.2nV/Hz$^{1/2}$** at **1kHz** for a gain of **G=1000.**

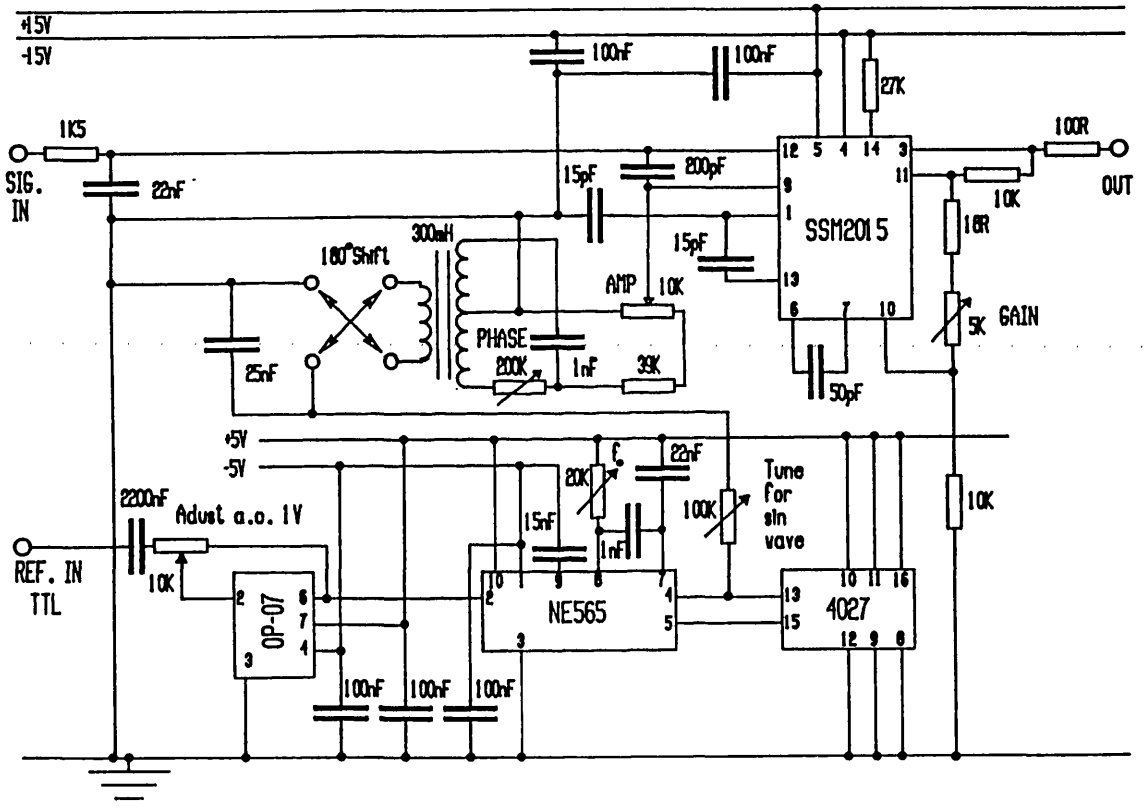

Figure 7.20 Circuit diagram for second harmonic filter.

7.6 Performance of the Shear Wave Magnetometer System.

7.6.1 Introduction.

The ultimate magnetic field noise floor of the shear wave magnetometer system was obtained by measuring the output of the magnetometer system operating under the optimum conditions dictated by the modulation amplitude and frequency, the feedback loop gain and the minimum noise operating conditions for the magnetometer instrumentation components. The magnetic field noise of the magnetometer was measured across the feedback resistor with the magnetic transducer and the feedback and modulation solenoids placed in the two layer Permalloy can. A further calibration solenoid was also placed in the can so that known external magnetic fields could be applied using either a Time Electronics d.c. Current Calibrator or a Brookdeal 9472 Signal Source for a.c. signals. From the noise measurements carried out on the lock-in amplifier and the other combination of system components in chapter 7.5 it would be expected that the noise floor of the system would be equal to or greater than the values estimated from these measurements. The measurements of chapter 7.5.3 would also suggest that the environmental noise within the shielding cans was less than the field noise generated by the instrumentation. The environmental noise was measured, however, using the same method described in chapter 7.5.3. The feedback and modulation coils were shorted and the calibration coil connected to the Current Calibrator. Figure 7.21 shows the output noise measured from the fluxgate magnetometer. The magnetic field noise averaged over a **1Hz** bandwidth corresponds closely to that specified for the magnetometer. This would suggest that the environmental noise was less than this and that also the current calibrator did not contribute significant noise. In addition to this no significant low frequency field noise was observed when connecting the modulation signal or the a.c. calibration signal.

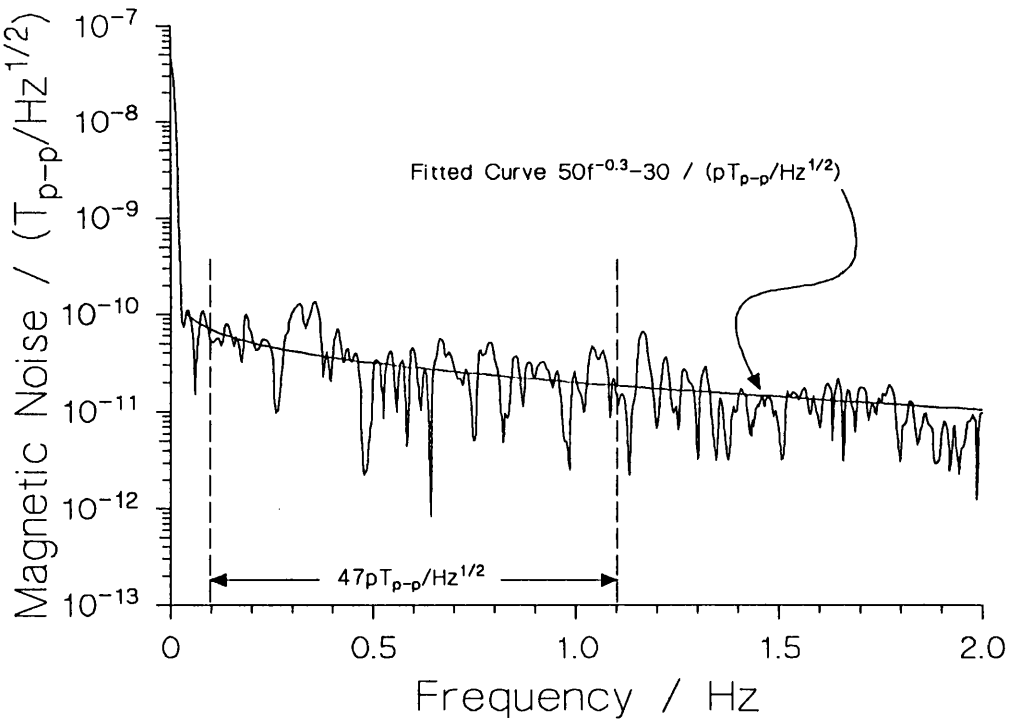

Figure 7.21 Magnetic noise measured in Permalloy shielding cans using Thorn EMI fluxgate magnetometer

The magnetic field frequency spectrum of primary interest for the application of a true d.c. magnetometer was d.c. and low frequency magnetic fluctuations. An approximate target specification was therefore chosen for the measurement of d.c. magnetic field up to a bandwidth of **10Hz**. This specification gave a target region for selecting lock-in amplifier time constant and total loop gain and hence the system operating bandwidth. A standard set-up procedure was adopted for the magnetometer system which was found in general to return reproducible optimum magnetometer performances.

1. The magnetic transducer was placed in the shielding cans along with the solenoid arrangement. The transducer was connected to the PM5193 drive oscillator and input matching unit and the output observed on an oscilloscope with a variable inductance tuning termination. The drive frequency was then tuned for resonance and the inductance for optimum output amplitude. The transducer output was then connected to the mixer element.
2. A modulation signal was then applied at the optimum frequency of $\mathbf{f_m}$**=870Hz** and a modulation current amplitude around $\mathbf{i_m}$**=5mA**. The mixer output was connected to the oscilloscope and the d.c. component zeroed by fine tuning the drive frequency about the resonance frequency. A signal at harmonics of the modulation frequency should be observed at the mixer output.
3. A large decaying a.c. demagnetising field was then applied to the calibration solenoid using a Variac. This demagnetised the transducer and produced a mixer output signal with a prominent second harmonic component.
4. The mixer output was then connected to the lock-in amplifier via the pre amp filter if required (the lock-in output unconnected). For a low lock-in amplifier sensitivity and a time constant τ**=100ms** the quadrature point was found by adjusting the reference phase. A 90° phase shift was then introduced so that on connecting the lock-in output to the feedback resistor and solenoid, nulling of the fundamental signal from the mixer occurred. The second harmonic filter was set up after complete locking of the magnetometer system.
5. With the system locked the modulation current was reduced to a lower amplitude to achieve the optimum gain discussed in chapter 7.3.
6. The time constant could then be increased followed by an increase in the lock-in amplifier sensitivity to compensate for the loss in magnetometer bandwidth. Any d.c. offset magnetic signals can be nulled using the d.c calibration source.

The effect on the noise performance of the magnetometer on reducing the modulation current amplitude is summarised in Figure 7.22. Adopting the set-up procedure described above the noise for the magnetometer system was averaged over a bandwidth of **1Hz** for a range of modulation amplitudes. The 5210 lock-in amplifier was used for these measurements along with the SRA-3 mixer. The lock-in amplifier time constant was τ**=3s** and the lock-in amplifier sensitivity on its adjustable vernier range between **1mV - 300**μ**V**. The feedback resistor was R_f**=2k**Ω.

Figure 7.22 shows a decrease in the magnetometer noise floor with decreasing modulation current. This corresponds to an increase in the slope of the fundamental response signal from the mixer as measured in chapter 7.3 and hence an increase in loop gain. The sensitivity of the lock-in amplifier was marginally adjusted for each measurement to retain a magnetometer measurement bandwidth of approximately **4Hz.** The discontinuities observed in the magnetic transducer amplitude and phase response curves have been suggested as the cause for the increase in the fundamental response. It was suggested that the modulation signal gives an averaging over its amplitude and hence the discontinuities become more prominent for lower modulation amplitudes down to a point where the modulation amplitude becomes less than the separation of the discontinuities on the amplitude and phase response hysteresis curves. This could possibly explain the increase in the noise floor below i_m**=2.5mA**. Other instrumentation noise sources also become more predominant for low modulation amplitude signals.

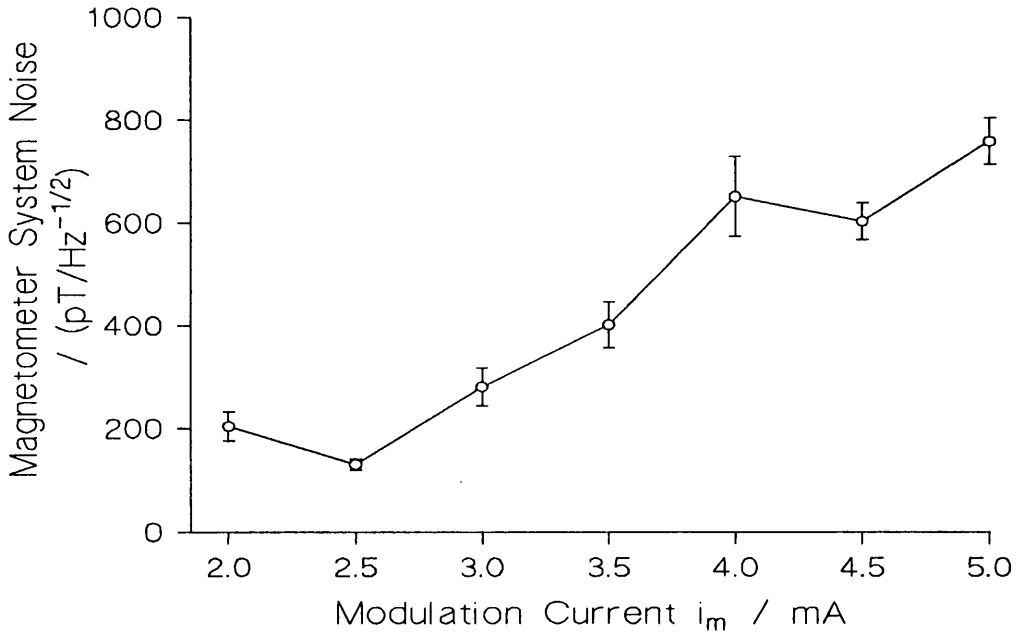

Figure 7.22 Magnetometer system noise measured as a function of the modulation amplitude (0.1 - 1.1 Hz frequency band).

7.6.2 Magnetometer Noise Characterisation in the Frequency Domain.

The magnetometer system was set-up as described in chapter 7.6.1 using a variety of different component models. The magnetometer output noise was measured across the feedback resistor using the Hewlett Packard Spectrum Analyser and in addition to the standard magnetometer arrangement the mixer output d.c. nulling feedback discussed in chapter 8 was implemented. The function given in chapter 2.7 equation 2.25 was fitted to all the magnetic field noise spectra shown. All the spectra were obtained using the **MT1** magnetic transducer tuned to its resonance at approximately $\mathbf{f_0=1MHz}$ giving a peak to peak output signal of approximately $\mathbf{4V_{p\text{-}p}}$ when fully matched. The modulation signal used in all cases was at a frequency $\mathbf{f_m=870Hz}$ and an amplitude $\mathbf{i_m=2.5mA}$. The lock-in time constant in all cases was τ**=3s**. The curves show the lowest field noises achieved for the instrumentation arrangements discussed.

Figures 7.23a & b show the magnetic field noise spectra for the magnetometer using the SR510 lock-in amplifier and the SRA-3 mixer. The bandwidth of the system operating with a lock-in sensitivity of **1mV** and a feedback resistor $\mathbf{R_f=2k\Omega}$ was approximately **7Hz**. These conditions were found to be an optimum for this arrangement and a magnetic field noise averaged over **1Hz** (0.1 - 1.1Hz) returned a figure of $\mathbf{130pT/Hz^{1/2}}$. The two separate traces in Figure 7.23b were successive measurements taken over different measurement bandwidths of the spectrum analyser. The non matching of the results at **0.1Hz** emphasises the difficulties encountered in making low frequency measurements of this type, Snare and McPherron [1973]. This also applies to Figures 7.24b & 7.26b; the spectra of Figure 7.25b are untypical in that they match at the overlap frequency.

For a sensitivity of **1mV** the lock-in amplifier was on the output amplifier dominated noise floor suggested by Figure 7.15 and although the measured noise figure was greater than that predicted by Figure 7.15 it is approaching this value. Increasing the lock-in amplifier time constant did not produce an increase in performance as a substantial increase in lock-in sensitivity was then required to compensate for the fall in bandwidth, Figure 7.3. This had the effect of taking the system into the higher gain region in Figure 7.15 where other noise contributions became prominent.

Substitution of the 429A mixer for the SRA-3 and the adjustment of the lock-in sensitivity to **5mv** to compensate for the increased loop gain and thus maintain the **7Hz** bandwidth gave a result of $\mathbf{253pT/Hz^{1/2}}$ for the averaged system noise. This increase would be expected from Figure 7.15 as the increase in gain when using the 429A was not sufficient to offset the increase in noise. The extra gain would have to allow the lock-in sensitivity to be reduced to the order of **50mV** to regain the previous conditions. Again this field noise was greater than the minimum predicted.

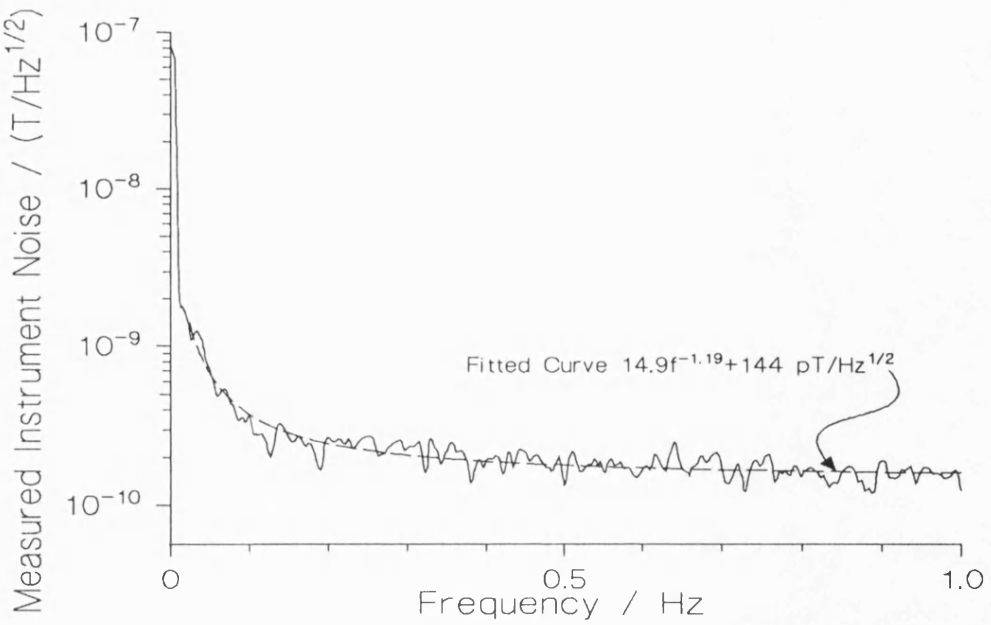

Figure 7.23a Linear frequency spectrum showing magnetic noise for magnetometer employing SR510 lock-in amplifier $\mathbf{R_f}$=**2kΩ**.

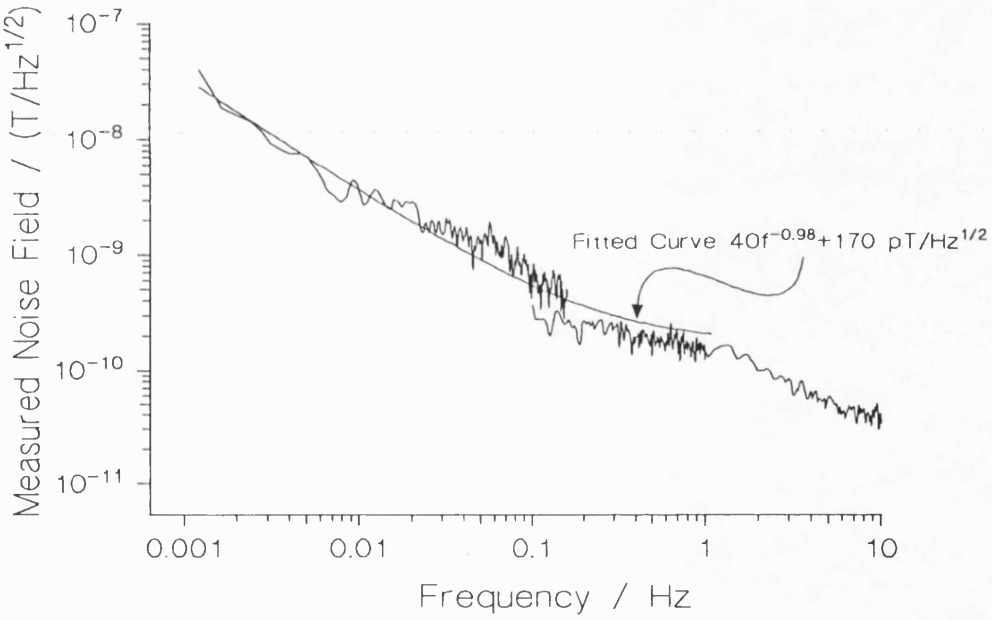

Figure 7.23b Logarithmic frequency spectrum showing magnetic noise for magnetometer employing SR510 lock-in amplifier $\mathbf{R_f}$=**2kΩ**.

Figures 7.24a & b show the magnetic field noise spectra for the magnetometer using the 5210 lock-in amplifier and the SRA-3 mixer. The bandwidth of the system operating with a vernier lock-in sensitivity of **1mV - 300μV** and a feedback resistor $\mathbf{R_f=2k\Omega}$ was approximately **4Hz**. This bandwidth reflects the loss in gain brought about by the higher lock-in amplifier output impedance. The low frequency magnetic noise can still be compared with that obtained for the SR510 as the bandwidth measured was below this three dB point. The field noise averaged over the **1Hz** (0.1 - 1.1Hz) bandwidth returned a figure of $\mathbf{122pT/Hz^{1/2}}$. This figure does not reflect the decreased noise floor for very low frequencies observed in Figure 7.24b. From Figure 7.15 in the lock-in sensitivity region used a decrease in the noise floor would be expected if the output was mixer and lock-in amplifier instrument limited. A decrease was observed, although, the noise floor was still greater than that predicted.

Figures 7.25a & b show the effect on the 5210 lock-in amplifier system on increasing the feedback resistance to $\mathbf{R_f=22k\Omega}$. The lock-in amplifier sensitivity was adjusted to the vernier scale **300μV - 100μV** to compensate for the loss in bandwidth on increasing the feedback resistance. An improvement in the noise floor was observed but not by an order of magnitude as would be expected if the lock-in amplifier output noise was the sole noise contribution. This would suggest a limiting noise contribution from the magnetic transducer. The **1Hz** bandwidth averaged noise was $\mathbf{112pT/Hz^{1/2}}$. Again this does not reflect the improved performance at low frequencies

Increasing the feedback resistance further to $\mathbf{R_f=42k\Omega}$ as shown in Figures 7.26a & b had little effect on the higher frequency performance and in-fact produced a degradation in the low frequency noise performance.

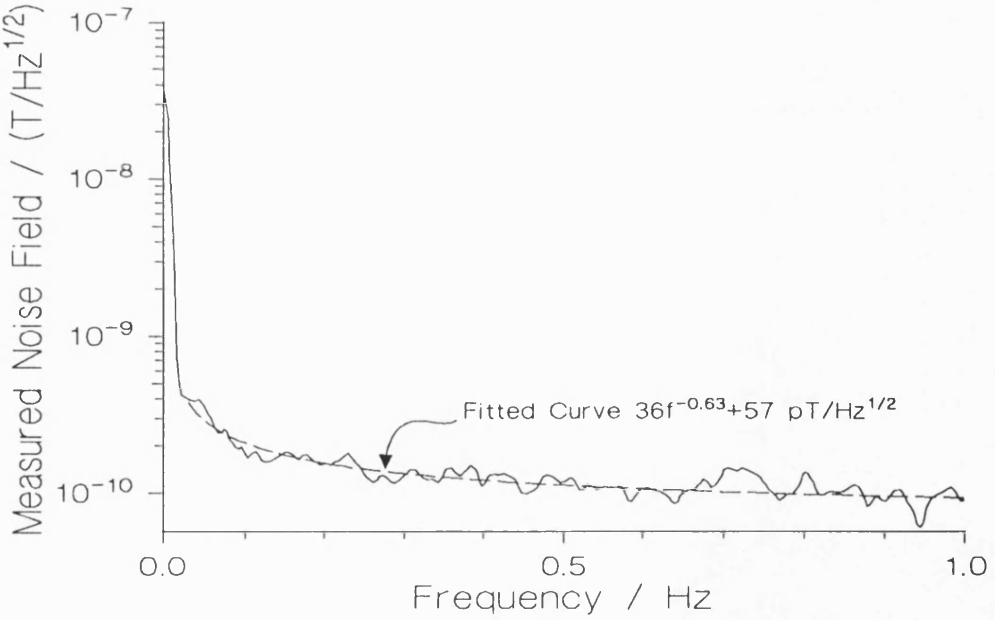

Figure 7.24a Linear frequency spectrum showing magnetic noise for magnetometer employing 5210 lock-in amplifier $\mathbf{R_f}$=2kΩ.

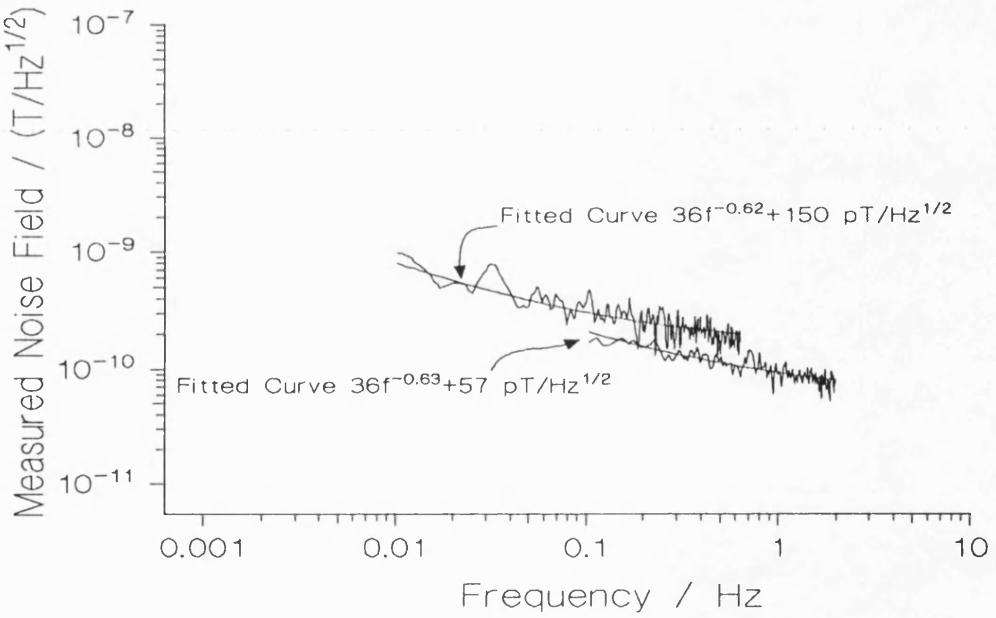

Figure 7.24b Logarithmic frequency spectrum showing magnetic noise for magnetometer employing 5210 lock-in amplifier $\mathbf{R_f}$=2kΩ.

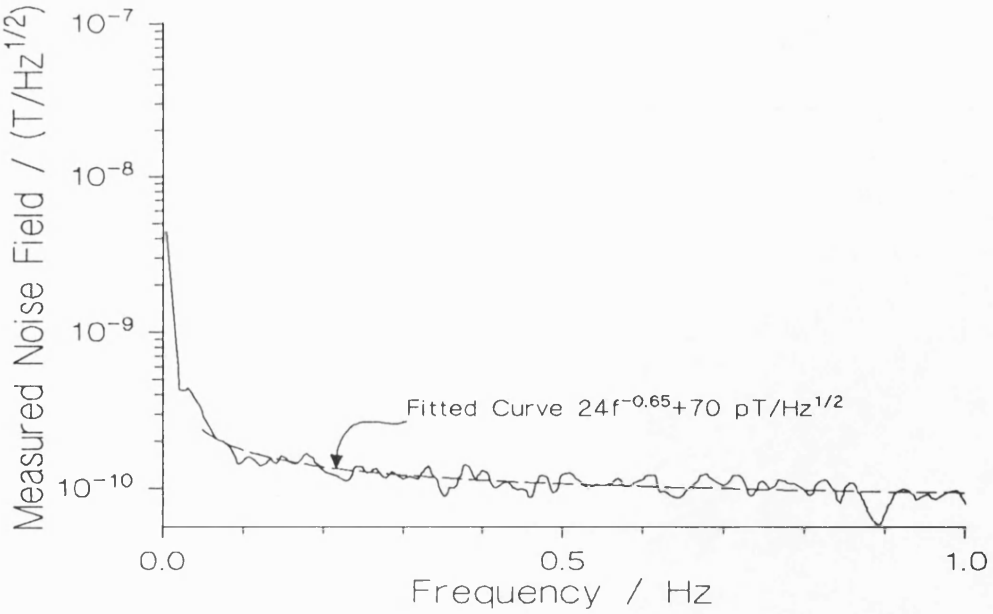

Figure 7.25a Linear frequency spectrum showing magnetic noise for magnetometer employing 5210 lock-in amplifier $\mathbf{R_f}$=**22kΩ**.

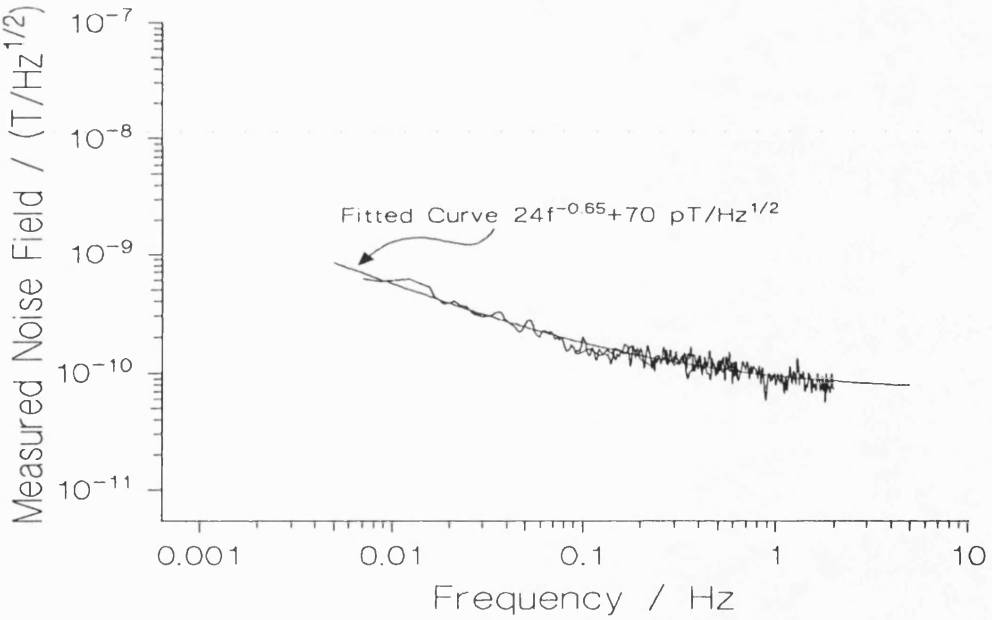

Figure 7.25b Logarithmic frequency spectrum showing magnetic noise for magnetometer employing 5210 lock-in amplifier $\mathbf{R_f}$=**22kΩ**.

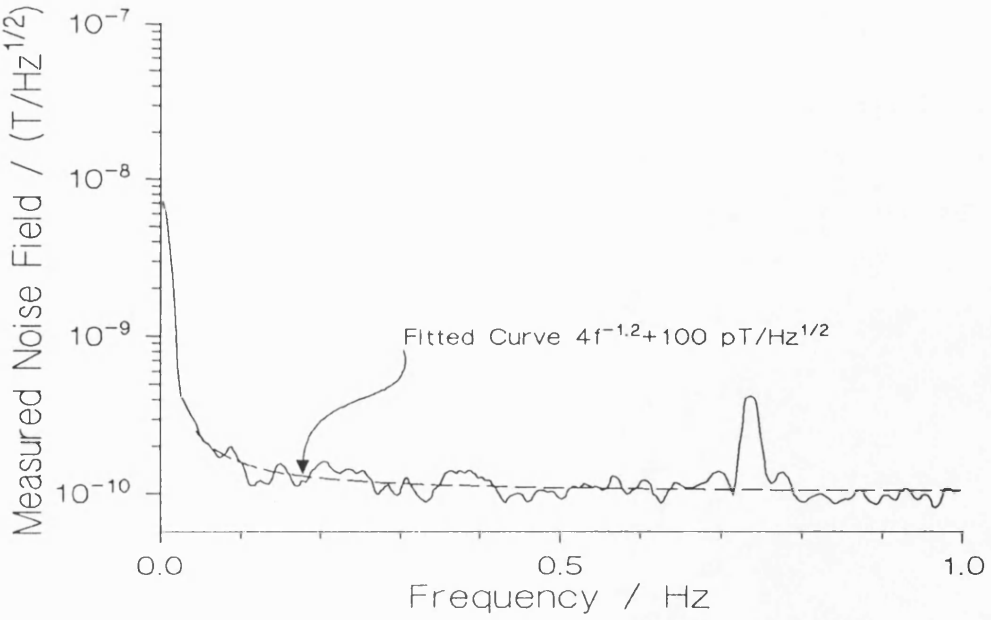

Figure 7.26a Linear frequency spectrum showing magnetic noise for magnetometer employing 5210 lock-in amplifier $\mathbf{R_f}$=**42kΩ**.

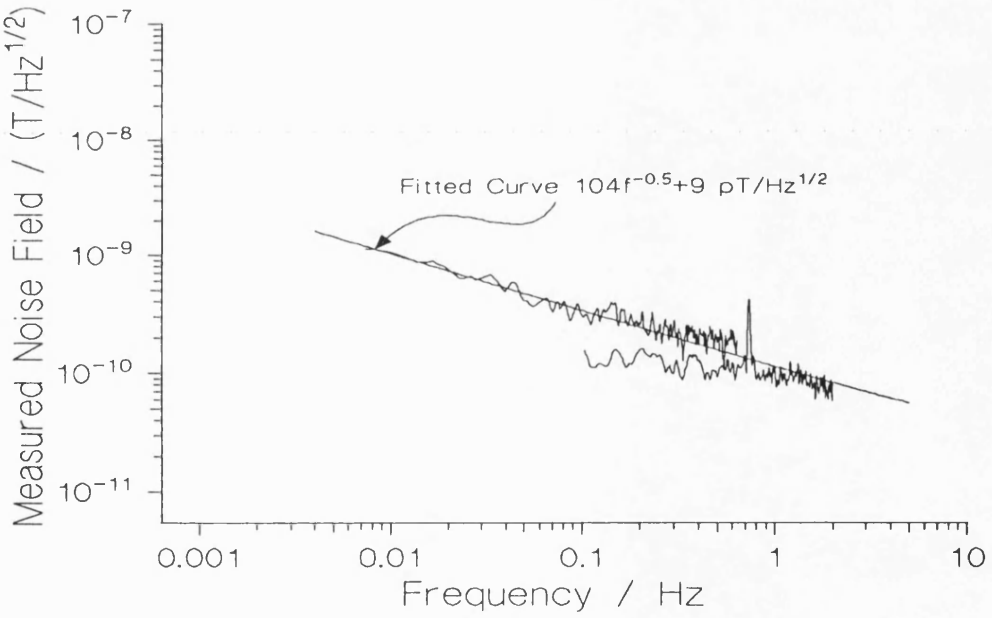

Figure 7.26b Logarithmic frequency spectrum showing magnetic noise for magnetometer employing 5210 lock-in amplifier $\mathbf{R_f}$=**42kΩ**.

Figure 7.27 compares the fitted noise curves for the magnetometer operated using the SR510 lock-in amplifier and the 5210 lock-in amplifier. For low frequencies an improvement of an order of magnitude was seen when using the 5210 in preference to the SR510.

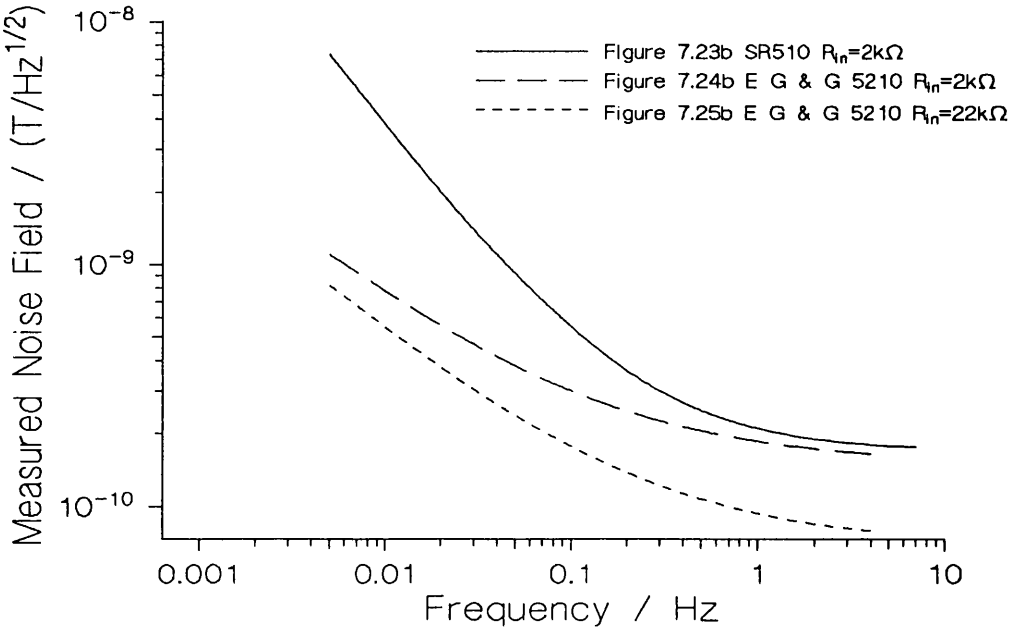

Figure 7.27 Comparison of the magnetic field noise for the magnetometer system. The curves shown are the curves fitted to the noise measured in Figures 7.23b, 7.24b & 7.25b

The magnetic field measurement bandwidth of the shear wave magnetometer was measured by applying a fixed magnitude sinusoidal signal over a range of frequencies to the calibration solenoid. This was accomplished using the 9472 Signal Source in series with a **110kΩ** resistor. The amplitude of the magnetometer output at the calibration frequency was measured using the spectrum analyser and the measured field calculated directly from the feedback resistance and the number of turns per metre on the feedback

solenoid. Figure 7.28 shows the results for the application of a **163nT/Hz$^{1/2}$** signal to the magnetometer arrangement the performance results of which are given in Figures 7.25a & b. The **-3dB** point was measured at approximately **4Hz**.

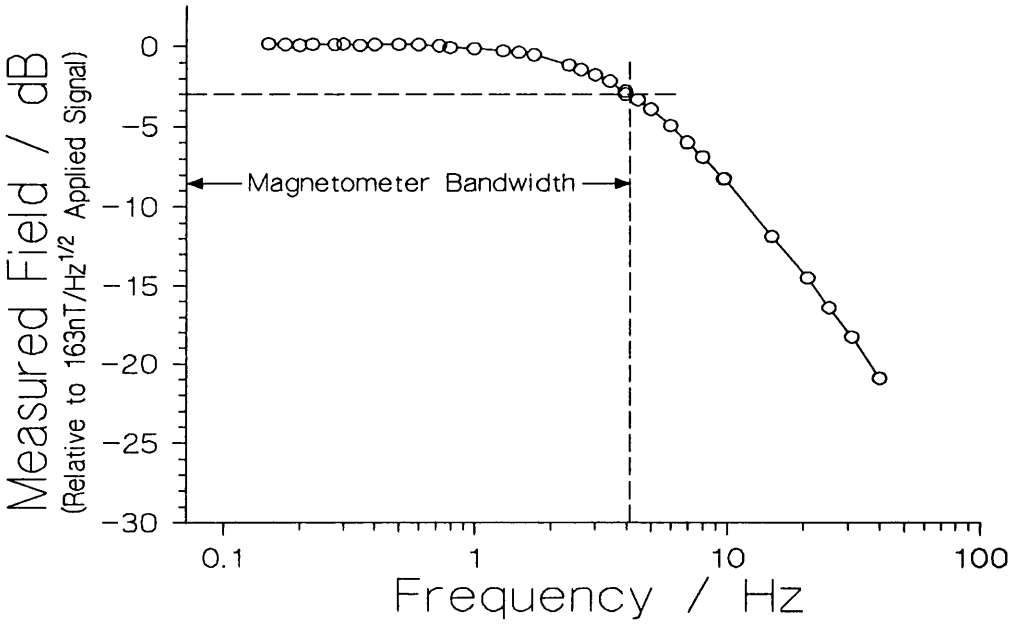

Figure 7.28 Frequency spectrum for the magnetometer system demonstrating the measurement bandwidth. The lock-in amplifier used was the 5210 with a feedback resistor of R_f=22kΩ.

7.6.3 Magnetometer Noise Characterisation in the Time Domain.

The magnetometer output signal was investigated in the time domain by recording the output signal of the magnetometer across the feedback resistor using a Goerz SE120 chart recorder. Figure 7.29 shows the output recorded for the magnetometer incorporating the 5210 lock-in amplifier for two different feedback resistances. The magnetometer set up was the same as that described for the equivalent frequency domain results in Figures 7.24a & b and Figures 7.25a & b. The results were taken over a recording time of one

minute with test signal d.c. field steps of **16.5nT** and **1.65nT** applied to the $\mathbf{R_f}$**=2kΩ** and the $\mathbf{R_f}$**=22kΩ** systems respectively. Figure 7.29 demonstrates more clearly the improvement in the magnetometer magnetic noise field floor on increasing the feedback resistor than the frequency domain results.

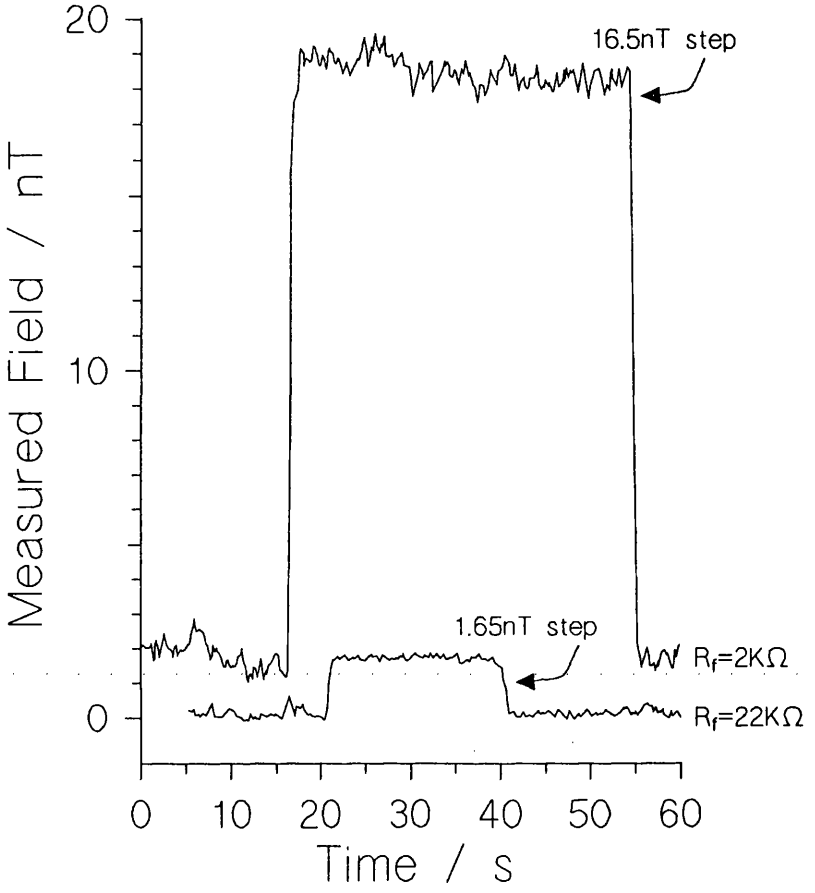

Figure 7.29 Comparison of the time domain magnetometer output for the magnetometer employing the 5210 lock-in amplifier for two different feedback resistors (equivalent to the frequency domain records shown in Figures 7.24a & b and Figures 7.25a & b).

The dynamic measurement range of the magnetometer system was limited only by the dynamic range of the lock-in amplifier and the magnitude of the feedback resistance. Figure 7.30 shows the application of a series of cumulative field steps over a measurement time of two minutes. The maximum field that could be recorded was approximately **±8700nT** for a feedback resistance of $\mathbf{R_f}$**=2kΩ**. The magnitude of the field range reflects the output range of the 5210 lock-in amplifier used taking into account the specified overhead of the output amplifier. Increasing the feedback resistor by an order of magnitude would reduce this dynamic range by an order of magnitude.

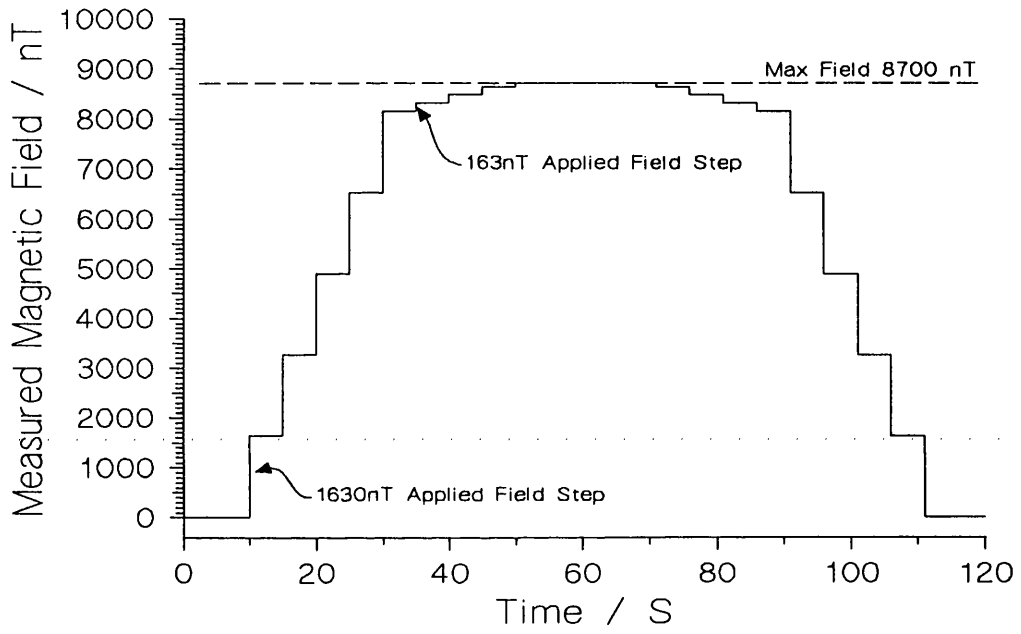

Figure 7.30 Demonstration of the dynamic range of the magnetometer system employing the 5210 lock-in amplifier with $\mathbf{R_f}$**=2kΩ**.

7.7 The Pulse Mode Shear Wave Magnetometer

The field annealed ribbons investigated by Bassir [1991a] & [1991b] were briefly discussed in chapter 5.3. These ribbons displayed a promising response to magnetic field

for the shear waves transmitted along the amorphous ribbons. The response in general took the form of an increased attenuation with applied field for pulsed shear waves travelling along short lengths of annealed ribbon. These type of magnetic field transducers are unsuited to the magnetometer system discussed so far and as a result an alternative pulse mode system was proposed. A system diagram of the closed loop pulse mode shear wave magnetometer system is shown in Figure 7.31. The system retains the same generic components as the continuous wave magnetometer. A modulation field was applied to the magnetic transducer and a lock-in amplifier referenced to the modulation frequency used to drive an identical field nulling feedback loop. Additional components were required to apply the pulse signal to the transducer and process the received signal. A linear gate was used to amplitude modulate the high frequency drive signal with a short pulse waveform. The modulated signal was then applied to the piezoelectric transducer which acted as both transmitter and receiver. The received signal was applied to the mixer element through a second linear gate delayed in operation for a time equivalent to the transit time along the ribbon by a scan delay generator. As with the continuous wave system the output of the mixer was a signal at the modulation frequency and its harmonics. The fundamental signal was proportional in amplitude to the magnetic field to be measured. A disadvantage with the system was a loss in signal to noise ratio of the mixer output signal due to the pulse operation of the system. This could be improved, however, if the transducers could be shortened so that the pulse rate could be increased with the added bonus of less non-magnetic transmission attenuation

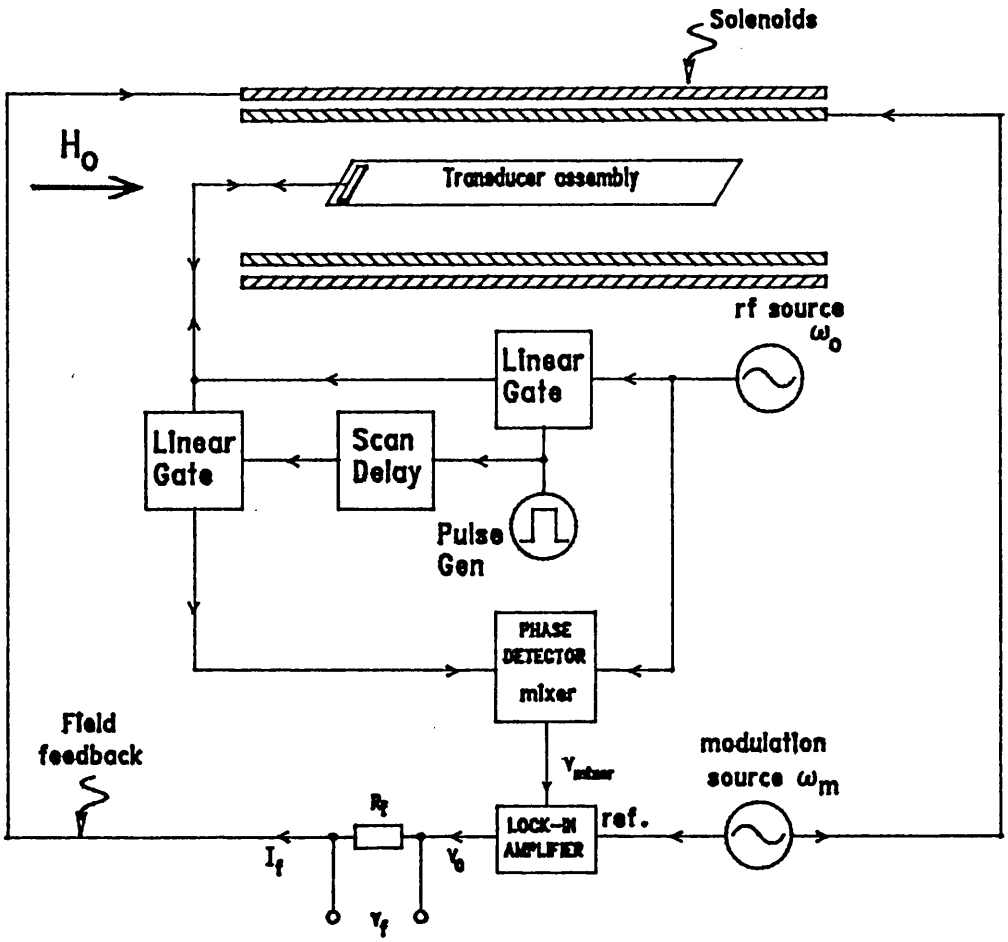

Figure 7.31 Schematic representation of the pulse mode shear wave magnetometer.

Figure 7.32 shows the time domain trace for the pulse mode magnetometer using a 45° field annealed METGLAS 2605S2 transducer. The ribbon sample was **80mm** in length with the long axis of the piezoelectric transducer mounted perpendicular to the ribbon long axis. The Feedback resistor was R_f=200Ω and the lock-in time constant τ=**100ms**. The modulation current used was i_m=**30mA** at a frequency of f_m=**1470Hz**. A brief investigation of the effects of altering the lock-in time constant and the feedback resistor showed no improvement in the magnetometer noise floor for increasing the time

constant over two orders of magnitude and the feedback resistor over one order of magnitude. The magnetic transducer described in chapter 5.3 with 45° mounted piezoelectric transducers was not investigated.

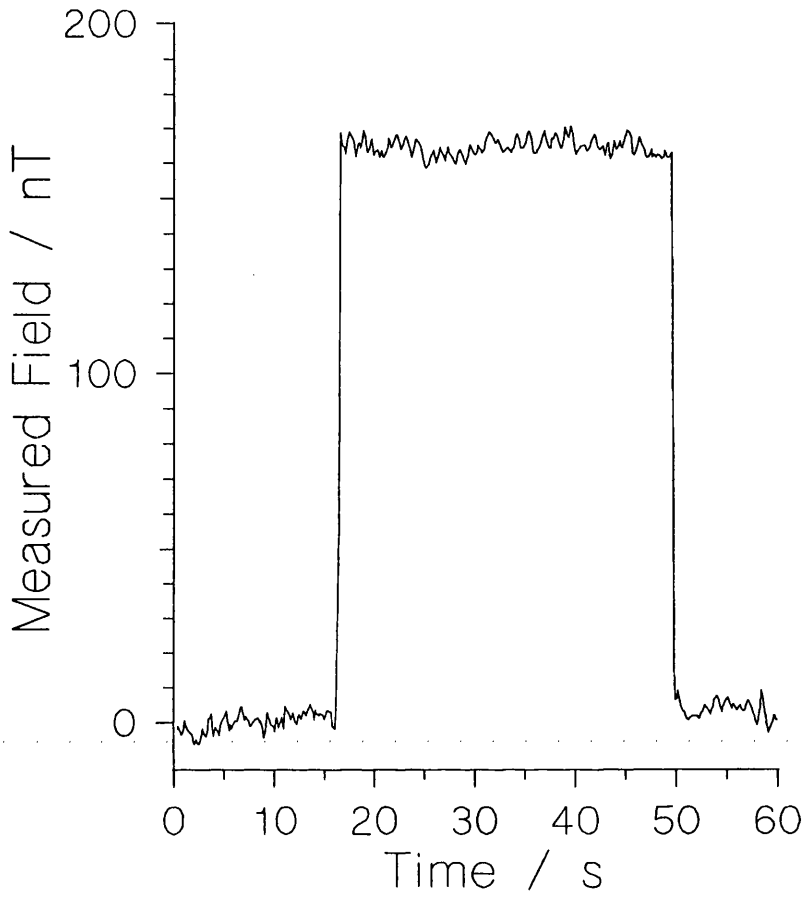

Figure 7.32 Time domain trace demonstrating the performance of the pulse mode system.

8 THE EFFECTS OF TEMPERATURE FLUCTUATIONS ON THE MAGNETOMETER SYSTEM.

8.1 Introduction.

The stability of magnetometers to fluctuations in temperature was found to be poorly documented in all the literature published on the devices reviewed in chapter 2. Although the effects of external perturbations such as acceleration on the performance of the fibre optic magnetometer have been examined by Bucholtz *et al* [1988] almost no consideration was given to any temperature effects. The stability of the fibre optic magnetometer was investigated by Koo *et al* [1986] but only in terms of its long term drift. This drift was not examined as a function of a controlled dynamic temperature fluctuation but at an unspecified ambient temperature subject to standard environmental variations which were not measured. Temperature effect were also omitted in the extensive paper on the magnetoelastic magnetometer of Mermelstein [1992]. The only truly well specified data obtained was that supplied by Willcock [1992] for a commercially available fluxgate magnetometer.

The effects on the stability of the shear wave magnetometer due to temperature fluctuations can be separated into a number of contributions. The instrumentation making up the system is subject to thermal drift. These thermal effects would be expected to be minimised by the adoption of the a.c. modulation technique for the system operation. The modulation and feedback solenoid formers also undergo thermal expansion. For large loop gains the expansion of the modulation solenoid should have no effect on the system performance; however, the expansion of the feedback solenoid changes its calibration and subsequently the magnitude of the feedback current used to obtain the field measurement. The solenoids were wound on cylindrical plastic formers which would be expected to have a coefficient of linear expansion anything up to **100ppm/°C.**

Taking this as a worse case and he magnetometer working at the full scale of the lock-in amplifier output, this equates tca maximum measured field deviation of approximately **800pT/°C**. Normally the systen would not be expected to operate at full scale and this figure would be considerably reduced. A further expansion effect comes about due to the linear expansion of the amorphous alloy magnetic transducer which has an expansion coefficient of the order of **10ppm/°C**. The thermal expansion of the transducer results in a temperature dependent phase change of the shear waves and thus a non-magnetic contribution to the overall phase change and an error in the magnetic measurement. Although this only approximates to a phase change of $\mathbf{4x10^{-3}rads/°C}$ which is of the same order of magnitude as the magnetostriction effect it could still equate to a sizable non-magnetic error term.

This chapter re-examines the operation of the magnetometer. A further mathematical analysis of the magnetometer system was undertaken with the emphasis directed towards the temperature effects. The drift of the shear wave magnetometer with controlled variations in ambient temperature was examined and an extension to the magnetometer system proposed in order to reduce the effect of these thermal fluctuations. The improved system was implemented and the performance of the system established and discussed.

8.2 The Differential Phase Equation.

In the introduction to the shear wave magnetometer given in chapter 1 the fundamental equation was developed for the change in the phase of the shear waves along the amorphous ribbon, equation 8.1, where **L** and **C** are the length of the active ribbon and the velocity of the shear waves respectively and ω, ρ and μ are the propagation frequency, the material density and the elastic shear modulus.

$$\phi = \omega L\sqrt{\frac{\rho}{\mu}} \qquad 8.1$$

In chapter 1 a differential phase equation was developed relating the change in the phase observed along the magnetic transducer for a change in magnetic field. The field dependent variables in this case were taken as the ribbon length due to magnetostriction and the field dependent shear modulus. It is possible to extend this analysis to a more complete and applicable form by considering not only the magnetic field dependence of the quantities but also their temperature dependence as shown in equation 8.2.

$$\Delta\phi = \left.\frac{\partial\phi}{\partial H}\right|_T \Delta H + \left.\frac{\partial\phi}{\partial T}\right|_H \Delta T \qquad 8.2$$

The quantities in the phase equation which can be considered to have both a magnetic field dependence and a temperature dependence are the length **L** the density ρ and the shear modulus μ. The dependence of the density on external perturbations comes about due to changes in the volume **V** the mass being constant. On applying equation 8.2 to equation 8.1 the phase change due to magnetic field and temperature perturbations can be expressed as shown in equation 8.3 with the field and temperature effects separated into two groups.

$$\Delta\phi = \frac{2\pi L}{\lambda}\left[\left\{\frac{1}{L}\frac{\partial L}{\partial H}\right|_T - \frac{1}{2}\frac{1}{\mu}\frac{\partial\mu}{\partial H}\Big|_T - \frac{1}{2}\frac{1}{V}\frac{\partial V}{\partial H}\Big|_T\right\}\Delta H + \left\{\frac{1}{L}\frac{\partial L}{\partial T}\right\|_H - \frac{1}{2}\frac{1}{\mu}\frac{\partial\mu}{\partial T}\Big|_H - \frac{1}{2}\frac{1}{V}\frac{\partial V}{\partial T}\Big|_H\Big\}\Delta T\Big] \qquad 8.3$$

The equation consists of six terms three temperature dependent and three magnetic field dependent. These terms can be identified as physical effects as follows:

$\frac{1}{L}\frac{\partial L}{\partial H}$ - Fractional change in length with applied field, Linear magnetostriction.

$\frac{1}{\mu}\frac{\partial \mu}{\partial H}$ - Fractional change in modulus with applied field κ. $\Delta\mu$ effect.

$\frac{1}{V}\frac{\partial V}{\partial H}$ - Fractional change in volume with applied field, Magnetovolume effect.

$\frac{1}{L}\frac{\partial L}{\partial T}$ - Thermal linear expansion.

$\frac{1}{\mu}\frac{\partial \mu}{\partial T}$ - Fractional change in shear modulus with temperature.

$\frac{1}{V}\frac{\partial V}{\partial T}$ - Thermal volume expansion.

8.3 Substitution of Physical Relations into the Differential Phase Equation.

The differential phase equation can be implemented in an analysis of the operation of the magnetometer provided that the variables associated with the six terms of equation 8.3 can be related through physically meaningful equations to variations in the magnetic field and the temperature. The magnetic field and temperature dependence of the magnetic transducer length, $L_{(H,T)}$, density, $\rho_{(H,T)}$ and shear modulus $\mu_{(H,T)}$ can be expressed to their lowest useful order by equations 8.4, 8.5 & 8.6. The temperature dependence of length and volume were taken as following classical linear expansion with thermal expansivity α_1 of the order of parts per million. The temperature dependence of the shear modulus was also taken as linear a valid approximation over small temperature changes. The constant of proportionality was denoted by α_2 again this would be expected to be of low order. The field dependence of the shear modulus was taken

as being quadratic for low fields with a quadratic coefficient γ. This approximation is not too far removed from the previous functions employed to describe the field dependence (re. equation 5.8 & 5.9), it being essentially an even function with magnetic field and far easier to manipulate mathematically. Fitting of the quadratic function to the data of Figures 5.15a & b and relating to a modulus change results in values of order of $\gamma \approx 10^{-5} A^{-2} m^2$. The length change of the transducer was related to magnetic field through the magnetostriction quadratic coefficient as defined in chapter 1. This has values of the order of $C_q \approx 10^{-16} A^{-2} m^2$ from Thomas [1991]. The magnetovolume effect can be ignored from the start as this is a very small effect compared with the linear magnetostriction at low fields, Bozorth (p642) [1951].

$$L = L_T(1 + \alpha_1 T)(1 + C_q H^2) \qquad 8.4$$

$$\mu = \mu_T(1 - \alpha_2 T)(1 - \gamma H^2) \qquad 8.5$$

$$V = V_T(1 + 3\alpha_1 T) \qquad 8.6$$

These functions can be substituted into the expression given in equation 8.3, the first order terms in the small coefficients α_1, α_2, C_q and γ only being retained. From the approximations for the magnitude of these terms the second order quantities for any combination of these terms would be expected to be minimally small. Further to this the second order terms consisting of the multiplication of either α_1, α_2 or γ are larger than the first order terms in C_q; however, all second order terms in α_1, α_2 and γ are many orders of magnitude less than the first order quantities in these coefficients. The magnetostriction term, therefore, could be dropped but was retained merely for consistency in first order terms. Equation 8.7 shows the result of this substitution with the definition of the coefficients ϕ_0, η and ψ given in equations 8.8, 8.9 & 8.10 respectively.

$$\Delta\phi = \phi_0(\eta\Delta T + \psi\Delta H) \quad 8.7$$

$$\phi_0 = \omega_0 L_T \sqrt{\frac{\rho_T}{\mu_T}} \quad 8.8$$

$$\eta = \frac{1}{2}(\alpha_2 - \alpha_1) \quad 8.9$$

$$\psi = (2C_q + \gamma)H = -\frac{1}{2}\kappa + 2C_q H \quad 8.10$$

Equation 8.7 describes the phase response of the magnetic field sensor in terms of both magnetic field and temperature. This function can be substituted into the idealised mixer output function of equation 6.1 which can be written as shown in equation 8.11 to give the output of the mixer element after low-pass filtering to remove the second harmonic of the drive signal.

$$V_{mix} = \frac{\beta A_{2_{(H,T)}}}{2}\cos(\phi_0 + \Delta\phi_{(H,T)}) \quad 8.11$$

The terms A_2 and β were defined in chapter 1 and chapter 6 respectively. The field dependence of A_2 will not be considered further here. The temperature dependence of the attenuation was also unstudied so no attempt will be made to model its behaviour.

The applied magnetic field once again consists of the field to be measured $\mathbf{H_0}$ and a modulation field at a frequency ω_m with a modulation depth **h** as depicted by equation 8.12.

$$H = H_0 + h\cos\omega_m t \quad 8.12$$

Substituting for equations 8.7, 8.10 & 8.12 into equation 8.11 yields the result for the mixer output shown in equation 8.13

$$V_{mix} = \frac{\beta A_{2_{(II)}}}{2}\cos\{\phi_0[1+\eta\Delta T+(2C_q+\gamma)(H_0+h\cos\omega_m t)h\cos\omega_m t]\} \qquad 8.13$$

As with the linear response model discussed in chapter 6 this is an oscillatory function with a d.c. term and terms at multiples of the modulation frequency ω_m. Of foremost interest to the operation of the magnetometer system is the fundamental component measured by the lock-in amplifier. This provides the magnetometer system feedback signal. The term at the modulation frequency and its immediate harmonics can be found by expanding the expression given in equation 8.13 using standard trigonometric identities leading to the expression given in equation 8.14.

$$\begin{aligned} V_{mix} = \frac{\beta A_{2_{(II)}}}{2}[& \cos\Phi\cos(e\cos\omega_m t)\cos(f\cos 2\omega_m t) \\ & -\cos\Phi\sin(e\cos\omega_m t)\sin(f\cos 2\omega_m t) \\ & -\sin\Phi\sin(e\cos\omega_m t)\cos(f\cos 2\omega_m t) \\ & -\sin\Phi\cos(e\cos\omega_m t)\sin(f\cos 2\omega_m t)\ ] \end{aligned} \qquad 8.14$$

$$\Phi = \phi_0\left\{1+\eta\Delta T+\frac{(2C_q+\gamma)}{2}h^2\right\}$$

$$e = \phi_0(2C_q+\gamma)hH_0$$

$$f = \phi_0\frac{(2C_q+\gamma)}{2}h^2$$

Equation 8.14 contains terms which can be expanded into an harmonic series by applying identities containing Bessel functions to the zeroth first and second order. Following through with the approximations made earlier for the relative magnitudes of first and second order terms the zeroth, first and second order Bessel functions can be approximated to by equations 8.15, 8.16 & 8.17 respectively.

$$J_0(e) \approx 1 \qquad J_0(f) \approx 1 \qquad 8.15$$

$$J_1(e) \approx \frac{e}{2} \qquad J_1(f) \approx \frac{f}{2} \qquad 8.16$$

$$J_2(e) \approx 0 \qquad J_2(e) \approx 0 \qquad 8.17$$

Expanding equation 8.14 then leads to the magnitudes for the d.c. fundamental and second harmonic terms given in equations 8.18, 8.19 & 8.20. The total output of the mixer up to the second harmonic is given by equation 8.21.

$$X_0 = \frac{\beta A_{2_{(II)}}}{2}\cos\Phi \qquad 8.18$$

$$X_1 = -\frac{\beta A_{2_{(II)}}}{2} e \sin\Phi \qquad 8.19$$

$$X_2 = -\beta A_{2_{(II)}} f \sin\Phi \qquad 8.20$$

$$V_{mix} = X_0 + X_1 \cos\omega_m t + X_2 \cos 2\omega_m t + ... \qquad 8.21$$

Equation 8.18 and Equation 8.19 demonstrate a temperature and total phase change dependence for the d.c. and fundamental terms of the mixer output; equation 8.19 shows that only the fundamental term has a bias field dependence. The important consequence of these two results was that the temperature dependence of the fundamental signal could

be removed by an appropriate setting of the total phase change along the magnetic transducer ϕ_0. If equation 8.22 is satisfied through appropriate tuning of the high frequency source to control the total phase change, then the d.c. mixer output term becomes zero and the fundamental term reduces to that of equation 8.23.

$$\phi_0 \approx \Phi = (2n+1)\frac{\pi}{2} \qquad n = 0, 1, 2, .. \tag{8.22}$$

$$X_1 = -\left\{\frac{\beta A_{2_{(II)}}}{2}(2C_q + \gamma)\phi_0 h\right\} H_0 \tag{8.23}$$

Equation 8.23 shows the expected linear magnetic field dependence of the mixer's output signal at the fundamental frequency. The result also suggests that the slope of the response depends on the magnitude of the modulation signal. This occurrence of the modulation amplitude is in keeping with the loop gain calculations of Koo *et al* [1987] but contradicts the results of the linear response model of chapter 6. The discrepancy in the two results can be explained simply in terms of the two different functional forms assumed for the phase response. For a linear response as in chapter 6 there is no increase in the slope of the response with increasing field, whereas, the quadratic response has an increasing slope for increasing magnetic field and consequently a modulation amplitude dependence. Both these results, however, are shown to be over simplified by the modulation amplitude dependence displayed by the actual magnetometer system measured in chapter 7.3.

8.4 The Shear Wave Magnetometer Temperature Dependence.

The effects of fluctuations in the ambient temperature on the output of the shear wave magnetometer system were investigated for the magnetometer system as described in chapter 7.6. The lock-in amplifier used was the SR510 with a feedback resistance

R_f=2kΩ. The temperature of the magnetic transducer MT1 was monitored using a Chromel Alumel thermocouple mounted on the region of the amorphous material where it was bonded to the Tico™ pad mount. The thermocouple was isolated electrically from the amorphous alloy by a thin layer of tape. With the magnetometer in operation and the d.c. component of the mixer output zeroed through small frequency adjustments, the magnetic transducer was raised in temperature by passing a stream of hot air along the inside of the feedback and modulation solenoids. Once a suitably high temperature was deemed to have been achieved the air stream was removed and the d.c. output of the mixer zeroed once again. The magnetic transducer was then allowed to cool through natural convection over a number of hours. The temperature of the transducer, the output of the mixer element and the output of the magnetometer in what was considered to be a constant field were all recorded with the recording starting almost immediately after the air stream was removed. Figures 8.1a, b & c show the results obtained for a recording time of two hours. Straight line fits were applied to the temperature profile and the magnetic signal for the time period **20 - 100 min** in order to obtain the temperature gradient and the magnetic field gradient with time. From this data the magnetometer temperature coefficient can be calculated. The magnetometer was found to display a thermal drift of;

$$\frac{\Delta B}{\Delta T} = 44.9\text{nT/°C}$$

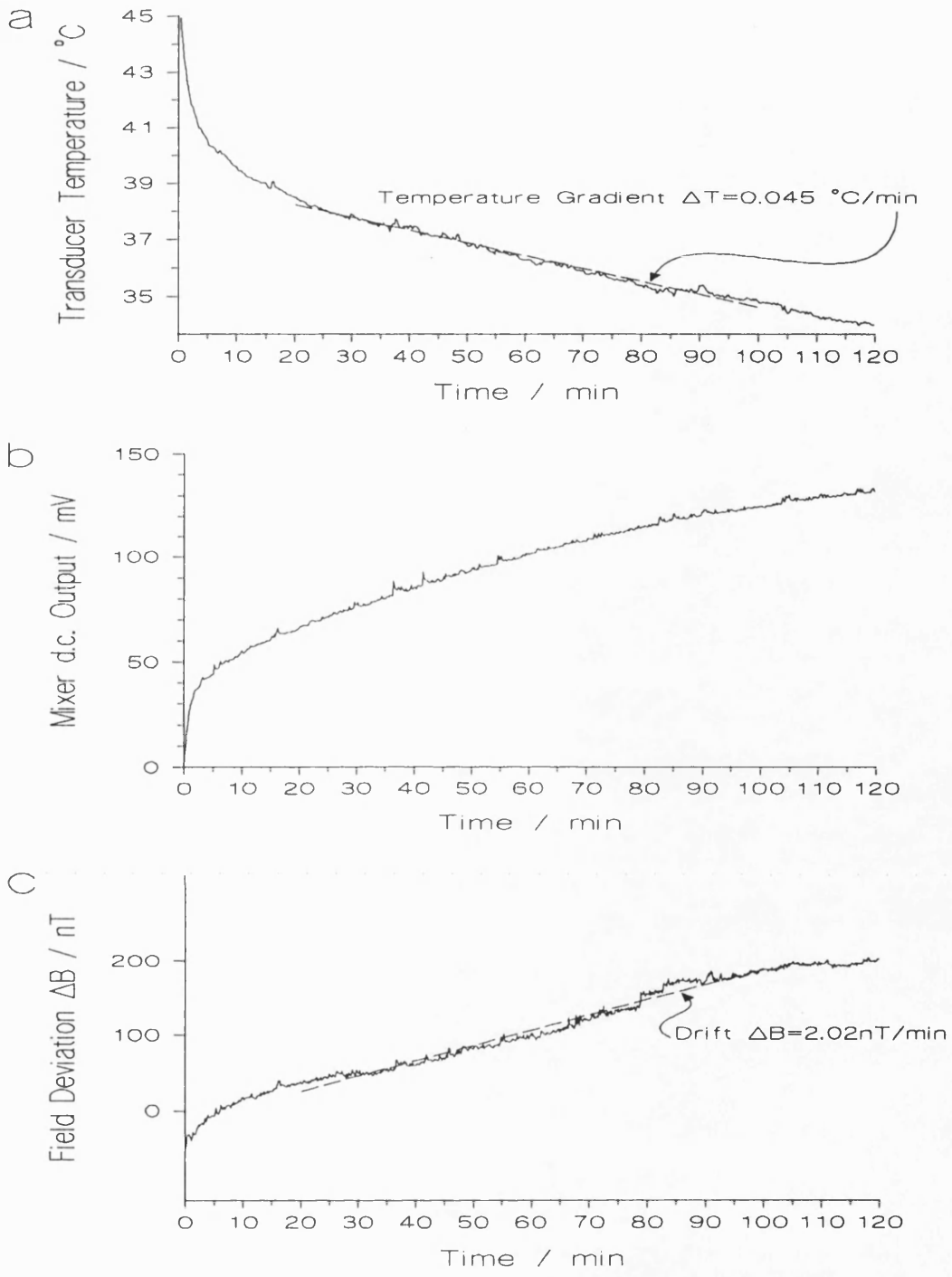

Figure 8.1 a Temperature profile applied to the magnetic transducer.

b Measured output of the mixer element.

c Measured output of the magnetometer.

8.5 Implementation of Temperature Stabilization.

The analysis of chapter 8.3 and the measurement of the d.c. output of the mixer element as a function of temperature shown by Figures 8.1a & b would suggest that the dependence of the shear wave magnetometer output on temperature can be removed. It was proposed in chapter 8.3 that this could be achieved by controlling the total phase change along the magnetic transducer through adjustment of the shear wave drive frequency. This would result in a zero d.c. output from the mixer element and a magnetometer output independent of temperature, equation 8.23.

Figure 8.2 shows the proposed temperature stabilized magnetometer system. The process is analogous to the scheme proposed by Jackson *et al* [1980] for the temperature stabilization of fibre-optic interferometers but more easily implemented. The high frequency oscillator used to drive the piezoelectric transducers is replaced by a voltage controlled oscillator with a free running frequency at the resonance frequency of the transducers. The voltage controlled oscillator is then controlled by a d.c. amplifier and filter arranged so as to apply a frequency correction signal to the oscillator so as to reduce the d.c. output of the mixer to zero.

A stable voltage controlled oscillator was unavailable for the implementation of this modification although the principle was demonstrated to be valid with a Topward Electronic Instruments TFG4613 Oscillator. This gave a much greater overall magnetometer noise than the Philips PM5193. The PM5193 could be used, however, in a computer controlled feedback arrangement. In this arrangement a CIL Microsystems Multifunction Computer Interface was used to measure the output of the mixer element. The result was processed using a BBC Microcomputer and the frequency of the PM5193 altered via an M.A. Instruments IEEE488.2 Controller. The frequency adjustment made was proportional to the voltage measured and of polarity such that the d.c. mixer output was reduced. This arrangement is essentially a digital voltage controlled oscillator.

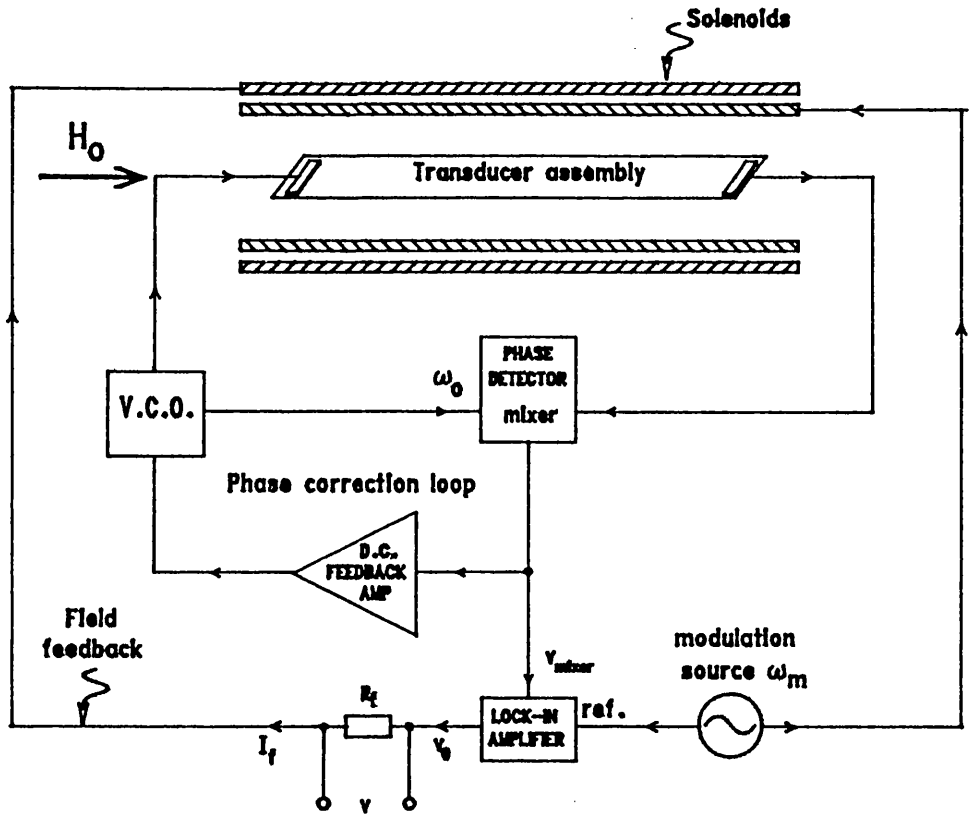

Figure 8.2 Shear wave magnetometer system including temperature stabilization feedback control.

The time constant of the computer controlled feedback arrangement was governed by the length of the measurement interval taken by the Multifunction Interface. Figure 8.3 shows the time taken to correct the frequency for the system after manually applying a fixed frequency shift of **570Hz** away from the frequency for a zero d.c. mixer output. This was investigated for a range of measurement intervals. The fitted time constants τ are seen to increase from τ=**0.13s** to τ=**1s** for measurement interval of **100ms** to **500ms** to **1s**. The computer controlled feedback can be seen to simulate closely the feedback response produced by an analogue arrangement.

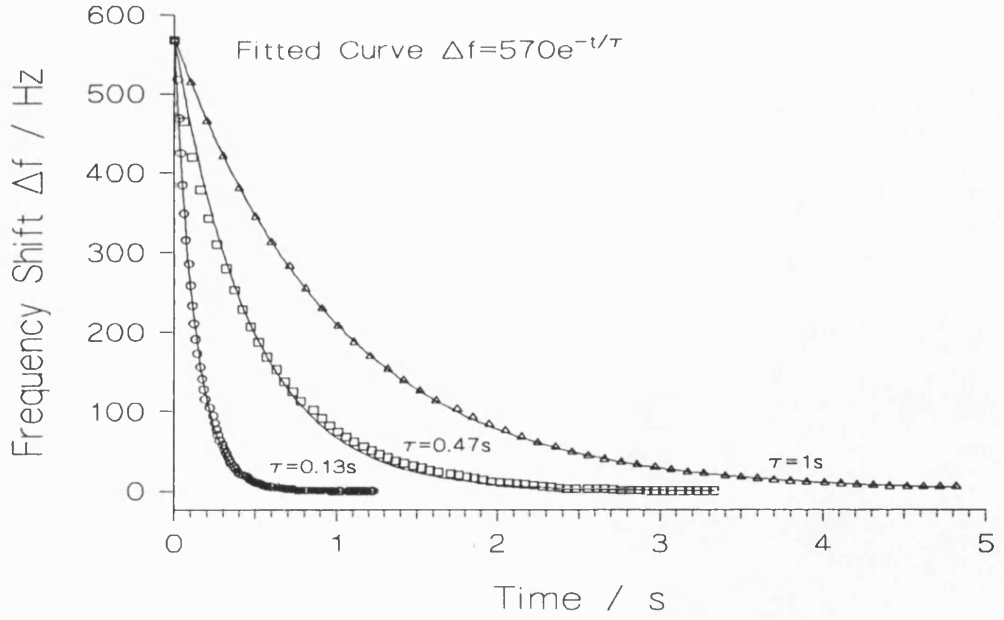

Figure 8.3 Measured time constants of computer controlled temperature feedback loop for correction measurement intervals of 100ms, 500ms and 1s.

With the implementation of the temperature correction feedback loop the effects of fluctuations in the ambient temperature on the output of the shear wave magnetometer system were investigated for the magnetometer system following the method described in chapter 8.4. The lock-in amplifier used was the SR510 with a feedback resistance $\mathbf{R_f=2k\Omega}$. The magnetometer was operated with the d.c. component of the mixer output zeroed by the correction loop with a time constant measured in Figure 8.3 of τ**=0.13s**. After raising to a suitably high temperature by a hot air stream the magnetic transducer was allowed to cool through natural convection over a number of hours. The temperature of the transducer, the output of the mixer element and the output of the magnetometer in what was considered to be a constant field were all recorded with the recording starting almost immediately after the air stream was removed. Figures 8.4a, b & c show the results obtained for a recording time of two hours.

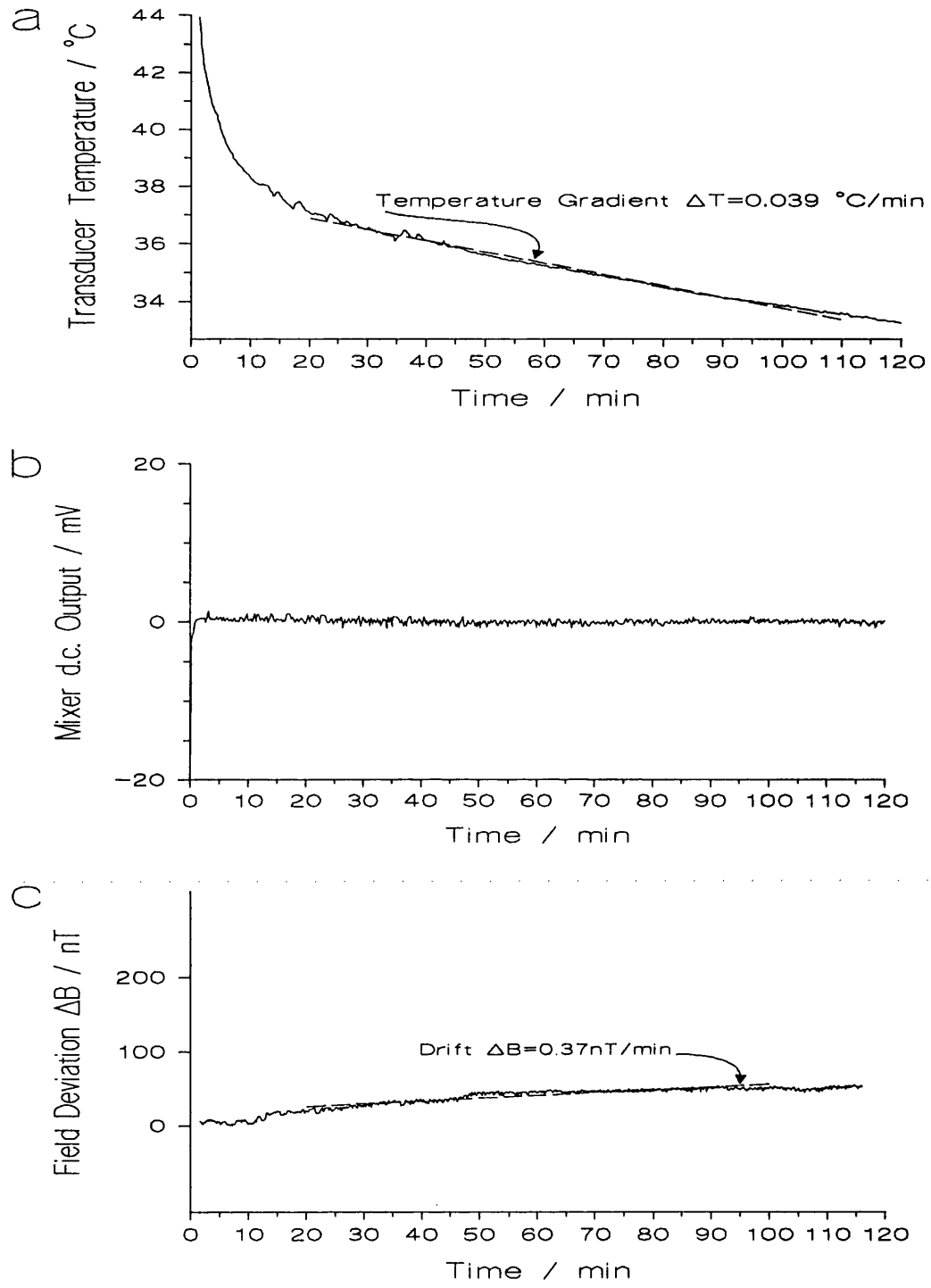

Figure 8.4 a Temperature profile applied to the magnetic transducer.

b Measured output of the mixer element.

c Measured output of the stabilized magnetometer.

Straight line fits were applied to the temperature profile and the magnetic signal for the time period **20 - 100 min** in order to obtain the temperature gradient and the magnetic field gradient with time. From this data the stabilized magnetometer temperature coefficient can be calculated. The magnetometer was found to display a thermal drift of;

$$\frac{\Delta B}{\Delta T} = 9.5\text{nT/°C}$$

The stabilized magnetometer temperature coefficient represents an approximate fivefold improvement in the magnetometer temperature stability. The straight line fits for the un-stabilized systems in Figures 8.1a & c give a representative average of the temperature dependent measured field drift. The fits in Figures 8.4a & c, however, can be seen to over-estimate the temperature drift. If the straight line fit was taken for a time interval **50 - 100 min** then a temperature coefficient of **3.8nT/°C** was returned. This represents an order of magnitude improvement in the temperature isolation. The short-coming of the procedure in totally removing the temperature dependence could possibly come about from either of two deficiencies in the analysis and implementation, the computer controlled feedback having the equivalent to insufficient gain because of the digital nature of the measurement or inappropriate approximations in the analysis introducing additional terms into either the d.c. or fundamental mixer output signals. The instrumentation shortfalls are difficult to validate; however, there would obviously be a form of hysteresis in the feedback loop because of the measurement limits of the analogue to digital converter and the minimum frequency deviation that could be programmed into the PM5193. From the approximations to the various physical quantities given in chapter 8.1 the initial order of smallness approximations would appear valid; however, the approximations made for the Bessel functions could possibly break

down introducing further terms in equations 8.15, 8.16 & 8.17 from f. Further to this the temperature dependence of $\mathbf{A}_2$ was ignored and would not be removed by the above scheme.

9 DISCUSSION AND CONCLUSIONS.

9.1 Introduction.

This chapter summarises the results from the experimental investigations undertaken on the shear wave magnetometer. The significant results from each chapter are discussed and the appropriate conclusions drawn. The magnetoelastic wave model of Inoue [1989] is not discussed further here as the evidence presented in chapter 4.5.3 suggested that without a much more detailed analysis the model would be inappropriate for predicting the behaviour of shear waves in amorphous ribbons.

9.2 Investigation of the Amorphous Alloy Magnetic Transducer.

9.2.1 Transducer Arrangements.

Two different arrangements of magnetic transducer were investigated over the duration of the project. A continuous wave (CW) transducer and a pulsed mode transducer. These are discussed in detail in chapter 5.2

The continuous wave magnetic transducer consisted of the amorphous material with piezoelectric transducers mounted at opposite ends of the ribbon. One transducer acted as the shear wave transmitter the other as a receiver to transform the shear waves back to an electrical signal. The ribbon was suspended between two mounts so that energy losses would not occur from the ribbon surface being in contact with another material. The geometry and mounting of the piezoelectric transducers followed a scheme widely accepted as a means of propagating shear waves in shear mode strip delay lines from May [1964]. The choice of piezoelectric material depended on the required shear wave propagation frequency. The important consideration with the two transducer continuous wave arrangement was resonance matching the two transducers. Although this was practically possible for the unmounted free transducers and in fact matched

lithium niobate transducers were supplied by Gooch and Housego Ltd, the matching was affected by the mounting of the transducers to the ribbon surface. Two effects are responsible for the resonance perturbation. The mass loading experienced by the transducer from the ribbon and the effect of the interface bond. This also presented a further problem of reproducibility between remounts of the transducers. Two different adhesives were investigated in order to provide the mounting bond, silver loaded epoxy and cyanoacrylate. Although the cyanoacrylate bond was expected to be superior to that of the silver loaded epoxy for the reproducibility of transducer remounts because of the reduced complexity in achieving the bond it was in-fact found to give no improvement.

The single piezoelectric transducer pulsed mode magnetic transducer did not suffer from the resonance matching problems of the continuous wave arrangement. This did have the disadvantage, however, of being useful only as a shear wave amplitude response transducer which required a different system arrangement to that described for the phase sensitive magnetometer of chapter 1.2.4.2. The pulse magnetometer arrangement was introduced in chapter 7.7 and is discussed further in chapter 9.4.4.

9.2.2 Field Annealed Magnetic Transducers.

The field annealed material studies conducted by Bassir [1991a] & [1991b] considered in chapter 5.3 concentrated on the study of transversely annealed METGLAS 2605S2. The field annealed materials did not perform well in the continuous wave mode transducers. The continuous wave transducers were susceptible to a degradation in performance from longitudinal stress and hence the procedure of allowing a controlled sag of the amorphous ribbon between the end mounts to reduce this stress in the "as-received" materials. The introduction of an in-plane anisotropy enhances not only the field dependence of the elastic moduli but also the magnetomechanical coupling and magnetomechanical damping making the ribbon even more stress sensitive. The field

annealing work, therefore, concentrated on optimisation of the amplitude response of pulse mode transducers in which the stresses could be minimised by supporting the magnetic transducer so that it hung vertically with the ribbon end without a piezoelectric transducer free and unsupported. The effect of changing the orientation of the long axis of the piezoelectric transducer to the field annealing direction was also studied and an optimum angle of α=45° was proposed. This arrangement gives a minimum attenuation of the shear wave while maintaining the field anneal direction perpendicular to the applied field facilitating the largest overall field response. The incident angle of 45° onto the ribbon edge also has the advantage of minimising the possibility of losses through mode conversion of the shear waves. Careful consideration of the transducer geometry had to be taken into account in order to achieve the correct path length. The amplitude responses to magnetic field obtained by Bassir [1991a] for an alternative two piezoelectric transducer magnetic transducer are shown in Figures 5.11a & b and demonstrate an optimum response at shear wave propagation frequencies below **1MHz.**

9.2.3 "As-Received" Amorphous Ribbon Magnetic Transducers.

The study on "as-received" amorphous ribbon magnetic transducers was carried out in-order to identify a suitable material for the construction of continuous wave magnetic transducers which would allow the characterisation and development of the magnetometer system.

The majority of the investigations undertaken concentrated on the use of METGLAS 2826MB which from chapter 5.4.1 was seen to give a superior field response for both the shear wave amplitude and phase change along the magnetic transducer compared to the other "as-received" materials considered, Table 5.1. The METGLAS 2826MB transducers displayed the expected shear wave amplitude and velocity dependences observed in the literature reviews of chapter 3 and chapter 4 (compare

Figures 3.6, 4.4a & b and 5.17 and Figures 3.7 and 5.16). Two different batches of the METGLAS 2826MB alloy were investigated and from the meticulous small field measurements undertaken were found to display different characteristics that were internally consistent for the two specimens. The REEL 1 material demonstrated very sharp response at low fields for both the phase and amplitude response. This went as far as observing discontinuities in the shear wave amplitude response to magnetic field, Figures 5.14a & b. The REEL 2 material gave a close agreement to the quadratic like dependence expected of both the shear wave amplitude and phase change from published results.

A study of the response of the magnetic transducer as a function of transducer length carried out in chapter 5.4.2 revealed an increased prominence in the overall effect on the field response curves from the low field anomalies of the REEL 1 material for increasing transducer length. This was not observed with the REEL 2 material. A more quantitative examination which involved the fitting of approximate curves to the response data was undertaken. Equations 9.1 & 9.2 show the functions which were fitted separately to the rising and falling field data of both the amplitude and phase responses respectively.

$$A_{2_{(H)}} = a_1\{1 - b_1|H - c_1| - d_1(H - e_1)^2\} \qquad 9.1$$

$$\Delta\phi_{(H)} = a_2 + b_2|H - c_2| + d_2(H - e_2)^2 \qquad 9.2$$

H is the internal field and the coefficients $\mathbf{a_1}$, $\mathbf{b_1}$ and $\mathbf{d_1}$ in the amplitude response equation are the peak zero field amplitude, the normalised linear amplitude response and the normalised quadratic amplitude response. The coefficients in the phase response fit are $\mathbf{a_2}$, a d.c. instrument phase shift, $\mathbf{b_2}$, the linear phase response and $\mathbf{d_2}$, the quadratic phase response. The coefficients **c** and **e** in both equations reflected in general the magnitude of the offset field of the response features.

The important coefficients describing the performance of the magnetic transducer

were in general $\mathbf{a_1}$, $\mathbf{b_1}$ and $\mathbf{b_2}$. These gave the peak amplitude of the received shear waves and the predominant responses to magnetic field. The received amplitude of the shear waves showed the expected exponential decrease with increasing transducer length for both samples of the material, Figure 5.29a. Greater losses were observed, however, with the REEL 1 sample. The normalised amplitude response for the REEL 2 transducers showed no variation with length, whereas, that of the REEL 1 transducers demonstrated an increase with increasing length. This reflected an increase in the prominence of the discontinuities. The phase response results for the REEL 1 data demonstrated an increase in response as was predicted by equation 1.14. A larger than expected increase was observed for the two longest transducers. Again this reflects the increased effect of the sharp response features. The REEL 2 magnetic transducer phase results were not discussed as spurious results observed in the data sets resulted in any variation being difficult to observe. It was assumed that the REEL 2 data would demonstrate the expected increase in phase response with length but to a lesser degree.

The effect of the length on the field responses was examined further for the sections which showed an increased response by constructing short magnetic transducers from the removed sections. These were found to behave similarly to the previously measured short section. It was concluded that the effect was related to the quantity of bulk material rather than isolated to individual material sections. Xray analysis undertaken in chapter 5.4.4 revealed a distinct surface crystallisation of one surface of the REEL 1 material. The crystallised surface was the surface on to which the piezoelectric transducers were mounted. Controlled surface crystallisation was proposed as a viable method for optimising magnetic sensor parameters by Thomas *et al* [1991].

An investigation of the amplitude and the phase responses as a function of shear wave propagation frequency established no frequency dependence for the shear wave

amplitude response over the limited range of frequencies investigated (0.8 - 1.8 MHz), Figure 5.30a. The phase response was shown to follow the expected linear dependence with frequency suggested by equation 1.14, Figure 5.30b.

9.3 Magnetometer System Response Model.

The mixer element used to demodulate the magnetic transducer modulation signal from the carrier signal at the shear wave propagation frequency was in general sensitive to both the phase and the amplitude of the input signal. The signal output of the mixer, therefore, consisted of signal terms at the modulation frequency and its harmonics. A function to model the output of the mixer element was proposed in chapter 6.3. The function was based on a linear amplitude and phase response to magnetic field of the magnetic transducer. The Linear Response Function is shown in equation 9.3, where β was the gain of the mixer, $\mathbf{a_1}$, $\mathbf{b_1}$ and $\mathbf{b_2}$ are the peak amplitude and the linear amplitude and phase response coefficients respectively. $\mathbf{H_0}$ and $\mathbf{h}$ are the applied bias field and the modulation field amplitude. ϕ_0 was the total phase change of the shear waves along the transducer length and ω_m the modulation frequency.

$$V_{mix} = \frac{\beta a_1}{2}\{1 - b_1|H_0 + h\sin\omega_m t|\}\cos\{\phi_0 + b_2|H_0 + h\sin\omega_m t|\} \qquad 9.3$$

The harmonic terms of the Linear Response Function were investigated through both an analytical solution of the function, chapter 6.3 and a numerical solution, chapter 6.4. Over the range of realistically attainable amplitude and phase responses the two solutions returned comparable results for applied fields $\mathbf{H_0 \ll h}$ with increased deviations for the higher values of both coefficients, $\mathbf{b_1 > 1.5x10^{-2}A^{-1}m}$ or $\mathbf{b_2 > 5x10^{-2}Rads/Am^{-1}}$. The analytical solution only will be discussed here.

The Analysis resulted in the terms for the mixer output signal shown in equation 9.4 for the d.c. term and equation 9.5 for the term at the fundamental frequency. The predicted mixer output being given by equation 9.6.

$$\frac{X_0}{2} = \beta a_1 \cos\left(\phi_0 + \frac{2hb_2}{\pi}\right)\left[\frac{1}{2} - \frac{hb_1}{\pi}\right] \qquad 9.4$$

$$Y_1 = -\beta a_1 \frac{2H_0}{\pi}\left[b_1 \cos\left(\phi_0 + \frac{2hb_2}{\pi}\right) + b_2 \sin\left(\phi_0 + \frac{2hb_2}{\pi}\right)\right] \qquad 9.5$$

$$V_{mix} \approx \frac{X_0}{2} + Y_1 \sin \omega_m t + ... \qquad 9.6$$

The response of the signal at the modulation frequency obtained from the analysis can be seen to be directly proportional to the applied magnetic bias field $\mathbf{H_0}$. The sensitivity of the magnetometer system depends on the sharpness of the slope of the output signal at the modulation frequency to the applied bias field. The only magnetometer system variable parameters in equation 9.5 are the modulation amplitude **h** and the total phase change ϕ_0. The model would suggest that these two coefficients do not contribute directly to the slope of the response but through a phase term. Three important results can be extracted from equation 9.5 in order to return different system operating conditions and relate the magnitude of the total phase change ϕ_0 to the other coefficients . The result shown in equation 9.7 for which the response to the magnetic field of the fundamental signal was a maximum given by $\partial^2 Y_1/\partial H_0 \partial \phi_0 = 0$. Equations 9.8 and equation 9.9 show the values for the total phase change for which the response was independent of the amplitude response and depends on the phase response, $\phi_{0_{phase}}$

and the total phase change for which the response was independent of the phase response and depends on the amplitude response, $\phi_{0_{amp}}$. The phase setting $\phi_{0_{phase}}$ also returns a zero d.c. mixer output signal when substituted into equation 9.4.

$$\phi_{0_{opt}} = \tan^{-1}\left(\frac{b_2}{b_1}\right) - \frac{2hb_2}{\pi} \qquad 9.7$$

$$\phi_{0_{phase}} = (2n+1)\frac{\pi}{2} - \frac{2hb_2}{\pi} \qquad n = 0, 1, 2, .. \qquad 9.8$$

$$\phi_{0_{amp}} = -\tan^{-1}\left(\frac{b_1}{b_2}\right) - \frac{2hb_2}{\pi} \qquad 9.9$$

The Linear System Response Model was studied in great detail for realistically attainable amplitude responses, $\mathbf{b_1=8x10^{-3}A^{-1}m}$ and phase responses , $\mathbf{b_2=3x10^{-2}Rads/Am^{-1}}$ from the magnetic transducers constructed from the REEL 1 METGLAS 2826MB amorphous alloy. It was observed that the phase for the optimum response, $\phi_{0_{opt}}$ was not far removed from that of the purely phase response dependent response $\phi_{0_{phase}}$ and that the magnitude of the response to magnetic field was only marginally reduced at $\phi_{0_{phase}}$. For a phase setting $\phi = \phi_{0_{opt}}$ increasing the phase response coefficient $\mathbf{b_2}$ above the measured value had a far greater effect on the overall magnitude of the mixer output field response than an increase in $\mathbf{b_1}$. The increase of $\mathbf{b_1}$ for a phase setting $\phi_{0_{phase}}$ had a detrimental effect on the field response. The converse of this would be expected to be true if $\mathbf{b_1>b_2}$. The slope of the fundamental system response was not only found to be independent directly of the modulation amplitude but also of the modulation frequency.

A further analysis carried out in chapter 6.6 used response functions obtained from direct digitisation of the measured curves. Although only a crude approximation could

be made to the effects of hysteresis the results suggested that the discontinuities observed in the measured data played an important role in producing the sharp fundamental frequency signal responses to field observed experimentally at the mixer output.

9.4 Magnetometer System Performance.

The magnetometer system was analysed as a whole and individual components studied in order to optimise the operation of the system. The magnetometer system was then fully characterised in order to specify its current capabilities.

9.4.1 The Analysis of the magnetometer Feedback Loop.

The effective time constant of the feedback loop was governed by not only the time constant of the lock-in amplifier but also by the total gain of the feedback loop. The relationship between the effective time constant and these two parameters was not immediately obvious. A study was, therefore, undertaken similar to that of Koo *et al* [1987] in order to elucidate the link. From a theoretical analysis of the feedback loop two important results were obtained. The tracking efficiency of the loop was how closely the feedback signal matched the signal to be nulled, how closely the feedback field nulled the field to be measured. The tracking efficiency was given by equation 9.10, where **K** was the total loop gain of the system. The effective time constant of the system was given by equation 9.11, where τ was the lock-in amplifier time constant. The effective time constant governs the response time of the magnetometer system and hence the magnetic measurement bandwidth.

$$T.E. = \frac{K}{1+K} \qquad 9.10$$

$$\tau_{eff} = \frac{\tau}{1+K} \qquad 9.11$$

These two results were verified experimentally for the magnetometer system Figure 7.2 and Figure 7.3. The total loop gain was calculated from the linear response model. This gave a short-fall in the required gain to obtain a match between the theoretical and the measured results as would be expected from Figure 6.5b. The short-fall was corrected by introducing an additional gain factor of eight, Figure 7.4. The significance for the operation of the magnetometer system was that the time constant of the lock-in amplifier could be increased reducing noise from the system components without sacrificing any bandwidth in the magnetic measurement simply by increasing the total loop gain. This was most easily achieved through an increase in the lock-in amplifier gain.

9.4.2 The optimisation of the Modulation Signal.

The modulation signal was optimised in chapter 7.3 by examining the response to magnetic field of the signal at the fundamental of the modulation frequency at the output of the mixer element. This was accomplished from a study of the lock-in amplifier output as a function of field with the magnetometer feedback loop disconnected. Both the effects of varying the modulation amplitude and the modulation frequency were established. The optimum conditions were determined from the slope of the magnetic field response about the field origin. An optimum modulation frequency of $\mathbf{f_m}$**=870Hz** was proposed. Above this frequency eddy current damping was proposed as the cause of the degradation in the response, whereas, for lower frequencies the more marked decrease could be attributed to either predominant magnetomechanical damping or a some unknown **1/f** effect.

The study of the modulation amplitude revealed an increase in the response slope with decreasing modulation amplitude. This was in disagreement with the result of the linear response model which suggested no modulation amplitude dependence. The digitised fitted model of chapter 6.6 possibly lends an explanation to this phenomena as

discussed in chapter 9.3. It was suggested that the amplitude and phase response low field "discontinuities" played a more important role for low modulation field amplitudes and that the effect of the less sharp regular response was reduced. The optimum modulation amplitudes were found to reflect the field positions of the features in the magnetic transducer amplitude and phase responses being of the order of $\mathbf{h \approx 3Am^{-1}_{peak}}$.

9.4.3 The Study of Individual System Components.

The individual components making up the magnetometer system were investigated in order to optimise their operating conditions and reveal any limiting factors. The main components potentially limiting the performance of the system were the mixer element and the lock-in amplifier. The performance of the individual devices was very much dependent on the design of the device and differed for example between two mixers performing an identical task but from a different design approach. The factors limiting the performance of the shear wave magnetometer from a number of different instruments was therefore investigated.

A detailed investigation of two different mixer elements was undertaken. One of which was a passive device (the SRA-3) the other contained active components (the 429A). Although these two devices performed the same operation their characteristics were starkly different. The passive device had a substantially smaller output noise which was related to the local oscillator input magnitude. For a local oscillator amplitude between **0.4 - 4.0V** the output noise was $\mathbf{v_{out} < 6nV/Hz^{1/2}}$. The active device had a local oscillator independent output voltage noise $\mathbf{v_{out} \approx 1.2\mu V/Hz^{1/2}}$. The gain of the mixer β was defined in terms of the magnitude of the output voltage relative to the signal input voltage for a specified local oscillator amplitude, see chapter 6.3 and chapter 7.4.2. The maximum measured gain of the passive device was $\beta \approx \mathbf{0.64}$ for a local oscillator amplitude of $\mathbf{v_{local} \approx 0.4V_{p\text{-}p}}$, whereas, that of the active device was $\beta \approx \mathbf{0.24}$ for a local oscillator

amplitude of $v_{local} \approx 10V_{p-p}$. The passive mixer was observed to saturate for input voltages much greater than $v_{in} > 0.7V_{p-p}$, Figure 7.7a. The active device was linear for inputs up to the magnitude of its supply rail voltages, Figure 7.7b. The consequence of the passive mixer saturation was that input amplitudes applied above the saturation level only produced an output signal equivalent to an input signal at the saturation level. Although the active device was linear over a greater range the device supply rails were only approximately an order of magnitude greater than the saturation limit of the passive device and its noise level more than two orders of magnitude greater than the passive device. The active device, therefore, was unlikely to out-perform the passive device even for signals above the saturation level of the passive device.

As with the mixer element the performance of a number of different lock-in amplifiers was studied with two typical instruments being covered in detail. This investigation demonstrated some of the primary considerations which have to be taken into account when implementing a lock-in amplifier into a feedback loop. The two instruments considered were the SR510 and the E.G & G. 5210.

The most significant parameter of the lock-in amplifiers was found to be the output noise voltage of the instrument. The output noise of the lock-in amplifier produces a current noise in the feedback loop and hence a magnetic field noise in the feedback solenoid. The current noise was inversely proportional to the feedback resistance and therefore the lock-in amplifier output noise was studied in conjunction with feedback resistance. From an approximate calculation the Johnson noise in the feedback resistance was dismissed as insignificant for $R_f < 1M\Omega$. The equivalent Johnson field noise was calculated to be $12fT/(\Omega Hz)^{1/2}$ for the feedback solenoid with **1311** turns per metre. The output voltage noise of the lock-in amplifiers depended on the gain of the lock-in amplifier and produced in general two distinct regions. For low gains the output noise was dominated by the noise of the lock-in amplifier d.c. output stage and was independent

of the a.c. gain of the input amplifier. In the case of the SR510 it was proposed that the limiting factor actually came from instabilities in the reference signal electronics. For high gains the input amplifier noise dominates and increases with increasing a.c. gain. The estimated minimum detectable field for the magnetometer dominated by lock-in amplifier output noise was calculated as $\approx$**3pT/Hz$^{1/2}$** for the E.G & G. 5210 and $\approx$**30pT/Hz$^{1/2}$** for the SR510. These measurements were taken over a **0.3 - 4.3Hz** bandwidth and are for a feedback resistor R_f=**2kΩ** and a lock-in amplifier peak to peak gain of **10^2**. The SR510 result was confirmed from field noise measurements taken with a very low noise fluxgate magnetometer. The equivalent field noise for the two lock-in amplifiers with a number of different input terminations including the two mixers were shown in Figure 7.15 for a feedback resistance of R_f=**2kΩ**. The results demonstrate that unless the magnetic transducer response was such that the gain of the lock-in amplifier could be reduced below **10^2** the passive mixer and the E.G & G 5210 would always out-perform any other arrangement. In reality the lock-in amplifier gain required to achieve a magnetic field measurement bandwidth greater than a few Hertz was of the order of **10^4** for a lock-in amplifier time constant of τ=**3s**. An increase in the time constant to reduce the lock-in amplifier output noise as shown in Figure 7.12 required an increase in gain of the lock-in amplifier to maintain the system bandwidth this would result in the amplification of input amplifier noise. For a specified magnetic measurement bandwidth the optimum amplifier condition was found to be a maximum time constant for which the gain was not sufficient to produce amplification of the input amplifier noise. Figure 7.3 demonstrates that for a minor increase in the time constant above τ=**3s** requires a substantial increase in total loop gain to maintain the system bandwidth.

The effects of the magnitude of the mixer output signal at the second harmonic of the modulation frequency on the lock-in amplifier output noise was also studied for the

SR510 and although in general this did not pose a problem, Figure 7.18, an active low noise second harmonic notch filter was constructed giving **18dB** of second harmonic rejection. This was described in detail in chapter 7.5.4.

9.4.4 Optimum Shear Wave Magnetometer Performance.

The magnetic field noise of the magnetometer system was investigated for the individual instrument components operating under optimum conditions. A measurement bandwidth for the magnetometer was chosen to be **<10Hz** as from chapter 2 this can be seen as the frequency range of most interest. A standard system set-up procedure was adopted and was found in general to return reproducible magnetometer performances for the METGLAS 2826MB REEL 1 magnetic transducer employed.

An investigation of the magnetometer performance as a function of modulation field amplitude revealed the expected dependence of the magnetometer system magnetic field noise. The noise was observed to be a minimum for a modulation amplitude corresponding to the approximate field positions of the amplitude and phase response low field features, Figure 7.22.

The effect of increasing the feedback resistor and thus reducing any noise contributions from the lock-in amplifier output can be seen most clearly in Figure 7.29. If the magnetic field noise was lock-in amplifier output noise dominated the order of magnitude increase in the feedback resistance would have been expected to produce an equivalent order of magnitude decrease in the measured field noise. This, however, was not observed suggesting a sizable contribution to the field noise from noise in the magnetic transducer. A further improvement in the performance by reducing the noise floor would require an increase in the response of the magnetic field transducer as implied by equation 9.12. $\mathbf{H}_n$ is the magnetic field noise, ϕ_n the phase noise, ϕ the total phase change and $\left(\frac{1}{\mu}\right)(\partial\mu/\partial H)$ the fractional change in the shear modulus with applied field,

chapter 7.1.

$$H_n = 2\left(\frac{\phi_n}{\phi}\right)\left[\frac{1}{\mu}\frac{\partial\mu}{\partial H}\right]^{-1} \qquad 9.12$$

The current optimum performance of the system was taken as being represented by Figures 7.25a & b with a feedback resistance $\mathbf{R_f=22k\Omega}$. The bandwidth of the magnetometer was measured as **4Hz**, Figure 7.28. For the lock-in amplifier time constant of τ**=3s** this represent an approximate total open loop gain of **K≈70**, Figure 7.4. The dynamic range of the lock-in amplifier with a feedback resistance $\mathbf{R_f=2k\Omega}$ was measured as **8700nT** this would be an order of magnitude smaller for $\mathbf{R_f=22k\Omega}$. Figure 9.1 shows the current measured performance of the shear wave magnetometer compared to other devices discussed in chapter 2.

The performance of the pulse mode shear wave magnetometer introduced in chapter 7 was also investigated although no extensive instrumentation optimisation scheme was undertaken. The performance was notably worse than that of the shear wave magnetometer and is clearly shown by a comparison of Figure 7.32 with Figure 7.29. The pulse mode system suffers from an inherent reduction in the signal to noise ratio of the system brought about by the pulse gating of the signal combined with this the amplitude response of the field annealed materials were only marginally better than those of the "as-received" materials, Figure 5.22.

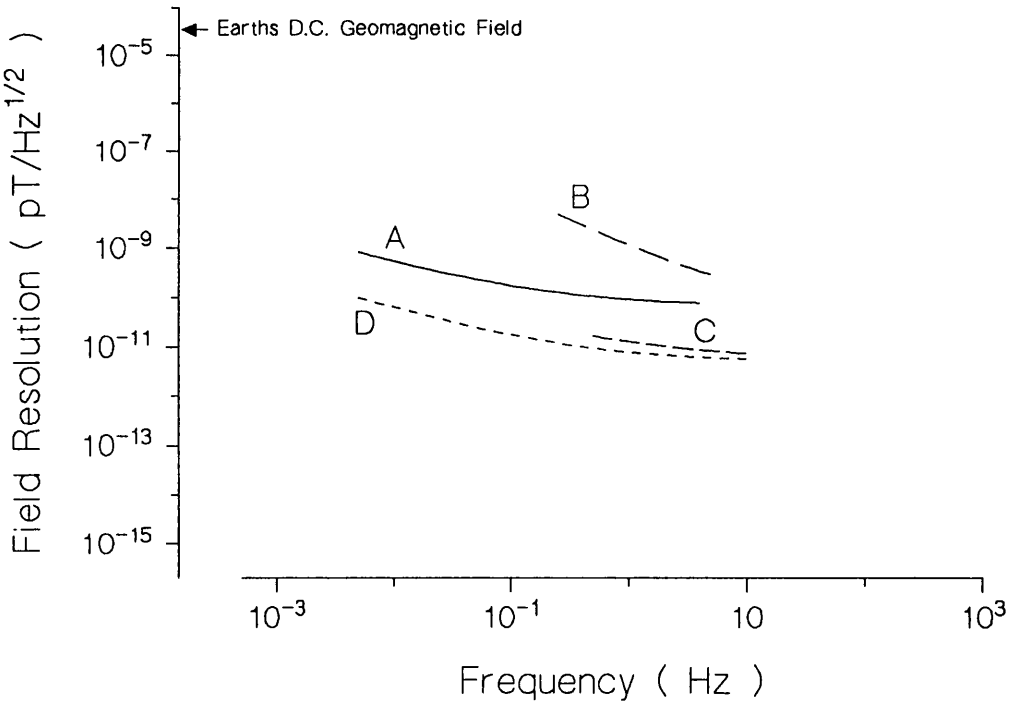

Figure 9.1 Comparison of amorphous alloy magnetometer performances.

A. Shear wave magnetometer

B. Amorphous wire fibre optic magnetometer, Koo *et al* [1989].

C. D.C. fibre optic magnetometer, Dagenais *et al* [1989].

D. Magnetisation strain mode, Mermelstein [1992].

9.5 The Shear Wave Magnetometer Temperature Analysis.

The effects of fluctuations in the ambient temperature on the magnetometer output were examined in chapter 8. This was achieved in terms of a further analytical model of the magnetometer system which included temperature effects. This was carried out in conjunction with experimental observations.

The temperature dependences of both the physical dimensions of the magnetic transducer and the shear modulus of the magnetic transducer were modelled using linear functions with coefficients of expansion α_1 and α_2 respectively. The field dependences

were assumed to be quadratic in nature with a magnetostriction quadratic coefficient of C_q and a shear modulus coefficient γ. With the exclusion of second order small quantities the analysis returned functions describing the harmonic content of the output of the mixer element given in equations 9.13 & 9.14, the d.c. and fundamental components respectively.

$$X_0 = \frac{\beta A_{2_{(II)}}}{2}\cos\left\{\phi_0\left[1+\eta\Delta T+\frac{(2C_q+\gamma)}{2}h^2\right]\right\} \qquad 9.13$$

$$X_1 = -\frac{\beta A_{2_{(II)}}}{2}\sin\left\{\phi_0\left[1+\eta\Delta T+\frac{(2C_q+\gamma)}{2}h^2\right]\right\}\phi_0(2C_q+\gamma)hH_0 \qquad 9.14$$

The important consequence of these two results was that the temperature dependence observed in the fundamental signal could be removed by an appropriate setting of the total phase change along the magnetic transducer. For $[\eta\Delta T+(2C_q+\gamma)h^2/2] \ll 1$ then the fundamental signal becomes temperature independent if equation 9.15 is satisfied. The fundamental term was then given by equation 9.16 for $\gamma \gg C_q$.

$$\phi_0 \approx \Phi = (2n+1)\frac{\pi}{2} \qquad n=0,1,2,.. \qquad 9.15$$

$$X_1 = -\left\{\frac{\beta A_{2_{(H)}}\phi_0\gamma h}{2}\right\}H_0 \qquad 9.16$$

The result shows the expected bias field dependence of the mixer output and also suggests that the slope of the response depends on the magnitude of the modulation signal. This contradicts the results of the linear response model and the experimental observations although it was in keeping with the analysis of the feedback loop of the

fibre optic magnetometer carried out by Koo *et al* [1987]. This discrepancy was due to the functional forms used to describe the responses. The phase nulling technique, however, was correct for any even function used to describe the magnetic field responses. Of further interest was that at this phase setting for ϕ_0 the d.c. mixer output term was in quadrature and hence zero in magnitude. The phase setting also corresponds to a phase response only dependence of the magnetometer system shown from the linear response model.

The zero condition of the d.c. mixer output term at the correct phase setting facilitated a phase feedback loop enabling a temperature cancellation to be implemented as shown in Figure 8.2. Experimental observations demonstrated that for the magnetometer system with no feedback the thermal drift was **44.9nT/°C**, whereas, for the stabilized system this was improved to **9.5nT/°C**. The feedback system employed was not fully optimised, and further improvements should be possible in this figure.

9.6 Future Considerations.

The approach to further improvements in the performance of the magnetometer would appear to be mainly from a materials aspect. An improvement in the magnetic transducer response was suggested as being crucial in reducing the phase noise of the magnetometer system. Two immediate alternative directions can be suggested: either a controlled surface crystallisation in order to enhance the response already observed in the METGLAS 2826MB REEL 1 material, or by amorphous thin film deposition following the route of Inoue discussed in chapter 4. A preliminary investigation into sputter deposition resulted in the production of an amorphous film, although no success was achieved in implementing the film as a magnetic transducer, Kilby [1990].

A further system improvement should result from the implementation of an (analogue) temperature stabilization phase feedback loop. An investigation into the

modulation field amplitude dependence of the magnetometer system employing the METGLAS 2826MB REEL 2 material could also prove informative. This was not carried out as this material gave a poor magnetometer performance compared to the partially crystallised REEL 1 material.

10 REFERENCES.

ABADEER W. & ELLIS D. : "Magnetic field detection using coherent magnetisation rotation in a thin magnetic film.", *J. Appl. Phys.*, **42**, pp1439-1440, 1971

ACUNA M. H. & PELLERIN C. J. : "A miniature two-axis fluxgate magnetometer.", *IEEE Trans. Geosci. Electron.*, **GE-7**, pp252-260, 1969

ACUNA M. H. : "Fluxgate magnetometers for outer planets exploration.", *IEEE Trans. Mag.*, **MAG-10**, pp519-523, 1974

ANDERSON P. M. : "Magnetomechanical coupling, ΔE effect and permeability in FeSiB and FeNiMoB alloys.", *J. Appl. Phys.*, **53**, pp8101-8103, 1982

ARAI K. I., TSUYA N., YAMADA M. & MASUMOTO T. : "Giant ΔE effect and magnetomechanical coupling factor in amorphous $Fe_{80}P_{13}C_7$ ribbons.", *IEEE Trans. Mag.*, **MAG-12**, pp936-938, 1976

ARAI K. I. & TSUYA N. : "Magnetomechanical coupling and variable delay characteristics by means of giant ΔE effect in Iron rich amorphous ribbon.", *J. Appl. Phys.*, **49**, pp1718-1720, 1978

ASCHENBRENNER H. & GONBAU G. : "Eine Anordnung zur Registrierung rascher magnetischer Stoerungen.",*Hochfreq Tech. Elektroakust.*, **47**, pp177-181, 1936

ATALAY S. & SQUIRE P. T. : "Comparative measurements of the field dependence of Young's modulus and shear modulus in Fe-based amorphous wire.", *J. Appl. Phys.*, **70**, pp6516-6518, 1991

ATALAY S. & SQUIRE P. T. : "Torsional pendulum system for measuring the shear modulus and internal friction of magnetoelastic amorphous wires.", *Meas. Sci. Technol.*, **3**, pp735-739, 1992a

ATALAY S. & SQUIRE P. T. : "Magnetoelastic properties of cold-drawn FeSiB amorphous wires.", Paper **JC-01** Intermag '92 St Louis, To appear in *IEEE Trans. Mag.* Sept. 1992b

BACZEWSKI L. T., KACZKOWSKI Z. & LIPINSKI E. : "ΔE effect and internal friction in Co-Si-B metallic glasses.", *J. Mag. Mag. Mater.*, **41**, pp346-348, 1984

BADER C. J. & FUSSELL R. L. : "A low power magnetometer utilising inductance variation in thin permalloy film.", *Proc. Intermag conference '65*, pp8.6-1 - 8.6-5 April 1965

BAGG M. T. : Private Communication, Admiralty Research Establishment, Portland, Dorset, 1989

BASSIR K. : "Ultrasonic Attenuation In Amorphous Alloys.", Internal Report, School of Physics, University of Bath, Claverton Down, Bath, Avon BA2 7AY, 1991a

BASSIR K. : Unpublished results, School of Physics, University of Bath, Claverton Down, Bath, Avon BA2 7AY, 1991b

BECKER J. J. : "A new mechanism for magnetic annealing in amorphous metals.", *IEEE Trans. Mag.*, **MAG-14**, pp938-940 , 1978

BECKER J. J. : "Effect of surface treatment and thinning on magnetic properties of rapidly quenched amorphous alloy ribbons.", *J. Appl. Phys.*, **52**, pp1905-1907 , 1981

BERLINCOURT D. A., CURRAN D. R. & JAFFE H. : "Piezoelectric and piezomagnetic materials and their function in transducers.", in Physical Acoustics, Mason W. P. Ed., New York: Academic Press, pp202-203, 1964

BERLINCOURT D. A. : "Piezoelectric Crystals and Ceramics.", in Ultrasonic Transducer Materials, Mattiat O. E. Ed., London: Plenum Press, pp63-124, 1971

BERRY B. S. & PRITCHET W. C. : "Magnetic annealing and directional ordering of an amorphous ferromagnetic alloy.", *Phys. Rev. Lett.*, **34**, pp1022-1025 , 1975a

BERRY B. S. & PRITCHET W. C. : "Vibrating reed internal friction apparatus for films and foils.", *IBM J. Res. Develop.*, **19**, pp334-343 , 1975b

BERRY B. S. & PRITCHET W. C. : "Magnetoelastic Phenomena in amorphous alloys.", *AIP Conf. Proc.*, **34**, 1976a

BERRY B. S. & PRITCHET W. C. : "Magnetoelastic and internal friction of an amorphous ferromagnetic alloy.", *J. Appl. Phys.*, **47**, pp3295-3301 , 1976b

BLOOM A. L. : "Principles of operation of the Rubidium vapour magnetometer.", *Appl. Opt.*, **1**, pp61-68, 1962

BOLL R. : "Sensors, A Comprehensive Survey.", Vol 5, Magnetic Sensors, Boll R. & Overshott K. J. Ed. Weinheim: VCH, 1989

BOZORTH R. M. : "Ferromagnetism.", New York: Van Nostrand, 1951

BROUHA M. & VAN DER BORST J. : "The effect of annealing conditions on the magnetomechanical properties of Fe-B-Si amorphous ribbons.", *J. Appl. Phys.*, **50**, pp7594-7596, 1979

BRUGEL D., GIBBS M. R. J. & SQUIRE P. T. : "On the choice of a magnetostrictive transducer for interferometric magnetometry.", *J. Appl. Phys.*, **64**, pp3149-3152, 1988

BUCHOLTZ F., KOO K. P., SIGEL G. H. & DANDRIDGE A. : "Optimization of the fibre/metallic glass bond in fibre optic magnetic sensors.", *J. Lightwave Tech.*, **LT-3**, pp814-817, 1985

BUCHOLTZ F., YUREK A. M. KOO K. P. & DANDRIDGE A. : "Low frequency submicrogauss Fibre Optic magnetometer.", *Electron. Lett.*, **23**, pp985-987, 1987a

BUCHOLTZ F., KOO K. P., YUREK A. M., McVICKER J. A. & DANDRIDGE A. : "Preparation of amorphous metallic glass transducers for use in fibre optic magnetic sensors.", *J. Appl. Phys.*, **61**, pp3790-3792, 1987b

BUCHOLTZ F., KOO K. P. & DANDRIDGE A. : "Effect of external perturbations on Fiber Optic magnetic sensors.", *J. Lightwave Tech.*, **LT-6**, pp507-512, 1988

BUCHOLTZ F., DAGENAIS D. M. & KOO K.P. : "Mixing and detection of RF signals in Fibre Optic magnetostrictive sensors.", *Electron. Lett.*, **25**, pp1285-1286, 1989a

BUCHOLTZ F., DAGENAIS D. M. & KOO K.P. : "High frequency Fibre Optic magnetometer with 20fT/$\sqrt{\text{Hz}}$ resolution.", *Electron. Lett.*, **25**, pp1719-1721, 1989b

CAMPBELL P. : "Magnetoresistive sensors for rotary position encoders.", *IEEE Trans. Mag.*, **MAG-26**, pp2029-2031, 1990

CANDIDI M., ORFEI R., PALUTAN F., & VANNAROMI G. : "FFT analysis of a space magnetometer noise.", *IEEE Geosci. Electron.*, **GE-12**, pp23-28, 1974

CASTRO P. S. & STUCKI F. F. : "Thin film field sensor.", U. S. patent 3 271 665, 1966

CHEN H. S. : "Structural Relaxation In Metallic Glasses", in Amorphous Metallic Alloys, Luborsky F. E. Ed. London: Butterworth, pp169-184, 1983

CHOU T., IGARASHI M. & NARUMIYA Y. : "Ultrathin Iron based amorphous ribbon cores.", Digest **FC-04**, Intermag '92, St Louis Missouri.

CHUNG R. & WEBER R. : "A Terfenol based magnetostrictive diode laser magnetometer.", *IEEE Trans. Mag.*, **MAG-27**, pp5358-5360, 1991

CHUNG R., WEBER R. & JILES D. C. : "Highly magnetostrictive rare earth Iron intermetallic compounds for a magnetostrictive laser diode magnetometer.", *J. Mag. Mag. Mater.*, **104-107**, pp1455-1456, 1992

COHEN D. & KAUFMAN L. A. : "Magnetic determination of the relationship between the S-T segment shift and the injury current produced by coronary artery occlusion.", *Circulation Res.*, **36**, pp414-424, 1976

CULLITY B.D. : "Introduction to Magnetic Materials.", London: Addison Wesley 1972

DAGENAIS D. M., BUCHOLTZ F., FOO K. P. & DANDRIDGE A. : "Detection of low frequency magnetic signals in a magnetostrictive Fiber Optic sensor with suppressed residual signal.", *J. Light. Tech.*, **LT-7**, pp881-886, 1989

DANDRIDGE A., TVETEN A. B., SIGEL G. H., WEST E. J. & GIALLORENZI T. G. : "Optical fibre magnetic field sensors.", *Electron. Lett.*, **16**, pp408-409, 1980

DANDRIDGE A., TVETEN A. B. & GIALLORENZI T. G. : "Homodyne demodulation scheme for Fiber Optic sensors using phase generated carrier.", *IEEE J. Quantum Elec.*, **QE-18**, pp1647-1653, 1982

DATTA A., NATHASINGH D., MARTIS R. J., FLANDERS P. J. & GRAHAM C. D. Jr : "Saturation and engineering magnetostriction of an iron base amorphous alloy for power applications.", *J. Appl. Phys.*, **55**, pp1784-1786, 1984

DAVIS J. R., DINGER R. J., & GOLDSTEIN J. : "Development of a superconducting ELF receiving antenna.", *IEEE Trans. Antennas Propagat.*, **AP-25**, pp223-231, 1977

DAVIS A. R., PATRICK S. S., DANDRIDGE A. & BUCHOLTZ F. : "Remote Fibre Optic AC magnetometer.", *Electron. Lett.*, **28**, pp271-273, 1992

DIBBERN U. : "Sensors based on the magnetoresistive effect.", *Sens. Actuators.*, **4**, pp221-227, 1983

DING B. Z., LU J., WANG J. T., LI S. L. & LI G. S. : "Effect of surface features on magnetic anisotropy for amorphous FeBSi ribbons.", *J. Mag. Mag. Mater.*, **89**, pp70-74, 1990

DUHAJ P. & KACZKOWSKI Z. : "Magnetomechanical coupling and ΔE effect in $Fe_{80.2}Cr_2Si_{3.8}B_{14}$ metallic glass.", *Mat. Sci. Eng.*, **A133**, pp223-225, 1991

DUPONT-ROC S. HAROCHE S. & COHEN-TANNOUDJI C. : "Detection of very weak magnetic fields (10^{-9}G) by ^{87}Rb zero field level crossing resonances.", *Phys. Lett.*, **28A**, pp638-639, 1969

DURET D., MOUSSAVI M. & BERANGER M. : "Use of high performance electron spin resonance materials for the design of scalar and vectorial magnetometers.", *IEEE Tran. Mag.*, **MAG-27**, pp5405-5406, 1991

DWIGHT K. : "Experimental techniques with general applicability for the study of magnetic phenomena.", *J. Appl. Phys.*, **38**, pp.1505-1509, 1967

DYAL P. & GORDON D. I. : "Lunar surface magnetometers.", *IEEE Trans. Mag.*, **MAG-9**, pp226-231, 1973

EDGAR A. : "Drift in low-cost lock-in amplifiers.", *J. Phys. E: Sci. Instrum.*, **22**, pp.551-553, 1989

EGAMI T. : "Structure and magnetism of amorphous alloys.", *IEEE Trans. Mag.*, **MAG-17**, pp2600-2605, 1981

ENGELTER A. : "A fluxgate magnetometer with a metallic glass core.", *IEEE Trans. Mag.*, **MAG-22**, pp.299-300, 1986

EWING W. M., JARDETZKY W. S. & PRESS F. : "Elastic Waves in Layered Media.", New York: McGraw-Hill, 1957

FAHMY A. H. & ADLER E. L. : "Propagation of acoustic surface waves in multilayers : A matrix description.", *Appl. Phys. Lett.*, **22**, pp495-497, 1973

FONER S. : "Special magnetic measurement techniques.", *J. Appl. Phys.*, **38**, pp.1510-1519, 1967

FONER S. : "Review of magnetometry.",*IEEE Trans. Mag.* , **MAG-17**, pp.3358-3363, 1981

FRANK C. E. : "Weak magnetic field measurement using permalloy film UHF resonance.", *Rev. Sci. Instrum.*, **37**, pp875-880, 1966

FUJII T., INOUE M. & MIYAMA T. : "Analysis of magnetoelastic wave propagation in a magnetic slab.", *J. Appl. Phys.*, **53**, pp8113-8115, 1982

GALLOP J. C. & PETLEY B. W. : "SQUIDs and their applications.", *J. Phys. E: Sci. Instrum.*, **9**, pp417-429, 1976

GANGULY A. K., DAVIS K. L., WEBB D. C. & VITTORIA C. : "Magnetoelastic surface waves in a magnetic film piezoelectric substrate configuration.", *J. Appl. Phys.*, **47**, pp2692-2704, 1976

GANGULY A. K., DAVIS K. L. & WEBB D. C. : "Magnetoelastic surface waves on the (110) plane of highly magnetostrictive cubic crystals.", *J. Appl. Phys.*, **49**, pp759-767, 1978

GERSHENSON M. : "High temperature superconductive Fluxgate magnetometer.", *IEEE Trans. Mag.*, **MAG-27**, pp3055-3057, 1991

GIBBS M. R. J. : "Anisotropy and magnetostriction in amorphous alloys.", *J. Mag. Mag. Mater.*, **83**, pp329-333, 1990

GIBBS M. R. J. : "The effect of large spread in moment directions on anisotropy and magnetostriction in amorphous alloys.", *Proc.* 5th int. conf. Physics of magnetic materials, Poland 1990, pp242-258, Publ., World scientific : Singapore 1991

GIBBS M. R. J. : "Magnetostriction 150 years from the discovery.", European Physical Society 12th Gen. conf. Condensed matter division, 1992

GORDON D. I. & BROWN R. E. : "Recent advances in fluxgate magnetometry.", *IEEE Trans. Mag.*, **MAG-8**, pp76-82, 1972

GREENOUGH R. D. & SCHULZE M. : "Detection of short range order from the ultrasonic and magnetic properties of annealed amorphous metals.", *Non Destr. Test. Eval.*, **5**, pp263-270, 1990

GREIG D., HALL M. J., HAMMOND C., HICKLEY B. J., HO H. P., HAWSON M. A., WALKER M. J., WISER N. & WRIGHT D. G. : "The giant magnetoresistance of Co/Cu superlattices grown by MBE.", *J. Mag. Mag. Mater.*, **110**, pp239-246, 1992

GRIVET P. A. & MALNER L. : "Measurement of weak magnetic fields by magnetic resonance.", *Advan. Electron. Electron phys.*, **23**, pp39-151, 1967

HARTMANN F. : "Resonance magnetometers.",*IEEE Trans. Mag.*, **MAG-8**, pp66-75, 1972

HEDGECOCK P. C. : "Magnetometer experiments in the European space research organization's HEOS satellites.", *Space Sci. Instrum.*, **1**, pp61-82, 1975

HERNANDO A., VAZQUEZ M. & BARANDIARAN J. M. : "Metallic Glasses and Sensing Applications." *J. Phys. E: Sci. Instrum.*, **21**, pp1129-1139, 1988

HERZER G. & HILZINGER H. R. : "Surface crystallisation and magnetic properties in amorphous iron rich alloys." *J. Mag. Mag. Mater.*, **62**, pp143-151, 1986

HODSON P.D. : "Magnetic property control in ferromagnetic amorphous alloys.", Doctorial thesis, University of Cambridge, 1986

HOFFMAN G. R., HILL E. W. & BIRTWISTLE J. K. : "Thin film magnetoresistive vector sensors with submicron gap width.", *IEEE Trans. Mag.*, **MAG-20**, pp957-959, 1984

HUMPHERY F. B. : "Magnetic measurement techniques for thin films and small particles.", *J. Appl. Phys.*, **38**, pp.1520-1527, 1967

IMAMURA M. & SASAKI T. : "A new spiral MEW element using amorphous ribbons with the field-induced anisotropy.", *IEEE Trans. Mag.*, **MAG-20**, pp1412-1414, 1984

IMAMURA M., SASAKI T., SUGIYAMA Y. & YAMASHITA Y. : "Delay characteristics of M.E. wave velocity in amorphous ribbons with induced anisotropy.", *IEEE Trans. Mag. Jap.*, **TJMJ-1**, pp228-230, 1985

INOUE M., FUJII T. & MIYAMA T. : "Propagation properties of magneto-elastic wave in a magnetic slab.", *J. Mag. Mag. Mater.*, **35**, pp158-160, 1983

INOUE M., FUJITA N. & FUJII T. : "Propagation characteristics of magnetoelastic surface waves in magnetic layer on non piezoelectric substrate.", *IEEE Trans. Mag.*, **MAG-20**, pp1406-1408, 1984

INOUE M. : "Analysis of propagation characteristics of magnetoelastic waves by taking account of micro-eddy current damping.", Reprint from the Bulletin of Osaka Prefectural College of Technology, 1985a

INOUE M., KAJIMA A., UENAKA H., MIYAMA T. & FUJII T. : "Fundamental magnetoelastic waves in a highly magnetostrictive slab.", *J. Jap. Appl. Mag. Soc.*, **9**, pp199-202, 1985b

INOUE M., TSUBOI Y., MAKITA A., FUJITA N., MIYAMA T. & FUJII T. : "Effect of eddy current loss on the propagation properties of Magneto-Surface-Acoustic-Waves in a highly magnetostrictive alloy film deposited on glass substrate.", *Jap. J. Appl. Phys.*, **25**, pp157-159, 1986

INOUE M., FUJITA N., YAMAMOTO S., & FUJII T. : "Magneto-Surface-Acoustic-Waves in highly magnetostrictive amorphous sputtered films.", Toyohashi Int. Conf. on Ultrasonic Tech. Toyohashi Japan. Tokyo: MYU Research, 1987a

INOUE M., YAMAMOTO S., FUJITA N. & FUJII T. : "Local detection of Magneto-Surface-Acoustic-Wave in highly magnetostrictive amorphous film by light probing technique.", *IEEE Trans. Mag.*, **MAG-23**, pp3334-3336, 1987b

INOUE M., FUJITA N., TSUBOI Y. & FUJII T. : "Diminution of micro eddy current losses in Magneto-Surface-Acoustic-Wave propagation utilising multilayered magnetostrictive film separated by insulating layers.", *Jap. Appl. Phys.*, **27**, pp169-171, 1987c

INOUE M. : "Study on the propagation properties of magnetoelastic waves in Fe-based highly magnetostrictive amorphous materials and their applications.", Doctorial Thesis; Osaka Pref. College of Technology, 1989.

INOUE M., TSUBOI Y., YOKOKAWA N. & FUJII T. : "Love-Type Magneto-Surface-Acoustic-Wave in multilayered highly magnetostrictive film separated by insulating layers.", *IEEE Trans. Mag.*, **MAG-26**, pp1465-1467, 1990

IRONS H. R. & SCHWEE L. J. : "Magnetic thin film magnetometers for magnetic field measurement.", *IEEE Trans. Mag.*, **MAG-8**, pp61-65, 1972

JAKUBOVICS J. P. : "Magnetism and Magnetic Materials." London: Institute of Metals, 1987

JACKSON D.A., PRIEST R., DANDRIDGE A. & TVETEN A.B. : "Elimination of drift in a single-mode optical fibre interferometer." *Appl. Opt.*, **19**, p2926, 1980

JILES D. : "Introduction to Magnetism and Magnetic Materials.", London: Chapman & Hall, 1991

JOULE J. P. : "On a new class of magnetic forces.", *Sturgeon's Annals of Electricity*, **8**, pp219-224, 1842

KACZKOWSKI Z. & MALKINSKI L. : "ΔE effect and internal friction in the amorphous Fe-Si-B alloy.", *J. Mag. Mag. Mater.*, **41**, pp343-345, 1984

KERNEVEZ N. & GLENAT H. : "Description of a high sensitivity CW scalar DNP-NMR magnetometer.", *IEEE Trans. Mag.*, **MAG-27**, pp5405-5406, 1991

KERSEY A. D., CORKE M. & JACKSON D. A. : "Phase shift nulling d.c. field fibre optic magnetometer.", *Electron. Lett.*, **20**, pp573-574, 1984

KERSEY A. D., JACKSON D. A. & CORKE M. : "Single mode fibre optic magnetometer with d.c. bias field stabilisation.", *J. Lightwave Tech.*, **LT-3**, pp836-840, 1985

KIKUCHI M., FUKAMICHI K., MASUMOTO T., JAGIELINSKI T., ARAI K. I. & TSUYA N. :"Giant ΔE effect and elinvar characteristics in amorphous Fe-B binary alloys.", *Phys. Stat. Sol. (a)*, **48**, pp175-181, 1978

KILBY C.F. : "Sputter deposition of amorphous films.", Unpublished results, School of Physics, University of Bath, Claverton Down, Bath, Avon BA2 7AY, 1990

KISS S., MAŁKINSKI L., POSGAY G. & POGANY L. : "Influence of tensile stresses on the magnetic field dependences of internal friction and of shear modulus of the FeSiB metallic glass.", *Acta. Phys. Pol.*, **A76**, pp157-161, 1989.

KITTEL C. : "Physical theory of ferromagnetic domains.", *Rev. Mod. Phys.*, **21**, pp541-583, 1949

KOBELEV N. P. & SOIFER YA. M. : "Magnetic-field-induced changes in the damping and velocity of acoustic waves in amorphous ferromagnetic materials.", *Sov Phys. Sol. Stat.*, **28**, pp236-240, 1986

KOBELEV N. P., SOIFER YA. M., SHTEINBERG V. G. & LEVIN YU. B. : " 'Giant' ΔE effect and magnetomechanical damping in amorphous ferromagnetic ribbons.", *Phys. Stat. Sol. (a)*, **102**, pp773-780, 1987

KOCH H. : "SQUID sensors" in "Sensors, A Comprehensive Survey.", Vol 5, Magnetic Sensors, Boll R. & Overshott K. J. Ed. Weinheim: VCH, pp381-446, 1989

KOO K. P., BUCHOLTZ F., DANDRIDGE A. & TVETEN A. B. : "Stability of a fibre optic magnetometer.", *IEEE Trans. Mag.*, **MAG-22**, pp141-144, 1986

KOO K. P., DANDRIDGE A., BUCHOLTZ F. AND TVETEN A. B. : "An analysis of a fiber-optic magnetometer with magnetic feedback.", *J. Lightwave Tech.*, **LT-5**, pp1680-1685, 1987

KOO K.P., BUCHOLTZ F., DAGENAIS D. & DANDRIDGE A. : "A compact Fiber Optic magnetometer employing an amorphous metal wire transducer.", *IEEE Photon. Technol.*, **1**, pp464-466, 1989

KULIK T., LATUSZKIEWICZ J. & MATYJA H. : "Effect of ribbon dimensions on the magnetic properties of metallic glasses.", *Mat. Sci. Eng.*, **A133**, pp236-240, 1991

LANZEROTTI L. J. : Private communication 1973 in PRIMDAHL F. "The Fluxgate Magnetometer.", *J. Phys. E: Sci. Instrum.*, **12**, p249, 1979

LEMCKE M. : "Metallographic examination of soft magnetic glasses.", *Struers Metallographic News*, **3**, pp13-15, 1989

LIEBERMANN H. H. : "Amorphous Metallic Alloys.", in Amorphous Metallic Alloys, Luborsky F. E. Ed. London: Butterworth, pp26-39, 1983

LIVINGSTON J. D. : "Magnetomechanical properties of amorphous metals.", *Phys. Stat. Sol. (a)*, **70**, pp591-596, 1982

LUBORSKY F., BECKER J. & RICHARDO M. : "Magnetic annealing of amorphous alloys.", *IEEE Trans. Mag.*, **MAG-11**, pp1644-1649, 1975

MADURGA V., VAZQUEZ M., BARANDIARAN J. M., NIELSEN O. V. & HERNANDO A. : "On the second order elastic effects in amorphous ribbons under torsion.", *J. Phys. D: Appl. Phys.*, **17**, ppL127-L132, 1984

MAŁKINSKI L. & MAŁKINSKI W. : "Electronic system for the measurement of elastic moduli and internal friction of thin metallic ribbons.", *Meas. Sci. Technol.*, **1**, pp277-281, 1990

MATTHEWS H. & VAN DER VAART H. : "Magnetoelastic Love waves.", *Appl. Phys. Lett.*, **15**, pp373-375, 1969

MAY J. : "Guided Wave Ultrasonic Delay Lines.", in Physical Acoustics, Mason W. P. Ed., New York: Academic Press, pp418-481, 1964

McPHERRON R. L., COLEMAN P. J. Jr & SNARE R. C. : "ATS-6 UCLA fluxgate magnetometer.",*IEEE Trans. Aerosp. Electron. Syst.*, **AES-11**, pp1110-1116, 1975

MEEKER T. R. & MEITZLER A. H. : "Guided Wave Propagation in Elongated Cylinders and Plates.", in Physical Acoustics, Mason W. P. Ed., New York: Academic Press, pp112-166, 1964

MEITZLER A. H. : "Ultrasonic delay lines for digital data storage.", *IRE Trans. Ultrasonic Eng.*, **UE-9**, pp30-37, 1964

MERMELSTEIN M. D. : "Fundamental limit to the preformance of Fibre optic metallic glass d.c. magnetometers.", *Electron. Lett.*, **21**, pp1178-1179, 1985

MERMELSTEIN M. D. : "Magnetoelastic amorphous metal fluxgate magnetometer.", *Electron Lett.*, **22**, pp.525-526, 1986a

MERMELSTEIN M. D. : "Fiber Optic polarimetric DC magnetometer utilizing a composite metallic glass resonator.", *J. Lightwave Tech.*, **LT-4**, pp.1376-1380, 1986b

MERMELSTEIN M. D. : "Coupled mode analysis for magnetoelastic amorphous metal sensors.", *IEEE Trans. Mag.*, **MAG-22**, pp442-444, 1986c

MERMELSTEIN M. D., ASKINS C. & DANDRIDGE A. : "Stress relieved magnetoelastic amorphous metal d.c. magnetometer.", *Electron Lett.*, **23**, pp280-281, 1987

MERMELSTEIN M. D. & DANDRIDGE A. : "Low frequency magnetic field detection with a magnetostrictive amorphous metal ribbon.", *Appl. Phys. Lett.* ,**51** , pp.545-547, 1987a

MERMELSTEIN M. D. & DANDRIDGE A. : "Directional Characteristics of field annealed magnetoelastic amorphous metal magnetometers.", *J. Appl. Phys.*, **61**, pp3793-3795, 1987b

MERMELSTEIN M. D. & DANDRIDGE A. : "Dynamic sensitivity and thermal noise analysis of a magnetoelastic amorphous metal low frequency magnetometer.", *Appl. Phys. Lett.*, **51**, pp1640-1642, 1987c

MERMELSTEIN M. D. & DANDRIDGE A. : "Magnetostrictive metallic glass ribbon gradiometer.", *Electron. Lett.*, **24**, pp895-896, 1988

MERMELSTEIN M. D. & DANDRIDGE A. : "Metallic glass ribbon probe for the measurement of magnetic field first and second order field gradients.", *Electron. Lett.*, **26**, pp501-502, 1990

MERMELSTEIN M. D. : "A magnetoelastic metallic glass low frequency magnetometer.", *IEEE Trans. Mag.*, **MAG-28**, pp36-56, 1992

MIKLICH A. H., KINGSTON J. J., WELLSTOOD F. C., CLARKE J., COLCLOUGH K., CHAR K. & ZAHARCHUK G. : "Sensitive $YBa_2Cu_3O_{7-X}$ thin film magnetometer.", *Appl. Phys. Lett.*, **59**, pp988-990, 1990

MITCHELL M. A., CULLEN J. R., ABBUNDI R., CLARK A. & SAVAGE H. : "Magnetoelastic effects in $Fe_{71}Co_9B_{20}$ glassy ribbons.", *J. Appl. Phys.*, **50**, pp1627-1629, 1979

MOORJANI K. & COEY J. M. D. : "Magnetic Glasses.", Amsterdam: Elsevier, 1984

NAROD B., BENNET J. R., STROM OLSEN J., NEZIL F. & DUNLAP R. : "An evaluation of the noise performance of Fe Co and B amorphous alloys in ring core Fluxgate magnetometers.", *Can. J. Phys.*, **63**, pp1468-1472, 1985

NIELSEN O. V., HERNANDO B., MADURGA V. & GONZALES J. M. : "Experiments concerning the origin of stress anneal induced magnetic-anisotropy in metallic-glas ribbons.", *J Mag. Mag. Mater.*, **46**, pp.341-349, 1985

NIELSEN O. V., GUTIERREZ J., HERNANDO B. & SAVAGE H.T. : "A new amorphous ribbon fluxgate sensor based on torsional-creep-induced anisotropy.", *IEEE Trans. Mag.*, **Mag-26**, pp.276-280, 1990

NIELSEN O. V., PETERSEN J. R., FERNANDEZ A., HERNANDO B., SPISAK P., PRIMDAHL F. & MOSER N. : "Analysis of a Fluxgate Magnetometer based on metallic glass sensors.", *Meas. Sci. Technol.*, **2**, pp435-440, 1991

NOWICK A. S. & BERRY B. S. : "Anelastic relaxation in crystalline solids.", New York: Academic Press, 1972

O'DELL T, H. : "Measurement of magnetomechanical coupling factor in amorphous ribbons.", *Phys. Stat. Sol. (a).*, **74**, pp565-572, 1982

O'HANDLEY R. C. : "Temperature dependence of magnetostriction in $Fe_{80}B_{20}$ glass.", *Solid State Comm.*, **22**, pp485-488, 1977

OK H. N. & MORRISH A. M. : "Origin of the perpendicular anisotropy in amorphous $Fe_{82}B_{12}Si_6$ ribbons.", *Phys. Rev. B.*, **23**, pp2257-2261, 1981a

OK H. N. & MORRISH A. M. : "Surface crystallization and magnetic-anisotropy in amorphous $Fe_{40}Ni_{38}Mo_4B_{18}$ ribbons.", *J. Appl. Phys.*, **52**, pp1835-1837, 1981b

OSBORN J. A. : "Demagnetising factors of the general ellipsoid.", *Phys. Rev.*, **67**, pp351-357, 1945

PANT B. B. & KRAHN D. R. : "High sensitivity magnetoresistive transducers.", *J. Appl. Phys.*, **69**, pp5936-5938, 1991

PANTINAKIS A. & JACKSON D. A. : "High sensitivity low frequency magnetometer using magnetostrictive primary sensing and piezoelectric signal recovery.", *Electron Lett.*, **22**, pp.737-738,1986

PAUL M. C., SAUTER G. F. & OBERG P. E. : "Thin ferromagnetic film magnetoresistance magnetometer sensitive to easy axis field components and biased to be insensitive to hard axis field components.", U. S. patent 3 546 579, 1970

PRATT R. H., JONES R. E., EXTANCE P., PITT G. D. & FOULDS K. W. : "Optical Fibre magnetometer using a stabilised semiconductor laser source.", Publ. Standard Telecommunication Laboratories LTD, Harlow Essex, 1984

PRIMDAHL F. : "Temperature compensation of Fluxgate magnetometers.", *IEEE Trans. Mag.*, **MAG-6**, pp819-822, 1970

PRIMDAHL F. : "The Fluxgate magnetometer.", *J. Phys. E: Sci. Instrum.*, **12**, pp.241-253, 1979

PRIMDAHL F., HERNANDO B. NIELSEN O. V. & PETERSEN J.: "Demagnetising factor and noise in the Fluxgate ring core sensor.", *J. Phys. E: Sci. Instrum.*, **22**, pp.1004-1008, 1989

PRUTTON M. : "Thin ferromagnetic films.", London: Butterworth, 1964

PUGH F. W. : "Physics of thin films.", vol 1, Hass G. Ed. New York: Academic press, 1963

RAO K. V. : "Electrical Transport Properties.", in Amorphous Metallic Alloys, Luborsky F. E. Ed. London: Butterworth, pp401-430, 1983

RIPKA P., JIRES F. & MACHACEK M. : "Fluxgate sensor with increased homogeneity.", *IEEE Trans. Mag.*, **MAG-26,** pp2038-2040, 1990

SCHWEE L. J. & IRONS H. R. : "Fast response magnetometer using ferromagnetic resonance in thin films.",*Rev. Sci. Instrum.*, **39**, pp220-222, 1968

SCOUTEN D.C. : "Sensor noise in low-level fluxgate magnetometers.", *IEEE Trans. Mag.*, **MAG-8**, pp223-231, 1972

SHEARD S. M., GAO WEI, GIBBS M. R. J. & CANTOR B. : "The effect of controlled crystallisation and oxidation on the magnetic properties of $Fe_{40}Ni_{40}B_{20}$, $Fe_{78}Si_9B_{13}$ and $Co_{58}Ni_{10}Fe_5Si_{11}B_{16}$ metallic glasses.", *J. Mag. Mag. Mater.*, **78**, pp347-351, 1989

SHIRAE K. : "Noise in amorphous magnetic materials.", *IEEE Trans. Mag.*, **MAG-20**, pp1299-1301, 1984

SMITH R. L. : "Use of unbiased MR sensors in a rigid disk file.", *IEEE Trans. Mag.*, **MAG-27**, pp4561-4566, 1991

SNARE R. C. & McPHERRON R. L. : "Measurement of instrument noise spectra at frequencies below 1 Hertz.", *IEEE Trans. Mag.*, **MAG-9**, pp232-235, 1973

SOBHENDU K., MITRA G. & MITRA A : "A simple fluxgate magnetometer using amorphous alloys.", *J. Mag. Mag. Mater.*, **103**, pp81-85, 1992

SPANO M. L., HATHAWAY K. B. & SAVAGE H. T. : "Magnetostriction and magnetic anisotropy of field annealed Metglas 2605 alloy via d.c. M-H loop measurements under stress.", *J. Appl. Phys.*, **53**, pp2667-2669, 1982

SQUIRE P. T. & GIBBS M. R. J. : "Shear-wave magnetometry using metallic glass ribbon.", *Electron Lett.*, **23**, pp.147-148, 1987a

SQUIRE P. T. & GIBBS M. R. J. : "Fibre-optic dilatometer for measuring magnetostriction in ribbon samples.", *J. Phys. E. Sci. Instrum.*, **20**, pp499-502, 1987b

SQUIRE P. T. & GIBBS M. R. J. : "Shear-wave magnetometry", *IEEE Trans Mag*, **MAG-24**, pp1755-1757, 1988a

SQUIRE P. T. & GIBBS M. R. J. : "Ultrasonic shear-wave absorption in amorphous magnetic ribbons.", *J. Appl. Phys.*, **64**, pp5408-5410, 1988b

SQUIRE P. T., SHEARD S. M., CARTER C. H. & GIBBS M. R. J. : "Digitial M-H plotter for low-coercivity metallic glasses", *J. Phys. E Sci. Instrum.*, **21**, pp1167-1172, 1988c

SQUIRE P. T. & GIBBS M. R. J. : "ΔE effect in obliquely field annealed METGLAS 2605SC.", *IEEE Trans. Mag.*, **MAG-25**, pp3614-3616, 1989

SQUIRE P. T. : "Phenomenological model for magnetisation, magnetostriction and ΔE effect in obliquely field annealed amorphous ribbons.", *J. Mag. Mag. Mater.*, **87**, pp299-310, 1990

STANFORD RESEARCH SYSTEMS INC : "Model SR510 lock-in amplifier.", 1290 D Reamwood avenue Sunnyvale, CA 94089.

STONER E. C. & WOHLFARTH E. P. : "A mechanism of magnetic hysteresis in heterogeneous alloys.", *Phil. Trans. Roy. Soc.*, **A240**, pp599-642, 1948

STUART R. V. : "Vacuum Technology, Thin Films, and Sputtering.", New York: Academic Press, 1983

SWITHENBY S. J. : "SQUIDs and their applications in the measurement of weak magnetic fields.", *J. Phys. E: Sci. Instrum.*, **13**, pp801-813, 1980

TAKEUCHI S. & HARADA K. : "A resonant type amorphous ribbon magnetometer driven by an operational amplifier.", *IEEE Trans. Mag.*, **MAG-20**, pp1723-1725, 1984

THOMAS A. P. : Private communication, University of Bath, Claverton Down, Bath, Avon BA2 7AY, 1990

THOMAS A. P. : "Magnetostriction in Transition Metal-Metalloid Metallic Glasses", Doctorial Thesis, University of Bath, Claverton Down, Bath, Avon BA2 7AY, 1991

THOMAS A. P., GIBBS M. R. J., VINCENT J. N. & RITCHIE S. J. : "Magnetostriction in surface crystallized Fe- and Fe-Ni-based Metallic Glasses", *J. Appl. Phys.*, **70**, pp6528-6530, 1991

THOMAS A. P. & GIBBS M. R. J. : "Anisotropy and magnetostriction in metallic glasses.", *J. Mag. Mag. Mater.*, **103**, pp97-110, 1992

THURSTON R. N. : "Wave Propagation in Fluids and Normal Solids.", in Physical Acoustics, Mason W. P. Ed., New York: Academic Press, pp2-109, 1964

TRIGG D. F., SERSON P. H. & CAMFIELD P. A. : "A solid state electrical recording magnetometer.", Publ. Earth phys. Branch, Dept Energy, Mines and resources, **41**, pp66-80, 1971

TSUYA N. & ARAI K. I. : "Theory of giant ΔE effect in magnetostrictive amorphous ribbons."; *IEEE Trans. Mag.*, **MAG-13**, pp1547-1549, 1977

TSUYA N., ARAI K. I. & YAMADA M. : "Role of magnetostriction on the high frequency magnetic characteristics in amorphous ferromagnetic ribbon."; *Physica*, **86-88B**, pp775-776, 1977

VAN DE VAART H. : "Magnetoelastic Love-wave propagation in metal coated layered substrates.", *J. Appl. Phys.*, **42**, pp5305-5312, 1971

VOHRA S. T. & BUCHOLTZ F. : "Low frequency magnetic field mixing near period doubling bifurcation of a Fiber Optic magnetometer.", *Appl. Phys. Lett.*, **59**, pp169-171, 1991

WANG J. : "Lock-in amplifiers - More complexity lower prices, An interview with Joe Wang.", *Lasers & Optronics*, pp69-76, October 1989

WEBB D.C., FORESTER D. W., GANGULY A. K. & VITTORIA C. : "Application of amorphous magnetic layers in Surface-Acoustic-Wave devices.", *IEEE Trans. Mag.*, **MAG-15**, pp1410-1415, 1979

WEST F. S., ODOM W. J., RICE J. A. & PENN T. C. : "Detection of low intensity magnetic fields by means of ferromagnetic films.", *J. Appl. Phys.*, **34**, pp1163-1164, 1963

WILLCOCK S. N. M. : Private communication , Thorn EMI Central Research Laboratories, Hayes, Middlesex, 1992

WUN-FOGLE M., CLARKE A. E. & HATHAWAY K. B. : "Permeability in "Frozen" high magnetomechanical coupling amorphous ribbons.", *J. Mag. Mag. Mater.*, **54-57**, pp893-894, 1986

WUN-FOGLE M., SAVAGE H. T. & SPANO M. L. : "Enhancement of magnetostrictive effects for sensor applications.", *J. Mater. Eng.*, **11**, pp103-107, 1989

YAGI M., SATO T,. SAKAKI Y., SAWA T. & INOMATA K : "Very low loss ultrathin Co based amorphous ribbon cores.", *J. Appl. Phys.*, **64**, pp6050-6052, 1988

YARIV A. & WINSOR H. : "Proposal for detection of magnetostrictive perturbation of optical fibers.",*Opt. Lett.*, **5**, pp.87-89, 1980

YI ZHANG, MUCK H. M., HERRMANN K., SCHUBERT J., ZANDER W. & BRAGINSKI A. I. : "Low noise $YBa_2Cu_3O_7$ rf SQUID magnetometer.", *Appl. Phys. Lett.*, **60**, pp645-647, 1992